A study of H $\rightarrow \tau\tau$ decays at the ATLAS Experiment

Ruby Ferguson

- Department Of Physics -

- This thesis submitted is for the degree of Doctor of Philosophy -

- Supervisor: Harald Fox -

- September 2024 -

Abstract

This thesis presents a measurement of the CP properties of the Yukawa coupling between the Higgs Boson and τ leptons. The Standard model predicts that CP symmetry is conserved when the Higgs Boson decays into a $\tau\bar{\tau}$ pair. An observable is constructed from the τ lepton decay products that is sensitive to the mixing angle of Higgs CP states, ϕ_τ. Two decay channels are used during this analysis, $\tau_{\text{had}} - \tau_{\text{had}}$, where both τ leptons decay hadronically and the $\tau_{\text{lep}} - \tau_{\text{had}}$ channel where one τ decays hadronically the other decays leptonically. This study was performed using 139 fb^{-1} of proton-proton collision data collected at the ATLAS experiment between 2015 and 2018 at a centre of mass energy, $\sqrt{s} = 13$ TeV. The Standard Model expectation value is $0 \pm 28^\circ$ at the 68% confidence level (CL) and -70/+75° at the 95.5% CL. The measured value of ϕ_τ is $9 \pm 16^\circ$ at the 68% confidence level and $\pm 34^\circ$ at 95.5% confidence level. The measured result disfavours the pure CP-Odd Higgs hypothesis to 3.4 standard deviations (σ). This observation is therefore consistent with the Standard Model.

Declaration of Authorship and Contribution of the Author

I declare that the work contained within this thesis is the author's own work and has not been submitted for the award of a higher degree at any other university. The work described is part of a collaborative effort of the Higgs to Tau Tau CP Analysis Group within the wider ATLAS Collaboration. My contributions to this analysis were primarily focussed around studies in systematic uncertainties (pruning, smoothing and symmetrisation options) detailed in Chapter 10, in addition to the exploration of different methods of calculating our main observable φ^*_{CP} detailed in Chapter φ^*_{CP}. In addition, I was also involved in unblinded data fit studies to understand the differences between simulated and observed results and fit optimisation studies.

The following publication is the published work of the author and others that contain work that has contributed to this thesis, correct as of the time of publication of this thesis:

ATLAS Collaboration. Measurement of the CP properties of Higgs boson interactions with τ-leptons with the ATLAS detector. Eur. Phys. J. C 83, 563 (2023). https://doi.org/10.1140/epjc/s10052-023-11583-y

Ruby Ferguson, MPhys (Hons)

Contents

"I don't make mistakes. I make prophecies which immediately turn out to be wrong."

— Murray Walker

Chapter 1.

Introduction

The Standard Model [1], [2], [3], [4] has proven time and again to be one of the most accurate theories at describing the behaviour of nature ever devised. It was not until 2012 however that a particle consistent with the Higgs boson was finally confirmed by both the ATLAS [5] and CMS [6] collaborations. This verified the mechanism of spontaneous symmetry breaking via the Higgs field; the process by which elemental particles aquire mass. Subsequent to the discovery, work began on investigating the properties of this new particle to confirm its compatability with the Standard Model.

In particular the CP properties of the Higgs are of interest. The SM predicts a CP-even Higgs. Though a purely CP-odd Higgs was excluded to a 99.98% confidence level by a study published in 2015 [7], a mixture of CP states is still possible and could point at physics beyond the Standard Model. If the Higgs were partially CP-odd, it may have contributed to, the matter-antimatter asymmetry that we observe within the universe [8].

In order to investigate the CP properties of the Higgs, a model independent variable can defined from the geometry of the Higgs decay products. In this thesis, specifically Higgs to τ lepton decays are explored using data collected by the ATLAS detector between 2015-2018 at a centre of mass energy $\sqrt{s}$ = 13TeV. The τ leptons are the second heaviest fermion, next to b-quarks, that the Higgs can decay into and they have too short a lifetime to be detected directly but may be reconstructed from its decay products. The τ lepton can decay via two channels, a hadronic and leptonic channel, where its visible decay products are neutral and charged pions for the former and muons and electrons for the latter. Both channels are used in this analysis. A reconstruction of the visible decay products allows a variable to be constructed which

is correlated to the mixing angle of the CP states. Through the use of a likelihood fit, the CP mixing angle of the Higgs may be determined.

For this analysis, where determining the compatability with the Standard Model is the goal, uncertainties play a crucial part. The systematic uncertainties are accounted for by including them in the likelihood fit, they arise primarily from the reconstruction of the physics objects such as jets, τ, π, μ and e. These systematic uncertainties are also subject to their own random fluctuations, the impact of which is reduced through studies into their treatment including smoothing and symmetrisation.

This thesis presents in, Chapter 2, a theoretical overview of the relevant physics, Chapter 3 describes the experiemental apparatus and detectors used for data taking and Chapter 4 details how the raw data is reconstructed into usable physics objects. Chapter 5 introduces the analysis strategy and the methods used to construct the observable for this analysis, Chapter 7 lists the data used, both simulated and measured, for the analysis and how it was generated while Chapter 8 lays out the criteria by which events from this data were selected and categorised. Chapter 9 describes the methods used for estimating the significant background signals for this analysis and Chapter 10 lists the major systematic uncertainties present within this analysis in addition to exploring three studies of smoothing, symmetrisation and pruning to justify their treatment. The results from the analysis are presented in Chapter 11 and Chapter 6 explores additional methods of observable construction for future analyses. Finally Chapter 12 reports the conclusions of this analysis.

Chapter 2.

Theoretical Background

2.1. Overview of the Standard Model

The Standard Model (SM) of particle physics has been developed over the last 70 years to best describe the interactions of fundamental particles and the forces that govern them. It is a powerful tool with very precise prediction powers. From a mathematical perspective the Standard Model is non-Abelian Yang-Mills relativistic field theory. It is described by the overall gauge symmetry $SU(3)_C \times SU(2)_L \times U(1)_Y$ where the $SU(3)_C$ portion describes quantum chromodynamics while the $SU(2)_L \times U(1)_Y$ portion describes the electroweak sector since $SU(2)_L$ is related to weak isospin and $U(1)_Y$ to weak hypercharge. This undergoes spontaneous symmetry breaking and becomes $SU(3)_C \times U(1)_{EM}$ in which the massless bosons associated with the $SU(2)_L \times U(1)_Y$ become the 3 massive bosons (Z, $W^{\pm}$) and the massless photon for the quantum electrodynamics.

The particles within the Standard Model can be divided into bosons and fermions. The Standard Model describes the mediation of the electromagnetic, weak and strong forces through the exchange of vector bosons (bosons of spin 1). Scalar bosons, of which the only known one is the Higgs, is covered in Section 2.1.3 onwards. Gravity is the only known fundamental force not included in the Standard Model. Each force has at least one associated vector boson; these are listed in Table 2.1. Bosons have integer spins and, barring the $W^{\pm}$ bosons, they do not have electromagnetic charge. One more important quantity related to bosons is the J^P where J is the total angular momentum defined as L + S, the sum of orbital angular momentum and spin. In the case of single bosons L=0, so J=S. P is the parity of the boson. This can take values of $+$ or $-$ or, if

not well defined, can be omitted as in the case of $W^{\pm}$ and Z bosons. Photons and Z bosons do not carry charge for the force that they mediate and therefore cannot self interact. Gluons carry colour charge (a colour and a non-corresponding anticolour) and $W^{\pm}$ have electroweak charge and therefore may interact with other bosons of the same species.

Interaction	**Exchanged Boson**	**Mass (GeV)/c^2**	J^P
Strong	Gluon	0	1^{-1}
Electromagnetic	Photon	0	1^{-1}
Weak	$W^{\pm}/Z$	80.377/91.188	1

Table 2.1.: A summary of the three fundamental forces described by the Standard Model.

The fermions in the Standard Model can be divided into two groups: leptons and quarks. These are defined by all having half integer spins, quarks however have colour charge whereas leptons do not. Both quarks and leptons can be further divided by their charges, charge $\frac{2}{3}$ quarks are designated "up-type" and $-\frac{1}{3}$, "down-type". The leptons can be split into charged leptons (with electrical charge -1) and the neutral, neutrinos. These are then divided into 3 generations, each generation contains one of each type (up/down type quarks and charged/neutral leptons). These are summarised in Table 2.2

Fermion Types			Elementary Particle Generation		
Type	Electric Charge	Color	First	Second	Third
Quarks	$-\frac{1}{3}$	r/g/b	down	strange	bottom
	$\frac{2}{3}$	r/g/b	up	charm	top
Lepton	-1	-	electron	muon	tau
	0	-	ν_e	ν_μ	ν_τ

Table 2.2.: A summary of the properties of the fermions of the Standard Model

The Standard Model, despite being an incredible powerful theory, is known to not be a complete description of nature there are a number of phenomena which lay outside its capacity to explain. These include the matter-antimatter disparity seen within our universe, the SM would predict that there should be equally as much matter as antimatter which would annihilate rather than the abundance of matter that

is observed (this is discussed in more detail in Section 2.2.8). It also does not predict neutrino flavour oscillations nor is a description of gravity included.

The particles discussed above are described in the Standard Model by the Lagrangian which consists of 4 parts:

$$\mathcal{L}_{\text{SM}} = \mathcal{L}_{\text{KT}} + \mathcal{L}_{\text{Higgs}} + \mathcal{L}_{\text{Yukawa}} \tag{2.1}$$

$\mathcal{L}_{\text{KT}}$ is the kinetic term (KT) which control the dynamics of the gauge and fermionic fields. $\mathcal{L}_{\text{Higgs}}$ describes the scalar field content of the Lagrangian and the final part $\mathcal{L}_{\text{Yukawa}}$ describes the coupling between the fermionic and the scalar fields. The 4 parts of the Lagrangian are discussed in length in the following sections.

2.1.1. Fermions

Dirac spinors [9], [10] are used to represent the quark and lepton fields (ψ^I) of the Standard Model. The fermionic kinetic term can be expressed as Equation 2.2

$$\mathcal{L}^{\text{Fermions}}_{\text{Kinetic}} = i \cdot \bar{\psi}^I (D^\mu \gamma_\mu) \psi^I \tag{2.2}$$

where $\bar{\psi}^I = \psi^{I\dagger}\gamma^0$ and D^μ is the covariant gauge derivative shown in Equation 2.3

$$D^\mu = \partial^\mu + i\left(g_C \cdot \lambda_a G^\mu_a + \frac{g_L}{2} \cdot \sigma_b W^\mu_b + q_Y \frac{g_Y}{2} \cdot B^\mu\right) \tag{2.3}$$

g_C, g_L and g_Y are the coupling constants for the corresponding gauge groups, λ and σ are the generators of SU(3) and SU(2) which are summed over the components of the gauge fields G,W and B.

2.1.2. Gauge Bosons

The general equation for a gauge field strength tensor is shown in Equation 2.4.

$$F_a^{\mu\nu} = \partial^\mu F_a^\nu - \partial^\nu F_a^\mu + g \cdot f^{abc} F_b^\mu F_c^\nu \tag{2.4}$$

The kinetic term from the gauge bosons is shown in Equation 2.5.

$$\mathcal{L}_{\text{Kinetic}}^{\text{Bosons}} = -\frac{1}{2}(Tr)\left(G^{\mu\nu}G_{\mu\nu}\right) - \frac{1}{2}(Tr)\left(W^{\mu\nu}W_{\mu\nu}\right) - \frac{1}{4}B^{\mu\nu}B_{\mu\nu} \tag{2.5}$$

The first term describes the gluon field strength, the second term describes the SU(2) field strength and the final term contains $B^{\mu\nu} = \partial_\mu B_\nu - \partial_\nu B_\mu$ which is the hypercharge field strength.

2.1.3. The Higgs Boson

The introduction of the Higgs Field and its associated Boson into the Standard Model solves the problem that the force carrying bosons of the electroweak force emerge from the Standard Model without mass. It is however observed that the $W^\pm$ and Z bosons are quite massive. The Brout-Englert-Higgs mechanism is a prescription for breaking of gauge theory spontaneously. It is necessary since if you simply added mass terms to the gauge bosons directly the theory becomes unrenormalisable. Instead a scalar field is introduced with a non-zero vacuum expectation value which breaks the $\text{SU}(2)_L \times U(1)_Y$ symmetry leading to mass terms for both the Higgs Boson itself and the electroweak bosons.

The Lagrangian to describe the Higgs ($\mathcal{L}_{\text{Higgs}}$) is Equation 2.6

$$\mathcal{L}_{\text{Higgs}} = (D^\mu \phi)^\dagger (D_\mu \phi) - V(\phi) \tag{2.6}$$

Where ϕ is two complex scalar fields in a weak isospin doublet shown in Equation 2.7 this has $U(1)$ charge $Y(\phi) = \frac{1}{2}$. $V(\phi)$ is the Higgs potential shown in Equation 2.9 which has a form required by renormalisability and the $SU(2)_L \otimes U(1)_Y$ symmetry.

The covariant derivative of ϕ,$D_\mu\phi$, is shown in Equation 2.8 where W_μ^i and B_μ are the gauge bosons related to the $SU(2)_L$ and $U(1)_Y$ symmetries respectively.

$$\phi = \begin{pmatrix} \phi^+ \\ \phi^0 \end{pmatrix} = \frac{1}{\sqrt{2}} \begin{pmatrix} \phi_1 + i\phi_2 \\ \phi_3 + i\phi_4 \end{pmatrix} \tag{2.7}$$

$$D_\mu\phi = \left(\partial_\mu + igT^iW_\mu^i + i\frac{1}{2}g^{'}B_\mu\right)\phi \tag{2.8}$$

$$V(\phi) = -\mu^2\phi^\dagger\phi + \lambda(\phi^\dagger\phi)^2 \tag{2.9}$$

Different values of μ and λ in the potential $V(\phi)$ can lead to three differing scenarios:

- $\boldsymbol{\lambda < 0}$ - In this scenario no stable minimum occurs.
- $\boldsymbol{-\mu^2\phi^\dagger\phi}$ **and** $\boldsymbol{\lambda > 0}$ - In this scenario, the minimum energy of the potential is at $\phi = 0$.
- $\boldsymbol{-\mu^2 < 0}$ **and** $\boldsymbol{\lambda > 0}$ - In this scenario, the minimum energy is at a non-zero ϕ value.

This last scenario is necessary to spontaneously break the symmetry since $-\mu^2 < 0$ produces a non-zero Vaccuum Expectation Value (VEV).

Due to the symmetry of the Higgs Potential, $V(\phi)$, shown in Figure 2.1, there are infinite amounts of solutions that satisfy the condition $\phi^\dagger\phi$ therefore an arbitrary solution is chosen in Equation 2.10

$$\langle\phi\rangle = \frac{1}{\sqrt{2}} \begin{pmatrix} 0 \\ v \end{pmatrix} \text{ where } v = \sqrt{\frac{-\mu^2}{\lambda}} \tag{2.10}$$

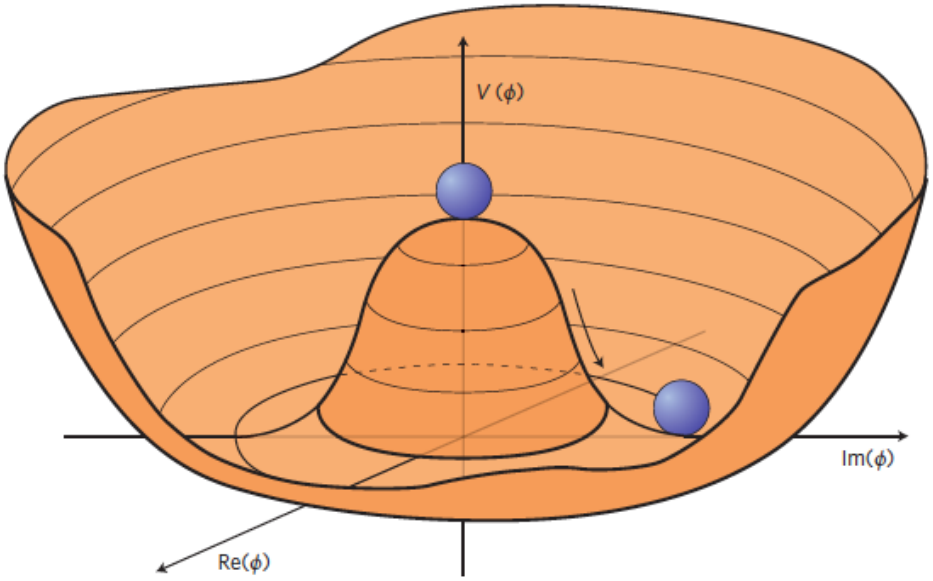

Figure 2.1.: The Higgs scalar field potential, $V(\phi)$, often referred to as the "Mexican hat" potential [11].

Due to the conservation of electrical charge only a neutral scalar field can have a non-zero VEV. Therefore in the solution above since ϕ^+ is 0 and ϕ^0 is interpreted as the neutral component. Importantly $Q(\phi) = 0$. Electromagnetism remains unbroken, but the non-zero vacuum expectation value means that the previous symmetry scheme is broken as described in equation 2.11.

$$SU(2)_L \bigotimes U(1)_Y \rightarrow U(1)_Q \tag{2.11}$$

Where the previous symmetry comprising of a product of SU(2) symmetry applied to only left-handed particles ($SU(2)_L$) and $U(1)_Y$ symmetry acting on hypercharge becomes a U(1) symmetry acting on charged particles through the presence of a non-zero scalar VEV.

In the unitary gauge, by construction there are no Goldstone Bosons, therefore the scalar doublet can be written as in Equation 2.12

$$\phi = \frac{1}{\sqrt{2}} \begin{pmatrix} 0 \\ v + h \end{pmatrix} \tag{2.12}$$

The Kinetic term from the Lagrangian in Equation 2.6 may be considered ignoring any h-mixed terms since the perturbation, h, can be considered insignificant.

$$\begin{aligned} (D^\mu \phi)^\dagger (D_\mu \phi) &= \left| \left(\partial_\mu + \frac{i}{2} g \tau^k W_\mu^k + \frac{i}{2} g' B_\mu \right) \frac{1}{\sqrt{2}} \begin{pmatrix} 0 \\ v \end{pmatrix} \right|^2 \\ &= \frac{v^2}{8} \left| \left(g \tau^k W_\mu^k + g' B_\mu \right) \begin{pmatrix} 0 \\ 1 \end{pmatrix} \right|^2 \\ &= \frac{v^2}{8} \left| \begin{pmatrix} g W_\mu^1 - i g W_\mu^2 \\ -g W_\mu^3 + g' B_\mu \end{pmatrix} \right|^2 \\ &= \frac{v^2}{8} \left[g^2 \left(\left(W_\mu^1 \right)^2 + \left(W_\mu^2 \right)^2 \right) + \left(g W_\mu^3 - g' B_\mu \right)^2 \right] \end{aligned} \tag{2.13}$$

Now the Lagrangian may be interpreted as corresponding to the fields of massive charged bosons defined in Equation 2.14.

$$W_\mu^\pm \equiv \frac{1}{\sqrt{2}} \left(W_\mu^1 \mp i W_\mu^2 \right) \tag{2.14}$$

In the Lagrangian the g^2 term can then be rewritten as 2.15

$$\frac{1}{2} \left(\frac{g v}{2} \right)^2 W_\mu^\dagger W^\mu \tag{2.15}$$

This gives a W mass, m_W shown in Equation 2.16

$$m_W = \frac{g\nu}{2} \tag{2.16}$$

Then it is possible to define two more bosons, Z and A described in Equations 2.17 and 2.18 with their masses

$$Z_\mu = \frac{1}{\sqrt{g^2 + g'^2}} \left(g W_\mu^3 - g' B_\mu \right) \text{ with mass } m_Z = \frac{\nu}{2}\sqrt{g^2 + g'^2} \tag{2.17}$$

$$A_\mu = \frac{1}{\sqrt{g^2 + g'^2}} \left(g' W_\mu^3 + g B_\mu \right) \text{ with mass } m_A = 0 \tag{2.18}$$

In summary:

- Z_μ is the neutral massive boson of the weak force
- $W_\mu^\pm$ are similarly the charged bosons of the weak force
- A_μ is associated with the massless boson exchanged in EM interactions, the photon.

2.1.4. Yukawa Coupling

$\mathcal{L}_{\text{Yukawa}}$ is the term which describes the strength of the the coupling between the Higgs and the fermions, which generates the masses for the fermions after spontaneous symmetry breaking.

$$-\mathcal{L}_{\text{Yukawa}} = \Gamma_u^{mn} \bar{q}_{m,L} \tilde{\phi} u_{n,R} + \Gamma_d^{mn} \bar{q}_{m,L} \tilde{\phi} d_{n,R} + \Gamma_e^{mn} \bar{q}_{m,L} \tilde{\phi} e_{n,R} + \Gamma_\nu^{mn} \bar{q}_{m,L} \tilde{\phi} \nu_{n,R} + \text{Hermitian Conjugate} \tag{2.19}$$

Equation 2.19 has an implicit sum over the indices m and n. Γ^{mn} are the Yukawa coupling matrices, these represent the coupling strength between the Higgs doublet, ϕ

and the different subgroups of fermions (up-type quarks, down-type quarks, charged leptons and neutrinos). The mass terms are required to have a hypercharge of 0, therefore two representations of the Higgs Field are used with hypercharge $Y = \frac{1}{2}$ and $Y = -\frac{1}{2}$ (Equations 2.20 and 2.21) to give masses to down-type quarks and charged leptons, and up-type quarks and neutrinos respectively. It should be noted that right-handed neutrinos do not exist in the SM and therefore they cannot aquire mass through the Yukawa coupling and are therefore ignored in the following derivation.

$$\phi = \begin{pmatrix} \phi^+ \\ \phi^0 \end{pmatrix} \text{ with } \mathrm{Y}(\phi) = +\frac{1}{2} \tag{2.20}$$

$$\phi = \begin{pmatrix} \tilde{\phi}^{0*} \\ -\phi^- \end{pmatrix} \text{ with } \mathrm{Y}(\phi) = -\frac{1}{2} \tag{2.21}$$

Using these representations the fermion masses may be calculated. Equation 2.22 demonstrates this using the first generation fermion family(e,u,d) as an example.

$$\mathcal{L}_{\text{Yukawa}} = f_e \bar{l}_L \phi e_R + f_u \bar{q}_L \tilde{\phi} u_R + f_d \bar{q}_L \phi d_R + \text{Hermitian Conjugate} \tag{2.22}$$

Then the values for ϕ are chosen as in Equation 2.23.

$$\phi = \frac{1}{\sqrt{2}} \begin{pmatrix} 0 \\ v+h \end{pmatrix} \rightarrow \frac{1}{\sqrt{2}} \begin{pmatrix} 0 \\ v \end{pmatrix} \Rightarrow \tilde{\phi} = \frac{1}{\sqrt{2}} \begin{pmatrix} v \\ 0 \end{pmatrix} \tag{2.23}$$

The Lagrangian can be written as in Equation 2.24 where the masses of the particles form the coefficients of each term as shown in Equation 2.25.

$$\mathcal{L}_{\text{Yukawa}} = \frac{f_e v}{\sqrt{2}} \underbrace{(\bar{e}_L e_R + \bar{e}_R e_L)}_{e\bar{e}} + \frac{f_u v}{\sqrt{2}} (\bar{u}_L u_R + \bar{u}_R u_L) + \frac{f_d v}{\sqrt{2}} (\bar{d}_L d_R + \bar{d}_R d_L) \tag{2.24}$$

$$m_i = \frac{f_i v}{\sqrt{2}}, i = e, u, d \tag{2.25}$$

2.2. Symmetries

The fact that symmetries lie at the heart of modern particle physics is undeniable. Their connection to conservation laws through Noether's theorem [12], which states that for every continous symmetry of the action there is a corresponding conservation law, is indepensable to physicists. Discrete symmetries, however, are also a valuable tool with which to examine the nature of the universe and will be explored in this section.

2.2.1. Charge Conjugation

Charge conjugation replaces a particle with its antiparticle while not changing, spin, momentum or mass. The process of charge conjugation is shown in Equation 2.26 where $|P\rangle$ is replaced by its antiparticle $|\bar{P}\rangle$ after charge conjugation.

$$\mathcal{C} : |P\rangle \rightarrow |\bar{P}\rangle \tag{2.26}$$

2.2.2. Parity Conjugation

Parity transformation is the inversion of spatial components. In the context of a 4-vector, the time component is unaffected by the transformation. The process of parity conjugation is shown in Equation 2.27.

$$r = \begin{bmatrix} t \\ \vec{\mathbf{x}} \end{bmatrix}, \mathcal{P} : r \rightarrow \begin{bmatrix} t \\ -\vec{\mathbf{x}} \end{bmatrix} \tag{2.27}$$

The effect of parity transformations on related vectors such as momentum (vector) and angular-momentum (pseudovector) must be considered. Momentum $\vec{\mathbf{p}}$ under a parity operation $\mathcal{P} : \vec{\mathbf{p}} \rightarrow -\vec{\mathbf{p}}$ whereas angular-momentum $\vec{\mathbf{l}} \equiv \vec{\mathbf{x}} \times \vec{\mathbf{p}}$, then when a parity transformation is applied $\mathcal{P} : \vec{\mathbf{l}} \equiv -\vec{\mathbf{x}} \times -\vec{\mathbf{p}} \equiv \vec{\mathbf{l}}$. This demonstrates that while vectors change sign under parity, pseudovectors are invariant. Scalars however such as $\vec{\mathbf{p}} \cdot \vec{\mathbf{p}}$ are invariant under parity whereas pseudoscalars such as $\vec{\mathbf{x}} \cdot \vec{\mathbf{l}}$ change sign.

2.2.3. Time Conjugation

Time Conjugation is the inverse to Parity conjugation, the time component is inverted by the transformation, representing the motion of the system reversing. Thus the process of charge conjugation is shown in Equation 2.28.

$$r = \begin{bmatrix} t \\ \vec{\mathbf{x}} \end{bmatrix}, \mathcal{T} : r \rightarrow \begin{bmatrix} -t \\ \vec{\mathbf{x}} \end{bmatrix} \tag{2.28}$$

2.2.4. C,P,T in Classical Electromagnetism

The behaviours of objects under $\mathcal{C}, \mathcal{P}$ and $\mathcal{T}$ transformations discussed in Sections 2.2.1, 2.2.2 and 2.2.3 can be applied to Maxwell's equations 2.32.

$$\vec{\nabla} \cdot \vec{\mathbf{E}} = 4\pi \cdot \rho \quad \text{Gauss's Law} \tag{2.29}$$

$$\vec{\nabla} \cdot \vec{\mathbf{B}} = 0 \quad \text{Gauss's Law for Magnetism} \tag{2.30}$$

$$\vec{\nabla} \times \vec{\mathbf{E}} = -\frac{1}{c}\frac{\partial \vec{\mathbf{B}}}{\partial t} \quad \text{Faraday's Law of Induction} \tag{2.31}$$

$$\vec{\nabla} \times \vec{\mathbf{B}} = \mu_0 \left(\epsilon_0 \frac{\partial \vec{\mathbf{E}}}{\partial t} + \vec{\mathbf{J}} \right) \quad \text{Ampere's Circuital Law} \tag{2.32}$$

The 4 non-scalar quantities that must transform are $\vec{\mathbf{E}}, \vec{\mathbf{B}}, \vec{\mathbf{J}}, \rho$. The sign changes of $\vec{\mathbf{J}}$ and ρ are trivial to derive based on Maxwell's equations. For charge conjugation, ρ as charge per unit area becomes $-\rho$ and since charge density, $\vec{\mathbf{J}}$, is a product of average velocity of charges($\vec{\mathbf{v}}$) and the charge density (ρ) hence when charge density is inverted by charge conjugation so is current density.For parity conjugation,ρ is unaffected by the transformation, however $J \xrightarrow{\mathcal{P}} -J$ because the direction of the average velocity is inverted by parity. In time conjugation transformations, ρ is unaffected but $\vec{\mathbf{v}}$ is inverted, so $\vec{\mathbf{J}}$ is inverted. In order to derive the sign changes for $\vec{\mathbf{E}}$ and $\vec{\mathbf{B}}$ it is necessary to impose additional conditions such that they can be resolved together and unambigiously which leads to the sign changes summarised in Table 2.3.

	ρ	$\vec{\mathbf{J}}$	$\vec{\mathbf{E}}$	$\vec{\mathbf{B}}$
Charge Conjugation	$\rho \xrightarrow{\mathcal{C}} -\rho$	$J \xrightarrow{\mathcal{C}} -J$	$E \xrightarrow{\mathcal{C}} -E$	$B \xrightarrow{\mathcal{C}} -B$
Parity Conjugation	$\rho \xrightarrow{\mathcal{P}} \rho$	$J \xrightarrow{\mathcal{P}} -J$	$E \xrightarrow{\mathcal{P}} -E$	$B \xrightarrow{\mathcal{P}} B$
Time Conjugation	$\rho \xrightarrow{\mathcal{T}} \rho$	$J \xrightarrow{\mathcal{T}} -J$	$E \xrightarrow{\mathcal{T}} E$	$B \xrightarrow{\mathcal{T}} -B$

Table 2.3.: Table showing the results of Charge, Parity and Time transformations on four variables of Maxwell's equations, electric field($\vec{\mathbf{E}}$), magnetic field ($\vec{\mathbf{B}}$), current density ($\vec{\mathbf{J}}$) and charge density (ρ).

It is possible to express these transformations in terms of the scalar electric potential, ϕ, and the vector magnetic potential, $\vec{\mathbf{A}}$. These transformations are summarised in Table 2.4.

2.2.5. C,P,T in Quantum Electrodynamics

$$\begin{array}{ll} \phi(t,\vec{\mathbf{x}}) \xrightarrow{\mathcal{C}} -\phi(t,\vec{\mathbf{x}}) & \vec{\mathbf{A}}(t,\vec{\mathbf{x}}) \xrightarrow{\mathcal{C}} -\vec{\mathbf{A}}(t,\vec{\mathbf{x}}) \\ \phi(t,\vec{\mathbf{x}}) \xrightarrow{\mathcal{P}} \phi(t,\vec{\mathbf{x}}) & \vec{\mathbf{A}}(t,\vec{\mathbf{x}}) \xrightarrow{\mathcal{P}} -\vec{\mathbf{A}}(t,-\vec{\mathbf{x}}) \\ \phi(t,\vec{\mathbf{x}}) \xrightarrow{\mathcal{T}} \phi(-t,\vec{\mathbf{x}}) & \vec{\mathbf{A}}(t,\vec{\mathbf{x}}) \xrightarrow{\mathcal{T}} -\vec{\mathbf{A}}(-t,\vec{\mathbf{x}}) \end{array}$$

Table 2.4.: Table summarising CPT transformations in terms of the scalar electric potential, ϕ, and the vector magnetic potential, $\vec{\mathbf{A}}$.

Starting with the Lagrangian of QED (Equation 2.33, the covariant form of Maxwell's equations (Equation 2.34) can be derived as the equation of motion.

$$\mathcal{L}_{\text{QED}} = -\frac{1}{4}\mathrm{A}^{\mu\nu}\mathrm{A}_{\mu\nu} - q \cdot \mathrm{J}^{\mu}\mathrm{A}_{\mu} \tag{2.33}$$

$$\partial_{\mu}\mathrm{A}^{\mu\nu} = q \cdot \mathrm{J}^{\nu} \tag{2.34}$$

The quantized forms of A^{μ} and J^{μ} are shown in Equations 2.35 and 2.36.

$$A^{\mu} = \begin{bmatrix} \phi \\ \vec{\mathbf{A}} \end{bmatrix} \tag{2.35}$$

$$J^{\mu} = \begin{bmatrix} \rho \\ \vec{\mathbf{J}} \end{bmatrix} \tag{2.36}$$

Using these definitions it is possible to derive how A^{μ} and J^{μ} change under $\mathcal{C}, \mathcal{P}$ and $\mathcal{T}$ transformations:

The Lagrangian describing the evolution of a spin-0 free particle($\phi(t,\vec{\mathbf{x}})$) is shown in Equation 2.37 while the Free Dirac Equation is shown in Equation 2.38.

$$\begin{aligned} A_\mu(t,\vec{\mathbf{x}}) &\xrightarrow{\mathcal{C}} -A_\mu(t,\vec{\mathbf{x}}) & J^\mu(t,\vec{\mathbf{x}}) &\xrightarrow{\mathcal{C}} -J^\mu(t,\vec{\mathbf{x}}) \\ A_\mu(t,\vec{\mathbf{x}}) &\xrightarrow{\mathcal{P}} A^\mu(t,\text{-}\vec{\mathbf{x}}) & J^\mu(t,\vec{\mathbf{x}}) &\xrightarrow{\mathcal{P}} J_\mu(t,\text{-}\vec{\mathbf{x}}) \\ A_\mu(t,\vec{\mathbf{x}}) &\xrightarrow{\mathcal{T}} A^\mu(-t,\vec{\mathbf{x}}) & J^\mu(t,\vec{\mathbf{x}}) &\xrightarrow{\mathcal{T}} J_\mu(-t,\vec{\mathbf{x}}) \end{aligned}$$

$$\mathcal{L}_{\text{Spin-0}} = \frac{1}{2} \cdot \partial_\mu \phi^\dagger \cdot \partial^\mu \phi - \frac{1}{2} m^2 \cdot \phi^\dagger \phi \tag{2.37}$$

$$\mathcal{L}_{\text{Dirac}} = \bar{\psi}(i \cdot \partial^\mu \gamma_\mu - m)\psi \tag{2.38}$$

The four-currents then associated with these Lagrangians are written as shown in Equations 2.40 and 2.40.

$$J^\mu_{\text{Spin-0}} = i(\phi^\dagger \cdot \delta^\mu \phi - \phi \cdot \partial^\mu \phi^\dagger) \tag{2.39}$$

$$J^\mu_{\text{Dirac}} = \bar{\psi}\gamma^\mu \psi \tag{2.40}$$

The following transformations of the scalar field ϕ under Charge and Parity, result in the correct overall transformation of the current, J^μ shown in Equation 2.2.5

$$\begin{aligned} \phi(t,\vec{\mathbf{x}}) &\xrightarrow{\mathcal{C}} \phi^\dagger(t,\vec{\mathbf{x}}) & \phi^\dagger(t,\vec{\mathbf{x}}) &\xrightarrow{\mathcal{C}} \phi(t,\vec{\mathbf{x}}) \\ \phi(t,\vec{\mathbf{x}}) &\xrightarrow{\mathcal{P}} \phi(t,\text{-}\vec{\mathbf{x}}) & \phi^\dagger(t,\vec{\mathbf{x}}) &\xrightarrow{\mathcal{P}} \phi(t,\text{-}\vec{\mathbf{x}}) \end{aligned}$$

$$\begin{aligned} i(\phi^\dagger \cdot \partial^\mu \phi - \phi \cdot \partial^\mu) &\xrightarrow{\mathcal{C}} i(\phi \cdot \partial^\mu \phi^\dagger - \phi^\dagger \cdot \partial^\mu \phi) \\ &\xrightarrow{\mathcal{C}} -i(\phi^\dagger \cdot \partial^\mu \phi - \phi \cdot \partial^\mu \phi^\dagger) \\ &\xrightarrow{\mathcal{C}} -J^\mu \end{aligned} \tag{2.41}$$

Similarly, using the same logic, it can be seen that this results in the correct transformation of J^{μ} shown in Equation 2.42

$$\begin{aligned} i(\phi^{\dagger} \cdot \partial^{\mu}\phi - \phi \cdot \partial^{\mu}\phi^{\dagger}) \quad &\xrightarrow{\mathcal{P}} \quad i(\phi^{\dagger} \cdot \partial_{\mu} - \phi \cdot \partial_{\mu}\phi^{\dagger}) \\ &\xrightarrow{\mathcal{P}} \quad J_{\mu} \end{aligned} \tag{2.42}$$

By comparison with the $\mathcal{C}$ transformation of the scalar, ϕ, the Dirac Spinor ψ transforms as, $\psi \xrightarrow{\mathcal{C}} C \cdot \bar{\psi}^{T}$, where, in the most general case, C represents a 4x4 matrix. Conversely the opposite transformation is therefore, $\bar{\psi} \xrightarrow{\mathcal{C}} \psi^{T} \cdot \gamma^{0} C^{\dagger} \gamma^{0}$. Equation 2.40 under charge transformation must conform to Equation with Dirac spinors inserted this would be, $\psi^{T} \cdot \gamma^{0} C^{\dagger} \gamma^{0} \gamma^{\mu} C \cdot \bar{\psi}^{T}$. This implies:

$$\gamma^{0} C^{\dagger} \gamma^{0} \gamma^{\mu} C = \gamma^{\mu T} \tag{2.43}$$

,this can be satisfied by setting $C = i \cdot \gamma^{2} \gamma^{0}$. For the $\mathcal{P}$ transformations, $\psi \xrightarrow{\mathcal{P}} \gamma^{0} \cdot \psi$ and conversely $\bar{\psi} \xrightarrow{\mathcal{P}} \bar{\psi} \cdot \gamma^{0}$.

A summary of the transformation of the various quantum objects under parity and charge transformations is provided in Table 2.5.

Field	$\xrightarrow{\mathcal{C}}$	$\xrightarrow{\mathcal{P}}$
$\phi(t, \vec{\mathbf{x}})$	$\phi^{\dagger}(t, \vec{\mathbf{x}})$	$\phi(t, -\vec{\mathbf{x}})$
$\phi^{\dagger}(t, \vec{\mathbf{x}})$	$\phi(t, \vec{\mathbf{x}})$	$\phi^{\dagger}(t, -\vec{\mathbf{x}})$
$\psi(t, \vec{\mathbf{x}})$	$C \cdot \bar{\psi}^{T}(t, \vec{\mathbf{x}})$	$\gamma^{0} \cdot \psi(t, -\vec{\mathbf{x}})$
$\bar{\psi}(t, \vec{\mathbf{x}})$	$\psi^{T}(t, \vec{\mathbf{x}}) \cdot \gamma^{0} C^{\dagger} \gamma^{0}$	$\bar{\psi}(t, -\vec{\mathbf{x}}) \cdot \gamma^{0}$
$V_{\mu}^{+}(t, \vec{\mathbf{x}})$	$-V_{\mu}^{-}(t, \vec{\mathbf{x}})$	$V^{+,\mu}(t, -\vec{\mathbf{x}})$
$A_{\mu}^{+}(t, \vec{\mathbf{x}})$	$A_{\mu}^{-}(t, \vec{\mathbf{x}})$	$-A^{+,\mu}(t, -\vec{\mathbf{x}})$

Table 2.5.: Summary of the transformation properties of scalars, Dirac Spinors, charged vector fields (V^{+}) and axial-vector fields (A^{+}). C is defined here as $i \cdot \gamma^{2} \cdot \gamma^{0}$. The derivations of both charged vector and axial-vector field transformations can be be found in [13].

2.2.6. CPT-Theorem

The Standard Model, as a Lorentz invariant field theory with a Hermitian Hamiltonian and unique ground state, must obey CPT-Symmetry where an interaction is invariant under combined CPT transformation. [14]. In experiment this places a number of constraints on the behaviour of particles relative to their anti-particles. Particles and anti-particles must have the same masses, lifetime and magnetic moments.

It has also been shown that any CPT-violation also violates Lorentz invariance [15] but no violation of CPT-symmetry or Lorentz invariance has been seen experimentally [16].

2.2.7. Experimental evidence of Violations

By the 1950s two particles known as the τ^+ and Θ^+ had been discovered. This presented a puzzle for physicists. τ^+ decays into three pions and Θ^+ into two (shown in Equation 2.44) since pions have parity -1, and parity is multiplicative, τ^+ should have parity -1 and Θ^+ should have parity +1.

$$\begin{aligned} \tau^{\pm} &\rightarrow \pi^{\pm} + \pi^{+} + \pi^{-} \\ \Theta^{+} &\rightarrow \pi^{\pm} + \pi^{0} \end{aligned} \tag{2.44}$$

This difference in parity implied that they should be different particles but evermore precise measurements of lifetimes and masses of these particles indicated they were in fact the same particle. This implies the decays were violating $\mathcal{P}$-parity [17]. The idea that parity violation might offer a solution to the $\tau - \Theta$ problem was proposed by Lee and Yang. They conducted an extensive literature review concerning the state of $\mathcal{P}-$parity violation in weak decays [18]. They found no experimental evidence for or against $\mathcal{C}$ or $\mathcal{P}$ $\mathcal{P}-$parity violating in weak decays, overlooking evidence from β-decays [19] [20]. They did, however, propose a number of experimental methods for determining $\mathcal{P}$-Parity violation in weak decays.

The Wu et al experiment, investigating β-decays of Co^{60} [21] was the first experiment to show P Symmetry was broken in weak interactions based off the proposals of Lee and Yang. The result showed that not only was $\mathcal{P}$-parity violated it was nearly maximally violated. A second experiment was conducted by Garwin and Lederman,

investigating the decays of mesons which showed that $\mathcal{C}-$ and $\mathcal{P}-$parity are broken in the decays.

In order to recover a symmetry, it is possible to combine multiple transformations under which a system is invariant. After showing that independently $\mathcal{C}-$ and $\mathcal{P}-$ parity are both violated, it was then assumed that $\mathcal{CP}$-Symmetry was a fundamental symmetry of nature. In 1964 the first evidence of $\mathcal{CP}$-Symmetry violation was found by Cronin,Fitch,Christenson and Turlay by investigating the decays of neutral kaons. The aim of the experiment was to show that the short lived kaon K_S always decayed into two pions. This would mean that you could assign the two eigenvectors K_1 and K_2 with opposite strangeness and CP to each of the known weak eigenstates K_S and K_L and thus K_L would always decay into 3 pions. The experiment showed, however, that K_S had a small probability of also decaying into 3 pions, thus these decays are a source of indirect CP-Violation. [22]. Evidence of direct CP-violation came in 1988 from the NA31 experiment in which two neutral kaons decayed to two pions [23]. This was confirmed by further evidence provided in 1999 from the KTeV experiment at Fermilab [24] and the NA48 experiment at CERN [25].

From this point onwards, multiple experiments went on to expose more CP-violation in different decays. In 2013 the LHCb experiment at the LHC reported [26] CP-violation in charmless charged two-body decays of B_0 mesons. In 2019, again LHCb announced evidence of CP violation in charmed neutral D mesons decays to both 2 pions and 2 kaons. [27]. In 2020 the T2K neutrino experiment released a paper constraining the value of δ_{CP}, a complex phase enabling CP-violation in the lepton sector; their results indicated CP-violation in the leptonic sector to a confidence interval of 3σ [28].

2.2.8. Motivation for Investigating CP-Violation

One of the most prominent puzzles in modern physics is the asymmetry of matter and antimatter. All currently known sources of CP symmetry are not enough to explain the huge disparity in the amounts of matter/antimatter that are observed, thus providing the motivation for looking beyond the Standard Model. In 1967, Sakharov proposed a set of 3 conditions which must be met by any theory that wishes to explain this asymmetry [29] they were as follows:

1. Baryon Number Violation

2. C-Symmetry and CP-Symmetry Violation
3. Interactions out of the thermal equilibrium

The first condition is fairly simple, if more matter than antimatter is produced, then baryon number cannot be conserved. Similarly, C-symmetry must be broken since the process which generates more baryons that anti-baryons doesn't have a counterpart than equally produces more anti-baryons than baryons resulting in no overall gain. Using the same logic the same must apply to CP-symmetry so that a process producing (right)left-handed (anti)baryons isn't balanced out by an opposite process producing (left)right-handed (anti)baryons. The final Sakharov condition is necessary to maintain the matter-antimatter disparity.

2.2.9. Mechanisms for CP Violation

In the Standard Model, the degree of CP violation for quarks is derived from the CKM Matrix which describes the strength of flavour changing weak interactions. Analogously the PMNS matrix describes lepton mixing and thus dictates the degree of CP violation in leptons. The degree to which both of these introduce CP-violation is not enough to explain the extreme disparity in ratio of matter to antimatter that formed in the early universe. In the SM the Yukawa matrix is real and thus cannot produce CP-violation. If, however, the Higgs that has been observed is actually a superposition of CP-odd and CP-even states as opposed to purely CP-even as predicted by the Standard Model, it allows for the mixing of CP eigenstates as seen in the case of kaons, as discussed earlier. This in turn allows a CP-violating phase to be possible.

2.2.10. Current State of Higgs CP Physics

Since its discovery in 2012, a number of analyses have probed the exact properties of the Higgs. The Standard Model predicts the Higgs to have a spin-parity of 0^+. In analyses conducted during Run 1 of operation at the Large Hadron Collider (LHC) spin parities of 0^-,$1^\pm$ $2^\pm$ were explicitly excluded to 99% Confidence Level (CL) at centre-of-mass energies($\sqrt{s}$) 7-8TeV. These analyses were conducted using Higgs decays to WW, ZZ and $\gamma\gamma$ at both the CMS and ATLAS experiments [30] [31] [32] [7]. During Run 2 where $\sqrt{s}$ had increased to 13-14 TeV, further analyses probed the properties using an variety of different production channels and decay modes. Higgs

produced through the Vector Boson Fusion (VBF) channel and their subsequent $\tau\tau$ decays found no evidence of CP violation [33]. Similarly analyses investigating the CP properties of the Higgs produced in associated with Top quarks (tH or $t\bar{t}H$) and their subsequent decays to $H \to b\bar{b}$ [34] and $H \to \gamma\gamma$ [35] both found the Higgs to have properties compatible with the Standard Model. These studies however are not tightly enough constrained to rule out the possibility of a Higgs being a superposition of CP-Odd and CP-even states,not being entirely CP-even and thus being a small source of CP-Violation.

2.3. Higgs Production

This section gives an overview of the production methods of the Higgs Boson. The Higgs Boson, as described by the Standard Model, can couple to any massive particle (this excludes a coupling to neutrinos). The dominant production model is through gluon-gluon fusion (ggF) with vector boson fusion being subdominant. The Higgs Boson can also be produced through an array of production modes described as "associated production" in which the Higgs is produced via $q\bar{q} \to HX$ where X can be, W,Z,$t\bar{t}$, $b\bar{b}$. The Feynman diagrams of these four main production modes are shown in Figure 2.2.

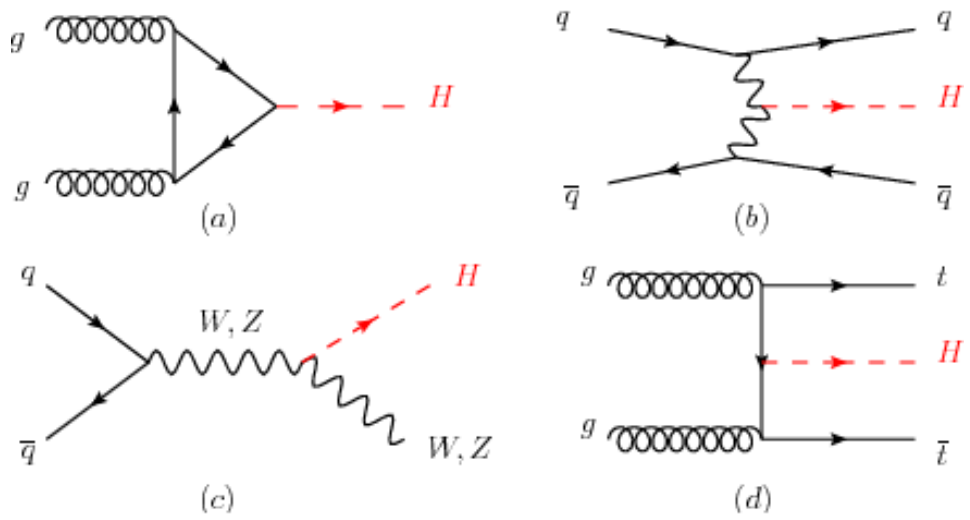

Figure 2.2.: The Feynman diagrams of the main Higgs production modes. (a) gluon-gluon fusion (ggF), (b) vector boson fusion (VBF), (c) W/Z-associated Higgs strahlung (WH/ZH), (d) top quark pair associated production ($t\bar{t}H$) [36].

$\sqrt{s}$(TeV)	ggF	VBF	WH	ZH	ttH	total
13	$48.5^{+4.6\%}_{-6.7\%}$	$3.78^{+2.2\%}_{-2.2\%}$	$1.37^{+2.0\%}_{-2.0\%}$	$0.88^{+4.1\%}_{-3.6\%}$	$0.50^{+7.0\%}_{-10.0\%}$	55.03
14	$54.6^{+4.6\%}_{-6.7\%}$	$4.27^{+2.2\%}_{-2.2\%}$	$1.51^{+1.8\%}_{-1.9\%}$	$0.98^{+4.1\%}_{-3.6\%}$	$0.60^{+7.2}_{-10.0}$	61.96

Table 2.6.: The theoretical production cross sections in pb for production modes of the Higgs Boson with a mass of $M_H = 125.1$ at centre of mass energies $\sqrt{s}$ of 13 and 14TeV [37]

gluon-gluon Fusion (ggF) production of Higgs proceeds through a Top loop as shown in Figure 2.2(a). While the Higgs can couple with all of the quarks, and therefore all their contributions should be accounted for in the cross-section calculation, the Higgs couples far more strongly to Top quarks than the next heaviest fermion, the Bottom quark (approximately 40x stronger). Thus the contribution to the cross section of the bottom quark is 40^2 times less. The cross section for gluon-gluon fusion is computed to next-next-next-to-leading order (N3LO). VBF, WH and ZH production are calculated to next-to-next-to-leading order (NNLO) and $t\bar{t}H$ is calculated to next-to-leading order (NLO). These are summarised in Table 2.6; since cross sections are dependent on $\sqrt{s}$ they are listed for both 13TeV and 14 TeV using a M_H = 125.1 GeV.

2.4. Higgs Decay

The Higgs Boson decays may be categorised one of three ways, it may decay directly into a heavy fermion or a massive boson or it can decay to two photons only by going through a W-Loop. The Feynman diagrams for these are show in Figure 2.3.

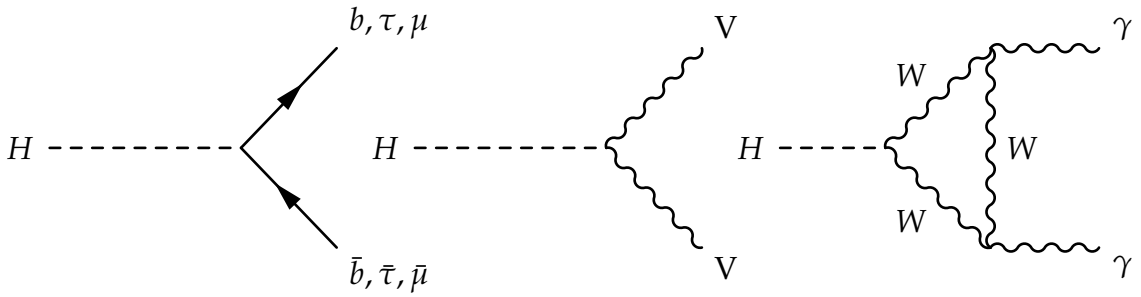

Figure 2.3.: The Feynman diagrams of leading order Higgs boson decays to two fermions (left), to bosons (centre) and to two photons (right)

The branching ratios of the various decay modes are shown in Figure 2.4 as a function of Higgs Mass. The highest branching ratio is that of the $b\bar{b}$ pair since it is the heaviest mass quark the Higgs can decay into given the energy constraints of the LHC. Due to the high QCD background present in the LHC this is a difficult decay to isolate precisely. It is often more fruitful to examine decay modes with lower branching ratios but cleaner signals. The most obvious example of this is the $H \to \gamma\gamma$ which was one of the discovery modes used by ATLAS [5] and CMS [6]; the signal simply consists of two high energy photons. $H \to ZZ$ and $H \to W^+W^-$ both produce similarly clean decay signals by avoiding QCD processes. The former produces secondary decays consisting of $Z \to \mu^+\mu\_$ and the latter $W^+W^- \to e^+\nu_e e^-\bar{e}_e$.

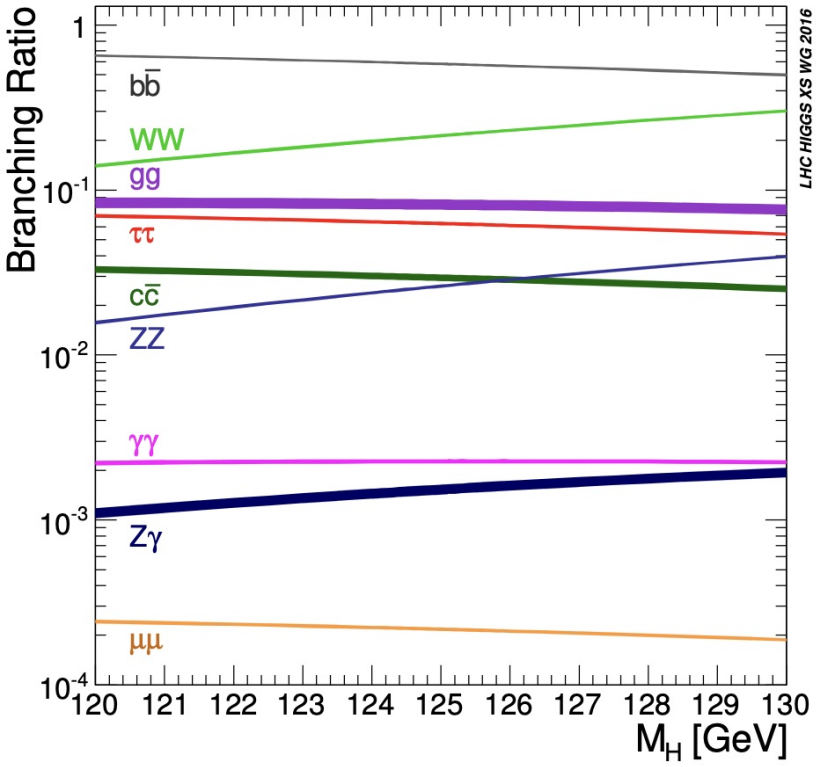

Figure 2.4.: The expected branching ratios for the main decays modes corresponding to different Higgs masses (M_H) [38]

Chapter 3.

Experimental Apparatus

The analysis presented in this thesis uses data collected by the ATLAS detector at the Large Hadron Collider (LHC). This chapter provides an overview of the LHC (Section 3.1 used to deliver the particle beams, the ATLAS detector (Section 3.2) and finally the Trigger System (Section 3.3) used to select data from the collisions.

3.1. The LHC

The CERN complex consists of a number of accelerators used for providing high energy particles for the study of wide ranges of physical phenomena and engineering purposes. The centrepiece of the complex is the Main ring of the Large Hadron Collider. The LHC [39] is the world's largest and most powerful operational particle accelerator. Conceieved in the 1980s with work starting on the collider in 1994, it was designed to explore higher energies than ever before in order to address a number of open questions of physics. One of the main goals to be to find evidence for the existence of the Higgs Boson, a goal which was sucessfully achieved in 2012. A diagram of the CERN and its major experiments are shown in Figure 3.1.

There are a seven detectors installed around the main ring of the LHC. ATLAS and CMS are two general purpose detectors exploring the widest range of physics while also allowing the results of one to be checked against the other. ALICE and LHCb are two specialist experiments the former focuses on making heavy ion measurements, the latter centres on making precise measurements of flavour physics and CP-violation. LHCf looks at particles in the extreme forward pseudorapidity range of ATLAS to simulate cosmic rays while TOTEM looks at the forward region of CMS take precise

measurements of protons. Finally MoEDAL is designed to search for evidence of magnetic monopoles.

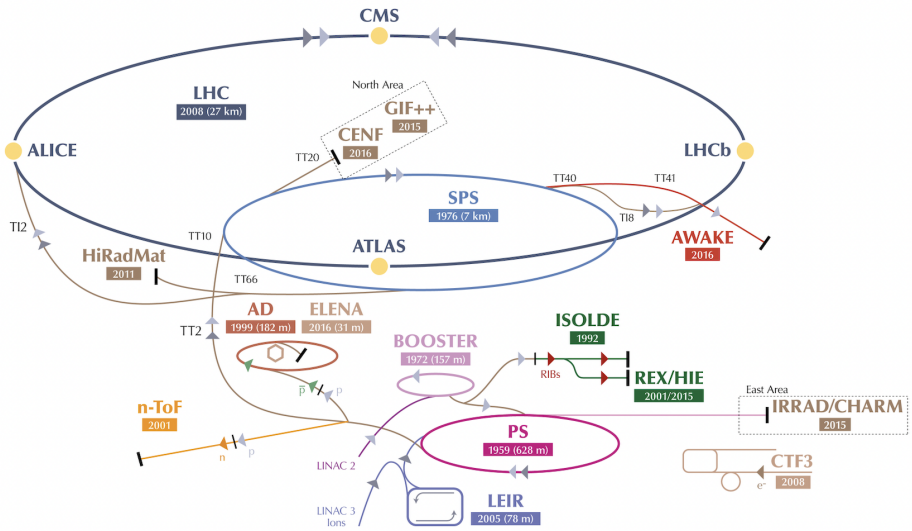

Figure 3.1.: The CERN accelerator complex with major experiments labelled. This image was modified from [40]

3.1.1. Injector Chain

The protons used in the main ring to produce the collider beams must go through a number of stages before they are ready to collide. These steps are performed by a sequence of smaller accelerators collectively known as the "Injector Chain". For generating pp beams, in the first stage, bottled H_2 gas is stripped of its eletrons via an electric field to produce protons which are injected into the *LINAC2* accelerator. This accelerates the protons up 50MeV in bunches from rest. Here they are passed to the *Proton Synchrotron Booster* (PSB) where they are accelerated up to an energy of 1.4GeV. After the PBS the protons are transferred to the *Proton Synchotron*(PS) where their energy is further boosted to 25GeV. At this point they pass into the final stage of the injector chain,*Super Proton Synchotron* (SPS) where their energy is increased up to 450GeV and they are ready to injected into the LHC main ring.

3.1.2. Main Ring

The main ring of the LHC is 27km in circumference and was constructed in the tunnel on the Swiss-Franco border that once housed the previous Large Electron Positron (LEP) collider. It is responsible for the final stage of the proton acceleration up to the 7TeV proton energy required to reach the centre of mass, $\sqrt{s} = 14$TeV (when both beams collide) that the LHC was designed for.

The acceleration is facilitated by 8 Radio frequency cavities per beam (16 in total) which are contained within 2 crymodules per beam. The maximum voltage of each cavity is 2MV resulting in a total of 16MV per beam. The protons are then guided around the ring by 1232 dipole magnets and 392 quadrupole magnets which focus the beams to increase the chances of collisions between the beams.

Along the main ring there are 4 points of interaction which correspond to each of the major experiments spaced around it: ATLAS, CMS, ALICE and LHCb.

3.1.3. Accelerator Physics Terminology

3.1.3.1. Luminosity

Lumonisity is defined as the proptionality factor between the rate of events and the cross-section of colliding particles this is shown in Equation 3.1

$$\frac{dN}{dt} = \mathcal{L} \cdot \sigma_N \tag{3.1}$$

where N is count of events and σ_N is the cross section for a given process.

For the luminosity of head-on bunch crossings this is expressed in Equation 3.2.

$$\mathcal{L} = \frac{N_1 N_2 N_b}{4\pi\sigma_a\sigma_b} \cdot f \tag{3.2}$$

where $N_{1,2}$ is the number of particles in each bunch crossing, N_b is the number of bunches,$\sigma_{a,b}$ is the Gaussian width of each bunch in the plane transverse to the

crossing and f is the frequency of bunch crossings. The term $\frac{N_1 N_2 N_b}{4\pi\sigma_a\sigma_b}$ is the luminosity of a single bunch cross, denoted $\mathcal{L}_{\text{bc}}$.

Since $\mathcal{L}$ often is dependent on time it can be useful to define integrated luminosity,L, as a measure of the total data output of a collider. It is necessary to recognise that the integrated luminosity total delivered by the collider is more than what is recorded. Furthermore not all data will be usable for scientific analysis which then also reduces the effective integrated luminosity of a collider. The differences in these luminosities at ATLAS are illustrated in Figure 3.2.

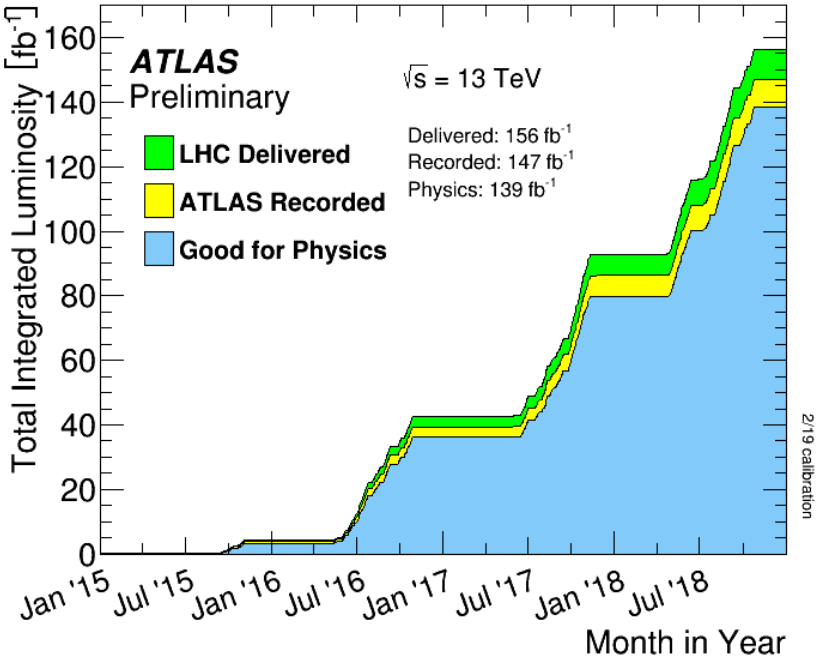

Figure 3.2.: The cumulative luminosity delivered by the LHC (green) against time during Run 2, where yellow represents the proportion recorded by ATLAS and blue represents the proportion that was sufficient quality for use in physics analyses [41]

3.1.3.2. Pile-Up

At each bunch crossing at an interaction point there is likely to be more than one pp interaction. The interaction with the highest p_T, as constructed from its associated vertices, is designated as the "hard-scatter" vertex. This is often the vertex of most interest to physicists. The rest of the interactions are known as "Pile-up". Pile-up is problematic for physics analyses since these unrelated physics, events can complicate

the reconstruction of the physics objects that are being identified from the hard-scatter vertex. Pile-up can be categorised using a Poisson distribution with a mean, μ, shown in Equation 3.3 where σ_{pp} is the pp interaction cross section and is luminosity of a bunch cross as described previously.

$$\mu = \mathcal{L}_{bc} \cdot \sigma_{pp} \tag{3.3}$$

Figure 3.3 shows the pileup distributions weighted to account for differences in luminosity for each of the data-taking years.

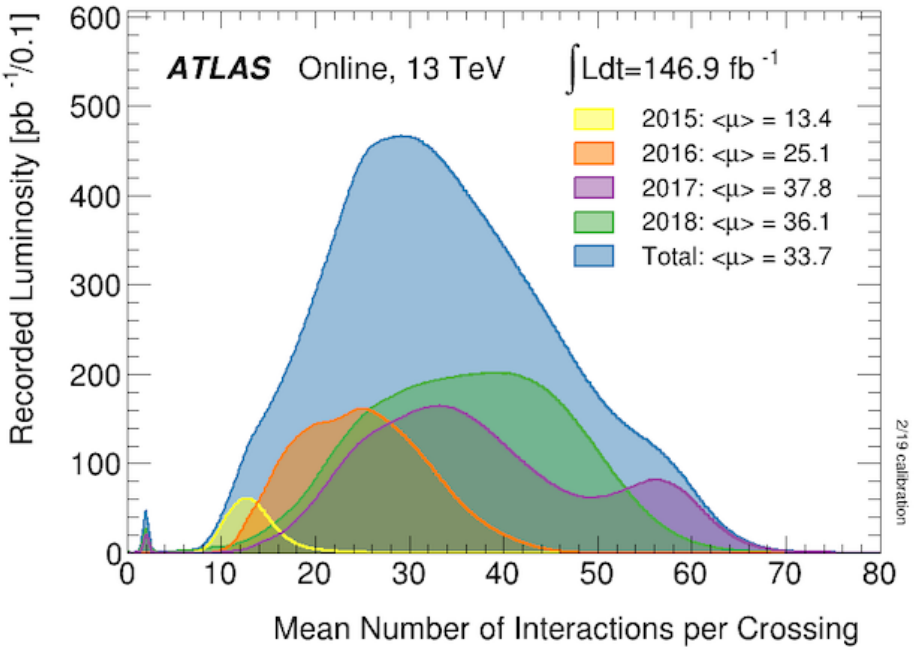

Figure 3.3.: The mean number of interactions per bunch cross, weighted by luminosity, across the years 2015-2018 in pp collisions at $\sqrt{s}$ = 13TeV [42].

3.2. ATLAS Detector

The ATLAS (A Toroidal LHC ApparatuS) is one of the two general purpose particle detectors situated around the Main Ring of the LHC. It is 44mm in length with a diameter of 25m, weighing in at 7000 tonnes it is the largest particle detector ever

built. It is composed of 3 "subdetectors" each performing a specialised role within the detector; the tracking detector, the calorimetry system and the muon spectrometer all of which are discussed in greater depth in the following section. The detector itself is split into three sections, the barrel and two endcaps to ensure near complete 4π solid angle coverage around the interaction point. Figure 3.4 shows an overall schematic of the ATLAS detector.

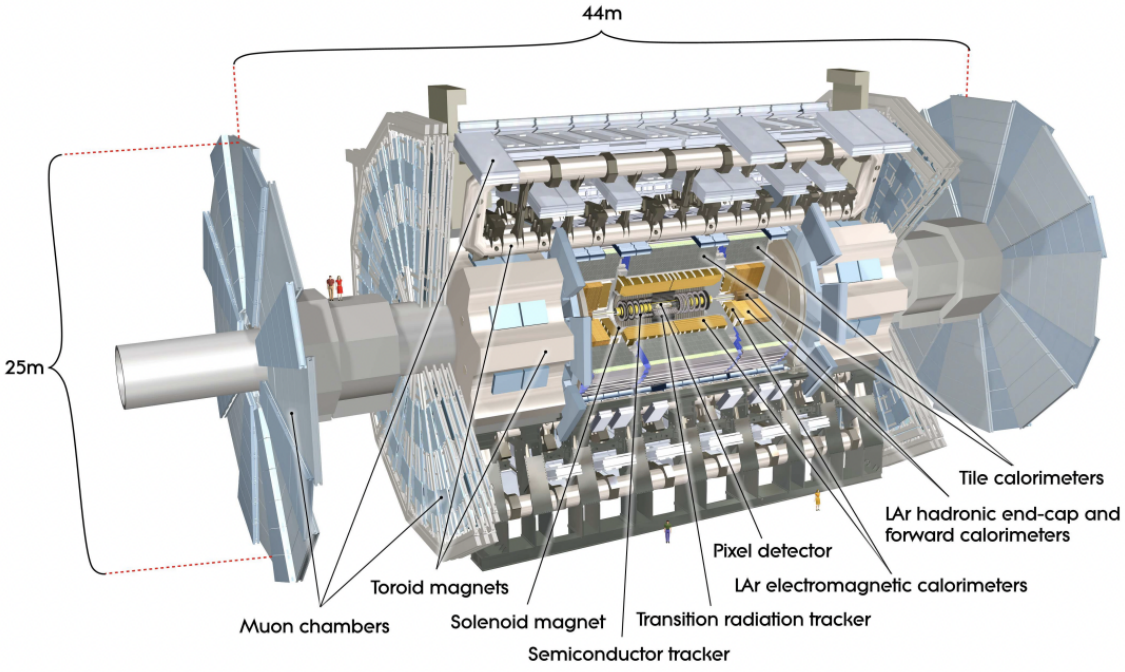

Figure 3.4.: A cutaway diagram showing the various components of the ATLAS detector. Image taken from [43]

3.2.1. ATLAS Specific Information

3.2.1.1. Co-ordinate System

Firstly the cartesian co-ordinates used at ATLAS can be summarised as follows: the interaction point forms the origin of the coordinates system, the z-axis runs along the beamline, and the x-y plane is perpendicular to the beamline. Where the x increases as the coordinate moves towards the centre of the accelerator ring and the y value increase as the coordinate moves upwards. These cartesian coordinates are summarised in Figure 3.5 [43].

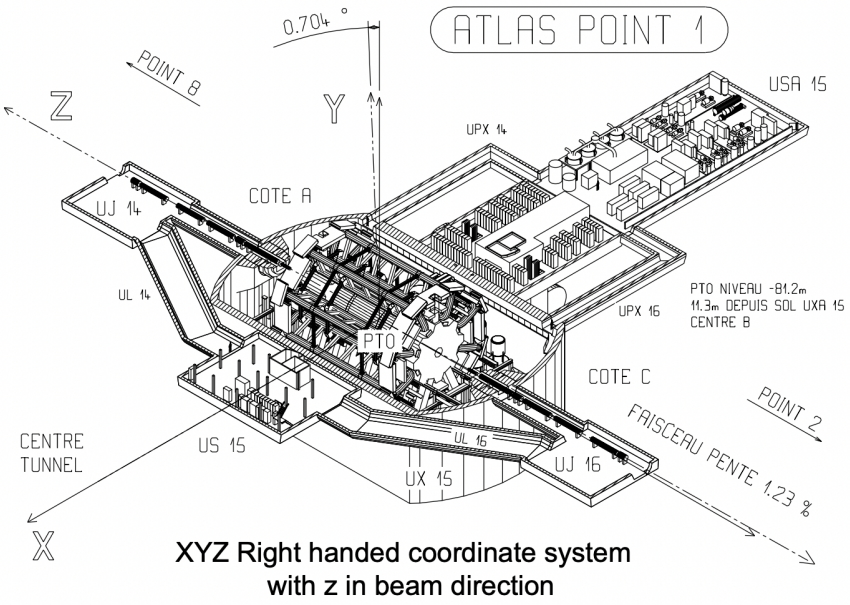

Figure 3.5.: The Atlas coordinate system. Image taken from /citeAad:1125884.

A polar coordination system is most often used when describing both the physics and the detector within the ATLAS Detector; this is described in terms of the cartesian system defined above. The radial distance, r, is taken with respect to the z-axis. The polar angle is the angle relative to the positive z axis. Finally the azimuthal angle, ϕ is the angle in the $x-y$ plane around the beamline that is measured anti-clockwise from the x-axis when viewed from the positive z direction.

A further important quanitity to define in this coordinate system is pseudorapidity which is used extensively in this section. It is defined in Equation 3.4.

$$\eta = -\ln \tan\left(\frac{\theta}{2}\right) \tag{3.4}$$

This results in $\eta = \pm \text{inf}$ when parallel to the z-axis and $\eta = 0$ when perpendicular. Using this definition of η the pseudorapidity-azimuthal angle distance ΔR is defined in Equation 3.5

$$\Delta R = \sqrt{\Delta\eta^2 + \Delta\phi^2} \tag{3.5}$$

3.2.1.2. Track Parameterisation

As the particles move through the ATLAS detector it is necessary to define a number of parameters that describe these helical paths, these variables are known as Perigee Parameters:

- q/p - The charge to momentum ratio of a particle
- θ - The polar angle of the track as described in 3.2.1.1
- ϕ - The azimuthal angle of the track as described in 3.2.1.1
- d_0 - The signed distance to the z-axis. The sign of d_0 is positive if ϕ_0 - $\phi = \pi/2$ (mod 2π) where ϕ is the azimuthal angle to the perigee.
- z_0 - The z coordinate of the track as described in 3.2.1.1

3.2.1.3. Particle Properties

Two common variables often used within ATLAS are the Rapidity,y, and the transverse Momentum, p_T. Using the example of a Particle with Energy E and momentum $\vec{\mathbf{p}}$, the rapidity is defined as shown in Equation 3.6, while p_T and transverse energy E_T are the components in the x-y plane.

$$y = \frac{1}{2}\ln\left(\frac{E + p_z}{E - p_z}\right) \tag{3.6}$$

These variables are shown in Figure 3.6.

3.2.1.4. ATLAS Terminology

There are a number of terms which have a precise meaning and specific usage with the context of the ATLAS experiment, these are often used throughout this thesis and are listed below.

- *Event* - An event is all of the data that is collected from a single bunch crossing.
- *Candidate* - The data from an event that is relevant to a particle physical process.

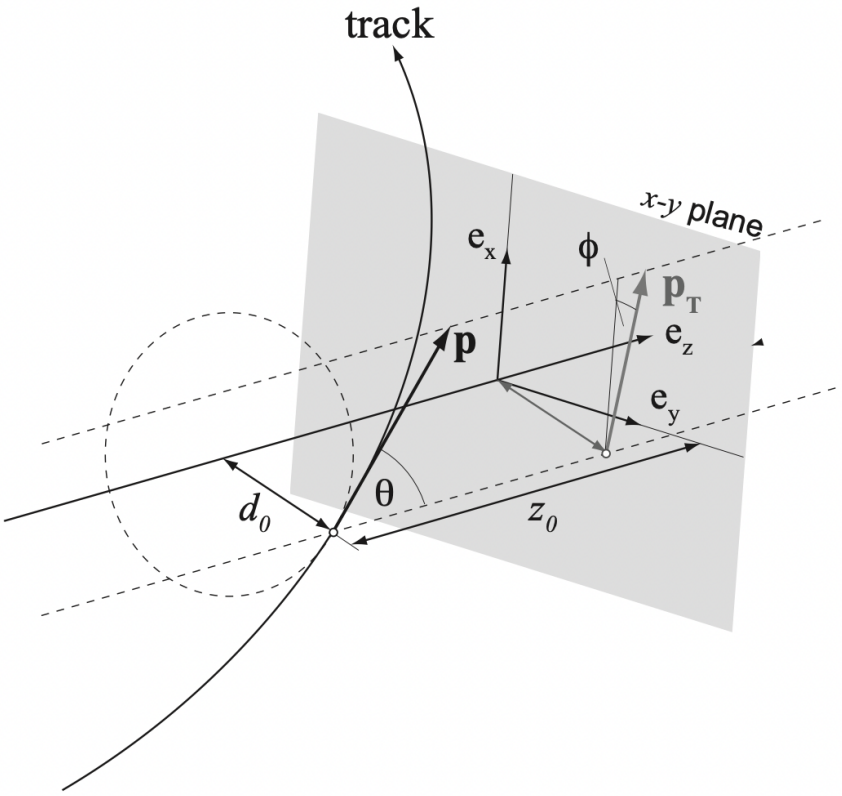

Figure 3.6.: The ATLAS charged track parametrisation. Image taken from [44]

- *Track* - The reconstruction of the path a particle takes through the detector.
- *Primary Vertices* - The reconstructed vertices from the initial pp interactions.
- *Secondary Vertices* - The reconstructed vertices for the decay processes.

3.2.2. Magnet System

The ATLAS magnet system is of fundamental importance to the operation of the detector. It provides the necessary magnetic field to deflect the trajectories of charged particles and thus provide accurate momentum measurements. The system is comprised of two subsystems; the central solenoid and the toroids. Both coils are made of superconducting Al-stabilised Niobium-Titanium/Copper alloy magnets cooled to less than 5K using liquid helium; these are described in detail in the following sections shown in Figure 3.7.

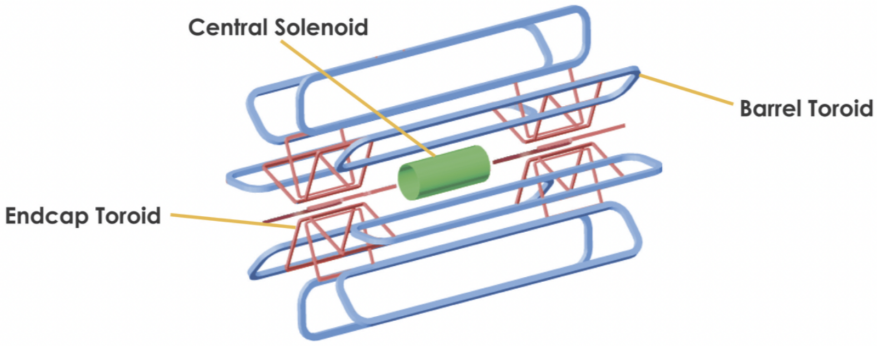

Figure 3.7.: A schematic of the ATLAS magnet system. Image taken from [45]

3.2.2.1. Central Solenoid

The central solenoid is responsible for supplying the 2T axial magnetic field (at 7.730 kA operating current) in the inner detector. The central solenoid has an interior diameter of 2.56m and an axial length of 5.8m with the coil weighing 5.4 tonnes. The coil stores a total of 40MJ of energy. In order to avoid excessive impact to the performance of the calorimeter the layout of the central solenoid was optimised so that it only contributes 0.66 radiation lengths of thickness in front of the calorimeter. [43].

3.2.2.2. Barrel and End-cap Toroids

The barrel and end-cap toroids produce an azimuthal magnetic field in the Muon Spectrometer. The barrel toroid consists of eight coils in a "racetrack" configuration surrounding both the central solenoid and the end-cap toroids; it is 25.3m in length with an inner diameter of 9.4m. It has a nominal operating current of 21.0 kA and the magnetic field it generates covers the pseudorapidity range $|\eta| < 1.4$. The end-cap toroids have an inner dimension of 1.65m, an axial length of 5.0m and weight a total of 239t each. They are capable of generating a peak magnetic current of 3.5T and covers the pseudorapidity range $1.4 < |\eta| < 1.6$. In total the toroids provide a magnetic field of 0.5T in the central region and 1T in the end cap regions.

3.2.3. Inner Detector

The aims of the inner detector [46] are to provide precise momentum resolution very close to the beam-line and to provide primary and secondary vertex measurements above a momentum of 0.5 GeV and below a pseudorapidity of $\eta < 2.5$. These goals are accomplished through the use of three sensor types discussed in more detail below. The first two layers are silicon detectors (Pixel and Semiconductor Tracker). These are used in conjunction with TRT (Transition Radiation Tracker) sensors that use ionised gas to detect particle tracks. A fourth layer has been added since the upgrades for Run 2 - this is the Insertable B Layer (IBL) [47] which forms the inner layer of the pixel detector and is designed to increase vertex reconstruction. The major considerations for the design of the inner detector include working around the size constraints of the Central Solenoid and being stable enough to provide accurate tracking and position data throughout the multiple freeze-thaw cycles required by the supercooled magnet systems. Figure 3.8 shows the layout of the ATLAS inner detector prior to the introduction of the IBL; Figure 3.9 shows a cut through of the inner detector with the IBL in place.

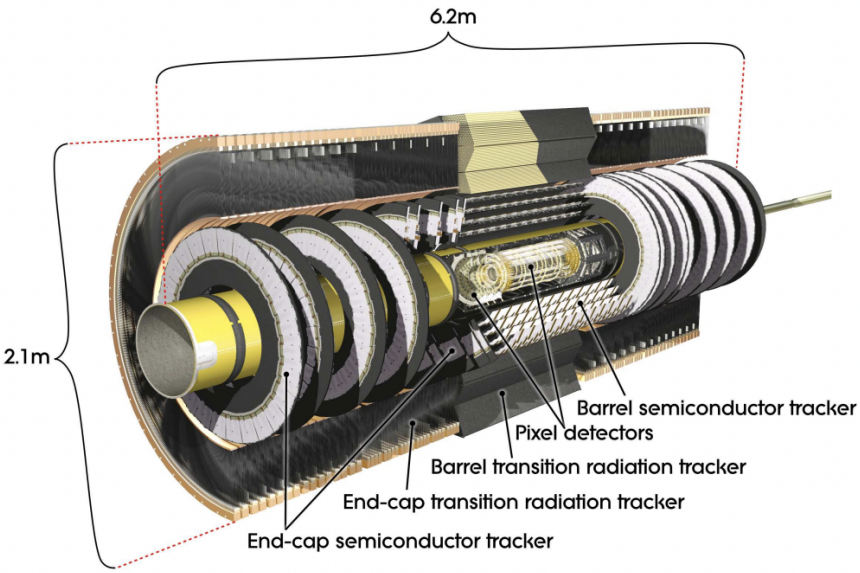

Figure 3.8.: A labelled diagram of the ATLAS inner detector. Image taken from [43].

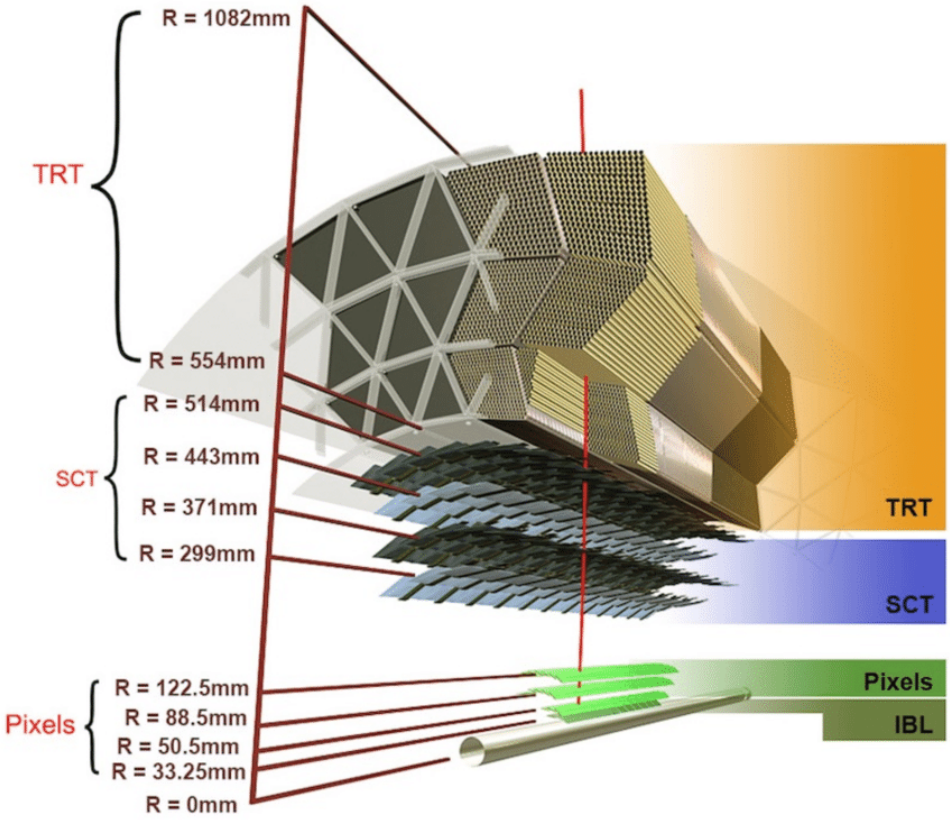

Figure 3.9.: A diagram of the thicknesses of the multiple layers that make up the ATLAS inner detector. Image taken from [48]

3.2.3.1. Insertable B-Layer (IBL)

The Insertable B-Layer was built around the new Beryllium beam pipe installed in the 2015 upgrades ready for Run 2. It is made up of 14 carbon-fibre staves tilted by 14° in ϕ. Each stave is equipped with 32 FE-I4 chips; each of these has 26880 pixel cells. The sensors are at a mean radius of 33mm from the beamline covered by the pseudorapidity range ± 3.

3.2.3.2. Pixel

The Pixel Subsystem is comprised of multiple detector modules. Each detector module consists of 3 layers, 16 front-end electronic chips and a sensor tile of area 63.4mm x 24.4mm comprising of 47232 individual pixels, though due space constraints, these only lead to 46080 actual readout channels. The sensor tile is bump-bonded using

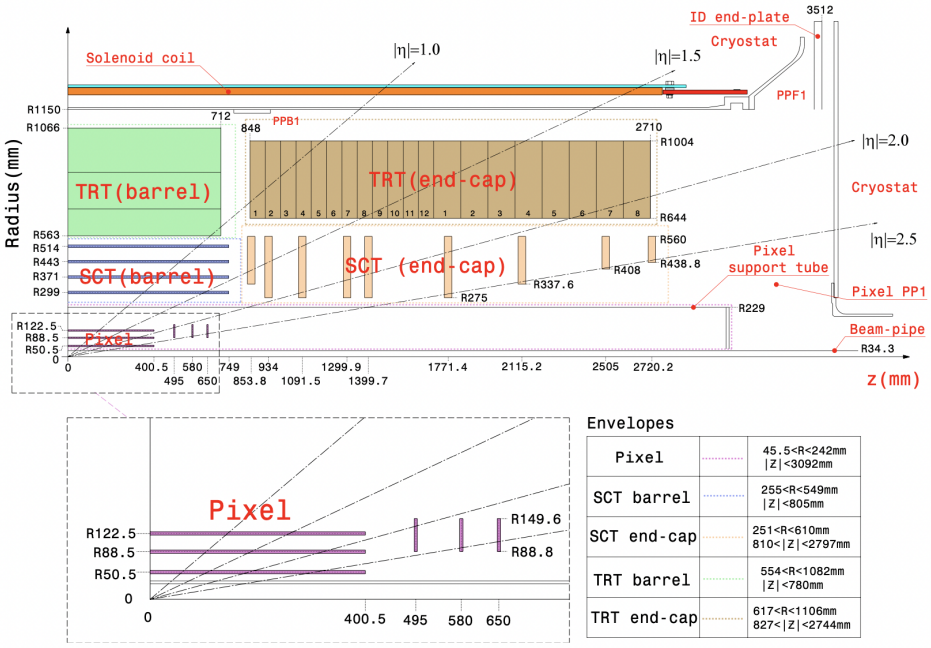

Figure 3.10.: The layout of the ATLAS inner detector using an R-z cross section. The lower left subfigure, shows the pixel detector in more detail. The subfigure on the lower right shows the R ranges for each of the detector subsystems. Image taken from [43]

either indium or a lead-tin solder and a flexible printed circuit board (PCB) mounted with a module control chip.

In total the pixel subsystem contains 1744 detector modules. These modules are distributed over 112 barrel staves and 48 endcap sectors (distributed 8 sectors per disk, with three disk layers per endcap). The barrel staves arrange the modules in 3 concentric layers around the beamline at 50.5 mm, 88.5 mm and 122.5 mm. All modules combined, the pixel detector subsystem is 48.4cm in diameter and 6.2m in length, which provides coverage for a pseudorapidity range of $|\eta| < 2.5$. This setup results in a position resolution of 10 μm $\times$ 115 μm which ensures the detector can be used for precise vertex reconstruction and accurate position measurements.

3.2.3.3. SemiConductor Tracker (SCT)

The SCT uses similar technology to the Pixel module, using silicon sensors to detect incoming charged particles, however rather than using pixels, SCT uses silicon strips. The SCT consists of 4088 modules. These are divided over four coaxial cylindrical

layers (at radii of 299, 371, 443, and 514 mm) around the beamline in the barrel region totaling 2112 modules with an additional nine disk layers (spread from $|z|$ = 854 to 2720 mm) in each end cap. The layout of these modules is shown in Figure 3.10. In total they cover an area of 63m^2. Each of the sensor modules consists of two 12cm long silicon strips glued back to back with a small stereoangle between them of 40 mrad to allow for the reconstruction of a 2d position measurement. This provides a spatial resolution in the $R-\phi$ plane of 17 μm and 580μm in the z plane. In total the SCT has 6.3 million readout channels.

3.2.3.4. Transition Radiation Tracker (TRT)

The TRT, unlike the Pixel and SCT, doesn't use silicon detectors. It relies on gaseous drift tubes instead. In the TRT the basic detector element is a tube of 4mm diameter made of carbon-fibre reinforced polymide with a 31 μm diameter tungsten wire running through the centre, plated in gold. Each of these straw tubes is filled with a gas mixture consisting of 70% Xe, 27% CO_2 and 3% O_2. In operation, the central wire is ground and the wall of the tube is held at voltage of 1530V. When a charged particle passes through the drift tube, it ionises the gas mixture and the free electrons drift towards the central wire, allowing a current to be measured.

In the barrel region (covering pseudorapidity $|\eta| < 1.0$) the TRT is split into three rings containing 32 modules, in total containing 52544 straws. These straws are embedded in a matrix of 19 μm-diameter polypropylene fibres which generate transition radiation photons which occur when charged particles move through a boundary transition between materials. Importantly the amount of radiated photons are related to the different types of charged particles and therefore this transition radiation is used for particle identification.

The end caps (covering pseudorapidity $1.0 < |\eta| < 2.0$) consist of 2 sets of wheels, the set closer to the interaction point consists of 12 wheels each containing 8 layers spaced 8mm apart, the outer set are comprised of only 8 wheels, again each with 8 layers but spaced 15mm apart. In the endcaps a polypropylene foil is used instead of fibres as in the barrel regions.

All charged tracks with a transverse momentum of $p_T > 0.5GeV$ and $|\eta| < 2.0$ will cross at least 36 straws except in the pseudorapidity region $0.8 < |\eta| < 1.0$,where the barrel meets the endcap, they will cross at least 22. As an example, it is expected that a

charged electron with an energy of more than 2Gev would generate approximately 7-10 "high-threshold" hits from transition radiation since it will not interact with all straws.

3.2.4. Calorimetry

The calorimetry system of the ATLAS detector is comprised of a number of individual calorimeters. It uses a combination of electronic and hadronic calorimeters, the former measures the energy of photons and electrons, the latter measures hadrons and jets. A diagram of the calorimetry system is show in Figure 3.11. Only the neutrino and the muon are not stopped by the calorimetry system. It wraps around the Inner Detector covering the pseudorapidity range $|\eta| < 4.9$. The construction of both the calorimeters used in the ATLAS detector rely on alternating layers of absorbing and detector layers. The absorbing layers are made of a dense medium for the particles to deposit energy into, while the detector layers detect the showers produced from the interaction with the absorbing layers and measure the energy deposited in the shower. The downside to this alternating layers approach is that worse energy resolution is achieved since only a proportion of the total energy is deposited into the detector layers. The dense absorber material allows the calorimeters to be more compact, which is necessary due to space constraints.

3.2.4.1. LAr Electronic Calorimeter

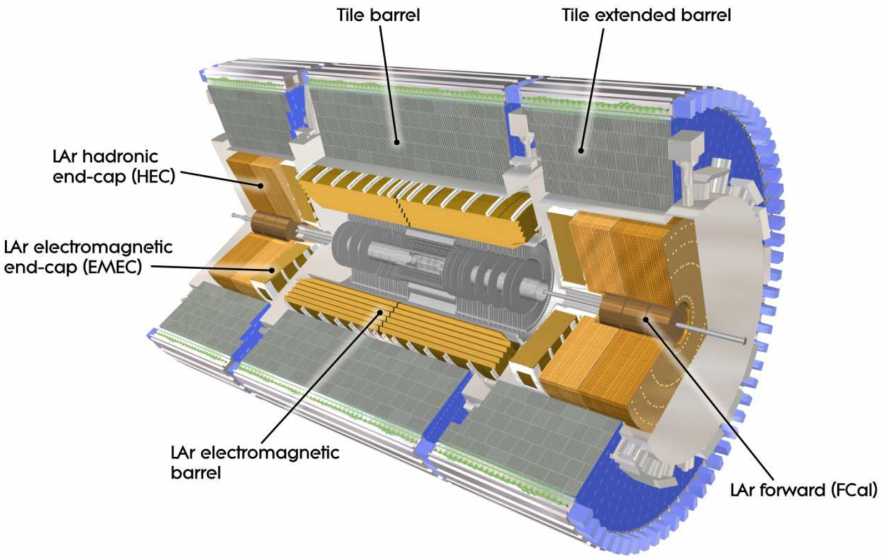

Figure 3.11.: A cutaway diagram of the Atlas Detector with all the calorimetry subsystems labelled. Image taken from [49]

The LAR electronic calorimeter is comprised of the barrel and two end caps. The barrel, covering pseudorapitiy range $|\eta| < 1.475$, is split into two halves each 3.2m long separated by a 4mm gap, with an inner and outer diameter of 2.8 and 4m. Each of these half-barrels is made of layers of liquid argon for the active medium,lead plates absorbers, reinforced with steel on either side for ridigity and copper electrodes arranged in an "accordion geometry" providing full coverage in ϕ. Readout cells are organised into 3 layers. The cells within each layer have different dimensions, decreasing in granularity as shown in Fig 3.12. The barrel ECAL sections are 22 radiation lengths thick in order to account for the high energy showers being absorbed; ensuring that the shower energy can be fully deposited.

The end caps consists of two "wheels", an inner and an outer wheel covering pseudorapidity ranges $2.5 < |\eta| < 3.2$ and $1.375 < |\eta| < 2.5$. Similarly to the barrel section, the end caps are also divided into the 3 readout layers of varying granuality. The end-caps are slightly thicker than the barrel ECAL sections, totalling 24 radiation lengths.

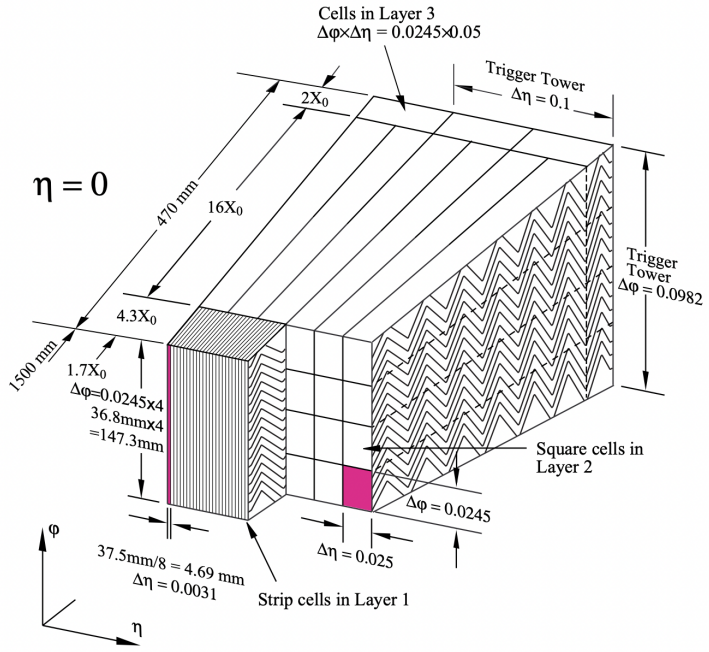

Figure 3.12.: The layout of a barrel liquid argon calorimetry module. Image taken from [43]

3.2.4.2. Hadronic Calorimeters

Hadronic calorimetery in the ATLAS dectector is provided by three subsystems, the Tile Calorimeter spanning the pseudorapidity range $|\eta| < 1.7$, the liquid argon hadronic calorimeters covering the pseudorapidity region $1.5 < |\eta| < 3.2$ and the forward calorimeter covering the high pseudorapidity region of $3.1 < |\eta| < 4.9$.

3.2.4.2.1. Tile Calorimeter The Tile Calorimeter is a sampling calorimeter that uses steel as its absorber medium and polystyrene/PTP scintillator tiles for the active medium. It is comprised of a barrel section that cover the $|\eta| < 1.7$ region and extended barrel sections which cover the range $0.8 < |\eta| < 1.7$. The inner diameter of the calorimeter is 2.28m and the outer diameter is 4.24m, the central barrel is 5.8m in length and each of the extended barrels is 2.6m long. Both the barrel and extended barrel sections are split into 64 modules azimuthally around the beamline. One of these modules is shown in Figure 3.13, in the same manner as the modules for the ECAL each of these modules is segmented in depth radially. For the modules in the barrel section, these segments are of depth 1.5, 4.1 and 1.8 interaction lengths (γ) for those in the extended barrel they are of depths 1.5, 2.6 and 3.3 γ. The ultraviolet light produced

by the interaction of the ionising particle with the scintillator material is converted to visible light by wavelength shifting fibres. This light is collected at the edge of the tile and used in conjunction with the segment (module subdivison) information to provide 3d information on the depth and η-segmentation of the interaction.

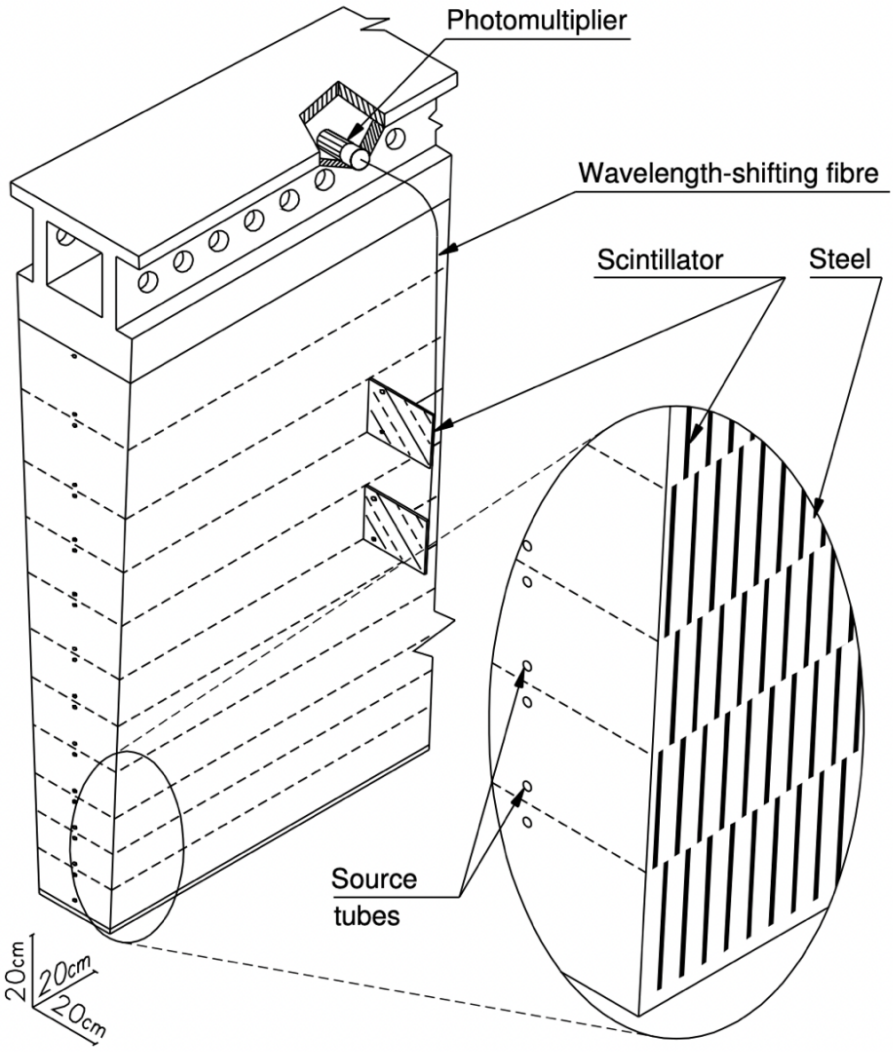

Figure 3.13.: A Tile Calorimeter sub module. Image taken from [43]

3.2.4.2.2. LAr hadronic end-cap calorimeter LAr hadronic end-cap calorimeter is located within the same cryostat as both the LAr forward calorimeter and the ECAL. Each endcap comprised of two independent wheels, which are made of 32 modules arranged radially around the wheel. They too are sampling calorimeters comprising of

24 layers of copper in the wheel closer to the interaction point (16 in the further wheel) forming the absorbing material and liquid argon for the active medium. In the closer wheels, the copper sheets are 25mm (50mm for those furthest from the interaction point) spaced with gaps of 8.5mm for the liquid argon.

3.2.4.2.3. LAr forward calorimeter The forward calorimeter, provides calorimetry for the high $|\eta|$ portion of the detector. The forward calorimeter is comprised of three modules in each endcap. These are formed in three layers, while all use liquid argon as their active medium (hence its inclusion within the end-cap cryostat) the first module uses copper as its absorber as it is optimised towards electromagnetic measurements the other two use tungsten as an absorber as they are designed for higher energy hadronic measurements. In total the FCal is approximately 10 interaction lengths in thickness. Each module of the FCal is made of a matrix formed of longitudinal channels containing the electrode elements made of concentric rods and tubes orientated parallel to the beamline. The space between the rod and the tube is filled with LAr.

3.2.4.3. Performance of the Calorimeters

One of the key statistics when measuring the performance of the calorimeters is the energy resolution measurement. This is a measure of the level of precision the detectors are able to determine the energy of incident particles. For this analysis specifically, which is heavily reliant on the energy of pions and electrons from the τ lepton hadronic and leptonic decay channels respectively, having high energy resolution is important.

$$\frac{\sigma(E)}{E} = \frac{a}{\sqrt{E}[GeV]} \bigoplus b \tag{3.7}$$

,where a is the stochastic term and b is a constant term reflecting the non-uniformities in the calorimeter response.

For the ECAL the fitted resolution was [43]:

$$\frac{\sigma(E)}{E} = \frac{(10.1 \pm 0.4)\%}{\sqrt{E}[GeV]} \bigoplus (0.2 \pm 0.1)\% \tag{3.8}$$

For the HCAL the fitted resolution was [43]:

$$\frac{\sigma(E)}{E} = \frac{(52.0 \pm 1.0)\%}{\sqrt{E}[GeV]} \bigoplus (3.0 \pm 0.1)\% \bigoplus \frac{(1.6 \pm 0.1)}{E}\% \tag{3.9}$$

,where the final term is to account for electronic-noise.

3.2.5. Muon Spectrometer

The muon spectrometer in the ATLAS detector serves two main purposes, the first is to provide functionality for triggers that require the detection of processes with muons in the final state, the second is to provide a means of measuring the transverse momentum of muons in the energy range of between approximately 3Gev and 1TeV. It is comprised of 4 subsystems Resistive Plate Chambers (RPCs), Thin Gap Chambers (TGCs), Monitored Drift Tube Chambers (MDTs) and Cathode Strip Chambers (CSCs). The former two provide the trigger information for both the barrel and endcaps while the latter provide tracking measurements in the forward and central regions. The layout of these subsystems is shown in Figure 3.14.

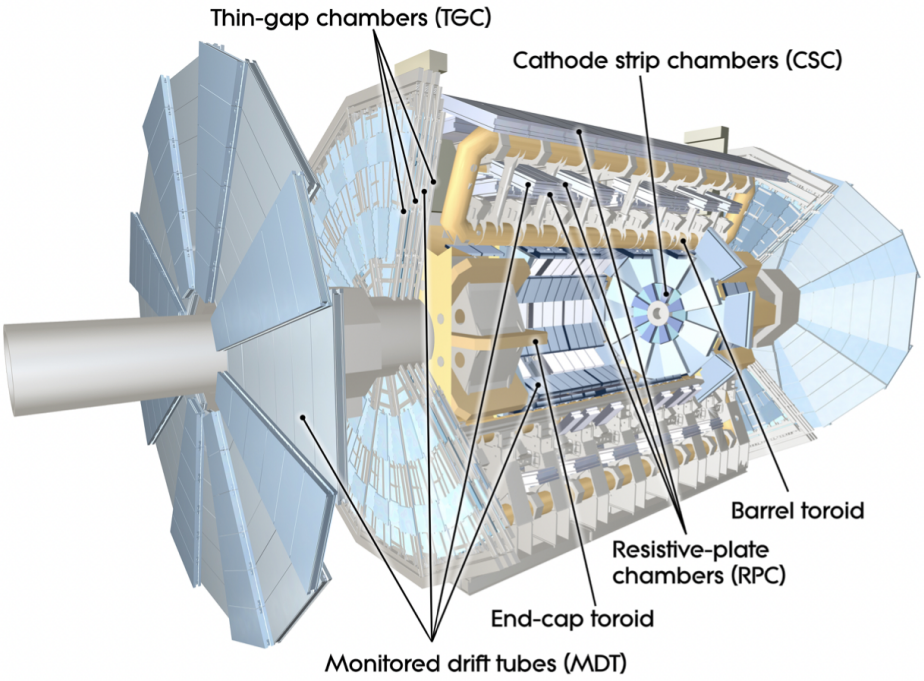

Figure 3.14.: A cutaway diagram showing each of the main subsystems comprising the muon spectrometer. Image taken from [43].

.

3.2.5.1. Resistive Plate Chambers

The resistive plate chambers provide trigger information in the pseudorapidity range $\eta < 1.05$. A resistive plate is made of two parallel phenolic resin plates, separated by a 2mm insulating spacer. Between the two plates there is an electric field of 4.9kV/mm; this electric fields allows "Townsend Avalanches" to form. In these avalanches an electron is displaced by an incoming muon and so it moves towards the anode, in turn displacing more electrons. This signal can then be read out by the 25mm-35mm copper readout sensors attached to the resistive plates.

3.2.5.2. Thin Gap Chambers

The thin gap chambers serve two purposes within the detector, the first is to provide trigger information in the $|\eta|$-range $1.05 < |\eta| < 2.4$. The second is to provide a

measurement of the azimuthal bending co-ordinates that are used in conjunction with the radial bending measurement produced by the MDTs. The TCGs are multi-wire proportional chambers they use a 55%/45%mixture of CO_2/n-C_5H_{12}. The anode wires, held at a nominal voltage of 2.9kV, are spaced 1.8mm apart while the distance from the anode wires to the cathode strips is 1.4mm. These parameters allow for a timing resolution of around 4ns due to a short drift time. The anode wires and cathode strips are run perpendicularly to one another to provide two-dimensional spacial measurements.

3.2.5.3. Monitored Drift Tube Chambers

The basic detection element of the Monitored Drift Tube Chambers consists of an aluminium drift tube with a diameter of 29.970mm, with a tungsten-rhenium wire of diameter 50μm running through their centre at a potential of 3080V. The drift tube is filled with an argon and carbon dioxide mixture (93%/7%) held at 3 bar pressure. This produces a maximum drift time of 700ns. The MDTs are arranged into chambers consisting of two groups of tube layers called multilayers, these are made of 4 layers in the innermost layer of the muon detector and made of 3 layers of tubes in the middle and outer layers of the muon spectrometer this arrangement increases spatial resolution. A diagram of one of these chambers is shown in Figure 3.15. The orientation of the tubes is such that they run along ϕ, so that the centres of the tubes are arranged tangentially to circles perpendicular to the beamline. In total within the MDT detector there are 1150 chambers consisting of 354,000 individual drift tubes.

3.2.5.4. Cathode Strip Chambers

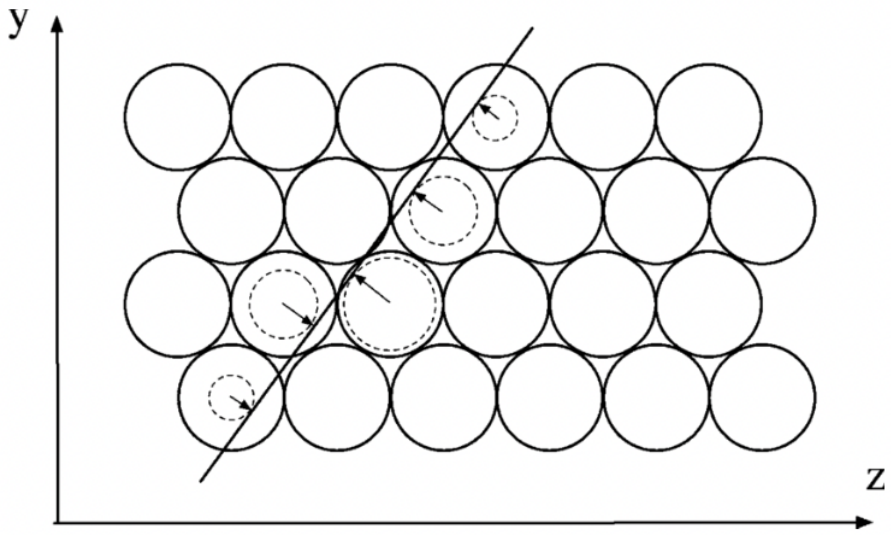

Figure 3.15.: A diagram showing track fitting using a MDT multilayer. Image taken from [50]

Cathode Strip Chambers are used in the pseudorapidity region $2.0 < |\eta| < 2.7$ in the first layer of the endcap where the particle flux exceeds the safe operating counting rate of MDTs of around 150Hz/cm^2. CSCs have a safe counting rate of up to 1000Hz/cm^2 which can handle this high flux. CSC are multiwire proportional chambers, the cathodes are segemented into strips and the anodes have a operating voltage of 1900V. The chambers are filled with a mixture of argon and carbon dioxide (80%/20%). The position of the track is obtained from interpolating the charges on neighbouring cathodes. The exact resolution is dependent on background noise and readout pitch, but the CSC can achieve resolution of around 60μm per CSC plane compared to only 80μm from a MDT.

The CSC are arranged in two disks (one small and one large). Each disk consists of 8 segments spaced around the beamline in ϕ, each chamber contains four CSC planes, this arrangement of chambers is shown in Figure 3.16.

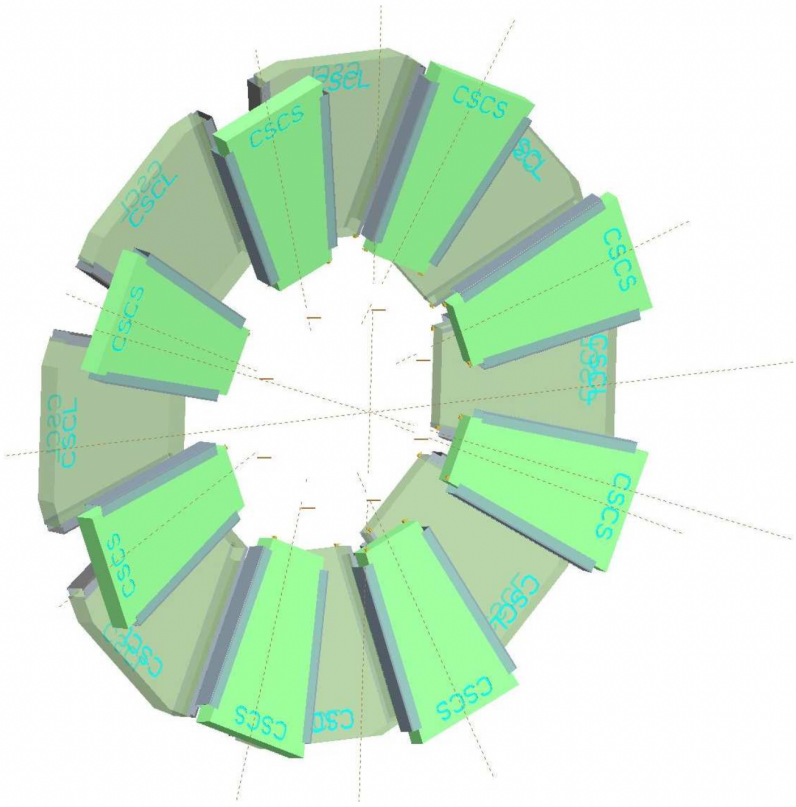

Figure 3.16.: The layout of the Cathode Strip Chambers showing the arrangement of the 8 segments in each of the small and large disks around the beamline. Image taken from [43]

3.3. Trigger and Data Acquisition System

One of the most crucial decisions at any high volume detector is deciding what data to store for use in physics analyses. At the ATLAS detector in Run 2, every 25ns a bunch crossing collided in the detector (40MHz), each collision generates 1.5Mb of data, so every second 60TB of data is generated. It is unfeasible to store everything due to limitations of storage devices costs and bottlenecks on writing speed. Large volumes of this data would not be useful for physics since it mostly consists of soft parton scattering and therefore can be safely discarded. The trigger system handles the task of gathering enough data for physics analyses while efficiently discarding data that is of no physics value. The aim is to reduce the event storage rate to a more managable 1000Hz.

The ATLAS detector uses a combination of hardware triggers (Level-1) which provides coarse filtering and software triggers (High-Level Triggers,HLT) which performs a more fine grained filter.

3.3.1. Level-1 Triggers

The L1 trigger uses data collected from both the calorimetry system and the muon spectrometer. The data from the calorimetry system identifies high-p_T objects such as photons, electrons, jets and hadronic decays from τ-leptons. In addition it also identifies events that have large missing $E^{\text{miss}}{}_T$ and large total transverse energy. It may also place restrictions on "isolation" where an object has a certain separation between it and other neighbouring objects. The L1 trigger identifies physical coordinates in η and ϕ space called Regions of Interest (ROI) where it has identified features which may be of interest to physics analyses this information can then be further used by the high level triggers. The L1 triggers are also capable of prescaling which can reduce the bandwidth by a constant factor to suit background and luminosity changes.

The latency of the L1 Trigger is designed to be less than 2.5μs with an aim for an ideal of 2.0μs. This aim is difficult to achieve especially in the calorimetry trigger since the length of a signal can often span around 4 bunch crossing, meaning that relevant data must be stored in memory while the trigger performs an identification.

3.3.2. The High-Level Trigger

The high-level trigger is the collective name of the Level-2 trigger and the event filter. The L2 trigger uses all of the available detector information within the ROIs as provided by the L1 trigger. This data accounts for approximately 2% of the total event data making the processing significantly more manageable. L2 triggers reduce the event rate down to 3.5kHz with an average processing time of 40ms per event. The final stage of the trigger is the event filter. This further reduces the even rate to approximately 200Hz with a typical latency of approximately 4s.

Chapter 4.

Reconstruction

4.1. Object Reconstruction

4.1.1. Primary Vertex and Track Reconstruction

In proton-proton collisions many vertices are constructed using the trajectories of particles through the inner detector with a transverse momentum (p_T) of greater than 500 MeV. Events must have at least one collision vertex that has at least two associated tracks. When there are many vertices the one with the highest combined p_T^2 from the tracks associated with it is used as the "primary vertex". However it is possible to reassign this vertex if, as is relevant in this analysis, the τ tracks are associated with a different vertex.

4.1.2. Electrons

The primary method used to reconstruct an electron in the ATLAS detector is to match the energy deposits in the electronic calorimeter (ECAL) to a track recorded within the Inner Detector (ID) [51]. As the electron moves through the inner detector it radiates photons due to bremsstrahlung, which decay into a positron and electron pair and themselves can interact with the detector, either producing additional tracks within the ID or forming part of the shower of energy deposited in the ECAL [51].

Electrons are identified using likelihood identification. For this two likelihoods are calculated, $L_S(\boldsymbol{x})$, $L_B(\boldsymbol{x})$, for likelihood of the electron being signal or background respectively, where $\boldsymbol{x}$ is a vector of various quantities such as energy deposited in the

different layers of the calorimeters, numbers of pixel hits and momentum loss [51]. These likelihoods are formed from products of probability distributon functions (PDFs) which describe the probability of a given quantity being associated with a prompt electron or a similar looking background signal. These background signals could be from a number of sources such as jets mimicking prompt electrons, electrons from photon conversion in the detector material or non-prompt electrons from heavy hadrons. From the two likelihoods a discriminant, d_L is formed shown in Equation 4.1

$$d_L = \frac{L_S}{L_S + L_B} \tag{4.1}$$

This discriminant, d_L is then used to define those electrons which are considered signal and which are background. Baseline Electrons must satisfy the "Loose And BLayer" LH identification criteria. The "Loose" criteria is one of four increasing thresholds for the discriminant (VeryLoose, Loose, Medium and Tight). The "Loose" threshold corresponds to an identification efficiency for a prompt electron with $E_T =$ 40GeV of 93% (88% for Medium, and 80% for Tight). The BLayer identification criteria, adds the criteria there must also be a hit on the innermost pixel layer. They must also have a transverse momentum of $p_T >$ 15 GeV and pseudorapidity of $\eta < 2.47$ though any falling in the crack region with $1.37 < |\eta| < 1.52$ are vetoed. These baseline electrons are entered into the overlap removal process (OLR) described in Section 4.1.6. Electrons that survive this are subject to further conditions, such as passing the "Medium" identification criteria and "FCLoose" (Fixed Cut Loose) [52] isolation criteria. The isolation criteria helps differentiate processes which produce isolated real electrons compared to those that produce non-isolated electron-like signals. In some sections, however (detailed in Section 9.3), electrons are required to fail this isolation criteria for the purpose of estimating numbers of jet-faking electrons and jet-faking $\tau_{\text{had-vis}}$.

4.1.3. Muon

Muon reconstruction is performed independently in the Inner detector and the Muon Spectrometer (MS) seperately. These reconstructions are then combined to produce the muons that are used within Physics anaylses.

In the MS, in each Monitored Drift Tube (MDT) chamber there are two multilayers consisting of 3 to 4 staggered layers of MDTs. First segements are constructed defined as common tangents of hits across two multilayers. The Resistive Plate Chambers(RPC) and Thin Gap Chambers (TGC) can reconstruct segements with a perpendicular component to the bending plane. However the Cathode Strip Chambers (CSC) only reconstruct segments in the η-ϕ plane.

Tracks are reconstructed by a combinatorial search which joins up segments to form tracks. They may be formed from either two segments or one high quality section. This is then combined with the information from the inner detector and calorimeters. When this combined reconstruction is performed four categories of muon can be defined [53]. These are as follows:

- Combined (CB) - This category uses a combination of ID and MS reconstructions to reconstruct the muon track. This is mostly performed using "outside-in pattern recognition" where a track from the MS will be matched with corresponding tracks from the Inner Detector by extrapolating inwards. "Inside-out" methods can also be used alongside this.
- Segment-Tagged (ST) - A track is classified as a Segment-tagged muon, if when a track is extrapolated out from the Inner Detector, it can be matched with at least one track segment in the Muon spectrometer. This category is used if a muon candidate has only crossed one layer of the MS, which may be due to either it crossing in specific low acceptance regions of the detector or low p_T.
- Calorimeter-Tagged (CT) - This category does not use the MS. Instead, calorimeter-tagged muons use tracks from the ID that can be matched to calorimeter deposits that are consistent with minimum-ionizing particles. Although these have the lowest purity of all the categories of muons, it allows for muon detection even in regions where there is less instrumentation in the detector due to cabling requirements.
- Extrapolated Muons (ME) - These are built from only MS tracks with a Loose requirement that the muons originate from the interaction point. This allows for muon detection in the pseudorapidity region $2.5 < |\eta| < 2.7$ that is not covered by the Inner Detector.

When two muons overlap, because they share the same ID Track, preference is given to CB then ST then CT muons. When an overlap occurs involving ME muons, the track with better fit quality and number of hits is chosen.

4.1.4. Tau

For this analysis the accurate detection and reconstruction of τ lepton visible decay products is vital. Hadronic tau (τ_{had}) decays consist of a neutrino and a number of visible decay products which can be identified within the ATLAS detector. The reconstruction of these visible decay products is performed from jets the reconstruction of which is discussed in more depth in Section 4.1.5. The additional requirement of $p_T > 10GeV$ and $|\eta| < 2.5$ [54] [55] are imposed on the jets used to reconstruct the τ_{had} visible decay products. The vertex associated with the tracks that carry the highest percentage of the jet's momentum withinn $R < 0.2$ is chosen to be the tau vertex. Tracks are then associated with either the *core* (the region of the jet where $0.2 > R > 0$) or the *isolation* (where $0.4 > R > 0.2$) provided some basic quality requirements are met. The tracks are required to have a minimum shortest distance from the tau vertex to the track in for both the transverse plane and longitudinal plane which are $|d_0| <$ 1mm and $\Delta z_0 \sin(\theta) <$ 1.5mm respectively. The direction is defined by the vector sum of the topoClusters within the *core* region of the jet and its energy is calculated from the energy deposits within the calorimeter.

It is important to filter jets usable for reconstructing τ_{had} visible decay products from those initiated by either quarks or gluons QCD processes. This filtering process is performed by a Recurrent Neural Network (RNN) [54], which uses energy deposits from calorimeters and track information amongst other variables. Another multivariate discriminant, the Electronic Boosted Decision Tree (eBDT), is used to reject electrons faking $\tau_{\text{had-vis}}$ candidates. In this analysis, these electrons primarily arise from $Z \to e^+e^-$ decays. The eBDT is built using information from the calorimetry and tracking systems in conjunction with information from the Transition Radiation Track (TRT).

Baseline taus must have either 1 or 3 tracks associated with them, a $p_T >$ 20 GeV, and a pseudorapidity $|\eta| < 2.47$ (excluding those in the crack region of $1.37 < |\eta| < 1.52$). A cut on RNN Tau ID is also imposed at 0.01 and a muon veto criteria (MUONORL) is applied to filter any muons incorrectly reconstructed as taus. Here, the baseline

requirements for the $\tau_{\text{had}} - \tau_{\text{had}}$ and $\tau_{\text{lep}} - \tau_{\text{had}}$ channels diverge. The former requires that the baseline $\tau_{\text{had-vis}}$ objects must match one leg of the ditau trigger, the latter keeps only the highest transverse momentum $\tau_{\text{lep}}\tau_{\text{had}}$ candidates as a baseline τ leptons and the rest are considered jets. Compared to the medium working point, the value of 0.01 for the RNN Tau ID requirement results in a slight loss of efficiency, in both the ggF and VBF channels of 2.5% and 4% respectively. This value also ensures that the anti-ID region which uses orthogonal selection criteria to the signal region is still sufficiently filled while minimising loss in efficiency. The anti-ID region is crucial for estimating the fraction of hadronic τ misindentified as jets in the approach used in this analysis.

4.1.5. Jet

The primary detectors used in jet reconstruction at ATLAS are the calorimeters. These provide the primary inputs for jet reconstruction, in conjunction with the ID for information on track trajectories. The first stage of jet reconstruction [56] involves the identification of so-called "seed cells" where a cell or group of cells have at least 4 times the energy of the expected noise (denoted σ), from both electronic and pileup sources. A topo-cluster is formed from these seed cells by adding all adjacent cells as long as they have at least 2σ. This is repeated until there are no longer cells that meet the requirement, finally the adjacent cells are also added regardless of their energy.

The next stage of jet reconstruction is using the anti-k_t algorithm [57]. This uses topo-clusters to identify cone shaped jets with a radius of R (for quark and gluon jets - so-called small-R jets - this sets R=0.4 [58]), where a hard particle has no neighbouring hard particles within a distance of 2R then cones are regular. In the situation where two jets overlap, if the momentum of the hard particles, around which the jets are constructed (k_t1 and k_t2) are equal, then both cones will be clipped and the overlap between them will be divided by a straight line. If $k_t1 \gg k_t2$ then jet 1 will be concical and jet 2 will be concical but missing the overlap with jet 1.

The reconstructed jets must be calibrated to bring their energy scale in line with the energy scale of jets reconstructed on the particle energy scale from truth data. This calibration takes place over several stages which are summarised in Figure 4.1.

First, the jet axis is realigned to point at the vertex of interest (in this case, the vertex with the highest $\sum p_T$). The pile-up jets are identified from the hard-scatter jets by use of the Jet Vertex Tagged (JVT). The JVT is a 2-dimensional likelihood used to identify

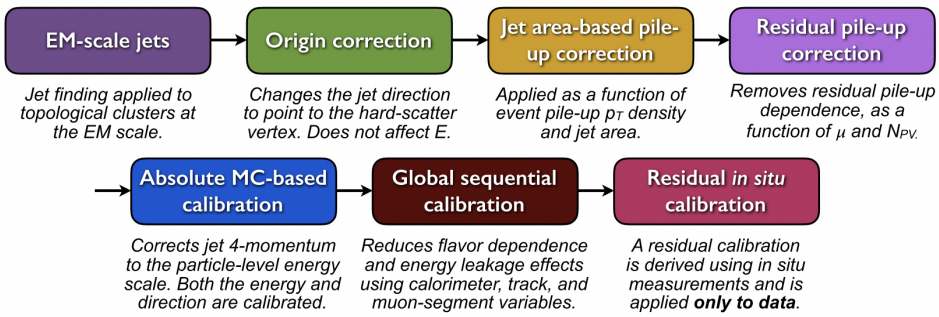

Figure 4.1.: A summary of the calibration stages performed on jets after reconstruction. [59]

jets in the range of 20GeV $< p_T <$ 50GeV and $|\eta| < 2.4$ as being either a hard-scatter or pileup event. The JVT returns a likelihood between 0 (least likely to be a hard-scatter) and 1 (most likely) [60] by using the energy density (ρ) of each jet combined with its jet area ($\mathcal{A}_{\text{jet}}$) to calculate the energy contribution of each of the pile up jets, which can then be removed. The residual pile-up is linearly dependent on μ, (the number of pp collisions per bunch crossing), and number of reconstruced primary vertices (N_{PV}), which are also found to be independent of one another. These are then fitted to the dataset so the residual pileup correction may be applied. The next step required for jet calibration is the energy corrections based on MC data. Large portions of the energy in a jet cannot be detected in the instrumentation at ATLAS. The reasons for this are numerous; however as an example this may be due to parts of the shower not contacting sensors but be accurately estimated to measure the jet energy. In order to correct for these effects, the jets are simulated in Monte Carlo to define a ratio of the recostructed response to the truth response that can be used to account for the missing energy. Finally, "in-situ calibrations" are used to ensure that the Monte Carlo calibrations for calculating the missing energy are valid. This is achieved by taking a double ratio, as shown in Equation 4.2, where a ratio of the response (X) of a well understood subsystem (B) is taken with a less well understood one (A) in data and compared to the same ratio in MC. $\mathcal{R}_{\text{trk}}$ can then be used to correct the previous MC corrections.

$$\mathcal{R}_{\text{trk}} = \frac{(X_{\text{A}}/X_{\text{B}})_{\text{Data}}}{(X_{\text{A}}/X_{\text{B}})_{\text{MC}}} \tag{4.2}$$

In addition, within this analysis the DL1r b-tagging algorithm is used to identify jets initiated by b-quarks. This is applied to all jets with a $p_T > 20$GeV and $|\eta| < 2.5$.

4.1.6. Overlap Removal

When the physics objects are reconstructed, it is possible that multiple objects can share tracks or calorimeter clusters. In order to remove this ambiguity, a proceedure known as overlap removal (OLR) is applied. This applied to the baseline objects through a package called ASSOCIATIONUTILS, in which the STANDARD configuration is used (the specification for which can be found in [61]).

4.1.7. Missing Transverse Momentum

In the proton-proton collisions, momentum conservation dictates that the transverse momenta of all particles in the final state should sum to zero. Any missing momenta implies that some particles are not being detected.This is expected for some, such as neutrinos, but may also imply the presence of non-Standard Model particles [62]. The missing transverse momentum (p_T^{Miss}) is calculated using all the signals from the final state particles (the hard term) in addition to tracks which are not used in the construction of any final state particles. This acts as an estimate for low p_T collisions (the soft term). The magnitude of this p_T^{Miss} vector is defined as the Missing Transverse Energy (MET).

The MET in this analysis is calculated using the official ATLAS Missing Transverse Energy Tool. The TIGHT criteria is used in this tool to ensure that forward jets (defined as jets with $|\eta| > 2.5$) have a transverse momentum above 30 GeV. The tool performs its own overlap removal proceedure ensuring there is no double counting between tracks and calorimeter deposits.

4.2. Reconstruction of Tau Lepton Decay Planes

In this analysis the Tau Particle Flow algorithm [63] is used to provide the 4-Vectors of the τ lepton decay products in addition to their decay mode classification. Accurate identification of both of these attributes is crucial to this analysis since the calculation

of the CP properties of the Higgs as discussed in 5 relies on these to build φ^*_{CP}. The 4-vectors of the visible decay products (neutral and charged pions) are determined from the tracking and calorimetry data. Boosted Decision Trees (BDTs) are used to identify the decay modes of the τ leptons using the numbers of charged and neutral pions in conjunction with properties of the tau decay and numbers of reconstructed photons. The BDTs are used to differentiate between decay modes with differing numbers of neutral pions; three BDTs are used to seperate 1p0n and 1p1n, 1p1n and 1pXn, and 3p0n and 3pXn decays. The small misidentifications shown in Fig. 4.2 between 1-prong and 3-prong decays come from the small probability of misidentified tracks. Fig. 4.2 [63] shows the efficiency of the Tau Particle Flow algorithm for $H \to \tau\tau$ decays using Run 2 data.

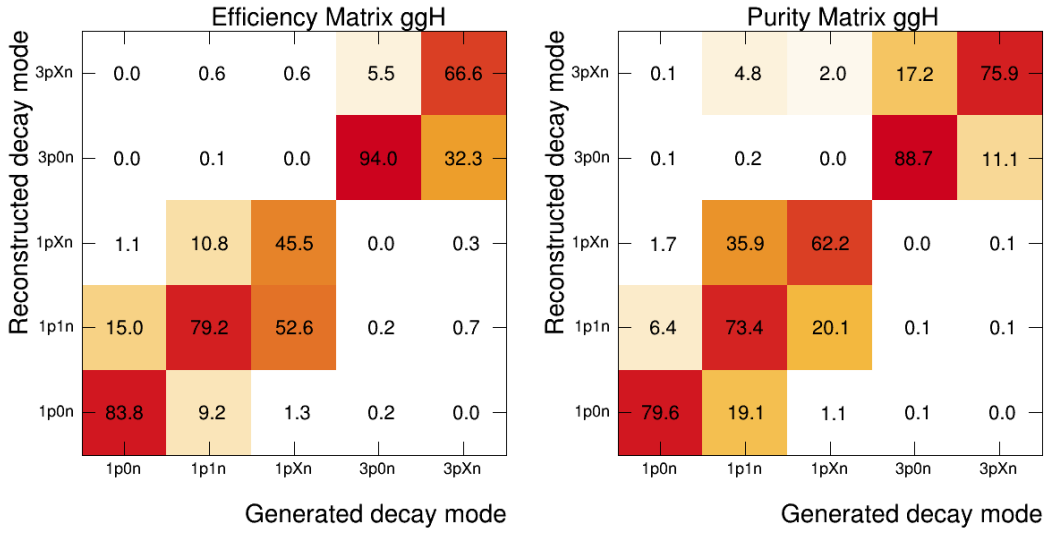

(a) efficiency matrix **(b)** purity matrix

Figure 4.2.: Efficiency and purity matrices of the $H \to \tau\tau$ ggH signal sample generated using POWHEG +PYTHIA8 used in the analysis. All elements in the efficiency matrix use the total number of events in the relevant generated decay mode shown in each column for normalisation. The elements in the purity matrix are normalised using the total events in the relevant reconstructed decay mode, shown here by the rows [63].

Chapter 5.

Analysis

5.1. Analysis Strategy

For the purposes of testing the CP properties of the Higgs Boson, the primary three decay modes, as discussed in Section 2.4, may be considered; the decay to two fermions, the decay to two bosons and the indirect decay to two photons. The direct fermionic decay is the most promising for CP measurements. The key to measuring the CP properties of the Higgs is measuring the transverse spin correlation of the two daughter fermions. This spin information is transferred to the angular distribution of their decay products due to the V-A structure of weak decays. Amongst this family of fermionic decays, the τ lepton is the most useful since unlike the muon it decays within the volume of the ATLAS detector and unlike the b quark it does not decay through QCD processes, leaving a much cleaner signal.

Using the $H \to \tau\tau$ decay, a measurement of the angle between the decay planes of the τ decay products can be used to acertain whether the Higgs is CP-even, CP-odd or a mixture of these states. This process is complicated by the presence of neutrinos in the τ decay products which cannot be directly detected in the ATLAS detector, so it is necessary to construct an observable from the visible decay products to approximate the truth level decay planes. For this an observable is constructed which is correlated with the CP-mixing angle of the Higgs, the exact method for construction depends on the decay mode of the τ in order to increase sensitivity.

In this section, the theoretical basis for the measurement of the CP-state of the Higgs is outlined, then a discussion of the methods used to construct an observable

for different decay modes is presented and finally a summary of the observable construction methods used for different decay mode combinations is shown.

5.2. CP Observable Theory

In order to measure the CP properties of the Higgs boson as it decays into τ leptons, it is necessary to define an observable that can be experimentally measured. In order to do this, first the Yukawa interaction between the Higgs (H) and τ lepton, which can be parametrised as in Equation 5.1, is considered using notation from Ref [64].

$$\mathcal{L}_{H\tau\tau} = -\frac{m_\tau}{v}\kappa_\tau(\cos\phi_\tau\bar{\tau}\tau + \sin\phi_\tau\bar{\tau}i\gamma_5\tau)H \tag{5.1}$$

where $v = 246$ GeV is the Higgs field vacuum expectation value, κ_τ is the reduced Yukawa coupling strength ($\sqrt{k_\tau}\frac{m_\tau}{vev}$, where k_τ is the Yukawa coupling and vev is the vacuum expectation value [65]) and ϕ_τ is the parameterisation variable known as the CP-mixing angle. It varies in the range $[-\frac{\pi}{2}, \frac{\pi}{2}]$ which parameterises the contributions from the CP-odd and CP-even components to the Yukawa coupling. The pseudoscalar coupling corresponds to the mixing angle $\phi_\tau = \frac{\pi}{2}$ and the scalar coupling, consistent with the predictions from the Standard Model corresponds to the mixing angle $\phi_\tau = 0$.

ϕ_τ is still not directly measurable through experiment. It is however possible to access it through consideration of the transverse spin correlation of the two daughter τ leptons in the $H \to \tau\tau$ decays. The spin correlation only depends on the CP nature of the Higgs and not its production mode. The differential decay width, Equation 5.2, can be written in terms of the tau spin components in the rest frame of the Higgs [64, 66].

$$d\Gamma_{h\to\tau^+\tau^-} \propto 1 - s_z^- s_z^+ + \cos(2\phi_\tau)(s_\perp^- \cdot s_\perp^+) + \sin(2\phi_\tau)[(s_\perp^- \times s_\perp^+)\cdot\hat{k}^-] \tag{5.2}$$

where $\hat{k}^-$ is the normalised spatial momentum of τ^- in the zero momentum frame of the Higgs. $s_\perp^\pm$ and $s_z^\pm$ are the perpendicular and longitudinal components respectively of the unit spin vectors of each τ lepton ($\tau^\pm$) in their own reference

frames. Equation 5.2 demonstrates that only the peripendicular components of the spin correlation of the two daughter τ leptons must be considered to calculate ϕ_τ.

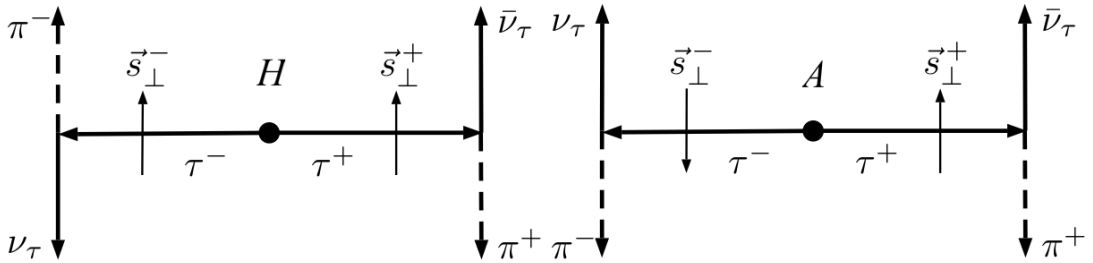

(a) Scalar **(b)** Pseudo-scalar

Figure 5.1.: A representation of how the angular directions of the decay products of the H/A$\rightarrow$ $\tau^+\tau^-$ decays correlate. Here H represents the scalar CP-even Higgs as predicted by the Standard Model and A is the pseudoscalar CP-odd Higgs [67].

Schematically the decay products of the $H \rightarrow \tau^+\tau^-$ decay are shown in Figure 5.1. Here the spin of the τ^- corresponds to the direction of the daughter π^- in the τ^- rest frame and similarly the τ^+ spin direction corresponds to the opposite direction of the daughter π^+. It is therefore possible to define an observable to use in experiment, $\varphi^*_{\mathrm{CP}} \in [0, 2\pi]$, which is the acoplanarity of the decay planes of each of the τ leptons constructed from the visible decay products (denoted here by the use of * notation) in the Zero Momentum Frame(ZMF) of the two daughter τ leptons. The ZMF is an approximation of the Higgs rest frame since we cannot detect the neutrinos in the ATLAS experiment. The graphical demonstration of φ^*_{CP} is shown in Figure 5.2.

Using φ^*_{CP} the decay can be rewritten at leading order as:

$$d\Gamma_{H\rightarrow\tau^+\tau^-} \approx 1 - b(E_+)b(E_-)\frac{\pi^2}{16}\cos(\varphi^*_{\mathrm{CP}} - 2\phi_\tau) \tag{5.3}$$

where $b(E)$ is a spectral function which describes the spin analysing power of a given decay mode. For decays containing no neutral particles b(E) is 1, otherwise it is largely energy dependent. Qualitatively, if the decay products are from a scalar Higgs the visible charged products mostly go in opposite directions thus the acoplanarity φ^*_{CP} peaks at π conversely those from a pseudoscalar Higgs tend to go in the same direction making the acoplanarity 0 thus φ^*_{CP} is at its maximum at 0 and 2π. This is demonstrated in Figure 5.3 where the CP-Even Higgs predicted by the Standard

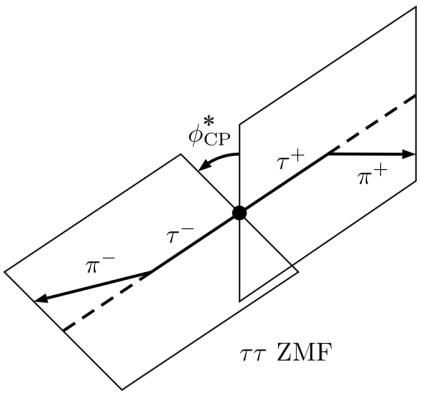

Figure 5.2.: Illustration shows the decay planes formed by the $H \to \tau^+\tau^- \to \pi^+\pi^- + 2\nu$ in the Zero Momentum frame of the di-tau system. It also illustrates that φ^*_{CP} is the angle formed between these two planes [67].

Model peaks at $\varphi^*_{CP} = \pi$, CP-odd is phased shifted by π and any non-integer phase shift would indicate some mixing of CP Odd and Even states. One crucial detail to observe from Figure 5.3 is that φ^*_{CP} for background processes (such as $Z \to \tau^+\tau^-$) does not introduce a bias to the φ^*_{CP} measurement.

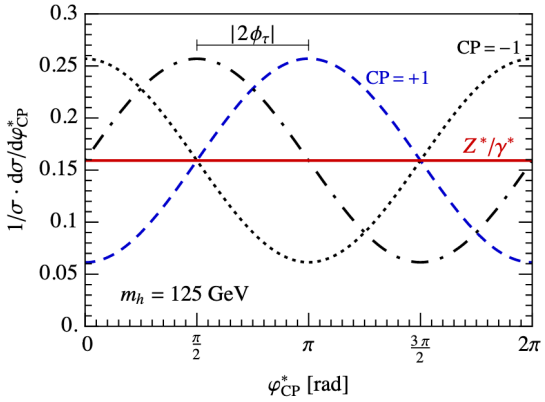

Figure 5.3.: Normalised φ^*_{CP} distributions for $pp \to H/Z*/\gamma^* \to \tau^+\tau^-$ decays. The blue long dashed line represents the CP-even distribution, the black short dashed line is the CP-odd distribution. The black dashed and dotted line is a CP-Mixed state where $\phi_\tau = -\frac{\pi}{4}$, an arbitrary mixing angle to show a mixed state and the red solid line show the flat distribution of φ^*_{CP} for Z^* and γ^* decays [66]

5.3. CP Observable Construction

The exact construction of the observable depends on the Higgs decay mode. The Higgs decay modes are categorised by how many positive and neutral particles are seen within the final state, not including neutrinos produced since this are not detected with the ATLAS detector. The nomenclature used for this classification is: XpYn where X represents the number of charged particles and Y is the number of neutral particles. For example the decay $\tau \to \pi^- \pi^0 \nu_\tau$ would be classified as 1p1n.

Figure 5.4 shows the construction of the tau decay planes in each of the following methods for calculating φ^*_{CP}. Each of the methods used in the analysis are based on the methods presented in Ref [64].

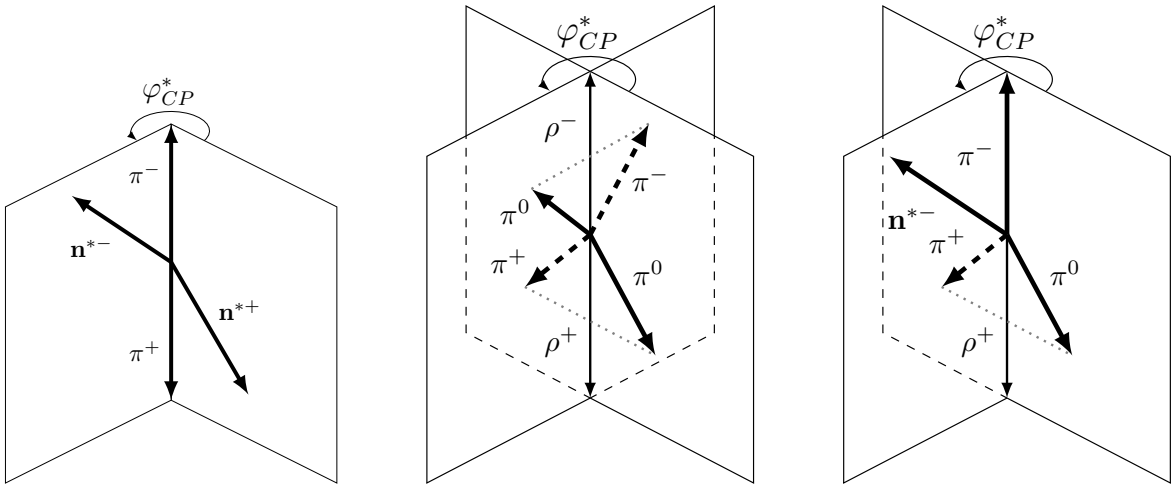

(a) $H \to \tau^+\tau^- \to \pi^+\pi^- + 2\nu$ decay where the IP Method is used, defining the two decay planes using the momenta of the pions and their impact parameters $\boldsymbol{n}^{*+}$

(b) $H \to \tau^+\tau^- \to \pi^+\pi^0\nu\pi^-\pi^0\nu$ decay where the ρ Method is used, where the decay planes are formed using the momenta of the charged and neutral pions.

(c) $H \to \tau^+\tau^- \to \pi^+\pi^0\nu\pi^-\nu$ decay where a combination of the IP and ρ methods are used, constructing one decay plane with each method.

Figure 5.4.: Three demonstrations of the how the different methods construct the φ^*_{CP} by using decay planes formed from the momenta and impact parameter [68].

5.3.1. IP method

The IP method is so called since it uses the spatial momentum vector of the charged decay product of the τ lepton decay and its Impact Parameter (hence IP). The impact

parameter is defined as the vector from the production vertex of the two τ leptons to the point of closest approach of the charged particles track to the τ production point. In practice the production poiont of the τ leptons is virtually identically to the Higgs production vertex found through the reconstructed primary vertex (PV) of the event.

The IP method can be applied to any decay mode that has at least one charged particle in the final state. In the analysis, it is used for decay modes with only a single visible decay product where that product is charged, such as $\tau \to \pi^{\pm}\nu$ or $\tau \to l^{\pm}\nu\nu$ where l is a muon or electron. The spatial momentum of the charged decay product $\boldsymbol{q}^{\pm}$ can be directly measured, the 3D impact parameter vector, $\boldsymbol{n}^{\pm}$, however must be constructed from the longitudinal and transverse 2d impact parameters (d_0 and z_0) respectively. Using d_0 and z_0, a 2d point of closest approach to the beamline can be defined. Helical extrapolation is then used from this point, to describe the particles track. The vector,$\boldsymbol{n}^{\pm}$, is defined as the vector between the primary vertex and the point of minimal distance between the extrapolated track and the primary vertex [69]. The 4-vectors of track momentum ($q_{\mu}^{\pm}$) and the impact parameter ($n_{\mu}^{\pm} = (0, \boldsymbol{n}^{\pm})$) are initially measured in the lab frame, these are then boosted into the zero momentum frame (ZMF) of the charged decay products and normalised to become $\hat{q}_{\mu}^{*\pm}$ and $\hat{n}_{\mu}^{*\pm}$ respectively, where the $*$ denotes the zero momentum frame of the charged decay products. This is then decomposed into its transverse and parallel components (relative to the spatial momentum ,$\hat{q}_{\mu}^{*\pm}$). The transverse component is designated as $\hat{n}_{\mu}^{*\pm}$. Equation 5.4 defines an angle φ^{*} and Equation 5.5 defines the T-odd triple correlation $\mathcal{O}_{CP}^{*}$ using the variables previously described. Finally Equations 5.4 and 5.5 define the observable φ_{CP}^{*}, which can have values between $0^{\circ} - 360^{\circ}$. It is important to note here that during leptonic decays a sign change is introduced and therefore to ensure the φ_{CP}^{*} is unchanged between lepton and hadronic decays a shift of 180° is introduced.

The IP method suffers from poor performance (here meaning it is a poor discrimator of CP-Odd and CP-Even Higgs) when the impact parameter vector is of small and is the same magnitude as the primary vertex uncertainty. It was found this poor performance occured when the significance of the d_0^{sig} was low, here defined as impact parameter in the transverse plane, d_0 divided by its uncertainty. 1p0n events have been separated into multiple sensitivity regions using different cuts for $\left|d_0^{\text{sig}}\right|$, discussed further in Chapter 8. Figure 5.5 shows the how different thresholds for $|\, d_0^{\text{sig}} \,|$ change the shape of the φ_{CP}^{*} distributions allowing for more clear differentiation of the scalar and pseudoscalar cases.

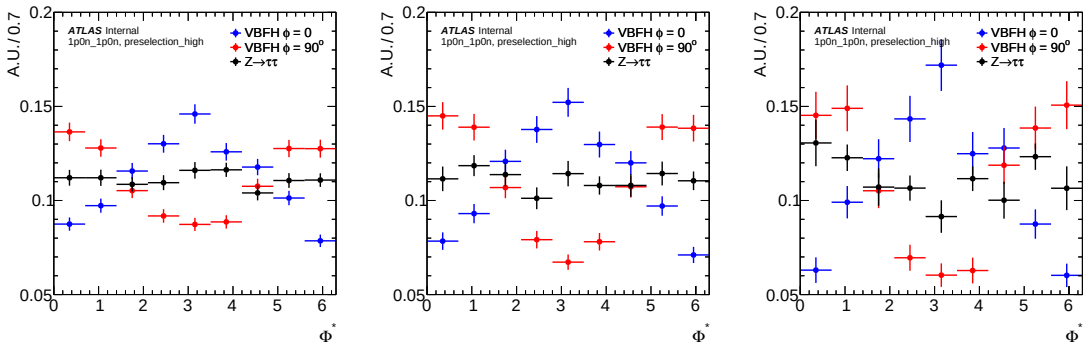

(a) $|d_0^{\text{sig}}| > 0.5$ **(b)** $|d_0^{\text{sig}}| > 1.5$ **(c)** $|d_0^{\text{sig}}| > 3.0$

Figure 5.5.: The effect of d_0^{sig} cuts on the shape of the φ^*_{CP} (here labelled Φ^*) distributions.

$$\varphi^* = \arccos\left(\hat{\boldsymbol{n}}_\perp^{*+} \cdot \hat{\boldsymbol{n}}_\perp^{*-}\right) \tag{5.4}$$

$$\mathcal{O}^*_{CP} = \hat{\boldsymbol{q}}^{*-} \cdot \left(\hat{\boldsymbol{n}}_\perp^{*+} \times \hat{\boldsymbol{n}}_\perp^{*-}\right) \tag{5.5}$$

$$\varphi^*_{CP} = \begin{cases} \varphi^*_{CP} & \text{if } \mathcal{O}^*_{CP} \geq 0 \\ 360^\circ - \varphi^*_{CP} & \text{if } \mathcal{O}^*_{CP} < 0 \end{cases} \tag{5.6}$$

5.3.2. Rho-method

The ρ-method, so called for its use in τ to ρ-meson decays, is used in cases where the decay products contain at least one neutral pion. Neutral pions occur in the final state in the case of two-stage decays such as $\tau \to \rho^\pm \nu, \rho^\pm \to \pi^\pm \pi^0$. The 4-vectors of track momentum for both the charged and neutral pions, $q^\pm$ and $q^{0\pm}$, are normalised and boosted into the ZMF of the visible tau decay products, giving $\hat{\boldsymbol{q}}^{*\pm}$ and $\hat{\boldsymbol{q}}^{*0\pm}$. The transverse component of $\hat{\boldsymbol{q}}^{0\pm}$ is taken with respect to the direction of the associated charged pion for each neutral pion, these are denoted as $\hat{\boldsymbol{q}}_\perp^{*0\pm}$. From these variables it is possible to calculate the angle, φ^*, and T-odd triple correlation using Equations 5.7 and 5.8 which are similar to Equations 5.4 and 5.5 used in the IP method, replacing the

impact parameter with the neutral pion vector or if there are multiple neutral pions, the sum of all of the momenta for the neutral pions.

$$\varphi^* = \arccos\left(\hat{\boldsymbol{q}}_\perp^{*0+} \cdot \hat{\boldsymbol{q}}_\perp^{*0-}\right) \tag{5.7}$$

$$\mathcal{O}_{CP}^* = \hat{\boldsymbol{q}}^{*-} \cdot \left(\hat{\boldsymbol{q}}_\perp^{*0+} \times \hat{\boldsymbol{q}}_\perp^{*0-}\right) \tag{5.8}$$

As before in the IP Method, using the variables calculated in Equations 5.7 and 5.8, it is possible to calculate $\varphi_{CP}^{*'}$.

$$\varphi^{*'} = \begin{cases} \varphi^* & \text{if } \mathcal{O}_{CP}^* \geq 0 \\ 360^\circ - \varphi^* & \text{if } \mathcal{O}_{CP}^* < 0 \end{cases} \tag{5.9}$$

$\varphi_{CP}^{*'}$ is not sensitive to the CP mixing angle ϕ_τ unless the sign of the tau spin-analysing function is accounted for. This is incoporated by calculating the value of $y_\pm^\rho$ in Equation 5.10 which is then used in Equation 5.11 to give a final value of φ_{CP}^*.

$$y_\pm^\rho = \frac{E_\pi^\pm - E_\pi^0}{E_\pi^\pm - E_\pi^0} \tag{5.10}$$

$$\varphi_{CP}^* = \begin{cases} \varphi^{*'} & \text{if } y_-^\rho y_+^\rho \geq 0 \\ \varphi^{*'} + 180^\circ & \text{if } y_-^\rho y_+^\rho < 0 \end{cases} \tag{5.11}$$

Events with a greater value of $\left|y_-^\rho y_+^\rho\right|$ are more sensitive to ϕ_τ. This means it can be used in an analogous way to $\left|d_0^{\text{sig}}\right|$ for IP method to define high and low sensitivity regions. This cut is discussed further in Chapter 8.

Figure 5.6 shows how the φ_{CP}^* distribution varies with the different $\left|y_-^\rho y_+^\rho\right|$ cuts.

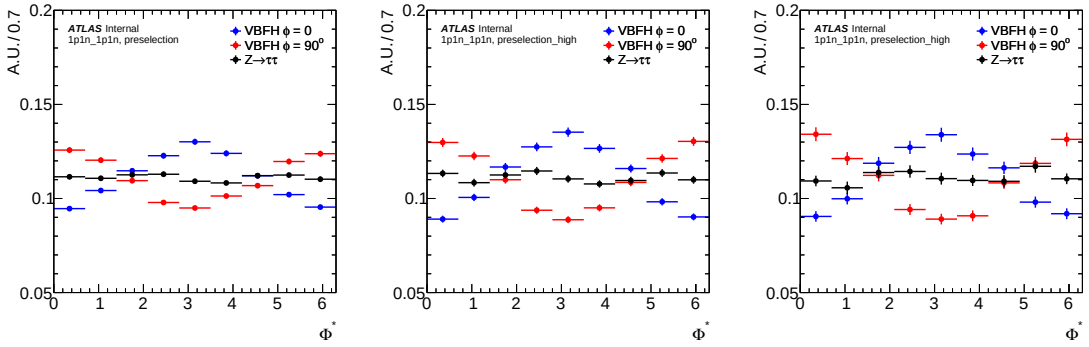

(a) $yy > 0$ **(b)** $yy > 0.2$ **(c)** $yy > 0.4$

Figure 5.6.: The effect of $y^{\rho}_{-}y^{\rho}_{+}$ cuts on the shape of the $\varphi^{*}_{\mathrm{CP}}$ (here labelled Φ^{*}) distributions.

5.3.3. Combined IP and Rho (IP-Rho) method

In situations where the two τ leptons decay through different modes, it is necessary to have a way of combining the IP and ρ methods to calculate φ^{*}_{CP}, for example $H \to \tau^{+}\tau^{-} \to \pi^{-}\rho^{+} + 2\nu_{\tau}$. This method is used for for 1p0n-1p1n, 1p0n-1pXn, l-1p1n and l-1pXn decays within the analysis. In the case where more than one neutral pion is present in the final state (1pXn) then the total sum of the spatial momentum vectors of the neutral pions is used. The (IP-ρ) method follows the framework of the ρ method but with a few notable changes as follows. The IP-ρ method, as before, defines φ^{*}_{CP} in the Zero Momentum Frame of the visible decay products so in the example of $H \to \tau^{+}\tau^{-} \to \pi^{-}\rho^{+} + 2\nu_{\tau}$ the ZMF would be defined in $\pi^{-}\rho^{+}$ frame. The decay planes are defined as they would be in the IP and ρ methods seperately; the first decay plane would be defined by π^{-} and its impact parameter and if the ρ^{+} from the example decays to $\pi^{+}\pi^{0}$ then second the decay plane would be described by the spatial momentum direction of π^{+} and the component of the spatial direction of π^{0} perpendicular to the direction of π^{+}.

From here Equations 5.12 and 5.13 can be used to calculate the angle φ^{*} and T-odd triple correlation, $\mathcal{O}^{*}_{CP}$.

$$\varphi^{*} = \arccos\left(\hat{\boldsymbol{q}}^{*0+}_{\perp} \cdot \hat{\boldsymbol{n}}^{*-}_{\perp}\right) \tag{5.12}$$

$$\mathcal{O}^*_{CP} = \hat{\boldsymbol{q}}^{*-} \cdot \left(\hat{\boldsymbol{q}}^{*0+}_{\perp} \times \hat{\boldsymbol{n}}^{*-}_{\perp} \right) \tag{5.13}$$

These can then be combined into one variable using Equation 5.14.

$$\varphi^{*'} = \begin{cases} \varphi^*_{CP} & \text{if } \mathcal{O}^*_{CP} \geq 0 \\ 360^\circ - \varphi^*_{CP} & \text{if } \mathcal{O}^*_{CP} < 0 \end{cases} \tag{5.14}$$

Then finally as with the ρ-method it is necessary to account for the signs of the tau spin-analysing function:

$$y^\rho_\pm = \frac{E^\pm_\pi - E^0_\pi}{E^\pm_\pi - E^0_\pi} \tag{5.15}$$

, where $E^\pm_\pi$ and E^0_π are the energies of the charged and neutral pions respectively.

$$\varphi^*_{CP} = \begin{cases} \varphi^{*'} & \text{if } y^\rho \geq 0 \\ \varphi^{*'} + 180^\circ & \text{if } y^\rho < 0 \end{cases} \tag{5.16}$$

Since IP method and ρ method are seperated into sensitivity regions by the use of $\left|d_0^{\text{sig}}\right|$ and $\left|y^\rho_- y^\rho_+\right|$ cuts respectively. When using the combined IP and ρ (IP-ρ) method it is necessary to use a combination of both $\left|d_0^{\text{sig}}\right|$ and $|y|$ for the same purpose. The exact cuts used are detailed in Chapter 8.

5.3.4. a_1-decay (a_1) method

The a_1 method is an extension of the ρ method for 3-prong (3 charged particles in the final state) tau decays where $\tau^\pm \to a_1^\pm \nu, a_1^\pm \to \rho^0 \pi^\pm, \rho^0 \to \pi^+ \pi^-$. In this method, a pair of final state pions (π^+ and π^-) are used to reconstruct ρ^0. ρ^0 in conjunction with the remaining charged pion, $\pi^\pm$ uses the ρ method to construct the tau decay planes, but with the ρ^0 forming the neutral component as opposed to π^0 as before. It should

be noted that since the choice of pions can effect the reconstruction though their choice is somewhat arbitrary, in this analysis the two $\pi^{\pm}$ with the lowest pT were chosen as the pair that forms the neutral component, no opposite sign requirement is applied here.

The ntuples and associated systematics used in this analysis are the same as those used in the Run 2 coupling analysis [61], which do not store charge information of the tracks. Alternative techniques that do include this charge requirement showed minimal improvements in CP sensitivity [70]. Therefore, to avoid delays in the analysis that a full reprocessing to include track charge information would incur, the opposite sign requirement was not implemented. In addition, it is necessary to not ignore the mass terms in the calculation of $y_{\pm}^{a_1}$ (the equivalent of $y_{\pm}^{\rho}$ from the ρ method). Unlike in the ρ method, the difference in masses between ρ^0 and $\pi^{\pm}$ is non-negligible as opposed to the difference in $\pi^{\pm}$ and π^0. The calculation for $y_{\pm}^{a_1}$ is shown in Equation 5.17.

$$y_{\pm}^{a_1} = \frac{E_{\rho^0} + E_{\pi^{\pm}}}{E_{\rho^0} - E_{\pi^{\pm}}} - \frac{m_{a_1}^2 - m_{\pi^{\pm}}^2 + m_{\rho^0}^2}{2m_{a_1}^2} \tag{5.17}$$

where X_{a_1} refers to variable constructed from all three final state pions, $X_{\pi^{\pm}}$ refers to the $\pi^{\pm}$ with the highest pT and X_{ρ^0} refers to the ρ_0 constructed from the remaining final state pions.

In this analysis only 3p0n are considered for this analysis and only in the combination of 1p1n-3p0n combination in the hadronic channel and ℓ-3p0n in the leptonic channel. As explored in [70] this is because CP sensitivity and statistics are poor for 3-prong decays with more than 1 neutral pion and for 3p-3p decays.

5.4. Decay Mode Combinations

In this analysis both the hadronic and leptonic decays of the τ leptons are used. For the hadronic decays, which comprise 65% of the branching fraction (though not all decay modes are included due to poor sensitivity to the CP-mixing angle), the products comprise mostly of charged hadrons and neutral hadrons (predominantly $\pi^{\pm}$ and π^0

and τ neutrinos. For the leptonic decays the products consist of either e or μ, their corresponding neutrino and a τ neutrino.

Decay mode	Branching fraction	Notation
$\mu^- \bar{\nu}_\mu \nu_\tau$	17.4 %	ℓ
$e^- \bar{\nu}_e \nu_\tau$	17.8 %	
$h^- \nu_\tau$	11.5 %	1p0n
$(\pi^- \nu_\tau)$	(10.8 %)	
$h^- \pi^0 \nu_\tau$	25.9 %	1p1n
$(\pi^- \pi^0 \nu_\tau)$	(25.5 %)	
$h^- \geq 2\pi^0 \nu_\tau$	10.8 %	1pXn
$(\pi^- 2\pi^0 \nu_\tau)$	(9.3 %)	
$3h^\pm \nu_\tau$	9.8 %	3p0n
$(3\pi^\pm \nu_\tau)$	(9.3 %)	

Table 5.1.: Branching fractions of τ decay modes [71] (both leptonic and hadronic) along with their notation that is used throughout this analysis. Note, $h^\pm$ encompasses both $\pi^\pm$ and $K^\pm$ since these decays are mostly $\pi^\pm$ decays their branching ratios have been included too in brackets

Each of the decay modes for single τ leptons that are used within this analysis, ℓ, 1p0n,1p1n,1pXn and 3p0n, are combined into pairs of decays for the $\tau_{\text{lep}}\tau_{\text{had}}$ and $\tau_{\text{had}}\tau_{\text{had}}$ channels to describe the decays of both taus. The decay modes used in this analysis are summarised in Table 5.2 along with the methods used to build φ^*_{CP} and the branching fractions for the di-τ decays. In general decays containing only 1p0n or 1p1n decays are most sensitive in φ^*_{CP} and form the dominant decays of the analysis, 1pXn and 3p0n are subdominant due to their decreases sensitivity and lower statistics due to the lower branching fractions.

Decay Channel	Decay Mode Combination	Method	Fraction in all τ lepton pair decays
$\tau_{\text{lep}}\tau_{\text{had}}$	ℓ-1p0n	IP	8.1%
	ℓ-1p1n	IP-ρ	18.3%
	ℓ-1pXn	IP-ρ	7.6%
	ℓ-3p0n	IP-a_1	6.9%
$\tau_{\text{had}}\tau_{\text{had}}$	1p0n-1p0n	IP	1.3%
	1p0n-1p1n	IP-ρ	6.0%
	1p1n-1p1n	ρ	6.7%
	1p0n-1pXn	IP-ρ	2.5%
	1p1n-1pXn	ρ	5.6%
	1p1n-3p0n	ρ-a_1	5.1%

Table 5.2.: The decay modes combinations for the decays of both τ leptons and their corresponding reconstruction method combinations used in this analysis

Chapter 6.

Study of construction methods for observable

6.1. Motivation

Data taking for Run 3 started in Spring 2022. Over the course of the run it is expected to deliver 280 fb^{-1} of proton-proton collision data compared to 160 fb^{-1} delivered in Run 2. These increased statistics are promising for further CP analyses investigating the CP properties of the $H \to \tau\tau$ decay. It is also necessary to improve the methods used for constructing the main observable. The polarimetric vector method for constructing φ^*_{CP}, investigated in this chapter, was used by the CMS collaboration [72] for constructing φ^*_{CP} in the case of the Higgs decaying to two τ which each decay to 3 charged pions. This study uses truth level data to investigate the sensitivity of the method on other decay modes.

6.2. Implementation of testing framework

In order to easily test multiple different methods of calculating acoplanarity in a convenient way, the "Sisyphus" framework was created. It is a flexible framework for generating events, processing them and shaping the output for consumption by other applications. It is generator, process and analysis agnostic. For the purposes of this analysis, Pythia8 was used as the event generator. A schematic of the Sisyphus framework is shown in Figure 6.1.

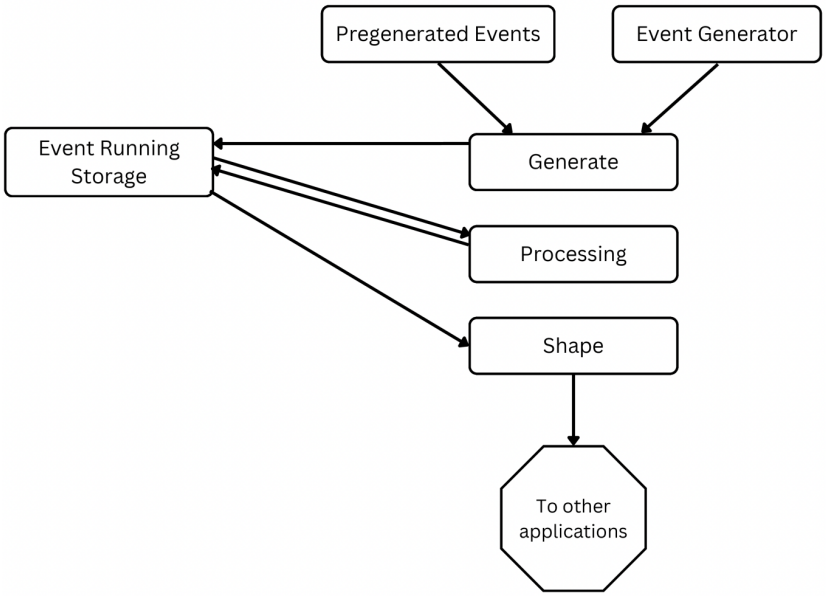

Figure 6.1.: A schematic showing the implementation of the "Sisyphus" framework that is used for testing the different acoplanarity calculation methods.

The first stage is the "Generate" step. This step's primary objective is to store events in the "Event Running Storage" in a consistent way. It can parse events from either a pregenerated source such as a text file or events generated on the fly using an event generator (for these studies, Pythia8 was used). The "Running Event Storage" (RES) is where events are stored throughout the running of the Sisyphus framework. The choice of what to use for this is up to the user of the framework, a Root TTree is used for the RES in this study. The next stage is the "Processing" step, this stage is where any major calculations used within the analysis are performed. In this study, this is primarily used for the calculation of acoplanarities for each event. This step retrieves events from the RES to complete any calculations necessary and then any results computed in this step that need to be carried over into subsequent steps can be stored in the RES along with the event data. Finally the "Shape" step retreives the events from the RES, along with any stored data from the previous step and shapes this data for consumption by subsequent processes. This could be as simple as returning a list of acoplanarities and weights, as is used in Section 6.3, or as complex as returning multiple variables for consumption in machine learning applications.

6.3. Validation of framework

In order to validate the framework, preliminary plots were produced using the ρ-ρ method (for more information see Section 5.3.2) and the "Neutral-Pion" method from [72] which is described below. Both methods produce an acoplanarity angle, which is then weighted for a given angle of ϕ_τ to produce the plots shown here. Each plot was generated from 90,000 events where the Higgs decays into two intermediate $\rho^\pm$ which then each decay into $\pi^\pm\pi^0\nu$.

6.3.1. Plots using ρ-ρ method

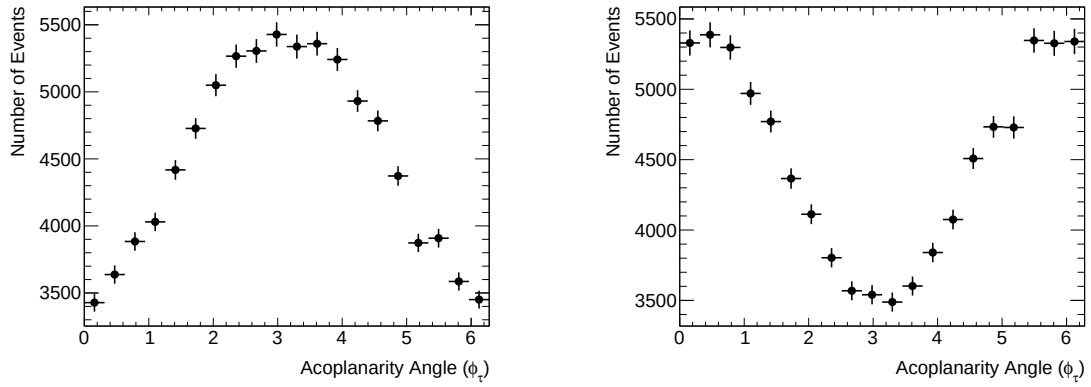

(a) Scalar **(b)** Pseudoscalar

Figure 6.2.: A plot of the weighted acoplanarities of scalar and pseudoscalar $H \to \tau\tau$ events using the ATLAS $\rho - \rho$ method produced using Sisyphus framework.

Figure 6.2 correctly shows a peak at π for the scalar case and peaks at 0 and 2π for the pseudoscalar case, verifying that this method is implemented correctly and working as expected.

6.3.2. Neutral Pion Method

The Neutral Pion Method (NPM) can be used for hadronically decaying τ leptons where they are decaying into more than one hadron. This description of the method will use the examples of a τ decaying to an intermediate $\rho^\pm$ to $\pi^\pm + \pi^0$. First a Zero Momentum Frame is defined using only the charged pions. All of the pions (both

charged and neutral) are then boosted into this ZMF and the angle between the decay planes ϕ^{ZMF}, can be calculated:

$$\phi^{\mathrm{ZMF}} = \arccos\left(\hat{a}_{\perp}^{\mathrm{ZMF}+} \cdot \hat{a}_{\perp}^{\mathrm{ZMF}-}\right) \tag{6.1}$$

where a is the 4 momentum of π^0. This, as with the $\rho - \rho$ method, must then use the T-Odd triple correlation to determine ϕ_{CP}:

$$O^{\mathrm{ZMF}} = \hat{q}^{\mathrm{ZMF}-} \cdot \left(\hat{a}_{\perp}^{\mathrm{ZMF}+} \times \hat{a}_{\perp}^{\mathrm{ZMF}-}\right) \tag{6.2}$$

$$\phi_{\mathrm{CP}} = \begin{cases} \phi^{\mathrm{ZMF}} & if O^{\mathrm{ZMF}} \geq 0 \\ \phi^{\mathrm{ZMF}} & if O^{\mathrm{ZMF}} < 0 \end{cases} \tag{6.3}$$

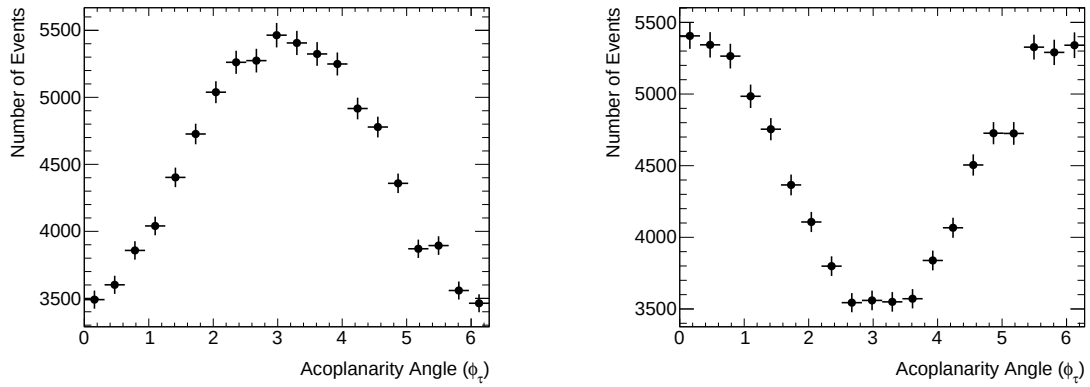

(a) Scalar **(b)** Pseudoscalar

Figure 6.3.: A plot of the weighted acoplanarities of scalar and pseudoscalar $H \to \tau\tau$ events using the CMS neutral-pion method produced using Sisyphus framework.

Figure 6.3, as with the $\rho - \rho$ method, correctly shows a peak at π for the scalar case and peaks at 0 and 2π for the pseudoscalar case, verifying that this method is implemented correctly and working as expected.

6.4. Calculation of acoplanarity using polarimetric vectors

A polarimetric vector, denoted as $\vec{h}$, is an estimate of the most likely direction of the spin vector $\vec{s}$ of the τ lepton in its own reference frame [73]. For the calculation of the polarimetric vectors this study used TAUOLA [74] [75] [76] which uses the $a_1^{3\text{pr}}$ model using parameters measured by the CLEO Collaboration [77].

Calculating acoplanarity from polarimetric vectors is a multi-stage process. The first step is to calculate vectors, $\vec{k}_1$ and $\vec{k}_2$. This is done with Equation 6.4, using the polarimetric vectors, $\vec{h}_{1,2}$ and the τ lepton momentum unit vectors defined in the H rest frame, $\vec{n}_{1,2}$. Once vectors $\vec{k}_{1,2}$ have been calculated, they can be used to calculate φ^* and $\mathcal{O}$ in Equations 6.5 and 6.6

$$\vec{k}_{1,2} = \frac{\vec{h}_{1,2} \times \vec{n}_{1,2}}{\left|\vec{h}_{1,2} \times \vec{n}_{1,2}\right|} \tag{6.4}$$

$$\varphi^* = \arccos\left(\vec{k}_1 \cdot \vec{k}_2\right) \tag{6.5}$$

$$\mathcal{O} = -(\vec{h}_1 \times \vec{h}_2) \cdot \vec{n}_1 \tag{6.6}$$

Finally,φ^* and $\mathcal{O}$ may be used to calculated the acoplanarity angle,φ_{CP}.

$$\varphi_{CP} = \begin{cases} \varphi^* & \text{if } \mathcal{O} \geq 0 \\ 360^\circ - \varphi^* & \mathcal{O} < 0 \end{cases} \tag{6.7}$$

6.5. Future Work

Due to time constraints, the completion of this study was not possible, however future work here would include to implementation of the polarimetric vector method for

constructing φ_{CP}. This would then allow for the comparison of the different methods of calculating φ_{CP} using truth level data. When performing the comparison on truth level data, due to the absence of detector or reconstruction effects, the main goal would be understanding how the different construction methods handle limited statistics. In order to do this, the data should be broken up into small sets of around 100 events, from each of these sets a value of ϕ_τ can be determined. Then this can be repeated multiple times for each method to assess the distribution of values of ϕ_τ as a difference from the truth-level value; enabling the evaluation of the sensitivity of each method.

Chapter 7.

Data and Simulated Samples

7.1. Data

This analysis uses the same dataset as the $H \to \tau\tau$ coupling analysis [61], the full Run 2 pp dataset of LHC data taken at 25ns operation corresponding to a total integrated luminosity of 139 fb^{-1}. Table 7.1 shows the intergrated luminosity for each of the Good Run Lists (GRL) files used for each data taking period.

Year	$\int \mathcal{L} dt (fb^{-1})$	Good Run List XML file
2015	3.22	data15_13TeV.periodAllYear_DetStatus-v89-pro21-02_ Unknown_PHYS_StandardGRL_All_Good_25ns.xml
2016	32.99	data16_13TeV.periodAllYear_DetStatus-v89-pro21-01_ DQDefects-00-02-04_PHYS_StandardGRL_All_Good_25ns.xml
2017	44.31	data17_13TeV.periodAllYear_DetStatus-v99-pro22-01_Unknown _PHYS_StandardGRL_All_Good_25ns_Triggerno17e33prim.xml
2018	58.45	data18_13TeV.periodAllYear_DetStatus-v102-pro22-04_Unknown _PHYS_StandardGRL_All_Good_25ns_Triggerno17e33prim.xml

Table 7.1.: Good Run List (GRL) files used in the analysis.

7.2. Monte Carlo

The Monte Carlo signal samples for this analysis use a toolchain consisting of the following; POWHEG [78] [79] [80] for generating the Higgs, PYTHIA 8 [81] handles the decay and hadronisation to produce unpolarised pairs of τ with no spin correlation between them and TAUSPINNER [82] [83] [84] adds τ lepton polarisation. The unpolarised samples generated by POWHEG and PYTHIA 8 then have an event weight assigned to them by TAUSPINNER to introduce spin correlations. In TAUSPINNER, the polarisation of the di-τ decay is estimated using the MC Truth level information of the tau kinematics. Next, the tree-level matrix element of the events is used to add spin effects through the assigning of an event weight. This technique is advantageous since rather than having to regenerate event for each specific CP-mixing angle scenario, the same data set can be reweighted for any given CP-mixing angle. In order to ensure the validity of the output of TAUSPINNER, an unpolarised sample, reweighted for different mixing scenarios (CP-Even,CP-Odd, CP-Mixed 45°), these was compared against CP-Even, CP-Odd and CP-mixed samples. These comparisons showed good agreement throughout.

In this analysis 4 Higgs production modes are considered; gluon-gluon fusion (ggF), Vector Boson Fusion (VBF), associated production (VH) and Top production ($t\bar{t}H$). ggF is the dominant production mode the cross sections for each of the production modes are displayed in Table 7.2.

Production Mode	Expected Cross Section (pb)
ggF	48.58
VBF	3.781
VH	2.2496
$t\bar{t}H$	0.507

Table 7.2.: The expected cross sections for the production modes of the Higgs Boson used in this analysis

7.3. Signal Generation

7.3.1. Gluon-Gluon Fusion

Gluon-Gluon Fusion production of Higgs bosons is simulated by using the POWHEG NNLOPS program [85] [86] [78] [79] [80] to next-to-next-to-leading order (NNLO) accuracy in QCD for arbitrary $gg \to H$ observables. This accuracy is achieved by reweighting the Higgs rapidity spectrum to HNNLO in Hj-MiNLO [87] [88] [89], the Higgs+Jet extension to the Multiscale Improved Next-To-Leading Order simulation. [90]. For the configuration of PYTHIA8 the parton distribution function set, PDF4LHC15 NLO [91], is used along with the ANZLO tune [92]. The next-to-next-to-next-to-leading order (N^3LO) cross section is used to normalise the gluon-gluon fusion predictions in QCD from the Monte Carlo samples plus the electroweak corrections at next-to-leading order. The decay branching ratios are handled by HDECAY [93] [94] [95] and PROPHECY4F [96] [97] [98].

7.3.2. Vector Boson Fusion

The simulation of Higgs bosons produced by vector boson fusion is generated by POWHEG [99], PYTHIA8 is then used to simulate parton shower and non-perturbative effects. POWHEG predictions are already accurate to NLO, which is the brought up to NNLO by tuning the predictions to account for effects due to finite heavy-quark masses and soft-gluon resummation. The PDF set, PDF4LHC15 NLO and ANZLO tune are used in PYTHIA8 as they were for the gluon-gluon fusion predictions, similarly the Monte Carlo predictions are also normalised using an approximately NNLO cross section in QCD with NLO electroweak corrections [100] [101] [102], once again using HDECAY and PROPHECY4F for decay branching ratio.

7.3.3. VH Production

The simulation of Higgs bosons generated in association with a vector boson are generated by POWHEG as with VBF production, PYTHIA8 is then used to simulate parton shower and non-perturbative effects. The prediction is accurate for NLO for the VH + jet production. The loop-induced $gg \to ZH$ production is simulated seperately

and only to leading order. For VH production, once again in PYTHIA8 PDF4LHC15 NLO and the ANZLO tune are used. The Monte Carlo predictions for this process are normalised to NNLO accuracy in QCD with NLO electroweak corrections for the pp $\rightarrow$ VH channel while for gg $\rightarrow$ ZH they are normalised to NLO and Next-to-leading-logorithm in QCD [103] [104] [105] [106] [107] [108] [109]. The decay branching ratio is also handled by HDECAY and PROPHECY4F.

7.3.4. ttH

The modelling of $t\bar{t}H$ events is performed using POWHEGBOX V2 [78] [79] [80] [110] [111], these are generated at NLO accuracy using the NNPDF3.0nlo PDF set [112]. The generated events are then interfaced with PYTHIA8.230 using the A14 tune [113], and NNPDF2.3lo PDF set. EvtGen v1.6.0 [114] handles the decays of the bottom and charm hadrons.

7.3.5. Summary of signal generation

Below is a table summarising the MC generators used for the generation of signal events

Process	Generator		PDF set		Tune	Order
	ME	PS	ME	PS		
$H \rightarrow \tau\tau/WW$						
ggF	Powheg	Pythia8	PDF4LHC15	CTEQ6L1	AZNLO	NNLO+NNLL
VBF	Powheg	Pythia8	PDF4LHC15	CTEQ6L1	AZNLO	(N)NLO
VH	Powheg	Pythia8	PDF4LHC15	CTEQ6L1	AZNLO	NNLO
$t\bar{t}H$	Powheg	Pythia8	NNPDF2.3		A14	NLO

Table 7.3.: A summary of the MC generators used for the production of simulated samples for signal processes, where ME and PS are matrix element and parton shower respectively.

7.4. Background Generation

7.4.1. V + Jets

For simulating the production of V+jets, Sherpa V2.2.1 [115] is used. When simulating 2 partons, NLO matrix elements are used whereas leading order matrix elements are used for considering three or four partons in a given process. These are calculated using the Comix [116] and OPENLOOPS 1 libraries [117] [117] [118] [119]. The matrix elements are then matched with SHERPA parton showers [120]. This matching is done using the MePs@NLO matching method [121] [122] [123] [124], using the tuned parameters developed by SHERPA. The PDF set, NNPDF3.0nnlo, is used for this channel and the sample is normalised using the next-to-next-to-leading order prediction [125].

7.4.2. Electroweak Production

The electroweak production of $lljj$, $lvjj$ and $vvjj$ final states, where l is a lepton, j is a jet and v is a neutrino, are handled in a very similar way to the V + Jet production. They are generated with the leading order matrix elements with a maximum of two additional parton emissions in Sherpa v2.2.1. The matrix elements are merged with the parton showers as before using MePs@NLO matching method and set of tuned parameters previously mentioned. The PDF set, NNPDF3.0nnlo, is used as before in the V+Jet production. The use of the VBF approximation (where t-channel typology only is considered) is employed here to avoid overlap with the semi-leptonic diboson typologies.

7.4.3. tt

The production of $t\bar{t}$ events to NLO accuracy uses POWHEGBox V2 [110], with the NNPDF3.0nnlo PDF set. During production the h_{damp} parameter is set to a value of 1.5 times the mass of the Top Quark [126]. The h_{damp} is a resummation damping factor, it is partially responsible for the matching of matrix elements and parton showers and therefore can be considered as regulating the high-p_T radiation. PYTHIA8.230 is used to model the hadronisation, parton shower and underlying events, for this both the

A14 tune and the NNPDF2.3lo PDF set [127] is used. EvtGen v1.6.0 is used to simulate the decays of bottom and charm quarks.

7.4.4. Single-top s-channel/t-channel

Single top s-channel (t-channel) production is modelled using POWHEGBox V2 [128] ([129]). These events are modelled at next-to-leading order in QCD using the five (four) flavour scheme using the NNPDF3.0nlo PDF set. These events are then interfaced with PYTHIA8.230 using the A14 tune and the NNPDF2.3lo PDF set.

7.4.5. tW

The production of top quarks associated with W-bosons is modelled in an almost identical way [130] to the s-channel top production. They are modelled in next-to-leading order in QCD using the five flavour scheme and NNPDF3.0nlo PDF set. Before these events are interfaced with PYTHIA8.230 using both the A14 tune and NNPDF2.3lo PDF set, the diagram removal scheme is used to remove interference and overlaps with $t\bar{t}$ production [131].

7.4.6. diboson

SHERPA v2.2.1 or v2.2.2 are used to generate diboson final states depending on the specific process. Final states where at least one of the bosons decays leptonically are generated in using matrix elements of NLO accuracy in QCD for a maximum of 1 additional parton emission or in LO accuracy for those with up to three additional parton emissions. Samples for the loop induced processes $gg \to VV$ are modelled using LO matrix elements for up to one additional parton emission regardless of if the final state is fully or semi leptonic. The matrix elements are then matched with parton showers in SHERPA using Catani-Seymour dipole factorisation [116] [120] using the MePs@NLO matching method as used for the V+jet and electroweak generation. The OPENLOOPS 1 library provides virtual QCD corrections and the NNPDF3.0nnlo set of PDFs is once again used along with a set of tuned parton-shower parameters created by the SHERPA developers.

Table 7.4 summarises the MC generators used for the generation of each of the background samples used in this analysis.

Process	Generator		PDF set		Tune	Order
	ME	PS	ME	PS		
V + jets	SHERPA 2.2.1		NNPDF30		SHERPA	NNLO
$t\bar{t}$	Powheg	Pythia8	NNPDF2.3		A14	NLO
Single top	Powheg	Pythia8	NNPDF2.3		A14	NLO
Di-Boson	SHERPA 2.2.1		NNPDF30		SHERPA	NNLO

Table 7.4.: A summary of the MC generators used for the production of simulated samples for background processes, where ME and PS are matrix element and parton shower respectively.

Chapter 8.

Event Selection

Event selection in the analysis occurs in a number of distinct steps. The first step is to first select events by decay channel through a combination of preselection cuts and trigger requirements. The next step isolates higgs events which are split by production mode (either through gluon-gluon fusion or vector-boson fusion) and different topologies (identified by BDTs) then finally events are split by decay modes so that specific cuts maybe introduced to differentiate high sensitivity events from low sensitivity events.

The triggers used in this analysis are the same as in the Run 2 $H \to \tau\tau$ coupling analysis [61] this based its preselection criteria on the previous $H \to \tau\tau$ coupling analysis [132] using 36 fb^{-1} Run 2 Data.

8.1. Trigger Selection

For the $\tau_{\text{lep}}\tau_{\text{had}}$ channel single electron and muon triggers are used. The lowest unprescaled triggers used are shown in Table A.1. These trigger requirements are also combined with preselection p_T cuts, for electrons these cuts are at 25GeV and 27GeV for the 2015 and 2016-2018 datasets respectively and for muons they are 21GeV and 27.3GeV for 2015 and 2016-2018. These p_T cuts ensure that the electron and muon candidates have a p_T that lies within the range where the trigger efficiency has plateaued. An example of this plateauing effect is demonstrated in Figure 8.1. The trigger threshold values are summarised in Table 8.2.

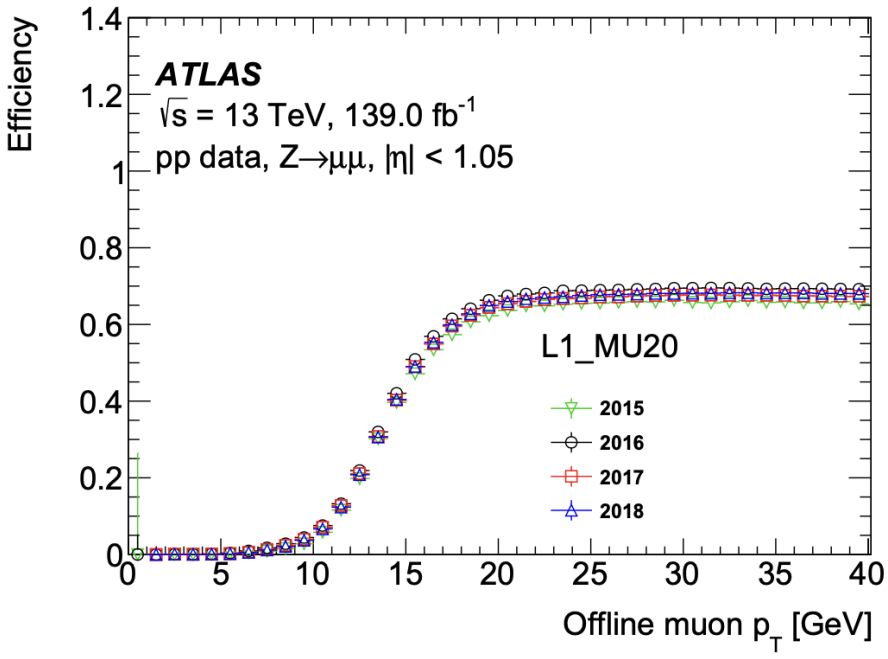

Figure 8.1.: The efficiency of the primary level-1 muon trigger specifically the L1_MU20 trigger which has a threshold of 20 GeV. This trigger is used in the analysis as a single muon trigger for the 2015 data. This graph demonstrates that the trigger does not exhibit perfect step function behaviour but instead increases rapidly but not instantaneously at the threshold value, an effect which must be accounted for when choosing event selection critieria [133].

Di-τ triggers used for the $\tau_{\text{had-vis}}$ channel across Run 2 are summarised in Table A.1. Each of the $\tau_{\text{had-vis}}$ candidates are then matched to the "legs" of the di-tau trigger using the individual single τ trigger objects. The Di-τ triggers, for the same reason as the single lepton triggers, also impose p_T cuts, these are summaried in Table 8.2.

2016-2018 triggers also include an extra level 1 trigger which requires a calorimeter trigger jet of $pT > 25GeV$ and $|\eta| < 3.2$. due to the rising instantaneous luminosity. Furthermore the leading jet in the event must be matched within $R < 0.4$ of the jet region of interest of the jet that met the trigger requirements. This aims to avoid biases due to turn on effects and ensures kinematically consistent selection between the 2015 and 2016-2018 datasets.

Trigger	Data period	HLT Chain name (in the menu)
Single electron	2015	`e24_lhmedium_L1EM20VH`, `e60_lhmedium` or `e120_lhloose`
	2016-2018	`e26_lhtight_nod0_ivarloose`, `e60_lhmedium_nod0` or `e140_lhloose_nod0`
Single muon	2015	`mu20_iloose_L1MU15` or `mu50`
	2016-2018	`mu26_ivarmedium` or `mu50`
Ditau	2015	`tau35_medium1_tracktwo_tau25_medium1_tracktwo_L1TAU20IM_2TAU12IM`
	2016	`tau35_medium1_tracktwo_tau25_medium1_tracktwo`
	2017	`tau35_medium1_tracktwo_tau25_medium1_tracktwo_03dR30_L1DR_TAU20ITAU12I_J25`
	2018	`tau35_medium1_tracktwoEF_tau25_medium1_tracktwoEF_03dR30_L1DR_TAU20ITAU12I_J25`

Table 8.1.: A summary of the trigger items used in this analysis. The $\tau_{\text{lep}}\tau_{\text{had}}$ channel uses single lepton triggers while the $\tau_{\text{had}}\tau_{\text{had}}$ channel uses di-hadronic τ triggers.

Trigger chain	Data period	HLT p_{T} threshold	Offline p_{T} threshold
Single electron	2015	p_{T} (e) > 24 GeV	p_{T} (e) > 25 GeV
	2016-2018	p_{T} (e) > 26 GeV	p_{T} (e) > 27 GeV
Single muon	2015	p_{T} (μ) > 20 GeV	p_{T} (μ) > 21 GeV
	2016-2018	p_{T} (μ) > 26 GeV	p_{T} (μ) > 27.3 GeV
Ditau	2015-2018	p_{T} (leading $\tau_{\text{had-vis}}$) > 35 GeV p_{T} (subleading $\tau_{\text{had-vis}}$) > 25GeV	p_{T} (leading $\tau_{\text{had-vis}}$) > 40 GeV p_{T} (subleading $\tau_{\text{had-vis}}$) > 30 GeV

Table 8.2.: A summary of the changes in p_T threshold for the triggers and offline stage that were made across the data taking period to account for increases in instantaneous luminosity for electrons, muons and $\tau_{\text{had-vis}}$.

8.2. Preselection

For the $\tau_{\text{lep}}\tau_{\text{had}}$ channel the event must consist of only an electron or muon (at least passing *medium* identification) as the τ_{lep} candidate and one τ_{had} candidate (passing at least *medium* identification criteria that rejects non-τ jets) classified as a 1p0n, 1p1n, 1pXn or 3p0n decay and these two candidates must be of opposite charges. The leading jet pT must be greater than 40GeV while the pT of the τ_{lep} candidate is greater than 21 (for 2015 data) or 27.3 (for data taken from 2016-2018) and the transverse momentum of the τ_{had} must be greater than 30 GeV. $\Delta R(\tau,\tau)$ defined as the angular distance between the two taus must conform to $\Delta R < 2.5$ and the pseudorapidity, $\delta\eta(\tau,\tau)$, between the taus must be $\delta\eta < 1.5$ and together these enable the rejection of non-resonant events. The τ_{had} candidate must have either 1 or 3 tracks which selects either 1 or 3 prong events. The Missing Transverse Momentum requirement is $E_T^{\text{Miss}} > 20GeV$

and the collinear approximation [134], the assumption that the invisible parts of the tau decay products are assumed to have been produced collinearly with the visible parts, is applied. For this approximation the fraction of visible momentum to total momentum, including E_T^{Miss} for the leading (x_1) and subleading (x_2) τ decay products are required to be $0.1 < x_1 < 1.4$, $0.1 < x_2 < 1.2$. Finally to reject W+Jet processes the sum of E_T^{Miss} and the lepton transverse mass are required to be less than 70GeV.

For the $\tau_{\text{had}}\tau_{\text{had}}$ channel must consist of two τ_{had} candidates with opposite charges classified as 1p0n, 1p1n, 1pXn or 3p0n and they must share a reconstructed primary vertex. Similarly to the $\tau_{\text{lep}}\tau_{\text{had}}$ channel there are conditions imposed by the use of the level 1 calorimetric trigger jet, the leading jet must have a transverse momentum $pT > 70GeV$ and pseudorapidity $|\eta| < 3.2$. One τ_{had} must have a transverse momentum $pT > 40$GeV while the other $pT > 30$GeV and both should pass *medium* tau RNN identification. There should be no electrons or muons present otherwise the events are automatically rejected. Pseudorapidity $\Delta\eta_{\tau\tau}$ and angular separation ΔR requirements are again imposed to reject non-resonant events; $\Delta\eta_{\tau\tau} < 1.5$ and $0.6 < \Delta R < 2.5$. As in the $\tau_{\text{lep}}\tau_{\text{had}}$ channel, the τ_{had} candidates are required to have either 1 or 3 tracks to select 1 or 3 prong decays. The missing E_T^{Miss} must be greater than 20GeV and finally the same collinear approximation requirements on the momentum fractions of the leading (x_0) and subleading (x_1) decay product momentum fractions as before are applied, $0.1 < x_1 < 1.4$, $0.1 < x_2 < 1.2$.

8.3. Signal Regions

After the preselection cuts are performed, the Missing Mass Calculator, an advanced likelihood-based algorithm [135], is used to calculate an estimate of the invariant mass $m_{\tau\tau}^{\text{MMC}}$ of the di-tau system. This is done through using a combination of four-momenta of the visible τ decay products, the missing transverse energy (E_T^{Miss}) and information on the type of τ decay. The signal region is defined as 110GeV $< m^{\text{MMC}_{\tau\tau}} <$ 150GeV to select specifically Higgs events, separating them from the largest source of background events, $Z \to \tau\tau$. This was determined in a series of optimisation studies examining the optimum bounds to achieve maximum signal sensitivity.

Category and Event Selection			
Preselection			
Leading jet with $p_{\mathrm{T}} > 40$ GeV			
One $\tau_{\text{had-vis}}$ candidate, classified as 1p0n, 1p1n, 1pXn and 3p0n			
Opposite Charges between $\tau_{\text{lep}}$and $\tau_{\text{had-vis}}$			
$p_{\mathrm{T}}(\tau_{\text{lep}}) > 21$ to 27.3 GeV, $p_{\mathrm{T}}(\tau_{\text{had}}) > 30$ GeV			
$\tau_{\text{had-vis}}$ passing *medium* tau identification with RNN			
Electron and muon passing *medium* identification			
Electron passing the FCLoose isolation and muon passing FCTightTrackOnly isolation			
$\Delta R_{\tau\tau} < 2.5$,$\Delta\eta_{\tau\tau} < 1.5$,$E_T^{\text{miss}} > 20$ GeV,$m_T < 70$ GeV			
Collinear approx.: $0.1 < x_1 < 1.4$, $0.1 < x_2 < 1.2$			
Signal regions			
$110 < m_{\tau\tau}^{\text{MMC}} < 150$ GeV			
VBF		**Boost**	
Second jet $p_T > 30$ GeV		Failed VBF selection	
$m_{jj} > 400$ GeV		$p_{\mathrm{T}}(\mathrm{H}) > 100$ GeV	
$\lvert\Delta\eta_{jj}\rvert > 3.0$; $\eta(j_0) \times \eta(j_1) < 0$			
Both τ_{had} candidates must lie between the two leading jets in pseudorapidity			
VBF 1	**VBF 0**	**Boost Tight**	**Boost Loose**
BDT(VBF) > 0.0	BDT(VBF) < 0.0	$\Delta R \leq 1.5$ and $p_{\mathrm{T}}(\mathrm{H}) \geq 140$ GeV	Not tight
Signal optimisation regions			
High			**Low**
ℓ-1p0n,	$(d_0^{\text{sig}}(e) > 2.5$ or $d_0^{\text{sig}}(\mu) > 2.0)$ and $d_0^{\text{sig}}(\tau_{\text{1p0n}}) > 1.5$		
ℓ-1p1n,	$(d_0^{\text{sig}}(e) > 2.5$ or $d_0^{\text{sig}}(\mu) > 2.0)$ and $\lvert y(\tau_{\text{1p1n}})\rvert > 0.1$		
ℓ-1pXn,	$(d_0^{\text{sig}}(e) > 2.5$ or $d_0^{\text{sig}}(\mu) > 2.0)$ and $\lvert y(\tau_{\text{1pXn}})\rvert > 0.1$		Not high
ℓ-3p0n,	$(d_0^{\text{sig}}(e) > 2.5$ or $d_0^{\text{sig}}(\mu) > 2.0)$ and $\lvert y(\tau_{\text{1p0n}})\rvert > 0.6$		
$Z \to \tau\tau$ Control regions			
Same Preselection except with $60 < m_{\tau\tau}^{\text{MMC}} < 110$ GeV			
VBF 1 Z CR	**VBF 0 Z CR**	**Boost Tight Z CR**	**Boost Loose Z CR**
Same VBF 1 selection	Same VBF 0 selection	Same Boost Tight selection	Same Boost Loose selection

Table 8.3.: Summary of the requirements for the signal region event requirements in the $\tau_{\text{lep}}\tau_{\text{had}}$ channel.

Category and Event Selection			
Preselection			
Leading jet with $p_{\mathrm{T}} > 70$ GeV, $\lvert\eta\rvert < 3.2$			
Two τ_{had} candidates with opposite charges, classified as 1p0n, 1p1n, 1pXn and 3p0n			
Both τ_{had} candidates associated to same reconstructed primary vertex			
$p_{\mathrm{T}}(\tau_1) > 40\,\mathrm{GeV}$, $p_{\mathrm{T}}(\tau_2) > 30\,\mathrm{GeV}$			
Both passing *medium* tau identification with RNN			
No electron or muons			
$0.6 < \Delta R_{\tau\tau} < 2.5$			
$\Delta\eta_{\tau\tau} < 1.5$			
$E_T^{\mathrm{miss}} > 20\,\mathrm{GeV}$			
Collinear approx.: $0.1 < x_1 < 1.4$, $0.1 < x_2 < 1.4$			
Signal regions			
$110 < m_{\tau\tau}^{\mathrm{MMC}} < 150\,\mathrm{GeV}$			
VBF		**Boost**	
Second jet $p_T > 30\,\mathrm{GeV}$		Failed VBF selection	
$m_{jj} > 400\,\mathrm{GeV}$		$p_{\mathrm{T}}(\mathrm{H}) > 100\,\mathrm{GeV}$	
$\lvert\Delta\eta_{jj}\rvert > 3.0$; $\eta(j_0) \times \eta(j_1) < 0$			
Both τ_{had} candidates must lie between the two leading jets in pseudorapidity			
VBF 1	**VBF 0**	**Boost Tight**	**Boost Loose**
BDT(VBF) > 0.0	BDT(VBF) < 0.0	$\Delta R \leq 1.5$ and $p_{\mathrm{T}}(\mathrm{H}) \geq 140\,\mathrm{GeV}$	Not tight
Signal optimisation regions			
High			**Low**
1p0n-1p0n,	$d_0^{\mathrm{sig}}(\tau_0) > 1.5$ and $d_0^{\mathrm{sig}}(\tau_1) > 1.5$		
1p0n-1p1n,	$d_0^{\mathrm{sig}}(\tau_{1p0n}) > 1.5$ and $\lvert y(\tau_{1p1n})\rvert > 0.1$		
1p0n-1pXn,	$d_0^{\mathrm{sig}}(\tau_{1p0n}) > 1.5$ and $\lvert y(\tau_{1pXn})\rvert > 0.1$		Not high
1p1n-1p1n,	$\lvert y_0 y_1\rvert > 0.2$		
1p1n-1pXn,	$\lvert y_0 y_1\rvert > 0.2$		
1p1n-3p0n,	$\lvert y(\tau_{1p1n})\rvert > 0.1$ and $\lvert y(\tau_{3p0n})\rvert > 0.6$		
$Z \to \tau\tau$ Control regions			
Same Preselection except with $60 < m_{\tau\tau}^{\mathrm{MMC}} < 110\,\mathrm{GeV}$			
VBF 1 Z CR	**VBF 0 Z CR**	**Boost Tight Z CR**	**Boost Loose Z CR**
Same VBF 1 selection	Same VBF 0 selection	Same Boost Tight selection	Same Boost Loose selection

Table 8.4.: Summary of the requirements for the signal region event requirements in the $\tau_{\mathrm{had}}\tau_{\mathrm{had}}$ channel.

8.3.1. Production Mode Split

When the Higgs events have been selected using the Missing Mass Calculator they are then split by production modes, either Vector Boson Fusion (VBF) or gluon-gluon Fusion (ggF), in this analysis often referred to as "Boost". The selection of the VBF category requires a second jet of $p_T > 30$GeV in addition to the leading jet of $p_T > 70$GeV needed for preselection and the invariant mass, m_{jj} must be more than 400 GeV. It is further required that the difference in pseudorapidity between the two jets is less than 3.0, that both τ_{had} candidates lie between the two jets in their pseudorapidity and that the product of the pseudorapitidies of the jets, $\eta(j_0) \times \eta(j_1)$ is less than 0.

If the event is not classified as VBF then if the transverse momentum of the Higgs, as calculated by the sum of the p_T of the visible tau decay products and the missing transverse momentum, is greater than 100 GeV then it is classified in the Boost Category.

In addition both of these categories are split in two for VBF they are called VBF_1 and VBF_0 and for Boost they are called Boost_Tight and Boost_Loose. The former for each is further enriched with events of the corresponding production mode. For VBF_1 this is done based off the Multivariant Analysis - Boosted Decision tree discriminant output coming from the VBF tagger [91]. The BDT cut point was chosen at BDT=0.0, this was optimised to provide a balance between enriching the VBF events while also providing enough statistics in all bins to ensure a stable fit was achieved. The details of this discriminant are discussed in $H \to \tau\tau$ coupling paper [61] for which it was originally developed. All other VBF events are categorised as VBF_0. In order to be classified as Boost_Tight the separation of the two τ_{had} candidates is less than 1.5 while the $p_T(H) > 140$GeV, all other events in Boost are classified as Boost_Loose.

8.4. Decay Mode and Optimised Sensitivity Regions

Both VBF and Boost categories are subdivided into subcategories based off their decay modes. For the $\tau_{\text{lep}}\tau_{\text{had}}$ channel these categories are simply ℓ-1p0n,ℓ-1p1n,ℓ-1pXn and ℓ-3p0n. For the $\tau_{\text{had}}\tau_{\text{had}}$ channel 3-prong decays are included in addition to 1-prong so the decay modes considered are 1p0n-1p0n, 1p0n-1p1n, and 1p1n-1p1n, 1p0n-1pXn, 1p1n-1pXn, and 1p1n-3p0n.

The regions VBF_1, VBF_0, Boost_Tight and Boost_Loose are split further into high and low sensitivity regions. These are defined by making the kinematic cuts as summarised in Tables 8.3 and 8.4 for each of the decay modes. The values of the decay mode cuts were chosen such that the highest maximum value of ΔNLL for the φ_τ variable is maximised in a stat-only fit.

8.5. Signal regions in the fit

In total, there are 48 signal regions in the $\tau_{\text{had}}\tau_{\text{had}}$ channel and 32 in the $\tau_{\text{lep}}\tau_{\text{had}}$. This presents the issue that with the signal regions being so subdivided that some will inevitably be low in statistics and therefore susceptible to large statistical fluctuations. For example 1p0n-1p0n suffers from low statistics due to being the lowest decay fraction. In order to combat this for each of the regions VBF_1,VBF_0, Boost_Tight and Boost_Loose for both the $\tau_{\text{lep}}\tau_{\text{had}}$ and $\tau_{\text{had}}\tau_{\text{had}}$ channels the dominant decay modes are merged together to form the high sensitivity region, the subdominant decay modes form the medium sensitivity region and those events not passings the high or medium selection criteria form the low sensitivity region. This gives 12 signal regions in each decay channel for a total of 24 overall. This merging scheme is summarised in Tables 8.5 and 8.6.

Region	Decay mode comb.	Selection	Event fraction
High	ℓ-1p0n	$d_0^{\text{sig}}(\ell) > 2.5$ (e) or 2.0 (μ) and $d_0^{\text{sig}}(\tau_{\text{1p0n}}) > 1.5$	12-15%
	ℓ-1p1n	$d_0^{\text{sig}}(\ell) > 2.5$ (e) or 2.0 (μ) and $\lvert y(\tau_{\text{1p1n}})\rvert > 0.1$	
Medium	ℓ-1pXn	$d_0^{\text{sig}}(\ell) > 2.5$ (e) or 2.0 (μ) and $\lvert y(\tau_{\text{1pXn}})\rvert > 0.1$	6-8%
	ℓ-3p0n	$d_0^{\text{sig}}(\ell) > 2.5$ (e) or 2.0 (μ) and $\lvert y(\tau_{\text{3p0n}})\rvert > 0.6$	
Low	All above	Not passing optimised selection	78-82%

Table 8.5.: Table summarising the signal regions for the $\tau_{\text{lep}}\tau_{\text{had}}$ channel which are repeated in the VBF_1, VBF_0, Boost Tight and Boost Loose regions.

Region	Decay mode comb.	Selection	Event fraction
High	1p0n-1p0n	$d_0^{\text{sig}}(\tau_0) > 1.5$ and $d_0^{\text{sig}}(\tau_1) > 1.5$	24-28%
	1p0n-1p1n	$d_0^{\text{sig}}(\tau_{\text{1p0n}}) > 1.5$ and $\lvert y(\tau_{\text{1p1n}})\rvert > 0.1$	
	1p1n-1p1n	$\lvert y(\tau_0)y(\tau_1)\rvert > 0.2$	
Medium	1p0n-1pXn	$d_0^{\text{sig}}(\tau_{\text{1p0n}}) > 1.5$ and $\lvert y(\tau_{\text{1pXn}})\rvert > 0.1$	18-22%
	1p1n-1pXn	$\lvert y(\tau_0)y(\tau_1)\rvert > 0.2$	
	1p1n-3p0n	$\lvert y(\tau_{\text{1p1n}})\rvert > 0.1$ and $\lvert y(\tau_{\text{3p0n}})\rvert > 0.6$	
Low	All above	Not passing optimised selection	50-57%

Table 8.6.: Table summarising the signal regions for the $\tau_{\text{had}}\tau_{\text{had}}$ channel which are repeated in the VBF_1, VBF_0, Boost Tight and Boost Loose regions.

8.6. Control regions for Z$\rightarrow \tau\tau$ and multijet backgrounds

The Z Control Region (ZCR) is defined by the same preselection used for general event selection with the extra criteria on the Missing Mass, $m_{\tau\tau}^{MMC}$ should be between 60 and 110GeV. Each event in ZCR is sorted randomly into two categories, ZCR_1 and ZCR_0. ZCR_1 is used for extracting the $Z \rightarrow \tau\tau$ normalisation factor. 1p1n-1p1n and ℓ-1p1n events in ZCR_0 are used to control π^0 uncertainties using distributions of $\pi^{\pm} - \pi^0$ invariant masses.

In a similar manner to the ZCR, the multijet background is estimated by selecting a region with the same preselection as for the signal but changing the requirement on the difference in pseudorapidity between the two tau candidates to be $|\Delta\eta(\tau,\tau)| < 2.0$.

Chapter 9.

Background Estimation

9.1. Introduction

For this analysis there are a number of sources of backgrounds which must be controlled in order to produce meaningful results. The most prominent backgrounds come from decays which produce two τ leptons, particularly $Z/\gamma* \rightarrow \tau\tau$ with small contributions from $t\bar{t}$ and diboson decays, and from the misidenfication of QCD jets as τ leptons. In some cases these sources of background occur together such as $W \rightarrow \tau\nu$+jets or top decays where there is a real τ and a jet which may be misidentified as a second τ. Beside Z$\rightarrow \tau\tau$ and misidentified QCD jets, which are discussed below, the other minor contributions are modelled using MC.

9.2. $Z \rightarrow \tau\tau$

The method for controlling the $Z \rightarrow \tau\tau$ background is reasonably simple. The background is modelled using SHERPA then it is normalised using the normalisation factors defined in each of the Z control regions (ZCR) (ZCR_1, ZCR_0). Theory and systematic uncertainties are evaluated also using the $Z \rightarrow \tau\tau$ simulated data. The definition of the ZCRs are detailed in Section 8.6.

9.3. Fake Background $\tau_{\text{lep}}\tau_{\text{had}}$

The other major background, the misindentification of jets as τ leptons, primarily occuring from W+Jets events with smaller contributions from QCD multijet production and top decays, is controlled using the Fake-Factor method which is outlined in this section. The first step of the Fake-Factor method involves defining a fake-enriched region where all the normal preselection criteria are enforced except it is required that the $\tau_{\text{had-vis}}$ candidates fail the $\tau_{\text{had-vis}}$ Medium selection. In addition, an extra criteria is introduced; a the minimum allowed $\tau_{\text{had-vis}}$ score of 0.01, this reduces the number of gluon-induced and pileup jets, since in the signal region the main background are jets induced by quarks. Using Equation 9.1 it is possible to calculate the number of fakes in the signal region (N^{SR}_{fakes}) by subtracting the number of events that do not correspond to fakes ($N^{anti-\tau}_{MC,\ no\ jet\to\tau}$, calculated using simulated events) from jets, from the total number of events in the fake region ($N^{anti-\tau}_{Data}$). This is then multiplied by the 'combined Fake-Factor' ($\mathcal{F}$) which corrects for the difference in selection efficiency between the Signal and the Fake-enriched regions.

$$N^{SR}_{fakes} = (N^{anti-\tau}_{Data} - N^{anti-\tau}_{MC,\ no\ jet\to\tau}) \times \mathcal{F} \tag{9.1}$$

The "Fake-Factor", $\mathcal{F}$, is constructed from the fake-factors of each of the relevant background processes, each weighted by their contribution in anti-$\tau_{\text{had-vis}}$ region shown in Equation . For the purposes of this analysis, top production does not play a significant role in the background and as with W + jets background it mostly produces quark initiated jets therefore its contribution has simply been absorbed by the W + jets background and so Equation 9.2 can be simplified to Equation .

$$\mathcal{F} = R_W F_W + R_{top} F_{top} + R_{QCD} F_{QCD} \tag{9.2}$$

$$\mathcal{F} = R_{QCD} F_{QCD} + R_W F_W \tag{9.3}$$

When there are only two components contributing to $\mathcal{F}$, the fractional contribution from W+jets becomes $R_W = 1 - R_{QCD}$. In order to obtain individual Fake-Factors, F_W and F_{QCD}, the first step is defining control regions for W+jets, QCD and top using the usual preselection criteria for the pass-$\tau_{\text{had-vis}}$ and anti-$\tau_{\text{had-vis}}$ regions with the inversion of certain criteria as detailed in Table 9.1. The next step is to calculate a the ratio of events in anti-$\tau_{\text{had-vis}}$ control region to the pass-$\tau_{\text{had-vis}}$ control region, subtracting the number of events where the $\tau_{\text{had-vis}}$ is not faked from a jet using simulated data, this calculation is shown in Equation 9.4, where i represents W and QCD in turn.

$$F_i = \frac{N_{Data}^{pass-\tau,CR_i} - N_{MC,\ no\ jet\to\tau}^{pass-\tau,CR_i}}{N_{Data}^{anti-\tau,CR_i} - N_{MC,\ no\ jet\to\tau}^{anti-\tau,CR_i}} \tag{9.4}$$

Control region	Definition with respect SRs
W + jets CR	Invert m_T cut ($m_T > 70$ GeV)
QCD CR	Invert lepton isolation requirement
Top CR	Invert B veto cut and $m_T > 40$ GeV

Table 9.1.: Summary of the definitions (relative to the signal regions) of the control regions used for the Fake-Factor method

In order to calculate the number of QCD events in the anti-$\tau_{\text{tau-vis}}$ signal region, an "isolation factor" is applied to the number in the anti-$\tau_{\text{tau-vis}}$ control region. This isolation factor is defined as the ratio of events passing lepton isolation criteria to those failing it.

9.4. Fake Background $\tau_{\text{had}}\tau_{\text{had}}$

For background estimation in the $\tau_{\text{had}}\tau_{\text{had}}$ channel the fake-factor method is employed again in order to estimate the amount of events with one or two fake $\tau_{\text{had-vis}}$ candidates. Background processes that generate two real $\tau_{\text{had-vis}}$ candidates are estimated using Monte Carlo simulations. Truth level cuts are applied here, rejecting reconstructed $\tau_{\text{had-vis}}$ jets that were intiated by a quark or a gluon, this ensures that the same events

will not be counted again in the background, since such $\tau_{\text{had-vis}}$ candidates would be considered fake and will be estimated using the fake factor method.

The first step in using the fake-factor method for the $\tau_{\text{had}}\tau_{\text{had}}$ region is to construct the anti-τ region as before when using the fake-factor method for the $\tau_{\text{lep}}\tau_{\text{had}}$ channel. This is done by inverting the $\tau_{\text{had}}\tau_{\text{had}}$ signal region preselection requirement on Tau ID; at least one tau must fail the *medium* RNN tau identification. It is also necessary to introduced a lower threshold that at least 1 $\tau_{\text{had-vis}}$ candidate must pass the *loose* RNN tau identification since the HIGG4D3 skim removes events where both candidates fail the *loose* RNN criteria and the BDT ID requirements. Without this lower threshold the analysis would default to relying on the out of date BDT. In this anti-τ region, all of them simulated prompt $\tau_{\text{had-vis}}$ backgrounds are removed from the data distribution (which amounts to about 6% at preselection) leaving just the fake background.

The constructed template needs to be scaled in order to be applicable to the $\tau_{\text{had}}\tau_{\text{had}}$ signal region. The W+Jets control region in the $\tau_{\text{lep}}\tau_{\text{had}}$ channel is used to compute the Fake Factors needed for scaling the fake-template. In order for the Fake-Factors to be applicable to the $\tau_{\text{had}}\tau_{\text{had}}$ channel, changes have to be made to the $\tau_{\text{had-vis}}$ selection to make it as similar as possible to the $\tau_{\text{had}}\tau_{\text{had}}$ selection. Three cuts had to be altered for this fake-factor measurement:

- $\tau_{\text{had-vis}}$, must now pass the tau25_medium1_tracktwo(EF) trigger
- b-tagging working point is altered to 70%
- The pseudorapidity between lepton and the $\tau_{\text{had-vis}}$, $\Delta\eta(\ell, \tau_{\text{had-vis}}) > 0.6$

In the interests of preserving statistics within the control region, certain preselection criteria were not changed such as keeping the leading pT cut at 40GeV from the $\tau_{\text{lep}}\tau_{\text{had}}$ channel as opposed to 70GeV from the $\tau_{\text{had}}\tau_{\text{had}}$ channel or dropping requirements such as $|\eta| < 3.2$.

Three regions that are all based on the W+Jets control region discussed above, but with differing $\tau_{\text{had-vis}}$ candidate requirements are used to define the two fake-factors (FF) shown in Equations 9.5 and 9.6. The three regions are defined as where $\tau_{\text{had-vis}}$ candidates must pass medium RNN selection (medium), where they do not pass medium (not-medium/nm) and where they pass loose but not the medium selection (loose-not-medium/lnm).

$$FF_{\text{nm}} = (\text{Data - MC})^{\text{WCR}}_{\text{medium } \tau_{\text{had-vis}}} / (\text{Data - MC})^{\text{WCR}}_{\text{not}-\text{medium } \tau_{\text{had-vis}}} \tag{9.5}$$

$$FF_{\text{lnm}} = (\text{Data - MC})^{\text{WCR}}_{\text{medium } \tau_{\text{had-vis}}} / (\text{Data - MC})^{\text{WCR}}_{\text{loose}-\text{not}-\text{medium } \tau_{\text{had-vis}}} \tag{9.6}$$

The anti-$\tau_{\text{had-vis}}$ is split into different regions based on the RNN ID of the leading and sub-leading $\tau_{\text{had-vis}}$ candidates these regions also inform the choice of product of Fake-Factors used to scale the region for example if both the leading and subleading $\tau_{\text{had-vis}}$ candidates are classified as "not-medium" then the Fake-Factor product $FF_{\text{nm}}\dot{F}F_{\text{nm}}$ is used for this region. The combinations used are summarised in Table 9.2. Any events with just one fake $\tau_{\text{had-vis}}$ candidate are simple scaled by either FF_{nm} or FF_{lnm}.

region	leading ID	sub-leading ID
anti-$\tau_{\text{had-vis}}$	not-medium	not-medium
lead-anti-$\tau_{\text{had-vis}}$	not-medium	medium
sublead-anti-$\tau_{\text{had-vis}}$	medium	not-medium
lead-anti-$\tau_{\text{had-vis}}$-loose	loose-not-medium	medium
sublead-anti-$\tau_{\text{had-vis}}$-loose	medium	loose-not-medium

Table 9.2.: The event categories used to derive and apply the fake-factors for background estimation. The requirement that the minimum requirement is the presence of one Loose classified τ is applied in all case, though not listed in this table.

Chapter 10.

Systematic Uncertainties

This section discusses the sources of systematic uncertainties that have been accounted for in this analysis. The most significant sources of uncertainty stem from the reconstruction of the physics objects used to calculate the observables, other less significant sources of uncertainty include luminosity and theoretical uncertainties. Systematic corrections are applied to these variables where applicable and the uncertainties presented in this section are ontop of these corrections. There is an in-depth examination of the treatment of nuisance parameters including the smoothing, symmetrisation and pruning proceedures, which together aim to counter low statistics, stabilise the fit and increase fit efficiency. An overview of their impact on the overall physics result is also shown. For a list of the impacts of the uncertainties discussed in this section, refer to Tables 11.2 and 11.4.

10.1. Experimental Uncertainties

The following experimental uncertainties are estimated using the reccomendations from the combined performance groups using the software tools provided in AnalysisBase-21.2.114.

10.1.1. Jet Uncertainies

The Jet Energy Scale (JES) and Jet Energy Resolution (JER) uncertainties are two of the most impactful groups of uncertainties for this analysis. The process of determining the JES and JER are complex processes consisting of multiple steps (details

of which can be found in Section 4.1.5) which results in the generation of around 80 uncertainties associated with them. For most analyses the use of all 80 uncertainties would increase the complexity of handling uncertainties significantly for little noticable benefit. Therefore these are simplified into around 40 nuisance parameters which are designed to maintain important correlations while not being as unwieldy to manage. This analysis uses the *R4 CategoryReduction FullJER uncertainty* set scheme, which includes the nuisance parameters listed below by source of uncertainty. These are estimated using the methods described in [56].

The following is a short summary of each of the jet uncertainty sources followed by a list detailing the exact list of uncertainties considered in this analysis.

- **Energy Scale**: The sources of these uncertainties are varied, they are all involved with the calibration of the jet energy scale. The PunchThrough uncertainty coming from the estimation of energy not captured by the calorimeter because it came from such high energy jets that they passed through the calorimeter, bJES is the uncertainty resulting from the detector response specifically to jets associated with a true B hadron, η-Intercalibration uncertainties coming from the correction of biases introduced to the η reconstruction, SingleParticle-HighPt is the uncertainty of estimating the JES uncertainty in high P_T ranges which have low statistics and Pilup uncertainties are related to the corrections to the JES due to pile up. There are also a number of EffectiveNPs relating to inherent statistical uncertainties, uncertainties due to modelling, due to the detector and from mixed sources.

- **Energy Resolution**: These uncertainties are a result of the calibration of the Energy Resolution. The techniques for the estimation of these uncertainties can be found in Ref. [136].

- **Flavor**: These uncertainties are due to the uncertainty on jet-flavour composition and the flavour dependence of the jet response.

- **Jet Vertex Tagger**: These systematics are results of the uncertainties in the efficiencies of the Jet Vertex Tagger, one from central region of the detector; the other for the forward region.

- **b-tagging**: These are decorrelated from the Flavor tagging and they originate from corrections to b-tagging efficiency between MC and Data.

The most impactful individual NPs for this analysis are summarised in Figures 10.5 and 10.6. A number of Jet related uncertainties feature amongst the most impactful,

specifically `FINAL_JET_JER_EffectiveNP_[1,2]`, `JET_EtaIntercalibration_Modelling`, `JET_Flavor_Response` and `JET_Pileup_RhoTopology`. The jet uncertainties on resolution and scale affect the signal and background through their impact on the E_T^{Miss} in addition to directly effecting the event categorisation for both VBF and ggF.

- **Energy Scale**:
  - JET-EffectiveNP-Statistical[1-6]
  - JET-PunchThrough-MC16
  - JET-BJES-Response
  - JET-EtaIntercalibration-[Modelling—Modelling-2018data—TotalStat]
  - JET-EtaIntercalibration-[NonClosure-highE—NonClosure-negEta—NonClosure-posEta]
  - JET-SingleParticle-HighPt
  - JET-EffectiveNP-Mixed[1—2—3]
  - JET-Pileup-[OffsetMu—OffsetNPV—PtTerm—RhoTopology]
  - JET-EffectiveNP-Modelling[1-4]
  - JET-EffectiveNP-Detector[1-2]
- **Energy Resolution**:JET-JER-EffectiveNP-[1-12restTerm], JET-JER-DataVsMC
- **Flavor**: JET-Flavor-Composition, JET-Flavor-Response
- **Jet Vertex Tagger**: JET-JvtEfficiency (central jets), JET-fJvtEfficiency (forward jets)
- **b-tagging**: FT-EFF-Eigen-B-[0-2], FT-EFF-Eigen-C-[0-2], FT-EFF-Eigen-Light-[0-3], FT-EFF- extrapolation, FT-EFF-extrapolation-from-charm.

10.1.2. Missing Transverse Energy Uncertainies

The missing transverse energy, E^T_{Miss}, is formed of two parts, the hard term and the soft term. The hard term refers to any E^T_{Miss} that is associated with a reconstructed object (muons, electrons, photons, hadronically decaying τ-leptons and jets). The soft term is comprised of E^T_{Miss} derived from calorimeter deposits not directly associated with

reconstructed objects. The uncertainty for the hard term is calculated by propogating all the uncertainties from each reconstructed object through to the E^T_{Miss}. The soft term is however only constructed for E^T_{Miss} and therefore its systematic uncertainty must be calculated too.

In an event with no true missing E^T_{Miss}, one where all particles are visible to the detector, the soft term and the hard term combined would be equal to the total energy of the incident particle(s). Detectors resolution effects unfortunately can warp this perfect scenario, the following method describes the uncertainty can be calculated to account for these detector effects. The soft term can be explored with the help of the following quantities.

- **The parallel scale (Δ_L)** - The Mean value of $p^{\text{soft}}_{\parallel}$ where $p^{\text{soft}}_{\parallel}$ is the component of p^{soft} projected along the direction of p^{hard} parallel to p^{hard}.
- **The parallel resolution ($\sigma_{\parallel}$)** - The Root Mean Square of $p^{\text{soft}}_{\parallel}$
- **The transverse resolution ($\sigma_{\perp}$)** - The Root Mean Square of the $p^{\text{soft}}_{\perp}$ where $p^{\text{soft}}_{\perp}$ is the component of p^{soft} projected along the direction of p^{hard}.

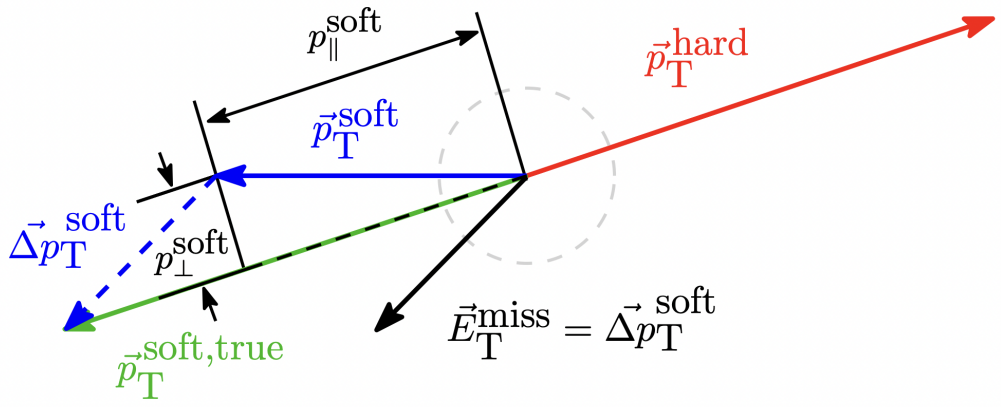

Figure 10.1.: An diagram showing the a representation of the projections of the soft term with respect to the hard track momentumn used for the calculation of Missing Transverse Energy uncertainty calculations [62].

This analysis considers three uncertainties related to the soft term Missing Transverse Energy:

- **MET Resolution**: MET-SoftTrk-ResoPara, MET-SoftTrk-ResoPerp
- **Soft track energy scale**: MET-SoftTrk-Scale

Figures 10.5 and only show `MET_SoftTrk_ResoPara` as having a greater than 5% effect in a single signal region.

10.1.3. Lepton Uncertainies

In addition to the obvious need to understand the uncertainties related to τ leptons for this analysis, the use of the $\tau_{\text{lep}} - \tau_{\text{had}}$ channel dictates the inclusion of the systematic uncertainties related to the other leptons, the muons and electrons. A number of sources of uncertainty are considered for e, μ and τ; these are energy resolution,energy scale, reconstruction efficiency and mis-identification for all leptons. In addition isolation uncertainty is considered for e and μ with the addition of charge identification for e and electron veto uncertainty for τ. The muon uncertainties use the latest recommendation in *AnalysisBase-21.2.114* estimated using the methods from [53]. The electron uncertainties are estimated using the techniques in [52] and use the set *Consolidated rel21*. Finally the τ lepton uncertainties are estimated using the techniques in [55] using the *2019-summer*. The full list of systematic uncertainties used in this analysis for e, μ and τ are summarised below:

10.1.3.1. Muon Uncertainties

- **Muon Resolution**: MUON-ID, MUON-MS, MUON-SAGITTA-RESBIAS, MUON-SAGITTA-RHO
- **Energy Scale**: MUON-SCALE
- **Reconstruction/Identification**: MUON-EFF-RECO-STAT, MUON-EFF-RECO-STAT-LOWPT, MUON-EFF-RECO-SYS, MUON-EFF-RECO-SYS-LOWPT
- **Isolation**: MUON-EFF-ISO-STAT, MUON-EFF-ISO-SYS
- **Trigger**:MUON-EFF-TrigStatUncertainty, MUON-EFF-TrigSystUncertainty

10.1.3.2. Electron Uncertainties

- **Resolution**: EG-RESOLUTION-ALL
- **Energy Scale**: EG-SCALE-ALL

- **Reconstruction**: EL-EFF-Reco-TOTAL-1NPCOR-PLUS-UNCOR
- **Identification**: EL-EFF-ID-TOTAL-1NPCOR-PLUS-UNCOR
- **Isolation**: EL-EFF-Iso-TOTAL-1NPCOR-PLUS-UNCOR
- **Charge Identification**: EL-CHARGEID-STAT, EL-CHARGEID-SYS
- **Trigger**:EL-EFF-Trigger-TOTAL-1NPCOR-PLUS-UNCOR

10.1.3.3. Tau Uncertainties

- **Energy scale**: TAUS-TRUEHADTAU-SME-TES-INSITUEXP,TAUS-TRUEHADTAU-SME-TES-INSITUFIT,TAUS-TRUEHADTAU-SME-TES-DETECTOR,TAUS-TRUEHADTAU-SME-TES-MODEL-CLOSURE, TAUS-TRUEHADTAU-SME-TES- PHYSICSLIST
- **Reconstruction**: TAUS-TRUEHADTAU-EFF-RECO-TOTA
- **Identification**: TAUS-TRUEHADTAU-EFF-RNNID-[1—3]PRONGSTATSYSTPT-[2025—2530—3040—GE40],TAUS-TRUEHADTAU-EFF-RNNID-SYST,TAUS-TRUEHADTAU-EFF-RNNID-HIGHPT
- **Trigger (2015-2017)**: TAUS-TRUEHADTAU-EFF-TRIGGER[STATDATA161718-—STATMC161718], TAUS-TRUEHADTAU-EFF-TRIGGER[SYST161718—SYSTMU161718]
- **Trigger (2018)**: TAUS-TRUEHADTAU-EFF-TRIGGER-[STATDATA2018—STATMC2018], TAUS- TRUEHADTAU-EFF-TRIGGER-[SYST2018—SYSTMU2018]
- **eVeto on fake $\tau_{\text{had-vis}}$** :TAUS-TRUEELECTRON-EFF-ELEBDT-STAT, TAUS-TRUEELECTRON-EFF-ELEBDT-SYST

The sources of the τ uncertainties are summarised below:

- **Energy Scale**: Two in-situ energy calibration uncertainties are derived from χ^2 fits of data from the visible mass using the tag-and-probe method using $\mu - \tau$ pairs.
- **Reconstruction**: These are estimated by comparing reconstruction efficiency of $Z \to \tau\tau$ decays generated using Pythia8 and Powheg with alternative geometries.
- **Identification**: These uncertainties are derived from the comparison of MC samples against data derived from a dedicated $\mu - \tau$ tag-and-probe method.

Uncertainties are generated for both 1 and 3 prong decays and for a range of p_T values.

- **eVeto on Fake Tau**: These uncertainties arise from the electron veto on fake $\tau_{\text{had-vis}}$. These are generated by comparing MC data against data collected in a $\mu - \tau$ tag-and-probe analysis.

10.1.4. Luminosity Uncertainies

The luminosity uncertainty for integrated luminosity over the period 2015-2018 was measured by LUCID-2 [137] at 1.7% [138], this affects all the Higgs signal regions and the simulated backgrounds not constrained by the signal region in data.

10.2. Theoretical Uncertainties

The theoretical uncertainities used in this analysis, relating to the $H \to \tau\tau$ decay and the most significant background decay $Z \to \tau\tau$ are mostly the same as those during the Run 2 $H \to \tau\tau$ coupling analysis [61].

10.2.1. Theoretical Uncertainties for Background Events

Below is listed the sources of theoretical uncertainties for the major background decays $Z \to \tau\tau$+jets and $Z \to ll$+jets. The impact of the theoretical uncertainties of other background sources are not considered for this analysis as they were estimated and found to have negligible effects on the final result.

- **PDF central value** - This uncertainty is estimated using the standard deviation of 100 replica event weights using the parton distribution function set,NNPDF3.0nnlo, used in SHERPA.
- **renormalisation and factorisation scales - $\mu R/\mu F$** - Calculated using the even-weights used in SHERPA
- **ckkw** - jet-to-parton matching uncertainty, evaluated using truth-level parameterisation with respect to jet multiplicity and $p_T(Z)$ [139]

- **qsf** - resummation scale uncertainty, evaluated using truth-level parameterisation with respect to jet multiplicity and $p_T(Z)$ [139]
- α_s - evaluated using event-weights provided by Sherpa
- **PDF alternative value** - The NNPDF3.0nnlo parton distribution function set is used as the nominal then compared against other PDF sets (h MMHT2014nnlo68cl and CT14nnlo).

10.2.2. Theoretical Uncertainties for Signal predictions

The Standard Model itself is not without uncertainties on its theoretical predictions and therefore these must be incoporated into the consideration of uncertainties of the signal for the analysis. The three major sources of this uncertainty are the following:

- Uncertainty of the QCD scale arising from use of perturbation theory as an approximate solution ignoring higher order perturbation.
- Non-perturbative parts of the calculation including hadronization and the underlying event itself.
- The uncertainties that arise from the parameters of the Standard model which are required to be experimentally measured. Examples of these relevant to this analysis are α_S and the parton density functions.

The approach for processing these uncertainties follows very closely the techniques applied in the $H \to \tau\tau$ coupling analysis [61]. The theoretical uncertainties for total cross section are calculated for each of the major production modes ggH, VBFH and VH. These are obtained by varying the input parameters such as PDFs, renormalisation factors and QCD factorisation. The impact of these uncertainties is limited by the choice to use data driven normalisation factors in the fit so only the shape information of the uncertainties on the constructed observable φ^*_{CP} is used to extract the best-fit value of φ_τ.

The uncertainties that arise from MC modelling are studied by comparing nominal event generator settings against multiple variations of alternative generators, models or parameters. In this way parton shower, hadronisation modelling, scale variations (for QCD factorisation, QCD normalisation and jet-to-parton matching) and PDF model uncertainties are tested.

The source of uncertainty resulting from the use of MC to subtract real events to estimate the number of fake events, described in section 9.4, resulted in a negligible level of contamination and therefore has been ignored.

The complete list of theoretical uncertainties used as nuisance parameters in the analysis is summarised in Table 10.1.

Name of nuisance parameter	Short description
$H \to \tau\tau$	
theory_sig_qcd_[0-8]_ggH	LHCHXSWG scheme for perturbative uncertainties on ggH
theory_VBFH_mur_muf_envelope	Renormalisation and factorisation scales μ_R/μ_F acceptance uncertainty for VBFH
theory_VH_mur_muf_envelope	Renormalisation and factorisation scales μ_R/μ_F acceptance uncertainty for VH
theory_ttH_mur_muf_envelope	Renormalisation and factorisation scales μ_R/μ_F acceptance uncertainty for ttH
theory_sig_AlphaS	α_S acceptance uncertainty for the signal
theory_sig_pdf_[0-29]	PDF acceptance uncertainties for the signal (PDF4LHC)
$Z \to \tau\tau$	
theory_z_AlphaS†	α_S acceptance uncertainty, evaluated using event-weights provided by Sherpa
theory_z_alt_pdf_envelope†	Comparison of predictions from alternative PDF sets
theory_z_pdf_envelope†	Standarnd deviation of the 100 NNPDF replicas event weights of NNPDF3.0nnlo PDF set used in Sherpa
theory_z_mur_muf_envelope†	Renormalisation and factorisation scales μ_R/μ_F uncertainty, evaluated using event-weights provided by Sherpa
theory_z_ckkw†	Jet-to-parton matching uncertainty, evaluated using truth-level parameterisation as a function of jet multiplicity and p_{T} (Z)
theory_z_qsf†	Resummation scale uncertainty, evaluated using truth-level parameterisation as a function of jet multiplicity and p_{T} (Z)
theory_z_CT14_pdfset	Comparison of predictions from NNPDF3.0nnlo PDF set (nominal) with CT14nnlo PDF set
theory_z_MMHT_pdfset	Comparison of predictions from NNPDF3.0nnlo PDF set (nominal) with MMHT2014nnlo68cl PDF set

Table 10.1.: A list of the theoretical uncertainties used in this analysis and a description of their origin [67].

10.3. Analysis Specific Uncertainties

While this analysis primarily uses the systematic uncertainties used for the Run-2 $H \to \tau\tau$ coupling analysis, it is necessary to include systematic uncertainties that are specific to this analysis. These uncertainties are ones that are directly linked to the main observable φ^*_{CP} used within this analysis. These analysis specific uncertainties include the decay mode classification which impacts the methods of reconstruction used for the di-τ system, track uncertainties effect on φ^*_{CP} shape, π^0 uncertainties can affect the reconstruction of 1P1N and 1PXN decay modes thus affecting the φ^*_{CP} shape and theory uncertainties are also assigned which arise from the TauSpinner reweighting proceedure used to build the templates for each of the different values of ϕ_τ.

10.3.1. Tau decay mode classification uncertainties

The uncertainties in this section were developed to account for the uncertainty in the classification of tau decay modes. These uncertainties are based on the Run 1 strategy where decay mode classification efficiencies are calculated from data to extract scale factors (and their associated uncertainties) which describe the effect that a given misclassification has on the observable φ^*_{CP} which allows MC to be matched to data. There is a seperate scale factor calculated for each of the individual τ decays modes at each of the different τ ID working points. The These scale factors are also considered for the efficiencies where the truth and reconstructed decay modes are different in the case of neighbouring decay modes for example 1P0N and 1P1N, 1P1N and 1PXN, and 3P0N and 3PXN.

The uncertainties of the decay mode efficiencies use the Tau ID Medium working point reccomendation and only the uncertainties of the scale factors enter the fit as nuisance parameters since it was observed that the agreement between MC and Data was improved by not applying the nominal scale factor values. The following are the uncertainties used as nuisance parameters in the analysis:

- `TAUS_TRUEHADTAU_EFF_JETID_DECAY_MODE_TRUE_1P0N_RECO_1P0N_TOTAL`
- `TAUS_TRUEHADTAU_EFF_JETID_DECAY_MODE_TRUE_1P1N_RECO_1P0N_TOTAL`
- `TAUS_TRUEHADTAU_EFF_JETID_DECAY_MODE_TRUE_1P1N_RECO_1P1N_TOTAL`

- TAUS_TRUEHADTAU_EFF_JETID_DECAY_MODE_TRUE_1P1N_RECO_1PXN_TOTAL
- TAUS_TRUEHADTAU_EFF_JETID_DECAY_MODE_TRUE_1PXN_RECO_1P1N_TOTAL
- TAUS_TRUEHADTAU_EFF_JETID_DECAY_MODE_TRUE_1PXN_RECO_1PXN_TOTAL
- TAUS_TRUEHADTAU_EFF_JETID_DECAY_MODE_TRUE_3P0N_RECO_3P0N_TOTAL
- TAUS_TRUEHADTAU_EFF_JETID_DECAY_MODE_TRUE_3PXN_RECO_3P0N_TOTAL

Truth decay mode	Reco Decay Mode	Uncertainty(%)
1p0n	1p0n	5.8
1p1n	1p0n	19.5
1p1n	1pXn	8.1
1pXn	1p1n	1.9
1pXn	1pXn	8.3
1p1n	1pXn	8.1
3p0n	3p0n	8.4
3pXn	3p0n	1.9

Table 10.2.: A summary of decay mode classification uncertainties, considering both the uncertainty in decay mode reconstruction in addition to migrations

10.3.2. Track uncertainties on φ^*_{CP} shape

The mismeasurement of the track reconstruction of all of the objects in both the $\tau_{lep}\tau_{had}$ and $\tau_{had}\tau_{had}$ channels causes track smearing in the final state. This smearing can affect the final shape of the φ^*_{CP} distribution since tracks are used to calculate φ^*_{CP} as shown in Section 5.3. It is necessary that the uncertainties result from this smearing are included in the analysis fit. These systematics are estimated following the reccomendations of the Tracking Combined Performance (CP) ATLAS group [140].

- TRK_BIASD0_WM
- TRK_BIAS_Z0_WM
- TRK_BIAS_QOVERP_SAGITTA_WM

- TRK_RES_D0_DEAD
- TRK_RES_D0_MEAS
- TRK_RES_Z0_DEAD
- TRK_RES_Z0_MEAS

10.3.3. π^0 uncertainties on φ^*_{CP} shape

The reconstruction of the π^0 has uncertainties assigned for both the angular resolution and energy scale. These uncertainties can the shape of φ^*_{CP} of decay modes with a neutral component such as 1p1n and 1pXn. These uncertainties are measured using the dedicated Z-enriched control region. The uncertainties used in the analysis to cover the π^0 reconstruction are the following:

- TAUS_PI0_RECALC_PHI_STAR_ETA_SMEAR
- TAUS_PI0_RECALC_PHI_STAR_PHI_SMEAR
- TAUS_PI0_RECALC_PHI_STAR_ENERGY_SCALE

10.3.4. Theory uncertainties on φ^*_{CP} shape

An uncertainty is estimated for the effects of the TauSpinner reweighting used to build templates for the different CP-mixing scenarios on the shape of the φ^*_{CP} distribution. This uncertainty is estimated by comparing a Standard Model, CP-Even, truth level sample and a template built by TauSpinner. This uncertainty enters the fit as a nuisance parameter called PHISTAR-THEORY-SHAPE.

10.4. Data Driven Fake Uncertainties

Another source of uncertainties within the analysis that must be considered are those arising from the fake-factor method for estimating the percentage of fakes within the signal. The sources of uncertainty are different for the $\tau_{lep} - \tau_{had}$ and $\tau_{had} - \tau_{had}$ channels. For the $\tau_{lep} - \tau_{had}$ channel the uncertainies arise from:

- Uncertainty of the fake-factors F_{W} and F_{QCD} arising from the limited statistics in the control regions where they are calculated.
- The uncertainty of R_{QCD}; this has a few contributing sources including the statistical uncertainty of the regions it is calculated in, statistical uncertainty on isolation factors also arising from limited statistics and uncertainty arising from differences in isolation factors calculated using same-sign and opposite-sign event selection.
- Uncertainty introduced during the MC substraction necessary for the calculation of F_{W}, F_{QCD} and R_{QCD}. The estimate for this uncertainty was produced by varying the MC subtraction value by 10%.
- The closure uncertainties are derived by taking the difference between data and prediction in closure tests where the fake-factor estimation is applied in the same sign region.

For $\tau_{\mathrm{had}} - \tau_{\mathrm{had}}$ channel the uncertainties are due to:

- The statistical uncertainty of the fake-factor calculated in the W+Jets CR region.
- The MC subtraction process as it was in the $\tau_{\mathrm{lep}} - \tau_{\mathrm{had}}$ channel
- The uncertainty due to the limitations of the fake-factor parametrization.
- The uncertainty of the closure of fake estimation using fake-factors derived from the $\tau_{\mathrm{had}} - \tau_{\mathrm{had}}$ channel in the high η region.

The following are the uncertainties used in the analysis which cover the areas discussed above, first for the $\tau_{\mathrm{lep}} - \tau_{\mathrm{had}}$ (lh) and then $\tau_{\mathrm{had}} - \tau_{\mathrm{had}}$ (hh) channel.

- statistical uncertainty on the fake-factor measurement:
  - `lh_fake_FF_QCD_1p0n_stat`
  - `lh_fake_FF_W_1p0n_stat`
  - `lh_fake_FF_QCD_1p1n_stat`
  - `lh_fake_FF_W_1p1n_stat`
  - `lh_fake_FF_QCD_1pXn_stat`
  - `lh_fake_FF_W_1pXn_stat`
  - `lh_fake_FF_QCD_3p0n_stat`
  - `lh_fake_FF_W_3p0n_stat`
- statistical uncertainty on RQCD derivation:

  - `lh_fake_RQCD_1p0n_stat`
  - `lh_fake_RQCD_1p1n_stat`
  - `lh_fake_RQCD_1pXn_stat`
  - `lh_fake_RQCD_3p0n_stat`

- statistical and systematic uncertainty on Isolation Factor used for RQCD derivations:

  - `lh_fake_RQCD_1p0n_isofac_stat`
  - `lh_fake_RQCD_1p0n_isofac_syst`
  - `lh_fake_RQCD_1p1n_isofac_stat`
  - `lh_fake_RQCD_1p1n_isofac_syst`
  - `lh_fake_RQCD_1pXn_isofac_stat`
  - `lh_fake_RQCD_1pXn_isofac_syst`
  - `lh_fake_RQCD_3p0n_isofac_stat`
  - `lh_fake_RQCD_3p0n_isofac_syst`

- uncertainty on MC subtraction for fake-factor, Isolation Factor and RQCD calculation:

  - `lh_fake_mc_subtr_1p0n`
  - `lh_fake_mc_subtr_1p1n`
  - `lh_fake_mc_subtr_1pXn`
  - `lh_fake_mc_subtr_3p0n`

- closure uncertainty derived in same-sign region:

  - `lh_fake_closure_1p0n`
  - `lh_fake_closure_1p1n`
  - `lh_fake_closure_1pXn`
  - `lh_fake_closure_3p0n`

The following are similarly the fake-factor uncertainties for the hh channel.

- statistical uncertainty on the fake-factor measurement:

  - `hh_fake_ff_stat_1p0n_nm`
  - `hh_fake_ff_stat_1p0n_lnm`
  - `hh_fake_ff_stat_1p1n_nm`
  - `hh_fake_ff_stat_1p1n_lnm`
  - `hh_fake_ff_stat_1pXn_nm`

  - `hh_fake_ff_stat_1pXn_lnm`
  - `hh_fake_ff_stat_3p0n_nm`
  - `hh_fake_ff_stat_3p0n_lnm`

- uncertainty on MC subtraction for fake-factor:

  - `hh_fake_ff_mcsubstr_1p0n_nm`
  - `hh_fake_ff_mcsubstr_1p0n_lnm`
  - `hh_fake_ff_mcsubstr_1p1n_nm`
  - `hh_fake_ff_mcsubstr_1p1n_lnm`
  - `hh_fake_ff_mcsubstr_1pXn_nm`
  - `hh_fake_ff_mcsubstr_1pXn_lnm`
  - `hh_fake_ff_mcsubstr_3p0n_nm`
  - `hh_fake_ff_mcsubstr_3p0n_lnm`

- closure uncertainty derived in $\tau_{\text{had}}\tau_{\text{had}}$high-$\Delta\eta$ region (measured per decay-mode combination):

  - `hh_fake_ff_composition_highdeta`

- uncertainty on the limitation of fake factor parameterisation (measured per decay-mode combination):

  - `hh_fake_ff_param`

Tables 10.3 and 10.4 summarise the fake uncertainties, where the percentage difference compared to the nominal fake uncertainty is shown for each decay mode.

	Boost				VBF			
	ℓ-1p0n	ℓ-1p1n	ℓ-1pXn	ℓ-3p0n	ℓ-1p0n	ℓ-1p1n	ℓ-1pXn	ℓ-3p0n
lh fake closure 1p0n	10.8				100.2			
lh fake closure 1p1n		-4.4				-27.0		
lh fake closure 1pXn			16.6				1.9	
lh fake closure 3p0n				13.3				-15.8
lh fake FF QCD 1p0n stat	1.5				2.3			
lh fake FF QCD 1p1n stat		1.1				2.9		
lh fake FF QCD 1pXn stat			1.8				3.1	
lh fake FF QCD 3p0n stat				2.4				4.1
lh fake FF W 1p0n stat	10.7				21.6			
lh fake FF W 1p1n stat		7.5				19.4		
lh fake FF W 1pXn stat			12.4				26.0	
lh fake FF W 3p0n stat				13.9				26.5
lh fake mcsubstr 1p0n	-11.0				-9.3			
lh fake mcsubstr 1p1n		-11.9				-16.2		
lh fake mcsubstr 1pXn			-9.8				-7.3	
lh fake mcsubstr 3p0n				-10.3				-8.6
lh fake RQCD 1p0n stat	0.3				-0.2			
lh fake RQCD 1p1n stat		0.1				0.8		
lh fake RQCD 1pXn stat			-0.1				-0.5	
lh fake RQCD 3p0n stat				0.0				-0.1
Total (systematic)	19	15	23	22	103	37	27	32
Statistical	1.1	0.6	0.8	0.5	3.2	1.5	2.3	1.6

Table 10.3.: Systematic uncertainties for the $\tau_{\text{lep}} - \tau_{\text{had}}$ channel. These are split by decay mode in each of the Signal regions (Boost and VBF) since the fake factor estimate is performed seperately in each decay mode region and also seperately between Boost and VBF. All uncertainties are presented as percentage differences of the varied from the nominal values of the fake estimation. Furthermore all uncertainties are assumed to be uncorrelated and therefore may be added in quadrature to obtain the total for each signal region. The statistical uncertainties have been included at the bottom of the table for comparison, showing that these uncertainties are dominated by systematic uncertainties. Note, the Isolation factor systematics have not been included in the table but are expected to be insignificant.

	1p0n-1p0n	1p0n-1p1n + 1p1n-1p0n	1p1n-1p1n	1p0n-1pXn + 1pXn-1p0n	1p1n-1pXn + 1pXn-1p1n	1p1n-3p0n + 3p0n-1p1n
hh fake ff composition highdeta (closure)	-18.2	-17.4	-13.6	-9.7	-9.3	-10.6
hh fake ff param	-0.9	-0.9	-0.9	-0.9	-0.9	-0.9
hh fake ff stat 1p0n lnm	-11.2	-5.5		-4.7		
hh fake ff stat 1p0n nm	12.0	6.2		5.5		
hh fake ff stat 1p1n lnm		-4.4	-7.5		-4.0	-4.0
hh fake ff stat 1p1n nm		3.8	8.2		4.0	4.0
hh fake ff stat 1pXn lnm				-6.1	-5.5	
hh fake ff stat 1pXn nm				5.7	5.9	
hh fake ff stat 3p0n lnm						-9.7
hh fake ff stat 3p0n nm						9.2
hh fake ff mcsubstr 1p0n nm	-8.8	-4.6		-4.1		
hh fake ff mcsubstr 1p0n lnm	6.3	3.1		2.7		
hh fake ff mcsubstr 1p1n nm		-5.1	-11.0		-5.3	-5.4
hh fake ff mcsubstr 1p1n lnm		4.2	7.1		3.7	3.8
hh fake ff mcsubstr 1pXn nm				-3.9	-4.0	
hh fake ff mcsubstr 1pXn lnm				3.1	2.8	
hh fake ff mcsubstr 3p0n nm						-6.1
hh fake ff mcsubstr 3p0n lnm						5.0
Total (systematic)	27	22	22	16	16	21
Statistical	32	13	1.3	2.5	1.3	1.7

Table 10.4.: Systematic uncertainties for the $\tau_{\text{had}} - \tau_{\text{had}}$ channel. These are split by decay mode in each of the Signal regions (Boost and VBF) since the fake factor estimate is performed seperately in each decay mode region and also seperately between Boost and VBF. All uncertainties are presented as percentage differences of the varied from the nominal values of the fake estimation. Furthermore all uncertainties are assumed to be uncorrelated and therefore may be added in quadrature to obtain the total for each signal region. The statistical uncertainties have been included at the bottom of the table for comparison, showing that these uncertainties are dominated by systematic uncertainties. Note, the Isolation factor systematics have not been included in the table but are expected to be insignificant.

10.5. Impact of Systematic Uncertainties

The following Tables 10.5 and 10.6, show the relative impacts of most impactful (those with impact of over 3%) nuisance parameters in the signal regions for the $\tau_{\text{had}} - \tau_{\text{had}}$ and $\tau_{\text{lep}} - \tau_{\text{had}}$ channels. These only show the different in total number of events due to variations in the nuisance parameter. This means the following impacts are for normalisation only. These tables do not show the impact they have on the shape of the φ_τ distribution, for this see the ranking plots in Section 11.3.2.

	hh VBF 1 high	hh VBF 1 low	hh VBF 0 high	hh VBF 0 low	hh Boost tight high	hh Boost tight low	hh Boost loose high	hh Boost loose low
FINAL_JET_JER_DataVsMC_MC16	3.5 / 1.3	0.6 / -3.3	-1.6 / 5.8	1.7 / 1.6	-1.2 / 1.3	-0.6 / 0.6	0.0 / 1.1	-0.1 / 0.1
FINAL_JET_JER_EffectiveNP_1	3.8 / -4.1	-1.8 / 2.5	8.1 / -6.7	7.5 / -0.3	5.9 / -2.4	5.5 / -2.7	2.2 / 0.3	2.7 / -0.8
FINAL_JET_JER_EffectiveNP_11	2.8 / -3.6	-0.3 / 1.0	-3.0 / -1.1	1.3 / -0.4	0.1 / 1.1	-0.4 / 1.7	0.8 / -0.5	0.4 / 0.7
FINAL_JET_JER_EffectiveNP_12restTerm	-3.5 / 4.2	1.0 / 3.3	1.7 / -1.1	0.2 / 0.4	1.6 / -0.2	1.6 / -0.2	-0.3 / 1.2	1.0 / -0.3
FINAL_JET_JER_EffectiveNP_2	-5.1 / 0.8	-1.0 / 4.3	3.3 / 0.2	0.6 / 1.7	5.6 / -2.6	5.4 / -2.2	2.2 / 0.5	3.4 / 0.1
FINAL_JET_JER_EffectiveNP_4	-0.2 / -3.2	-1.3 / 1.8	1.0 / 1.0	1.5 / 0.2	2.0 / 0.3	1.3 / 0.4	0.5 / 0.4	0.8 / 0.7
FINAL_JET_JER_EffectiveNP_8	3.1 / -4.0	-1.1 / 5.4	-1.4 / -1.7	0.8 / 1.0	-0.1 / 0.5	0.1 / 0.7	0.6 / 0.6	-0.3 / 0.7
FINAL_JET_JER_EffectiveNP_9	-3.7 / 2.1	1.5 / -0.0	-0.2 / -0.2	-1.7 / 0.1	1.5 / -0.0	0.8 / 0.2	0.1 / 1.0	1.1 / 0.4
hh_fake_ff_composition_highdeta	-3.4 / -3.4	-5.5 / -5.5	-3.9 / -3.9	-6.4 / -6.4	-0.5 / -0.5	-1.0 / -1.0	-3.0 / -3.0	-5.8 / -5.8
JET_EffectiveNP_Mixed1	-2.9 / -3.9	0.1 / -0.2	0.9 / 0.6	1.0 / 0.2	1.4 / -1.0	1.4 / -1.0	-0.4 / -1.7	0.7 / -0.4
JET_EffectiveNP_Mixed2	-3.2 / -2.7	-1.3 / 0.9	1.6 / 1.2	0.1 / 0.6	-0.6 / 0.9	-0.7 / 1.0	-1.1 / -0.6	-0.8 / 0.5
JET_EffectiveNP_Mixed3	-3.9 / -3.6	-0.7 / -2.0	0.5 / -0.3	-0.3 / -0.5	0.3 / -0.0	-0.1 / -0.0	-0.5 / -0.7	0.0 / 0.1
JET_EffectiveNP_Modelling1	-1.4 / -5.5	0.1 / -4.0	4.4 / -3.8	0.9 / -2.3	4.0 / -3.3	3.5 / -2.9	1.1 / -2.9	2.2 / -1.9
JET_EffectiveNP_Modelling2	-2.7 / -4.0	1.2 / 0.3	1.1 / -0.8	1.0 / -0.6	0.6 / -0.0	0.5 / -0.1	-0.3 / -0.7	0.0 / -0.3
JET_EffectiveNP_Statistical2	-4.0 / -3.6	-0.1 / -0.2	-0.9 / -0.3	-0.1 / 0.2	-0.3 / 0.2	-0.1 / 0.2	-0.9 / -0.5	0.1 / 0.1
JET_EtaIntercalibration_Modelling	-3.4 / -7.1	1.5 / -6.3	8.6 / -5.4	5.6 / -4.0	2.9 / -2.2	2.3 / -2.0	0.5 / -2.3	1.4 / -0.8
JET_EtaIntercalibration_TotalStat	-3.5 / -0.3	0.2 / -1.0	1.4 / -1.8	1.4 / 0.0	0.3 / -0.4	0.3 / -0.3	-0.3 / -1.1	0.3 / -0.1
JET_Flavor_Composition	-1.8 / -4.5	0.5 / -1.7	0.6 / 0.1	2.3 / -2.0	1.2 / 0.2	0.9 / -0.3	-0.5 / -0.8	0.5 / -0.0
JET_Flavor_Response	-2.6 / 4.4	-2.1 / 0.4	-4.9 / 5.7	-2.3 / 3.8	-5.0 / 6.0	-5.0 / 5.8	-4.9 / 2.9	-3.0 / 4.0
JET_Pileup_OffsetMu	3.0 / -4.2	-0.9 / -1.9	7.0 / -4.4	2.0 / -2.2	1.4 / -1.0	1.9 / -1.2	0.2 / -1.8	1.0 / -0.4
JET_Pileup_OffsetNPV	-1.9 / -5.3	-3.2 / -1.1	2.5 / -2.9	1.0 / -1.9	2.1 / -1.3	2.7 / -1.6	0.4 / -2.1	1.1 / -0.9
JET_Pileup_PtTerm	-2.8 / -3.4	1.4 / -1.3	1.0 / -0.6	-0.2 / 0.5	1.0 / -1.0	1.3 / -0.7	-0.5 / -1.1	1.0 / -0.9
JET_Pileup_RhoTopology	1.3 / -5.0	-0.6 / -4.8	7.9 / -6.5	2.1 / -1.8	4.2 / -3.1	4.5 / -3.5	2.0 / -3.6	3.2 / -2.8
MET_SoftTrk_ResoPara	-6.6 / -0.0	-1.4 / 0.0	-0.7 / -0.0	-0.9 / -0.1	-2.4 / -0.1	-1.7 / -0.1	-2.5 / -0.1	-1.0 / -0.1
MET_SoftTrk_ResoPerp	-4.0 / -0.0	-3.2 / 0.0	-3.3 / -0.0	-1.4 / -0.1	-3.1 / -0.1	-1.5 / -0.1	-2.5 / -0.1	-1.7 / -0.1
MET_SoftTrk_Scale	-4.2 / -4.4	0.2 / -0.4	0.3 / 2.1	-2.7 / 0.8	-2.7 / 3.5	-2.6 / 2.6	-3.1 / 0.5	-1.6 / 1.6
TAUS_TRUEHADTAU_EFF_JETID_DECAY_MODE_TRUE_1P1N_RECO_1P1N_TOTAL	7.0 / -6.7	7.2 / -6.8	6.9 / -6.6	4.9 / -4.6	8.8 / -8.4	8.1 / -7.8	6.9 / -6.6	5.4 / -5.2
TAUS_TRUEHADTAU_SME_TES_INSITUEXP	-3.0 / -3.8	-0.0 / -1.8	0.9 / -2.3	-1.0 / -2.5	0.8 / -1.0	1.3 / -0.9	0.8 / -1.7	1.0 / -1.0
TAUS_TRUEHADTAU_SME_TES_INSITUFIT	-1.1 / -4.3	1.6 / -1.5	2.0 / -1.7	0.8 / -1.2	1.7 / -1.4	1.8 / -1.6	1.7 / -2.8	2.1 / -1.5
TAUS_TRUEHADTAU_SME_TES_MODEL_CLOSURE	-1.5 / -2.1	1.5 / -1.1	1.3 / -3.4	-0.7 / -1.5	1.5 / -0.6	0.7 / -0.6	0.6 / -1.3	1.2 / -0.4
TAUS_TRUEHADTAU_SME_TES_PHYSICSLIST	-1.4 / -4.1	0.8 / -1.7	2.3 / -2.2	0.8 / -1.5	2.0 / -1.8	1.8 / -1.9	1.2 / -2.8	1.7 / -1.4

Table 10.5.: Relative impact of the nuisance parameters on the total number of events in different signal regions for the $\tau_{\text{had}} - \tau_{\text{had}}$ channel. All impacts are given as percentage difference in yield for up/down variations, only NPs that result in a percentage yield difference of greater than 3% in at least one signal region are included in this table. Any variation of less than 0.05% is rounded to 0.0% and any that are greater than 5.0% are highlighted in pink.

	lh VBF 1 high	lh VBF 1 low	lh VBF 0 high	lh VBF 0 low	lh Boost tight high	lh Boost tight low	lh Boost loose high	lh Boost loose low
FINAL_JET_JER_DataVsMC_MC16	-3.0 / 3.1	0.6 / -0.5	-1.9 / 0.6	-0.3 / 1.4	0.1 / 0.7	-1.4 / 1.2	-1.0 / 1.0	-1.0 / 1.5
FINAL_JET_JER_EffectiveNP_1	4.8 / -5.4	3.2 / -0.8	3.9 / -1.7	3.2 / -1.9	5.4 / -3.1	4.3 / -2.0	3.2 / -3.3	3.6 / -1.6
FINAL_JET_JER_EffectiveNP_10	-0.2 / 2.5	-1.7 / -0.4	0.2 / 3.2	-0.5 / 0.1	1.1 / 0.6	1.1 / 0.1	0.2 / -0.7	0.2 / 0.4
FINAL_JET_JER_EffectiveNP_2	0.7 / 0.2	2.6 / -1.8	-0.9 / 4.8	2.2 / 2.3	6.7 / -3.1	3.7 / -1.1	1.3 / -1.3	3.5 / -1.2
FINAL_JET_JER_EffectiveNP_3	0.6 / 1.9	-3.3 / 2.4	3.1 / 2.1	0.3 / 3.1	-0.2 / 1.6	-0.5 / 2.0	-1.0 / 2.2	-0.9 / 1.8
FINAL_JET_JER_EffectiveNP_4	2.2 / 2.2	-0.6 / -0.5	2.3 / -0.6	3.5 / -0.1	1.8 / -0.2	1.9 / -0.2	1.5 / 0.1	-0.2 / 0.8
FINAL_JET_JER_EffectiveNP_5	-3.5 / 6.0	0.8 / -1.8	2.9 / 5.2	1.8 / 1.5	-0.2 / 0.6	-0.5 / 0.9	0.4 / 0.8	0.3 / 1.1
FINAL_JET_JER_EffectiveNP_6	-5.3 / 4.4	0.5 / 0.6	3.8 / -1.8	-0.5 / 2.6	-1.0 / 2.5	-0.7 / 1.6	-0.1 / 2.0	0.0 / 1.3
FINAL_JET_JER_EffectiveNP_8	4.3 / 0.2	-0.9 / -0.2	-1.7 / -2.6	1.9 / 1.5	-0.4 / -0.3	0.3 / 0.2	-0.1 / -0.2	0.5 / 0.5
JET_EffectiveNP_Detector2	-0.1 / 0.5	0.4 / 0.2	-0.2 / -4.0	-0.4 / -0.1	0.6 / -0.0	-0.2 / -0.1	0.2 / -0.8	0.4 / -0.3
JET_EffectiveNP_Modelling1	1.5 / -0.5	1.8 / -5.0	0.1 / -5.7	4.1 / -2.1	4.4 / -2.0	3.3 / -3.3	3.9 / -3.0	2.2 / -2.8
JET_EffectiveNP_Modelling4	0.6 / 0.4	-0.2 / -0.4	-0.7 / -3.4	0.7 / -0.7	0.3 / 0.8	0.1 / 0.1	0.2 / -0.6	-0.0 / -0.0
JET_EffectiveNP_Statistical4	-0.6 / -0.2	0.8 / -0.3	-4.3 / 1.4	0.2 / -0.3	0.3 / -0.6	-0.1 / -0.0	-0.1 / -1.1	-0.1 / 0.0
JET_EffectiveNP_Statistical6	0.5 / -2.1	0.5 / -0.2	0.6 / -4.1	0.3 / -1.1	0.8 / 0.5	-0.1 / -0.3	0.2 / -0.8	0.0 / -0.1
JET_EtaIntercalibration_Modelling	4.5 / -3.3	4.0 / -6.1	4.7 / -8.0	6.1 / -5.2	3.1 / -1.9	1.5 / -2.5	3.3 / -1.5	1.7 / -1.8
JET_Flavor_Composition	5.5 / -2.2	4.6 / -1.9	2.0 / -4.0	3.1 / -2.2	1.7 / -0.3	0.8 / -1.1	0.8 / -1.9	1.0 / -1.1
JET_Flavor_Response	-3.3 / 3.4	-4.7 / 3.7	-5.8 / 3.1	-3.7 / 3.2	-3.9 / 5.1	-4.4 / 4.0	-4.1 / 6.9	-3.5 / 4.0
JET_Pileup_OffsetMu	2.1 / -2.4	1.0 / -3.2	-1.8 / -6.5	3.2 / -3.2	1.8 / -0.2	0.6 / -1.0	2.3 / -0.9	1.2 / -1.4
JET_Pileup_OffsetNPV	2.3 / -0.3	0.7 / -2.8	2.6 / -2.1	3.2 / -2.1	3.3 / -2.0	1.4 / -1.8	2.8 / -2.0	2.1 / -1.9
JET_Pileup_RhoTopology	3.5 / -1.5	1.3 / -3.1	3.5 / -8.1	4.5 / -3.7	5.2 / -3.2	3.0 / -2.5	5.2 / -3.7	3.3 / -3.2
lh_fake_closure_1p0n	0.8 / -0.8	5.4 / -5.4	2.0 / -2.0	8.5 / -8.5	0.1 / -0.1	0.4 / -0.4	0.1 / -0.1	0.7 / -0.7
MET_SoftTrk_ResoPara	-0.5 / 0.0	-2.7 / 0.0	-3.3 / 0.0	-1.3 / -0.0	-0.5 / 0.0	-2.0 / -0.0	-0.9 / 0.0	-1.4 / 0.0
MET_SoftTrk_ResoPerp	0.2 / 0.0	-2.1 / 0.0	-3.4 / 0.0	0.4 / -0.0	-0.6 / 0.0	-1.7 / -0.0	-1.3 / 0.0	-1.0 / 0.0
MET_SoftTrk_Scale	-0.2 / 0.3	-0.1 / 0.9	-3.1 / -0.6	-0.5 / -0.3	-2.1 / 2.6	-2.3 / 1.7	-2.3 / 1.5	-2.2 / 1.8
TAUS_TRUEHADTAU_EFF_JETID_DECAY_MODE_TRUE_1P1N_RECO_1P1N_TOTAL	3.9 / -3.9	2.9 / -2.9	3.8 / -3.8	2.5 / -2.5	4.2 / -4.2	2.9 / -2.9	3.8 / -3.8	2.4 / -2.4
TAUS_TRUEHADTAU_SME_TES_INSITUFIT	-0.3 / -2.2	1.3 / -0.8	3.5 / -0.4	1.7 / -1.7	1.3 / -0.4	0.8 / -1.0	1.6 / -2.5	1.0 / -1.7
theory_z_mur_muf_envelope_constrained	3.8 / -5.5	0.5 / -1.1	1.4 / -2.0	-1.0 / 1.6	2.1 / -3.5	1.2 / -2.3	0.5 / -0.5	-1.0 / 1.8

Table 10.6.: Relative impact of the nuisance parameters on the total number of events in different signal regions for the $\tau_{\text{lep}} - \tau_{\text{had}}$ channel. All impacts are given as percentage difference in yield for up/down variations, only NPs that result in a percentage yield difference of greater than 3% in at least one signal region are included in this table. Any variation of less than 0.05% is rounded to 0.0% and any that are greater than 5.0% are highlighted in pink.

10.6. Smoothing

Smoothing is the process of reducing the impact of noise on a histogram. This can be achieved by a number of methods which are discussed in detail below. In general these algorithms will bring neighbouring bins more inline with one another. In the case of this analysis smoothing is used to combat the effects of low statistics on the nuisance parameter plots by smoothing the noise so the systematic plots better describe the underlying shape of the systematic.

10.6.1. Types of Smoothing Algorithms

10.6.1.1. Rebinning

The simplest smoothing algorithmns rebin histograms to smooth them. TRExFitter has two such algorithmns (SMOOTHREBINMONOTONIC and SMOOTHREBINPARABOLIC [141]). They use the following steps:

1. If the MC statistical uncertainty is greater than a threshold percentage of 5%, the histogram is rebinned to a single bin and shape is lost since it is assumed that the error is so large the shape cannot be reconstructed in any meaningful way.
2. If MC integral error is less than 5 %, then most compatible neighbouring bins are merged until either 2 or 3 extrema are left (for for SMOOTHREBINMONOTONIC and SMOOTHREBINPARABOLIC respectively). Compatibility is assessed by χ^2 between the average of neighbouring bins and target bin. Extrema are defined as bins where it has a different value to its neighbours.
3. Finally rebin the histogram until the MC statistical uncertainty is less than 5 %.

10.6.1.2. Kernel Smoother

The Kernel Smoother takes each bin labelled x_0 and modifies it value, $\hat{y}(x_0)$ with the formula shown in Equation 10.1

$$.\hat{y} = \frac{\sum_{i \in bins} K(x_0, x_i) y(x_i)}{\sum_{i \in bins} K(x_0, x_i)} \tag{10.1}$$

Where K is the Kernel function:

$$K(x_0, x_i) = f\left(\frac{x_0 - x_i}{h}\right) \tag{10.2}$$

In TRExFitter there are two available functions, uniform or gaussian. In addition there is also the option to choose to smooth either the difference between the nominal and the systematic or the ratio of the two.

In order to calculate the optimal value for the free parameter,h, the technique "leave-one-out-cross-validation" is used. The steps for this algorithm are as follows:

1. Loop through each bin denoted by the iterator variable i
2. Loop through a list of values of h.
3. Smooth the points using the kernel algorithm described above, excluding the ith bin.
4. Calculate the "distance", d, between the smoothed and nominal points (for all points) as shown in Eq. 10.3.
5. Take the value of h_i that minimises the value d for specific bin, i.
6. Sum each of these values of h_i and divide by the number of bins as in Equation 10.4

$$d = \sum \left(s_j - n_j\right)^2 \tag{10.3}$$

$$h = \sum \frac{h_i}{n} \tag{10.4}$$

10.6.1.3. 353QH Twice

The 353QH Twice algorithm gets its name from the following 6 steps. y represents the sequence of numbers that are being smoothed. z represents the sequence of smoothed values derived from y.

1. This step runs a median of 3 consecutive numbers in y to produce the equivalent in z. $z_i = \text{median}(y_{i-1}, y_i, y_{i+1})$. This requires specials cases at either end of the sequence since for the first element and last element there is no y_{i-1} and y_{i+1} elements respectively, therefore the algorithm uses: $z_1 = \text{median}(3z_2 - 2z_3, y_1, z_2)$ and $z_n = \text{median}(z_{n-1}, y_n, 3z_{n-1} - 2z_{n-2})$.

2. This step is very similar to the previous, but uses a median of 5 instead of 3. This is run on the output from the previous step. $z_n = \text{median}(z_{n-2}, z_{n-1}, z_n, z_{n+1}, z_{n+2})$. Using a median of 5 means there are now 4 special cases, two at each end of the sequence. For the two end points (z_1 and z_n) these are just directly copied from the previous step. z_2 and z_{n-1} use a median of 3 instead so $z_{n-1} = \text{median}(z_{n-2}, z_{n-1}, z_n)$ and $z_2 = \text{median}(z_1, z_2, z_3)$.

3. This step repeats step 1 on the output of the previous step. Instead of the special cases used then however, it copies the values of z_1 and z_n from the previous step.

4. This step uses quadratic interpolation on points of 3 adjacent values which form either a peak or a valley. This is necessary, as the use of medians of 3 clips minima and maxima causing discontinuities in the derivative. The quadratic fit is performed through the two points adjacent to the 3 flat points and the point in the flat which is next to the adjacent point which has the value most different from the value of the 3 flat points.

5. For remedying monotonic discontinuities this operation copies the end values as before ($z_1 = z_1$ and $z_n = z_n$) but each other value is calculated from the results of the previous step by the following: $z_i = \frac{1}{4}z_{i-1} + \frac{1}{2}z_i + \frac{1}{4}z_{i+1}$.

6. A problem of the previous steps is they tend to oversmooth peaks. One way to reduce the impact of this effect is by adding an additional step known as "twicing". The original sequence y is smoothed into sequence z, r can be defined as $r = y - z$, the final output of z is defined as either z = smooth(y) + smooth(r) OR z = smooth(y) - smooth(y-smooth(y))

10.6.1.4. TRExFitter MaxVariation

The MaxVariation algorithm sets a limit of the ratio of the nominal histogram to the systematic histogram. It has 3 steps:

1. Rebin the histogram until the relative statistical uncertainty is either lower than a predefined tolerance or the number of bins.
2. Check the number of slope changes, also called variations, in a histogram formed from the ratio of the nominal to the systematic. If there are more slope changes than N, a user defined maximum number, then half the tolerance and repeat the previous step. A slope change is defined as as the point at which the consecutive bin values change direction. For example assuming a histogram with 5 bins; bin values of 1,2,3,4,1 would have one slope change between 4 and 1 whereas 5,7,6,5,8,9 would have one between 7,6 and one between 5,8.
3. After the previous steps have completed. Run the ROOT smoothing algorithm "TH1::Smooth". This uses the "353QH twice" algorithm this ensures the re-binning hasn't created artificially flat uncertainties.

10.6.1.5. TRExFitter TTbarResonance

In the following description N is the nominal and S is the systematic variation, where δN and δS are their respective statistical errors.

For each bin in the systematic histogram the quantity $x_{i-1,i}$ is calculated.

$$x_{i-1,i} = \left| \frac{S_i - N_i}{N_i} - \frac{S_{i-1} - N_{i-1}}{N_{i-1}} \right| \tag{10.5}$$

In addition the relative statistical uncertainty is also calculated.

$$\delta x_{i_1,i} = \sqrt{\frac{\delta M_i^2}{N_i^2} - \frac{\delta M_{i-1}^2}{N_{i-1}^2}} \tag{10.6}$$

where M is defined as:

$$\delta M = \sqrt{\delta S^2 + \delta N^2} \tag{10.7}$$

The algorithm checks if any of the bins meet the following criteria.

$$x_{i-1,i} < \delta x_{i-1,i} \tag{10.8}$$

If any meet the criteria, the algorithm compares the ratio of $\frac{\delta x_{b-1,b}}{x_{b-1,b}}$ for pairs of neighbouring bins. It merges the pairs of bins with the highest ratio until no more bins satisfy Equation 10.8

$$x_{i-1,i} < \delta x_{i-1,i} \tag{10.9}$$

After this as with the MaxVariation algorithm, the ROOT smoothing algorithm "TH1::Smooth" is used on $\frac{S-N}{N}$ to smooth transitions between bins thats have been merged.

10.6.2. Smoothing Studies

For the purposes of this analysis four smoothing algorithms within TRExFitter are compared. These are:

- CommonToolSmoothMonotonic
- CommonToolSmoothParabolic
- MaxVariation
- TTBARResonance

When assessing the four algorithms for the optimum one to use in the analysis, a number of comparisons are made. The first and most basic check is to examine the effect the smoothing algorithmns had on the envelope plots of the nuisance parameters. Supplied here are example comparisons of a typical NP from a high sensitivity region (HH VBF 1 High) to demonstrate the effects that smoothing has on the nuisance parameters.

It can be seen in Figure 10.2 how much more destructive TTBARRResonance and CommonToolSmoothMonotonic, is on the shape of the NP envelopes than MaxVariation. CommonToolSmoothParabolic also preserves the shape better but struggles with the same sign bins. The goal of the smoothing algorithm is to smooth out noise without destroying the underlying shape of the nuisance parameter. From these results

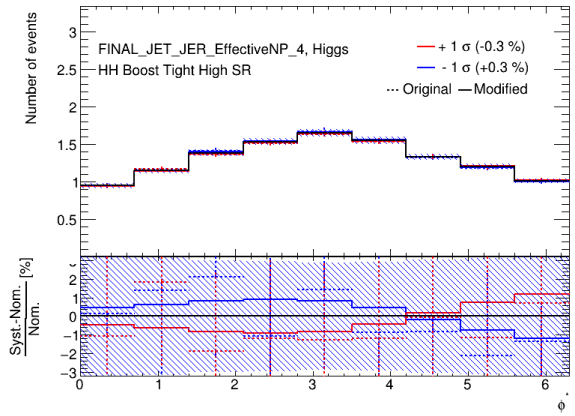

(a) VBF 1 high sr MaxVariation

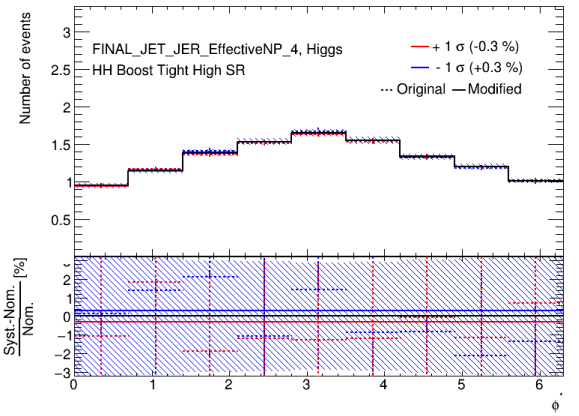

(b) VBF 1 high sr TTBARResonance

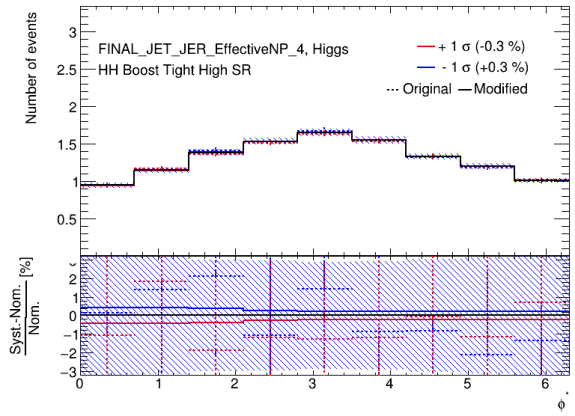

(c) VBF 1 high sr CommonToolSmoothMonotonic

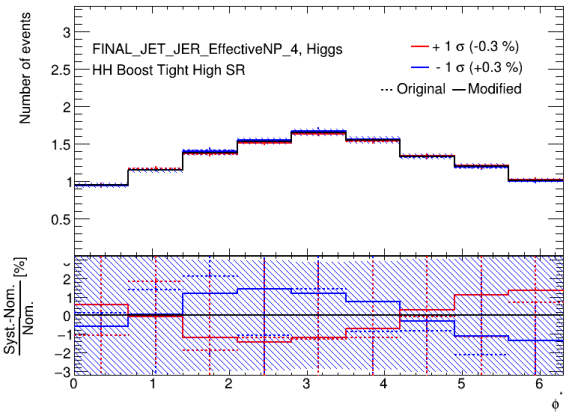

(d) VBF 1 high sr CommonToolSmoothParabolic

Figure 10.2.: A comparison of plots from one of the high sensitivity regions (VBF 1 High) to demonstrate the effect that smoothing has on the nuisance parameter histograms, specifically in this the NP "FINAL_JET_JER_EffectiveNP_4" is used.

and the comparison of many other nuisance parameter plots. MaxVariation was the most promising algorithmn.

The next check conducted to assess the suitability of the smoothing algorithmns was the production of ranking plots. These assess the 40 most impactful NPs. Though choice of smoothing algorithmn will have an effect on these plots, it should not drastically alter the most impactful groups of NPs nor should it produce unexpected pulls. The ranking plots produced are shown in Figures 10.3 and 10.4. While a number of the NPs are reordered, none of the smoothing options results in a drastic change to the fact that JET NPs are still the mostly highly ranked NPs. Only CommonToolSmoothParabolic changed the top ranked NP, this taken in combination with the fact it is

increasing pulls across the top 40 NPs is indicative of a worse fit environment. The MaxVariation and TTBarResonance are quite similar in their pulls on the top 40 and though CommonToolSmoothMonotonic exhibits a marked reduction in the pulls of the NPs, this is primarily as a result over flattening out the shape too aggressively in the NP distributions.

The final check to conduct, is to look at the sensitivity changes between the different smoothing algorithmns. The higher the maximum negative log likelihood, the more sensitive the analysis. When investigating smoothing however this comes with a number of caveats, an increase in NNL is possible through an effect of oversmoothing and removing real shape data from the uncertainties, falsely increasing the NNL. In previous investigations it was shown that MaxVariation preserved the shape of the NPs better, this however resulted in larger post-fit impacts for the highest ranked NPs, this translated into a slight drop in sensitivity as shown in Figure 10.5. This drop is however acceptable for the better preservation of the uncertainty shapes.

The result of this smoothing investigation was that MaxVariation was used as the smoothing algorithmn for this analysis.

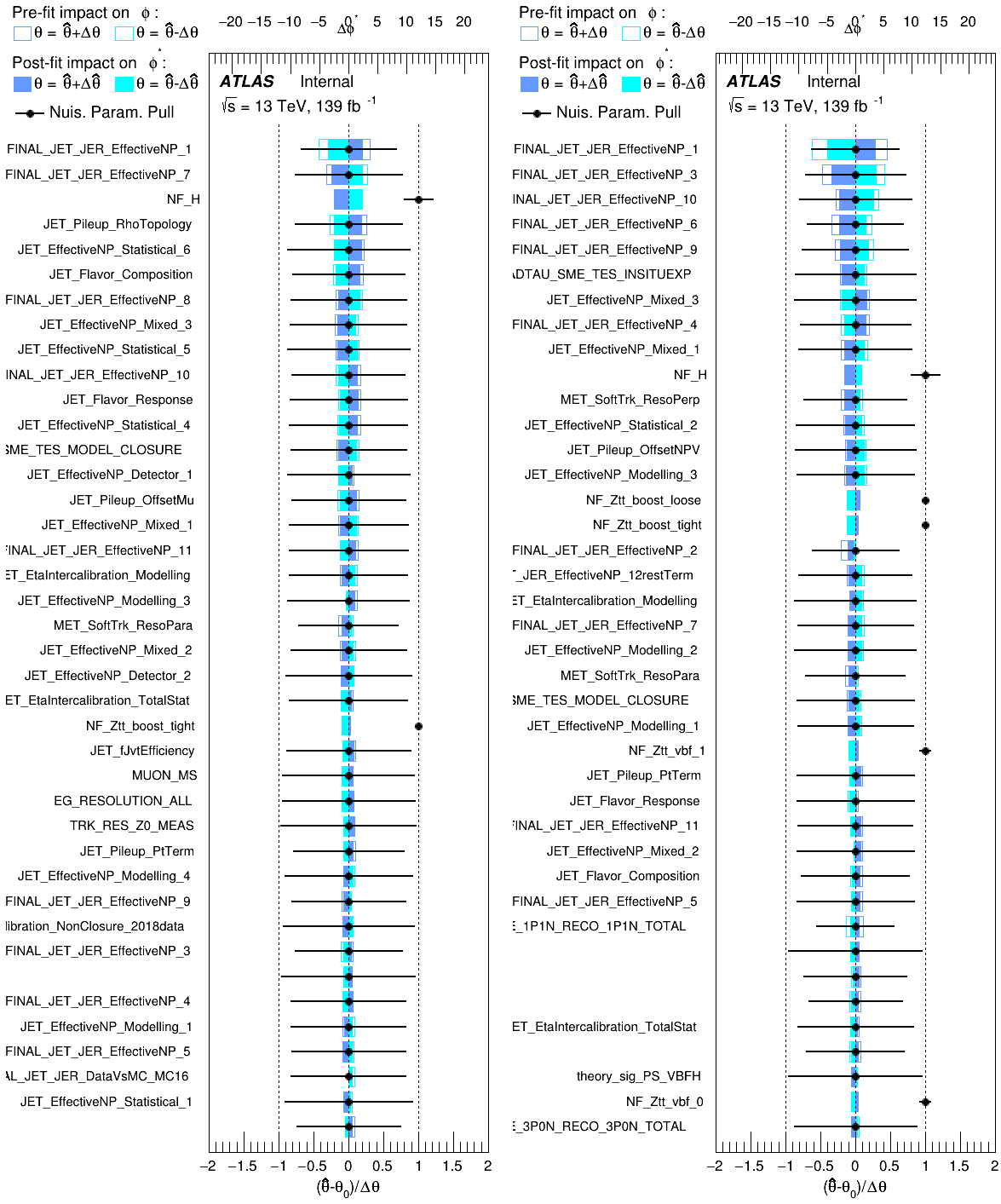

(a) MaxVariation **(b)** TTBARResonance

Figure 10.3.: The nuisance parameter rankings for the top 40 nuisance parameter for the (a) MaxVariation and (b) TTBARResonance smoothing algorithmns. Produced using Asimov data. Note the normalisation factors (beginning with NF_) are showing their values (around 1), not a pull of this value.

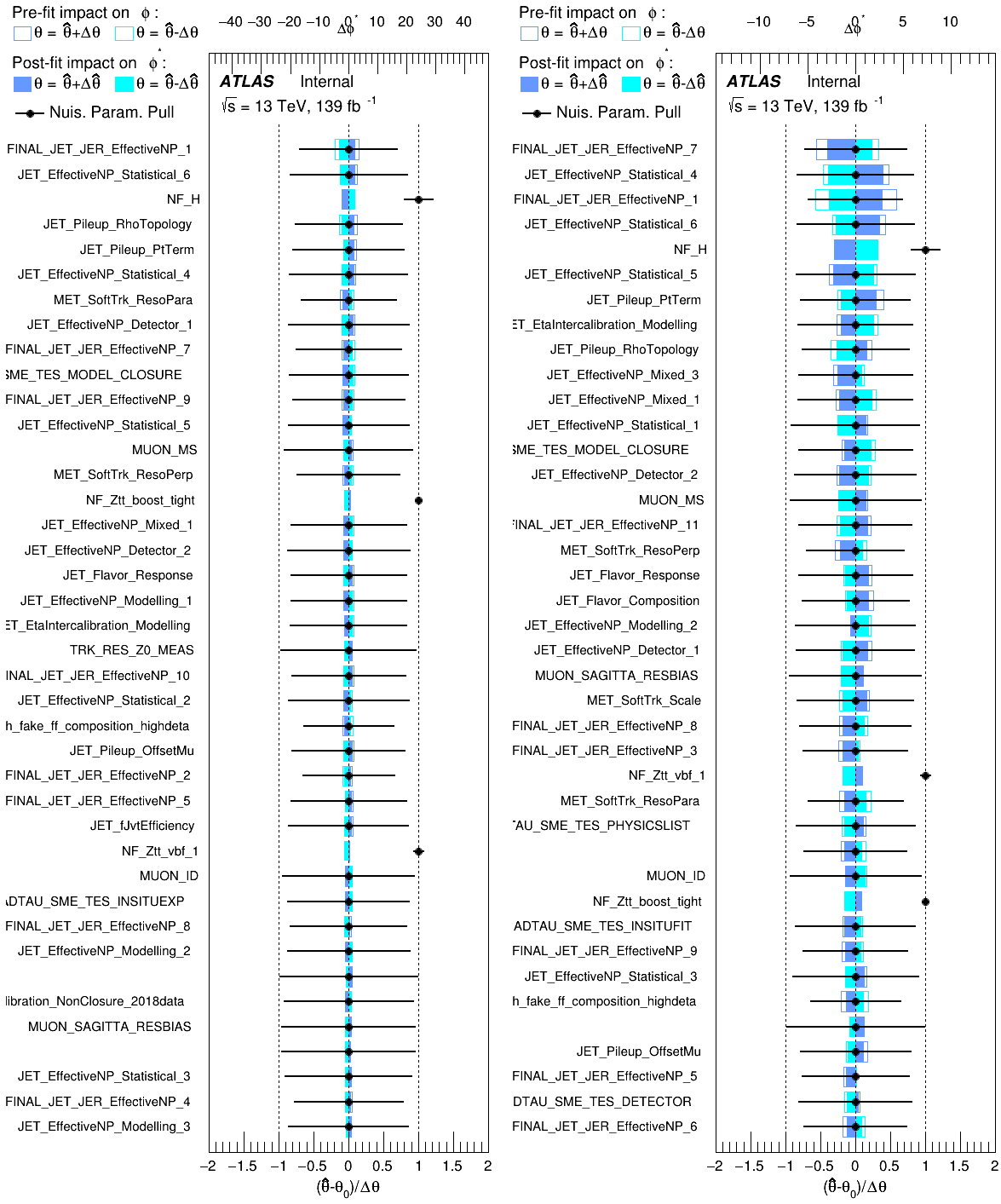

(a) CommonToolSmoothMonotonic **(b)** CommonToolSmoothParabolic

Figure 10.4.: The nuisance parameter rankings for the top 40 nuisance parameter for the (a) CommonToolSmoothMonotonic and (b) CommonToolSmoothParabolic smoothing algorithmns. Produced using Asimov data. Note the normalisation factors (beginning with NF_) are showing their values (around 1), not a pull of this value.

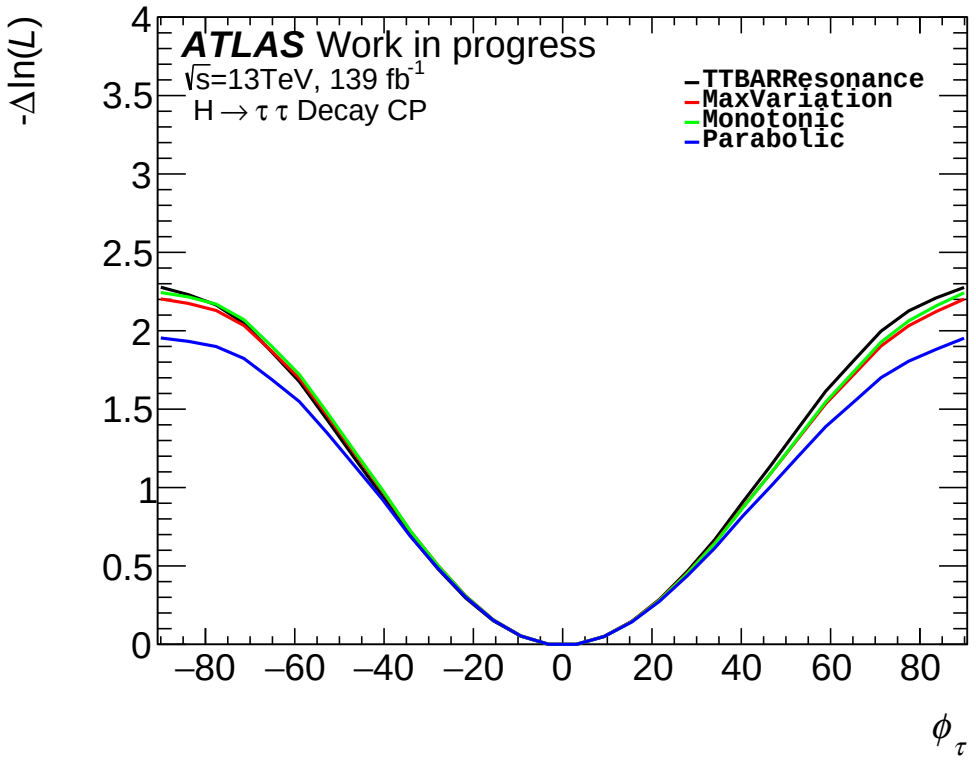

Figure 10.5.: A graph showing the negative log likelihood comparisons of four different smoothing algorithms (CommonToolSmoothMonotonic,CommonToolSmoothParabolic,MaxVariation,TTBARResonance) tested on Asimov datasets.

10.7. Symmetrisation

Symmetrisation reduces the chances of discontinuities in the interpolation, ensuring that it is differentiable and that the fit can proceed without issues. In addition, in situations where both the up and down envelopes lie on the same side of the nominal for individual bins, it can be used to ensure the size of the uncertainty of the envelopes is actually representative.

10.7.1. Symmetrisation Algorithms

TRExFitter provides a number of symmetrisation algorithms which are described below.

10.7.1.1. One-Sided

In the case of a one-sided systematic, where only one variation is provided(for example the up variation) a very simple symmetrisation algorithm is used where the mirrored variation on the other side of the nominal will be added (in this example the down variation).

10.7.1.2. Two-Sided

This takes the total size of the envelope and distributes it equally so the nominal lies in the centre of the two. Equation 10.10 takes the unmodified values for the up and down variation values, and the nominal value. It calculates the new value of the up variation and the difference between this new value and the nominal is then mirrored to obtain the value for the down variation (Equation 10.11).

$$\text{up} = \left[\frac{\left(\frac{\text{up}}{\text{nom}} - 1\right) - \left(\frac{\text{dn}}{\text{nom}} - 1\right)}{2} + 1 \right] \cdot \text{nom} \tag{10.10}$$

$$\mathrm{dn} = \mathrm{up} \tag{10.11}$$

10.7.1.3. Maximum

The maximum symmetrisation algorithm, compares the size of the up and down variations, which ever is bigger is set to both the variation for up and down envelopes. This behaviour is summarised in Equations 10.12 and 10.13.

$$\mathrm{up} = \begin{cases} \mathrm{up} & \left|\frac{\mathrm{up}}{\mathrm{nom}} - 1\right| \geq \left|\frac{\mathrm{dn}}{\mathrm{nom}} - 1\right| \\ \mathrm{dn} & \left|\frac{\mathrm{up}}{\mathrm{nom}} - 1\right| < \left|\frac{\mathrm{dn}}{\mathrm{nom}} - 1\right| \end{cases} \tag{10.12}$$

$$\mathrm{dn} = \mathrm{up} \tag{10.13}$$

10.7.1.4. Absolute

The Absolute symmetrisation uses the up and down variations and the nominal. Depending on certain conditions it symmetrises them differently. These conditions are summarised in Figure 10.6. This symmetrisation scheme was used by the $H \to \tau\tau$ coupling analysis. This algorithm is designed to handle situations where both the variations fall on the same side of the nominal better than either the "Two-Sided" or "Maximum" algorithms which can result in the inversion of the up and down variations of the uncertainties.

up=nom && dn=nom	up=up
up=nom && dn!=nom	$up = \left[\left(-1 \cdot \frac{dn-nom}{\lvert dn-nom\rvert}\right)\left(\frac{\lvert up-nom\rvert+\lvert dn-nom\rvert}{2}\right)\right] + nom$
(up-nom)(dn-nom)< 0	$up = \left[\left(\frac{up-nom}{\lvert up-nom\rvert}\right)\left(\frac{\lvert up-nom\rvert+\lvert dn-nom\rvert}{2}\right)\right] + nom$
$\lvert up - nom\rvert \geq \lvert dn - nom\rvert$	$up = \left[\left(\frac{up-nom}{\lvert up-nom\rvert}\right)\left(\frac{\lvert up-nom\rvert+\lvert dn-nom\rvert}{2}\right)\right] + nom$
else	$up = \left[\left(-1 \cdot \frac{up-nom}{\lvert up-nom\rvert}\right)\left(\frac{\lvert up-nom\rvert+\lvert dn-nom\rvert}{2}\right)\right] + nom$

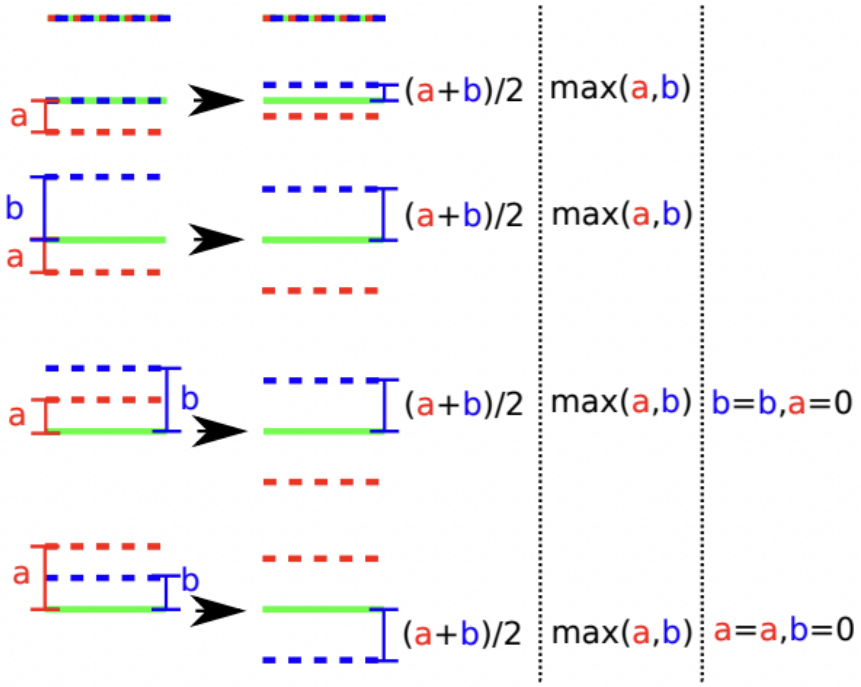

Figure 10.6.: A visual representation of the treatment of different scenarios involving the relative values of up and down envelopes to the nominal when using the "Absolute" symmetrisation algorithmn [142]

.

10.7.2. Symmetrisation Study

In the symmetrisation study, the "Onesided" algorithm is always used for NPs with onesided variation and "Absolute" and "Twosided" algorithms are compared. This study primarily focused on examining bins where problems were known to exist and understanding how both the Absolute and Twosided algorithms effected sign flips in various situations. The following are example thats all exhibit "same-sign errors" where both the up and down envelopes lie on the same side of the nominal (for at least one bin). Ensuring the correct behaviour of the algorithms when dealing with these kind of errors was essential to the symmetrisation study. In all the examples in Figures 10.7, 10.8, 10.9 and 10.10 smoothing has been turned off so the behaviour of the symmetrisation is more clear.

In the examples above, both Twosided and the Absolute correct the same sign errors, however Absolute will inflate the size of the envelope so that is a more reasonable size to represent the envelope pre-symmetrisation, this effect can be seen most clearly in Figure 10.10.

Ranking plots were generated for this study, as in the smoothing study. In this study their primary purpose is to spot any major differences between symmetrisation options, to understand if any groups of NPs are more significantly affected by symmetrisation than others. In Figure 10.11 the smoothing option used in the analysis has been reintroduced so the fit environment is closer to the fit environment used in the final analysis. While the Absolute option for the symmetrisation exhibits more NPs with larger impacts, this is an artifact of inflating the sizes of various envelopes for the reasons discussed previously. Neither ranking plot exihited any strange or unexpected behaviours and therefore they are both acceptable. This analysis therefore chose to proceed with the choice of "Onesided" symmetrisation for onesided NPs and "Absolute" for NPs with both up and down envelopes.

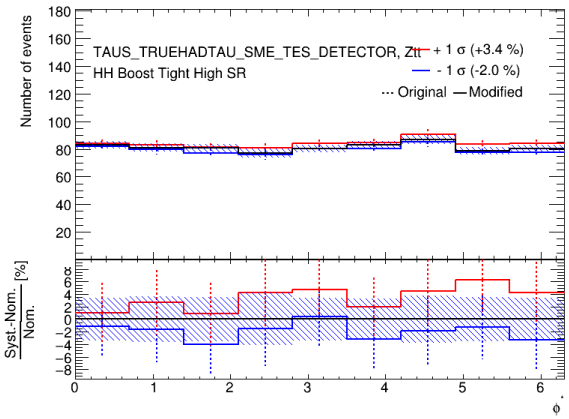

(a) No Symmetrisation

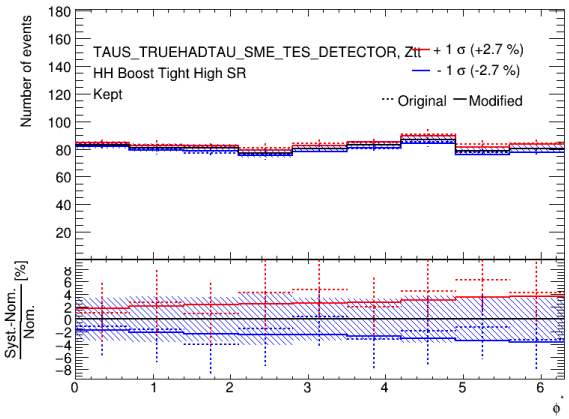

(b) Onesided/Twosided

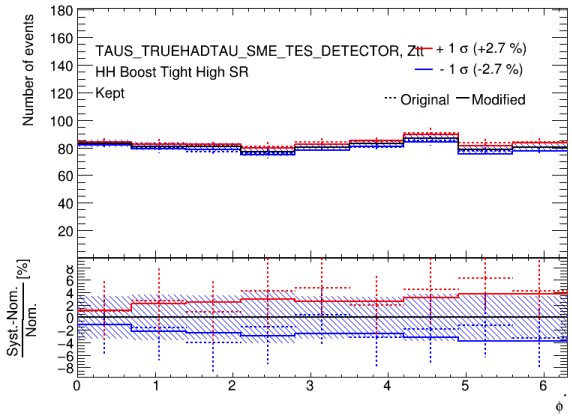

(c) Onesided/Absolute

Figure 10.7.: A comparison of different symmetrisation methods. There is a comparison to the unsymmetrised plot, then both of the symmetrisation algorithms use Onesided symmetrisation for NPs with only a single envelope defined (though not relevant to this plot) then for any NPs with both envelopes defined, either Twosided or Absolute symmetrisation is applied. No smoothing is applied to these plots so the differences due to symmetrisation are more obvious. These are all plotted for the NP "TAUS_TRUEHADTAU_SME_TES_DETECTOR"

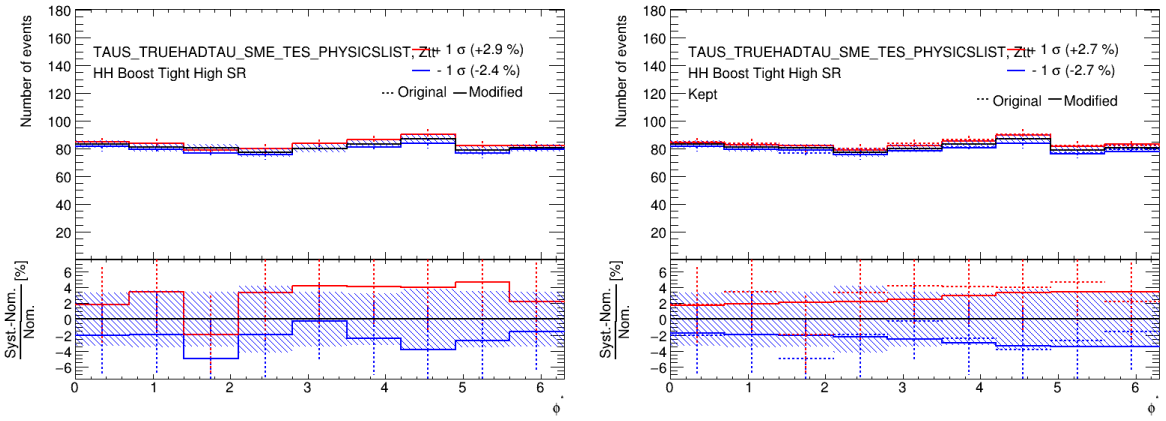

(a) No Symmetrisation

(b) Onesided/Twosided

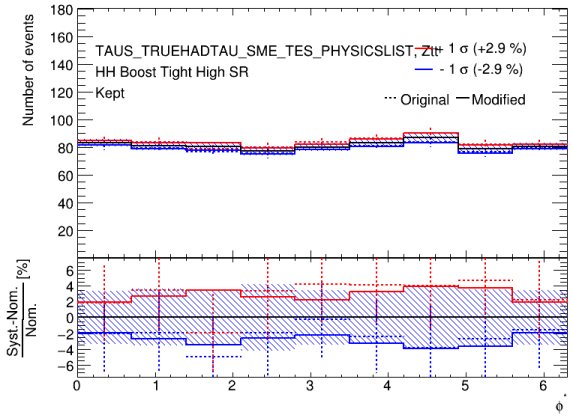

(c) Onesided/Absolute

Figure 10.8.: A comparison of different symmetrisation methods. There is a comparison to the unsymmetrised plot, then both of the symmetrisation algorithms use Onesided symmetrisation for NPs with only a single envelope defined (though not relevant to this plot) then for any NPs with both envelopes defined, either Twosided or Absolute symmetrisation is applied. No smoothing is applied to these plots so the differences due to symmetrisation are more obvious. These are all plotted for the NP "TAUS_TRUEHADTAU_SME_TES_PHYSICSLIST"

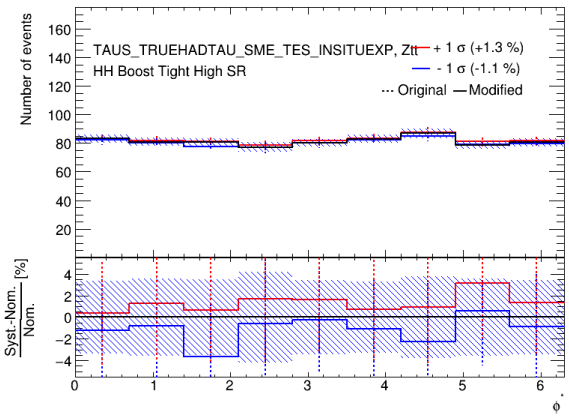

(a) No Symmetrisation

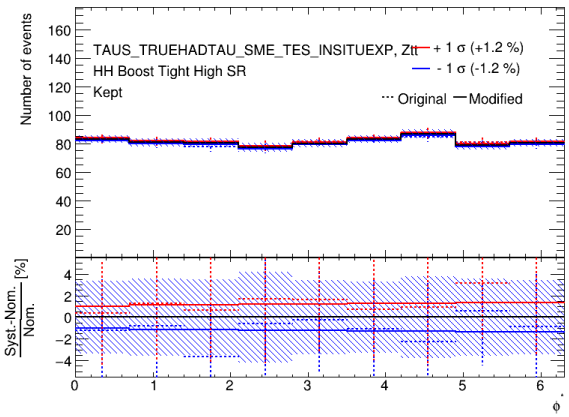

(b) Onesided/Twosided

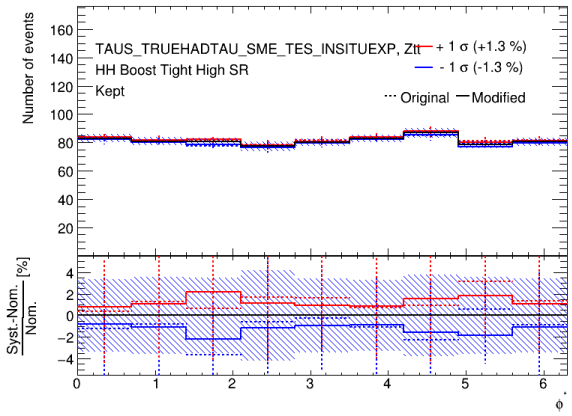

(c) Onesided/Absolute

Figure 10.9.: A comparison of different symmetrisation methods. There is a comparison to the unsymmetrised plot, then both of the symmetrisation algorithms use Onesided symmetrisation for NPs with only a single envelope defined (though not relevant to this plot) then for any NPs with both envelopes defined, either Twosided or Absolute symmetrisation is applied. No smoothing is applied to these plots so the differences due to symmetrisation are more obvious. These are all plotted for the NP "TAUS_TRUEHADTAU_SME_TES_INSITUEXP"

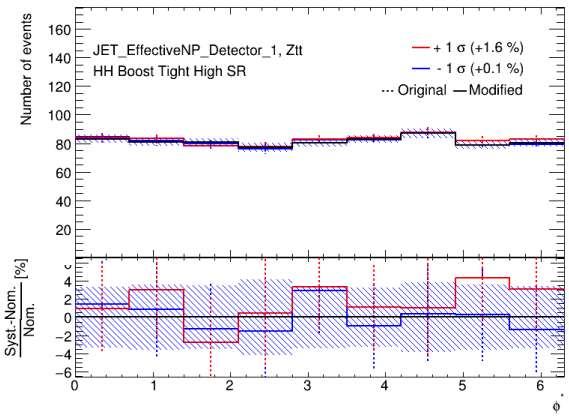

(a) No Symmetrisation

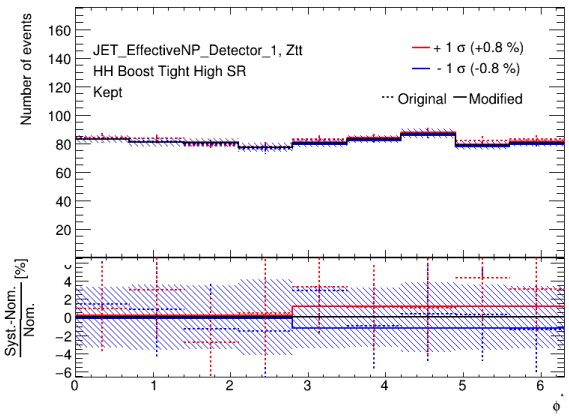

(b) Onesided/Twosided

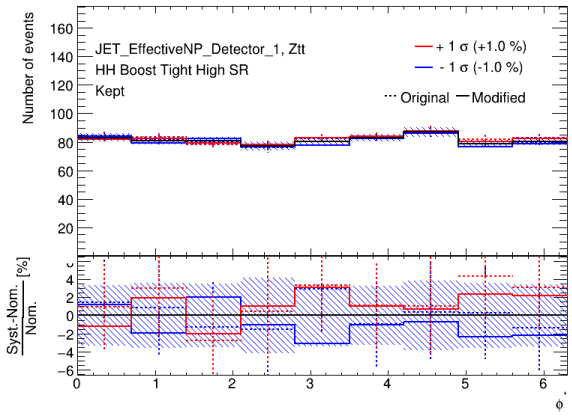

(c) Onesided/Absolute

Figure 10.10.: A comparison of different symmetrisation methods. There is a comparison to the unsymmetrised plot, then both of the symmetrisation algorithms use Onesided symmetrisation for NPs with only a single envelope defined (though not relevant to this plot) then for any NPs with both envelopes defined, either Twosided or Absolute symmetrisation is applied. No smoothing is applied to these plots so the differences due to symmetrisation are more obvious. These are all plotted for the NP "JET_EffectiveNP_Detector_1"

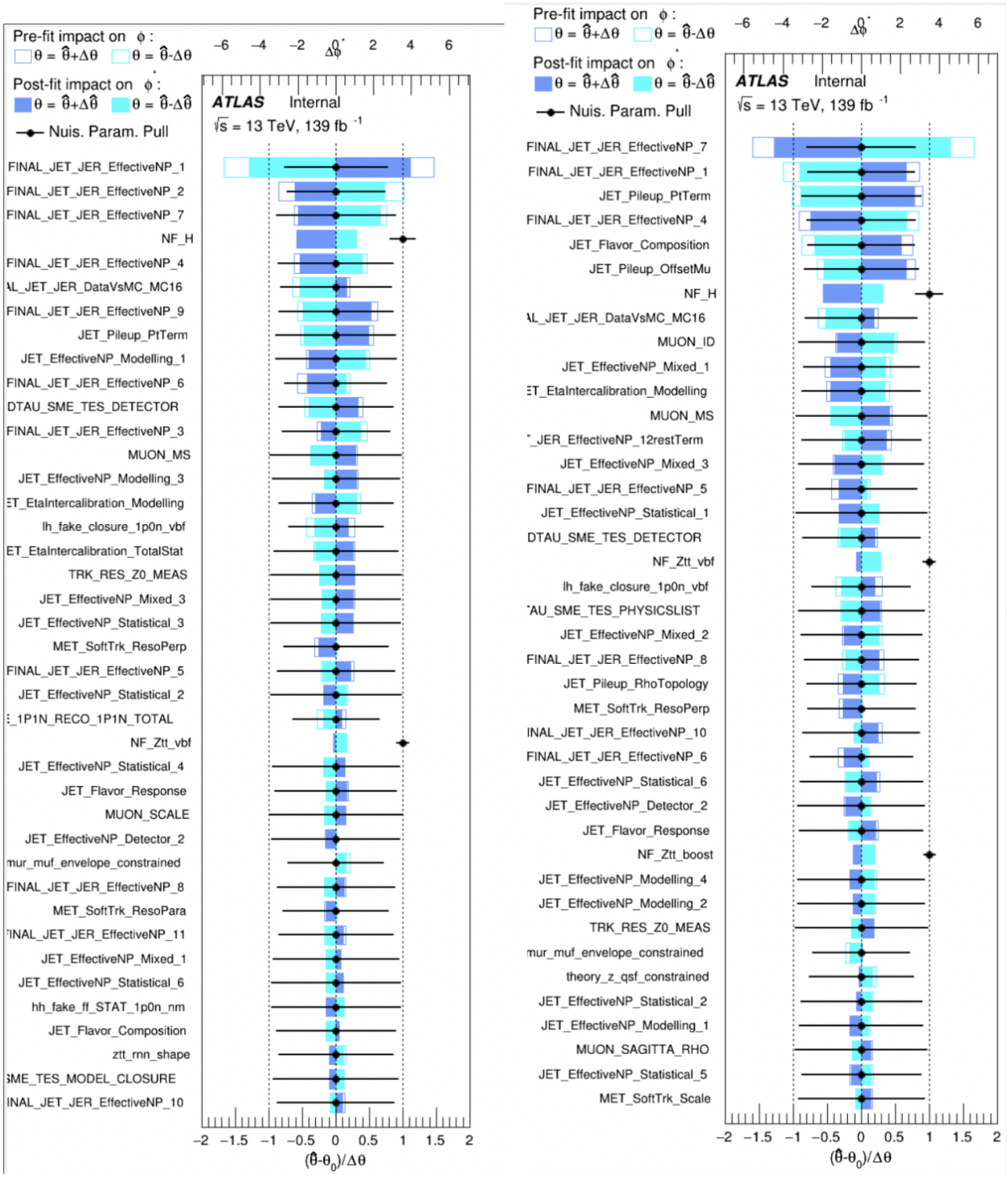

(a) Onesided/Twosided **(b)** Onesided/Absolute

Figure 10.11.: A comparison of NP ranking plots between the two symmetrisation options that were studied; the combinations Onesided/Twosided and Onesided/Absolute. Note the normalisation factors (beginning with NF_) are showing their values (around 1), not a pull of this value.

10.8. Pruning

During the pruning step, systematics that would have a low impact on the fit are dropped from the fit model, this simplifies the fitting process and allows it to run quicker however if a model is over-pruned there is the danger of ignoring non-negligible uncertainties. In an ideal world of infinite computing resources, all systematics would be included and processed by the fit model, however since this is not realistic, finding a balance between fit time and including all necessary uncertainties is paramount.

TRExFitter has two variables that can be tuned, SystPruningShape and SystPruningNorm. The former sets the threshold for pruning shape systematics and the latter sets the threshold for normalisation systematics. For the purposes of this study, SystPruningShape is investigated.

Figure 10.12 shows that as the pruning threshold decreases, the sensitivity decreases. One might naively assume that therefore, increasing the threshold is better, however as mentioned previously, this increase in sensitivity is simply an artifact of not being constrained by more nuisance parameters which are not negligible. There is an dramatic increase in sensivity when the threshold is raised above $\sim$0.01 - 0.015 this implies this is the threshold for overpruning. There is also not much reduction seen in sensitivity by lowering the threshold below $\sim$0.01, implying that NPs that would be included by lowering this threshold have a negligible impact on the fit result.

The next metric to consider was how long the fits would take, while choosing a lower threshold would incorporate more of the nuisance parameters it would also take much longer to run. Being able to run multiple fits in a reasonable time frame is also an important consideration. In order to investigate the time taken for the fits to run, the fits were run on Condor on the CERN lxplus server in parallel. While not perfect this means that each of the jobs is running on a machine that is roughly under the same load, since the load can vary from day to day. Three metrics of time were measured. Real, User and Sys Time. Real Time is the time it takes from start to end of the process as the user experiences it, User measures the amount of time spent running user defined code and any libraries it needs to run (not including any time the process spent blocked) and Sys is the time spent running kernel level operations for the process to run. For the purposes of this investigation, the theoretical minimum time the process could run in is Sys Time + User Time. The Real time can be great

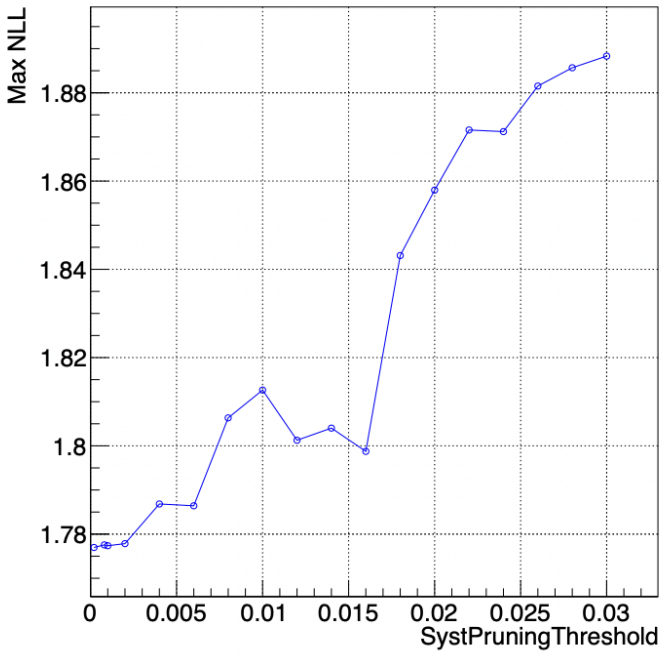

Figure 10.12.: Max NLL as a function of SystPruningShape (here labelled SystPruningThreshold). The graph shows as the value of SystPruningShape is increased the value of the the Maximum Negative Log Likelihood increases.

affected by the load on the server and is therefore more variable than the other two metrics. Figure 10.13 shows a comparison of all three time metrics, these all start to show marked increased in time taken when the threshold is reduce below 0.01.

The value for SystPruningShape of 0.01 was settled on. This value provided a suitable balance between speed and keeping necessary NPs so as to not introduce over-pruning, any lower a threshold would result in the time taken to run growing exponentially, but if the threshold was much higher we would be falsely raising the sensitivity.

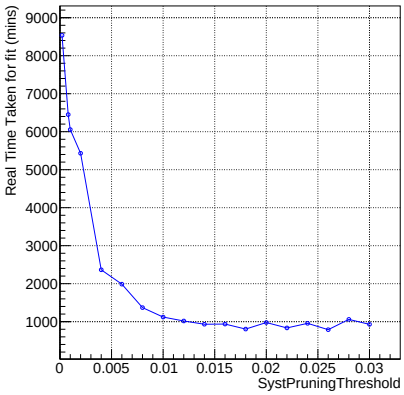

(a) Real Time

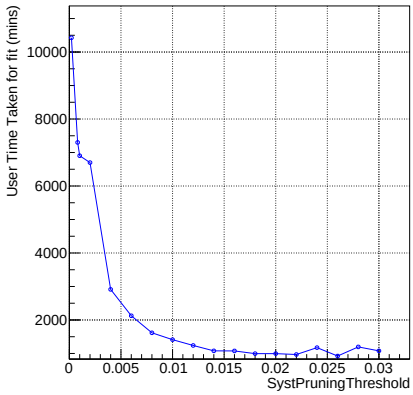

(b) User Time

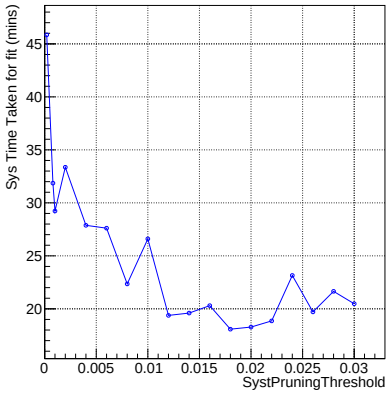

(c) Sys Time

Figure 10.13.: Three graphs showing how the time taken to run the fit increases as the value of SystPruningShape decreases (here labelled SystPruningThreshold). The three graphs show different ways of measuring time using the Unix "time" command, Real, User and Sys.

Chapter 11.

Results

11.1. Fit Model

The main observable of this analysis is φ^*_{CP}, it is from this observable that the CP mixing angle ϕ_τ is estimated. This estimation is done through the use of a Maximum Likelihood fit performed using the TReXFitter Package [143] with the support of other packages for specific tasks including Histfactory [144], RooFit [145] and RooStats [146].

The fit uses 24 signal regions and 10 normalisation regions, these are described in Section 8.5 and summarised below. In each signal region the φ^*_{CP} templates for multiple decay modes are merged. The control regions are used to constrain the normalisation for background processes or constrain uncertainties related to the neutral pion. Nuisance parameters are used to insert the systematic uncertainties into the fit.

In signal regions, the entire φ^*_{CP} distribution is used by the Maximum Likelihood fit, whereas in the ZCR a single-bin histograms are used to extract the normalisation factor of $Z \to \tau\tau$ or ρ mass distributions for constraining of the π^0 uncertainties. It should also be noted that the signal normalisation is not constrained and is not used in the estimation of ϕ_τ, only the shape of the distribution is used.

- Signal Regions(12SR for each τ_{lep}-$\tau_{\text{had}}$and τ_{had}-τ_{had}channels)
  - VBF 1, High, Medium, Low
  - VBF 0, High, Medium, Low
  - Boost 1, High, Medium, Low

  - Boost 0, High Medium, Low

- Z($\rightarrow \tau^+\tau^-$)+ jets control regions (4CR for each τ_{lep}-$\tau_{\text{had}}$and τ_{had}-τ_{had}channels)
  - VBF 1
  - VBF 0
  - Boost 1
  - Boost 0
- ρ constraint Z($\rightarrow \tau^+\tau^-$)+jets control regions
  - Inclusive ℓ-1p1n or 1p1n-1p1n

Five normalisation factors are left free-floating in specific regions to allow them to be determined by the fit, these determine the normalisation of signal $H \rightarrow \tau\tau$ and the background $Z \rightarrow \tau\tau$. The four normalisation factors are:

- NF H
- NF Ztt VBF 1
- NF Ztt VBF 0
- NF Ztt Boost 1
- NF Ztt Boost 0

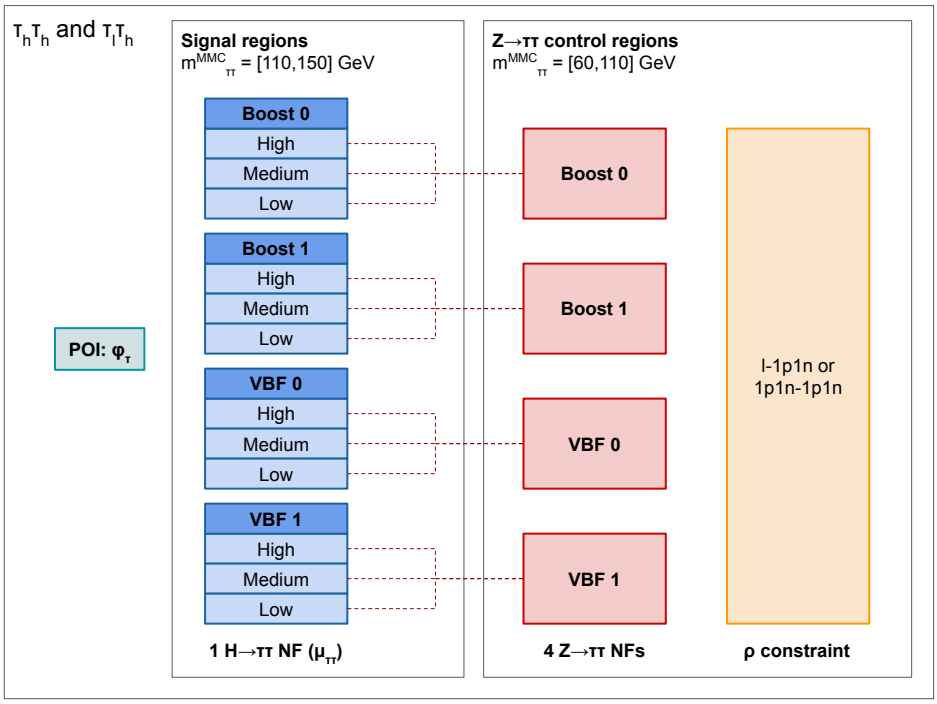

Figure 11.1.: A diagram summarising the fit model for the analysis [67]

11.1.1. CP Templates

In this analysis, the binned likelihood function uses a series of nineteen templates each corresponding to intevals of 10° in ϕ_τ added to the expected background. ϕ_τ has been constructed in such a way that when $\phi_\tau = 0^\circ$ corresponds to the Standard Model, CP-even Higgs, where as $\phi_\tau = \pm 90^\circ$ corresponds to a full CP-odd Higgs, with values between this indicating a mixture of states. The likelihood function used in this analysis is a product of Poisson probability terms, each term corresponding a different bin of the observable φ^*_{CP}. A one-dimensional morphing with linear interpolation [147] is used to create a continuous distribution of ϕ_τ from the discrete distribution created in the fit.

The templates used in this analysis were created using CP-flat distributions of signal samples of $H \to \tau\tau$ events from all production sources (VBFH, ggH, VH, and ttH) then reweighting them for the different mixing angles needed to construct the templates using TAUSPINNER [82].

11.1.2. Treatment of Nuisance Parameters

11.1.2.1. General Setup

The normalisations of the CP-even and CP-mixed signal samples and the Z$\rightarrow \tau\tau$ are all introduced into the fit as unconstrained nuisance parameters. The other nuisance parameters describe the experimental and theoretical uncertainties discussed in Section 10, these enter the fit with either Gaussian or Log-Normal constraints. The up and down variations of the NPs use the +1σ -1σ variations of the input histograms. The statistical uncertainty of the MC templates are also included as nuisance parameters with a Poisson constraint and a nominal value of 1.

11.1.2.2. Symmetrisation

Symmetrisation studies that inform the choices stated here are dicussed in Section 10.7. Symmetrisation is applied to the +1σ -1σ variations. The Trexfitter "Absolute" algorithm is applied to all nuisance parameters except those where only one variation is supplied. The one-sided nuisance parameters used in the fit are: ztt_rnn_shape, theory_sig_pdf_[0-29], theory_sig_qcd_[0-8]_ggH, theory_z_MMHT_pdfset, theory_z_CT14_pdfset, hh_fake_ff_*, lh_fake_*, MET_SoftTrk_ResoPara and MET_SoftTrk_ResoPerp. If the symmetrisation proceedure results in a negative bin the yield is set to a tiny value (1E-6).

11.1.2.3. Smoothing

For a full discussion of the smoothing proceedure used in this analysis, see Section 10.6, this analysis uses the TRExFitter smoothing algorithmn "MAXVARIATION" for smoothing the nuisance parameters.

11.1.2.4. Pruning

For a full discussion on reasoning for the choice of pruning threshold, see Section 10.8. A nuisance parameter is pruned away if the total yield (shape) systematic variation, is below 1 %.

11.1.3. Pre-fit Distribution

This section shows the distributions which are fed into the likelihood fit along with the systematic distributions that have been treated through the various stages (symmetrisation, smoothing and pruning). Most signal regions are binned with 9 bins in φ^*_{CP}, with a few exceptions. Both the VBF 1, High and Medium regions are binned to only 7 bins due to sample size restrictions and all Low regions are binned to 4 bins due to their low sensitivity. All 8 control regions are binned to a single bin, since these are used to just extract the yield, not the shape information, for the construction of normalisation factors. Finally the two ρ mass distributions, using just ℓ-1p1n and 1p1n-1p1n decay modes, these are binned with 11 bins.

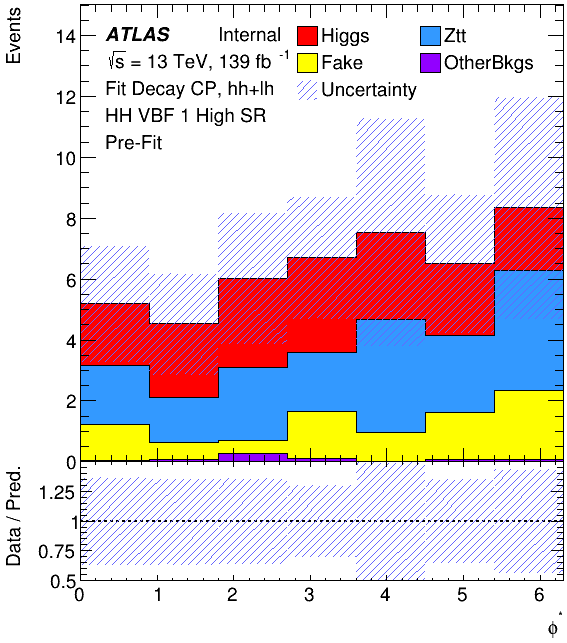

(a) $\tau_{had}\tau_{had}$VBF 1 high sr

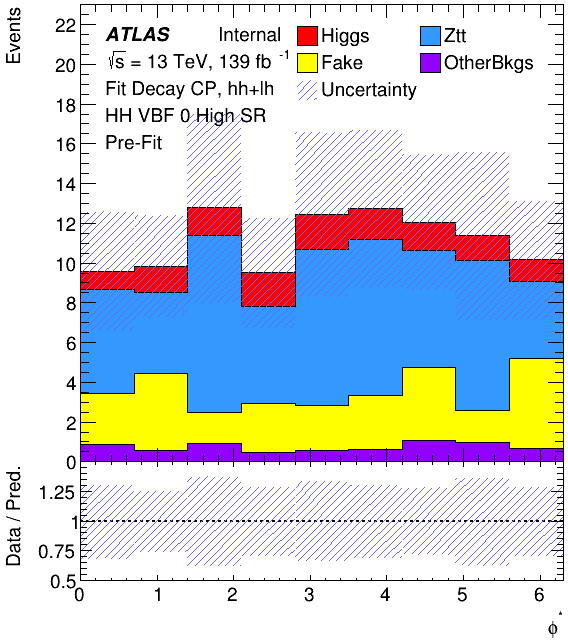

(b) $\tau_{had}\tau_{had}$VBF 0 high sr

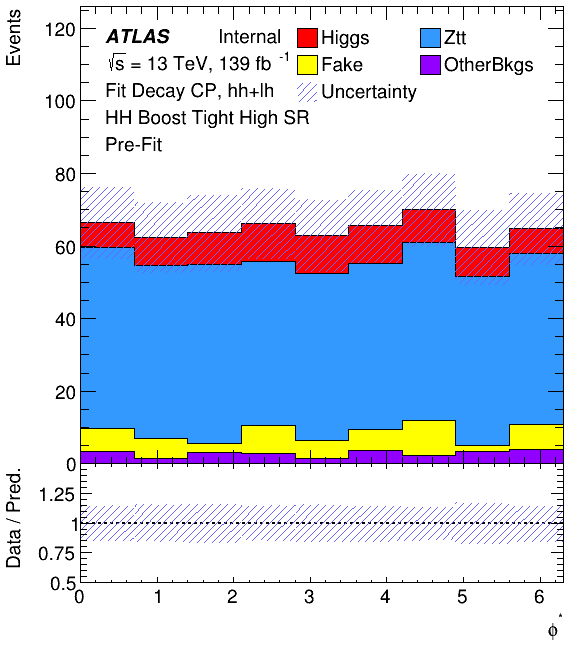

(c) $\tau_{had}\tau_{had}$Boost 1 high sr

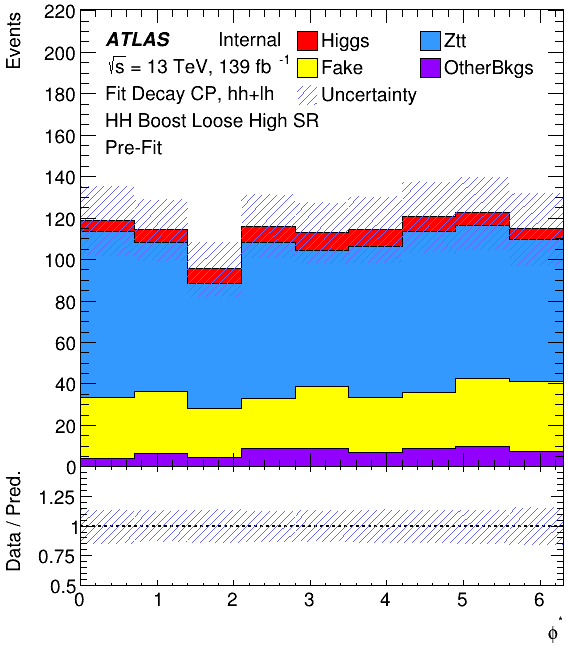

(d) $\tau_{had}\tau_{had}$Boost 0 high sr

Figure 11.2.: The prefit distributions for the $\tau_{had} - \tau_{had}$ channel in the Higgs $\rightarrow \tau\tau$ signal regions within the "high" signal optimisation region. The category "OtherBkgs" such as W, diboson,top, $Z \rightarrow ll$ and $H \rightarrow WW$.

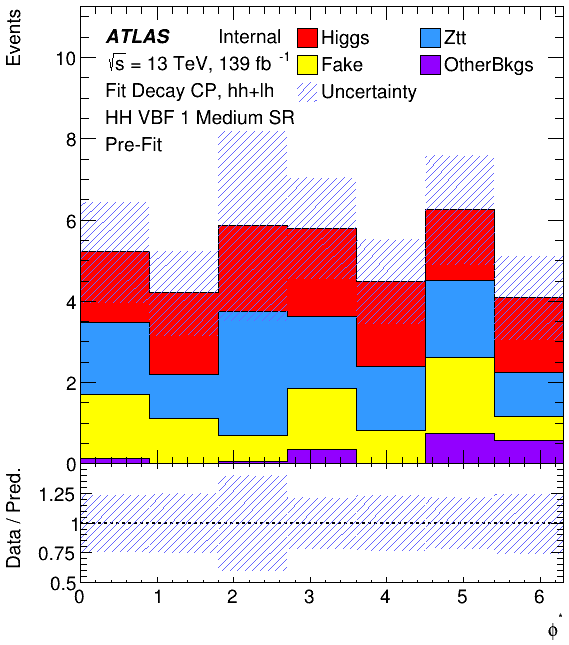

(a) $\tau_{had}\tau_{had}$VBF 1 medium sr

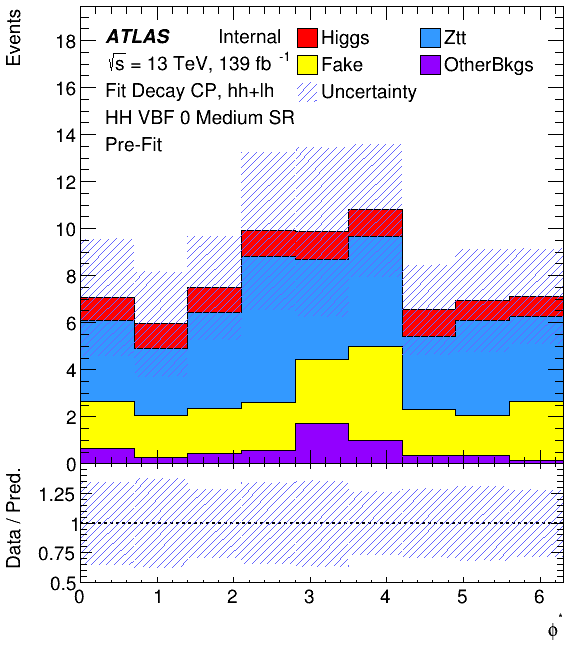

(b) $\tau_{had}\tau_{had}$VBF 0 medium sr

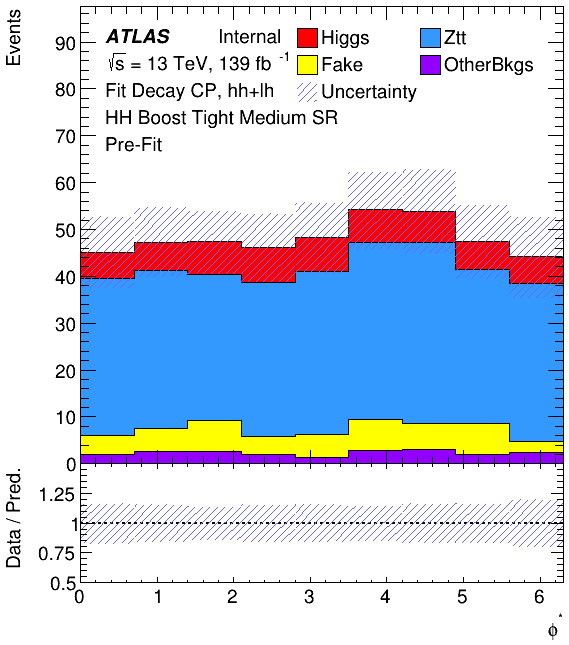

(c) $\tau_{had}\tau_{had}$Boost 1 medium sr

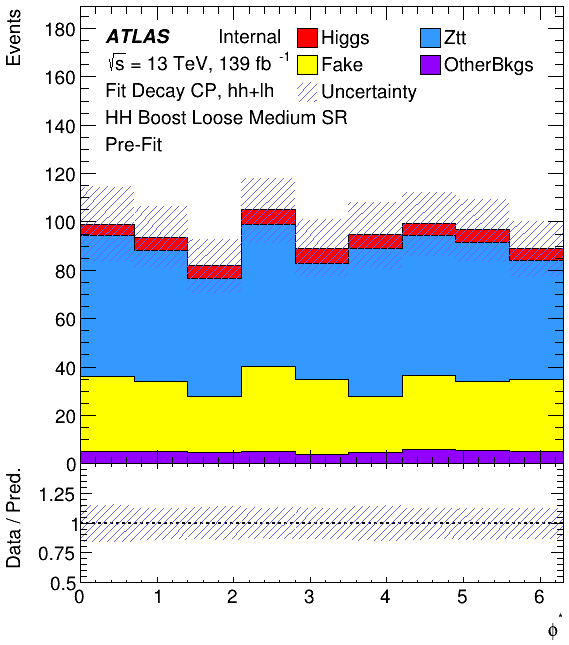

(d) $\tau_{had}\tau_{had}$Boost 0 medium sr

Figure 11.3.: The prefit distributions for the $\tau_{had} - \tau_{had}$ channel in the Higgs $\rightarrow \tau\tau$ signal regions within the "medium" signal optimisation region. The category "OtherBkgs" such as W, diboson,top, $Z \rightarrow ll$ and $H \rightarrow WW$.

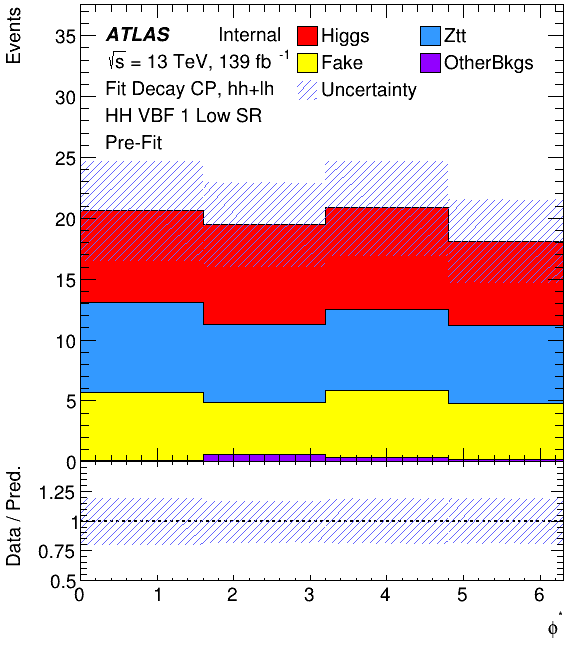

(a) $\tau_{had}\tau_{had}$VBF 1 low sr

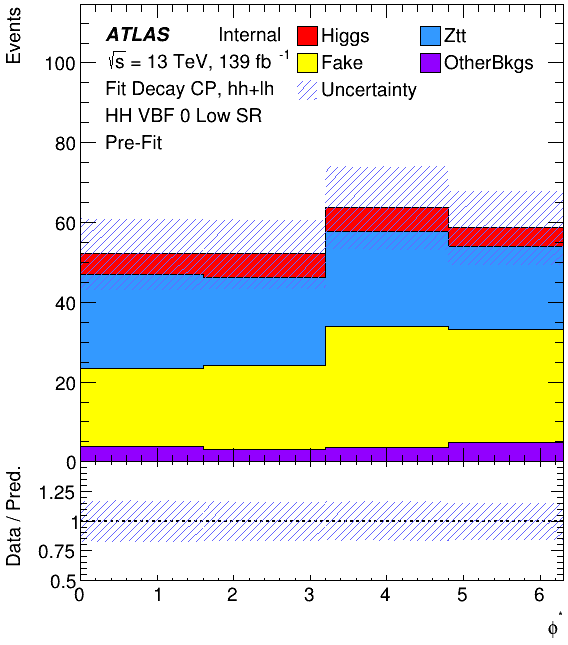

(b) $\tau_{had}\tau_{had}$VBF 0 low sr

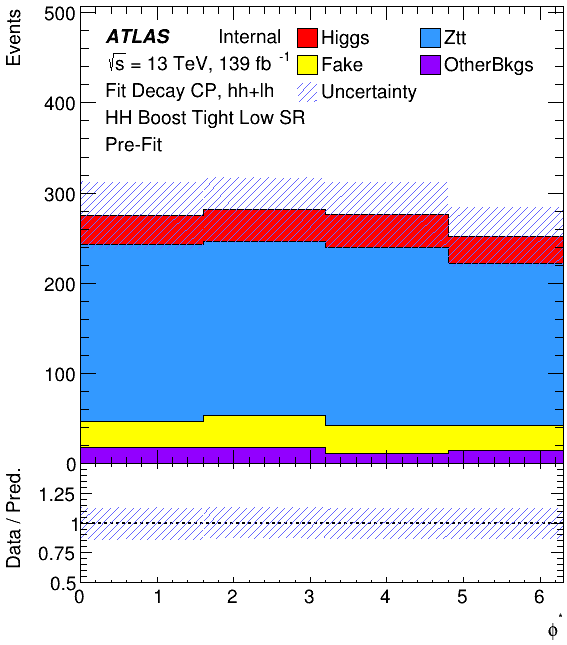

(c) $\tau_{had}\tau_{had}$Boost 1 low sr

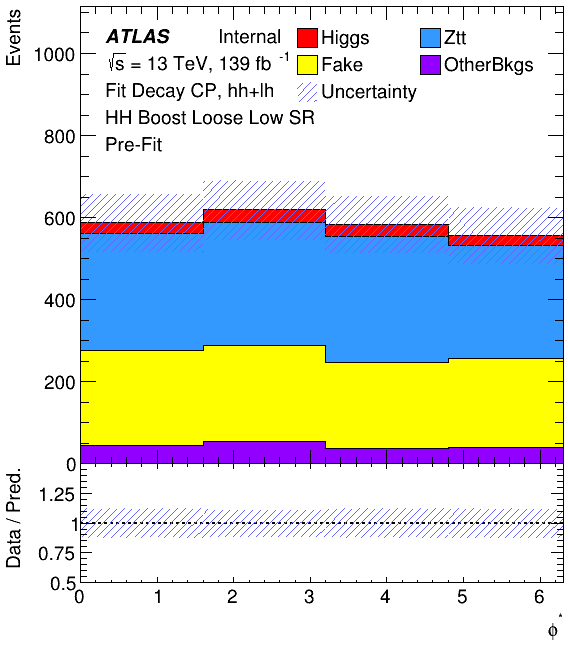

(d) $\tau_{had}\tau_{had}$Boost 0 low sr

Figure 11.4.: The prefit distributions for the $\tau_{had} - \tau_{had}$ channel in the Higgs $\rightarrow \tau\tau$ signal regions within the "low" signal optimisation region. The category "OtherBkgs" such as W, diboson,top, $Z \rightarrow ll$ and $H \rightarrow WW$.

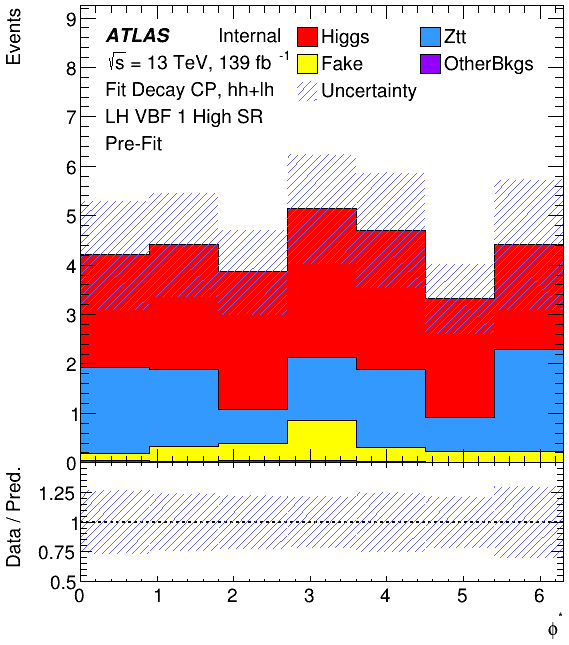

(a) $\tau_{lep}\tau_{had}$ VBF 1 high sr

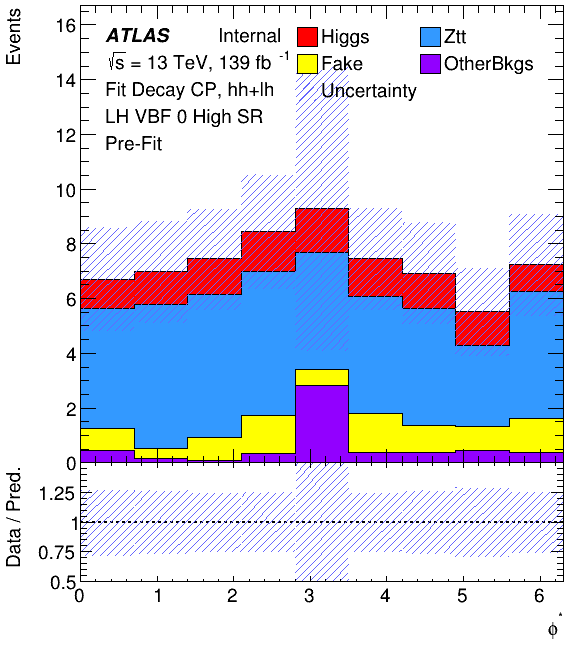

(b) $\tau_{lep}\tau_{had}$ VBF 0 high sr

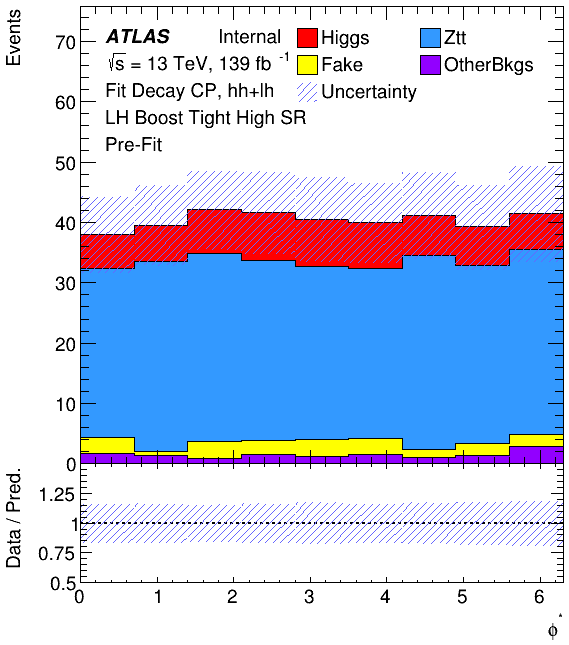

(c) $\tau_{lep}\tau_{had}$ Boost 1 high sr

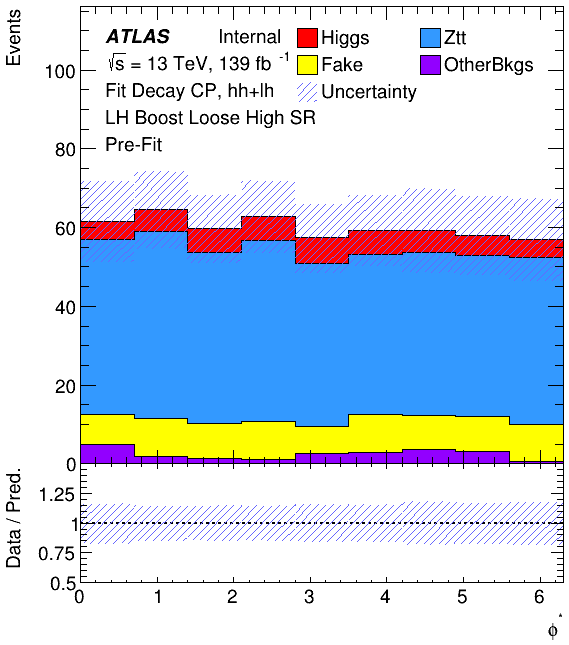

(d) $\tau_{lep}\tau_{had}$ Boost 0 high sr

Figure 11.5.: The prefit distributions for the $\tau_{lep} - \tau_{had}$ channel in the Higgs $\rightarrow \tau\tau$ signal regions within the "high" signal optimisation region. The category "OtherBkgs" such as W, diboson,top, $Z \rightarrow ll$ and $H \rightarrow WW$.

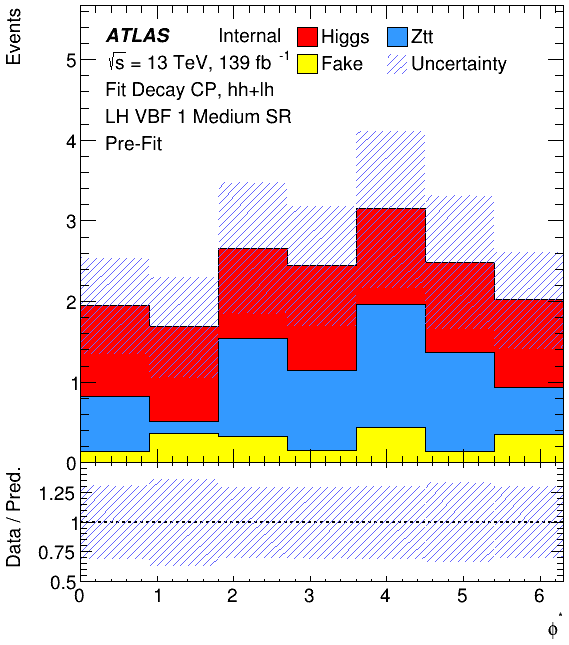

(a) $\tau_{\text{lep}}\tau_{\text{had}}$VBF 1 medium sr

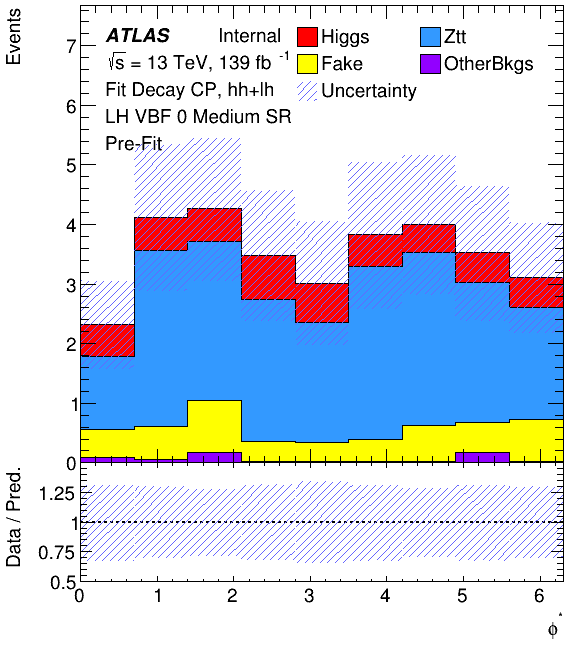

(b) $\tau_{\text{lep}}\tau_{\text{had}}$VBF 0 medium sr

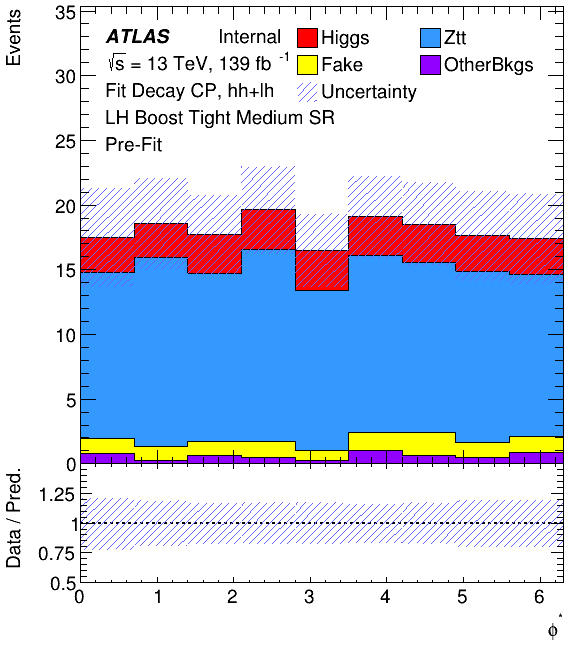

(c) $\tau_{\text{lep}}\tau_{\text{had}}$Boost 1 medium sr

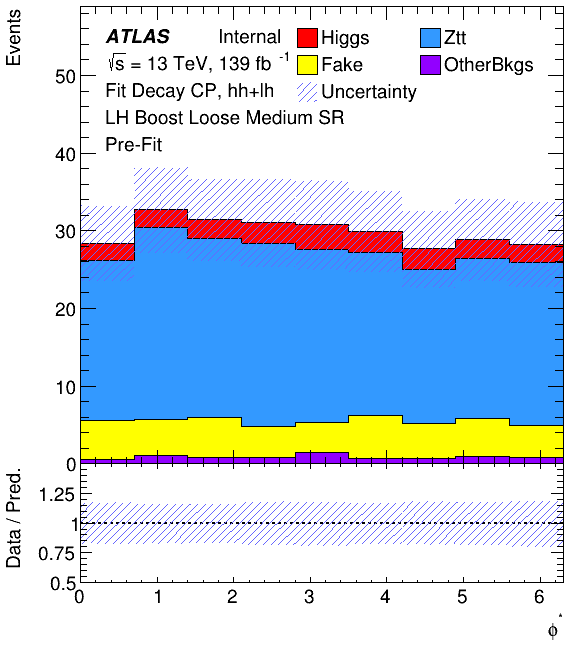

(d) $\tau_{\text{lep}}\tau_{\text{had}}$Boost 0 medium sr

Figure 11.6.: The prefit distributions for the $\tau_{\text{lep}} - \tau_{\text{had}}$ channel in the Higgs $\rightarrow \tau\tau$ signal regions within the "medium" signal optimisation region. The category "OtherBkgs" such as W, diboson,top, $Z \rightarrow ll$ and $H \rightarrow WW$.

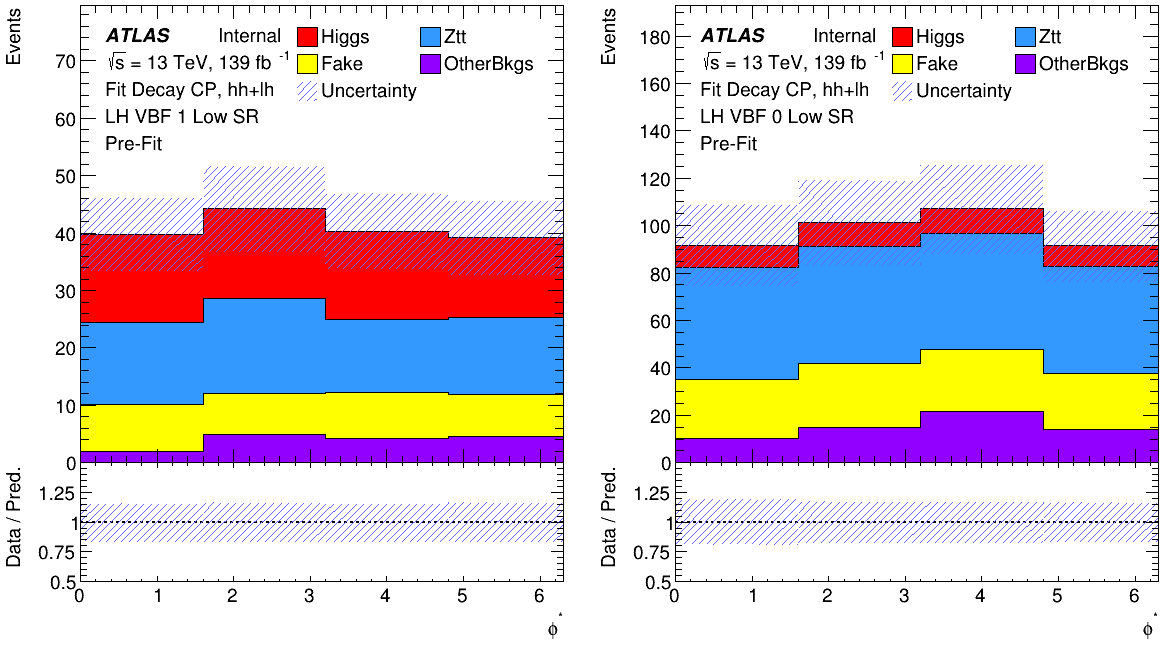

(a) $\tau_{lep}\tau_{had}$VBF 1 low sr

(b) $\tau_{lep}\tau_{had}$VBF 0 low sr

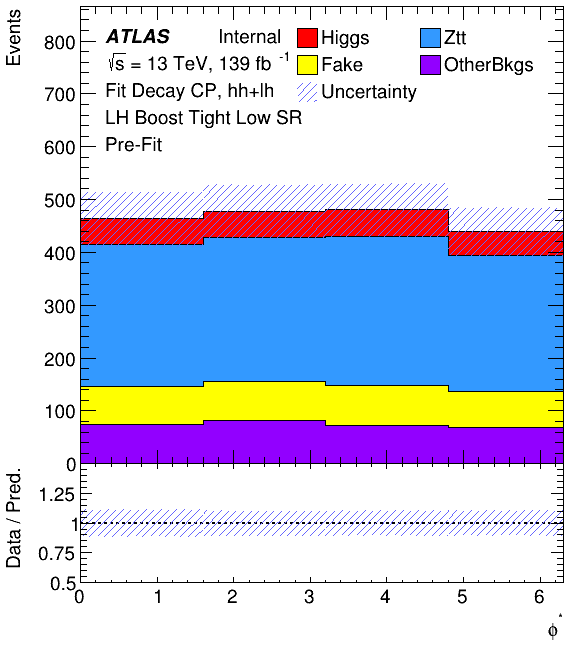

(c) $\tau_{lep}\tau_{had}$Boost 1 low sr

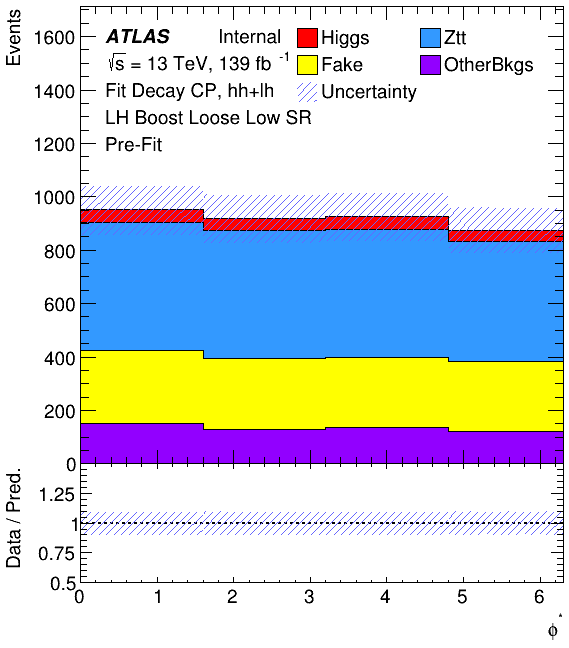

(d) $\tau_{lep}\tau_{had}$Boost 0 low sr

Figure 11.7.: The prefit distributions for the $\tau_{lep} - \tau_{had}$ channel in the Higgs $\rightarrow \tau\tau$ signal regions within the "low" signal optimisation region. The category "OtherBkgs" such as W, diboson,top, $Z \rightarrow ll$ and $H \rightarrow WW$.

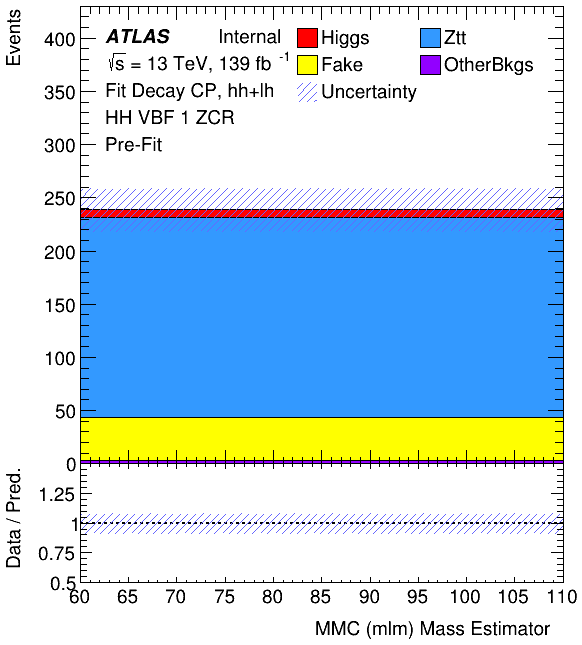

(a) $\tau_{had}\tau_{had}$VBF 1 CR Z$\rightarrow \tau\tau$

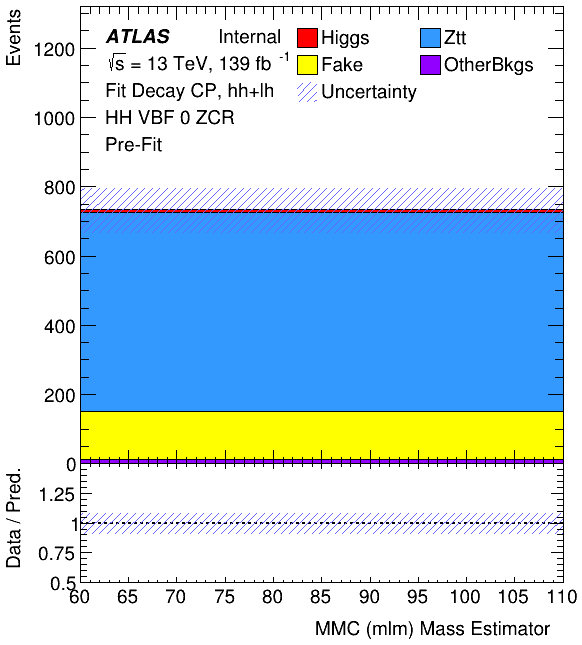

(b) $\tau_{had}\tau_{had}$VBF 0 CR Z$\rightarrow \tau\tau$

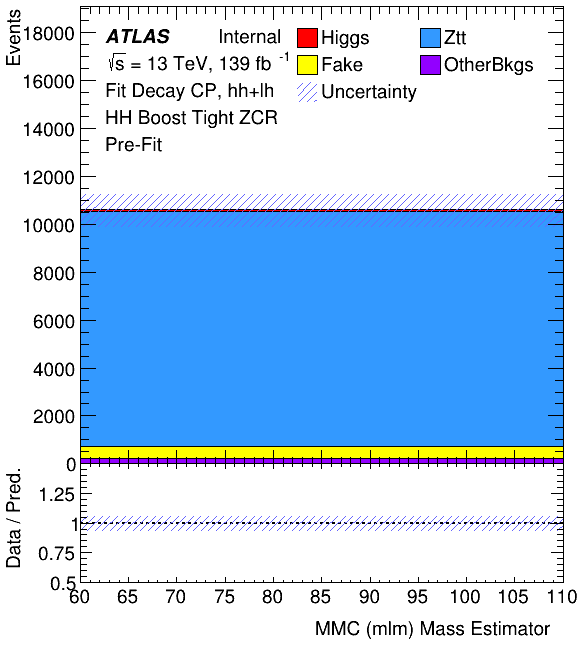

(c) $\tau_{had}\tau_{had}$Boost 1 CR Z$\rightarrow \tau\tau$

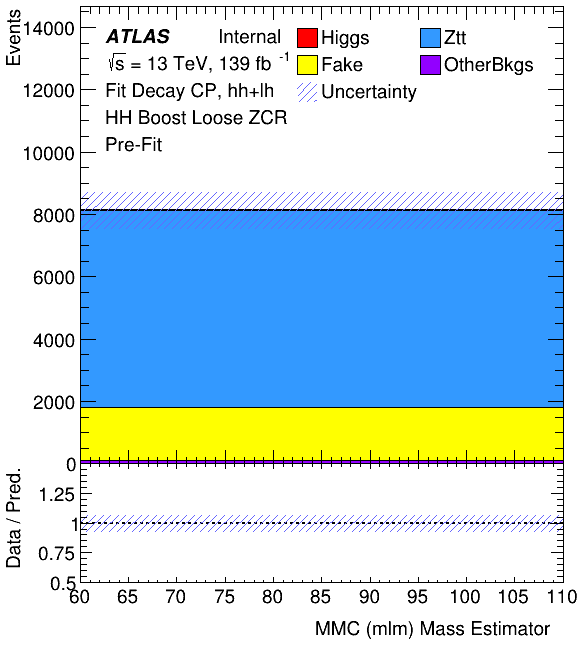

(d) $\tau_{had}\tau_{had}$Boost 0 CR Z$\rightarrow \tau\tau$

Figure 11.8.: The prefit distributions for the $\tau_{had} - \tau_{had}$ channel in the $Z \rightarrow \tau\tau$ control region (ZCR). The category "OtherBkgs" such as W, diboson,top, $Z \rightarrow ll$ and $H \rightarrow WW$.

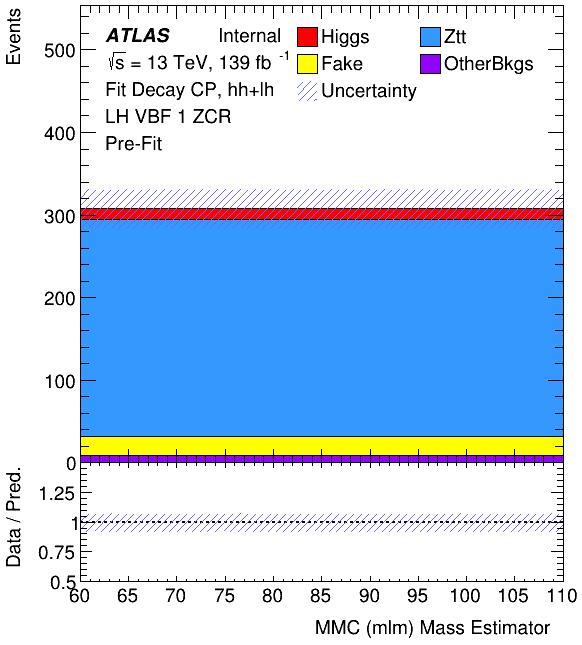

(a) $\tau_{\text{lep}}\tau_{\text{had}}$VBF 1 CR Z$\rightarrow \tau\tau$

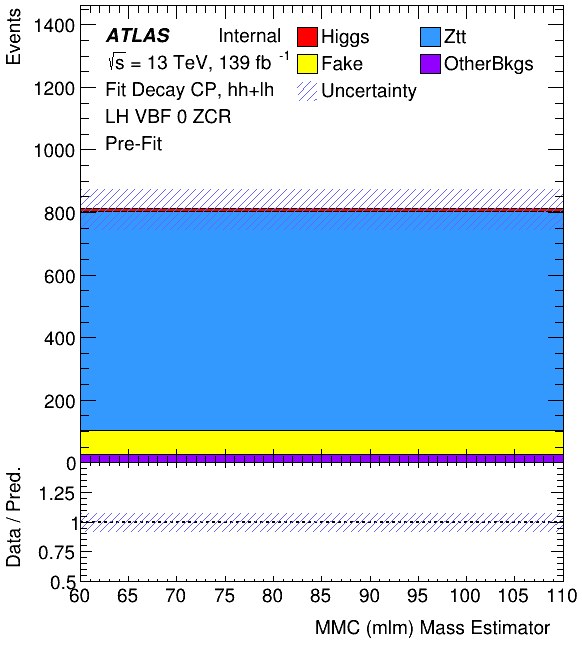

(b) $\tau_{\text{lep}}\tau_{\text{had}}$VBF 0 CR Z$\rightarrow \tau\tau$

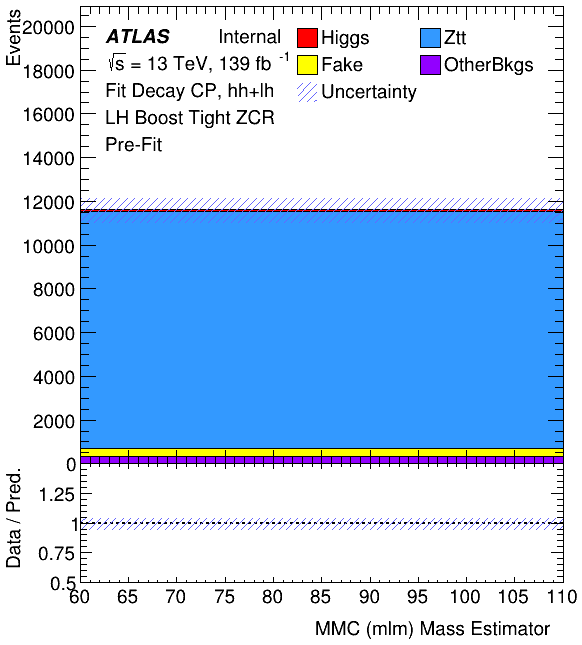

(c) $\tau_{\text{lep}}\tau_{\text{had}}$Boost 1 CR Z$\rightarrow \tau\tau$

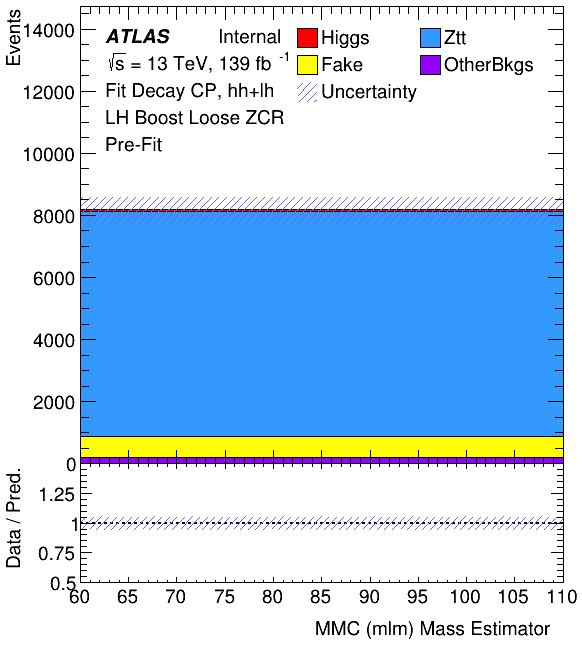

(d) $\tau_{\text{lep}}\tau_{\text{had}}$Boost 0 CR Z$\rightarrow \tau\tau$

Figure 11.9.: The prefit distributions for the $\tau_{\text{lep}} - \tau_{\text{had}}$ channel in the $Z \rightarrow \tau\tau$ control region (ZCR). The category "OtherBkgs" such as W, diboson,top, $Z \rightarrow ll$ and $H \rightarrow WW$.

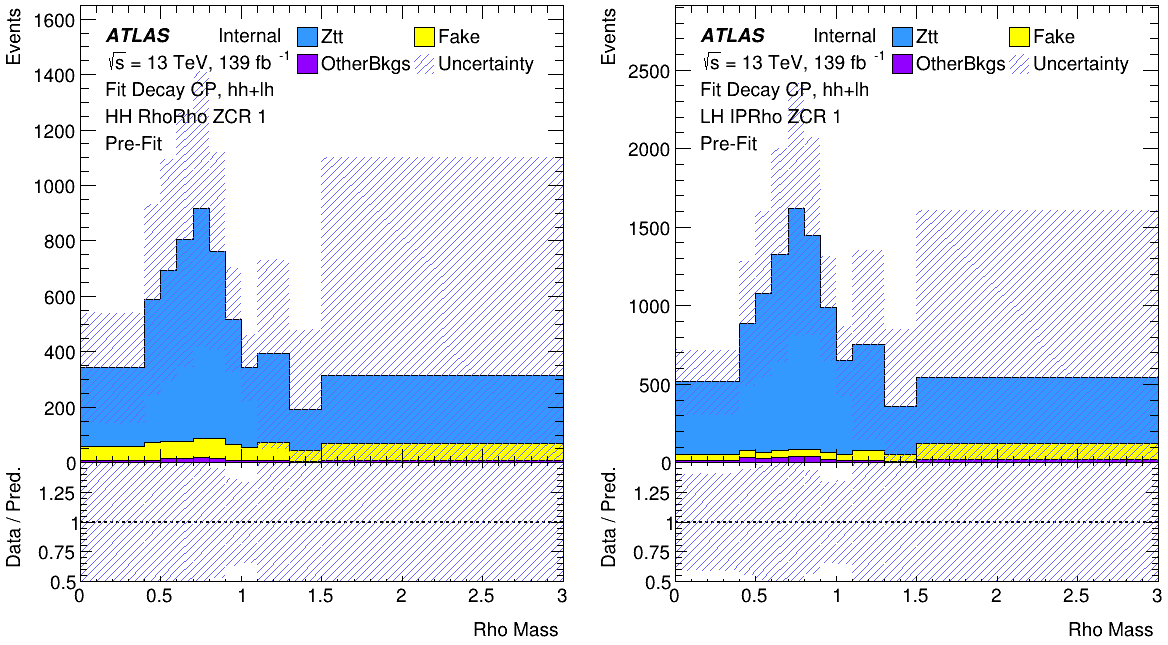

(a) $\tau_{\text{had}}\tau_{\text{had}}$1p1n-1p1n CR Z$\to \tau\tau$ **(b)** $\tau_{\text{lep}}\tau_{\text{had}}\ell$-1p1n CR Z$\to \tau\tau$

Figure 11.10.: The prefit distributions for the $\tau_{\text{had}} - \tau_{\text{had}}$ 1p1n-1p1n and $\tau_{\text{lep}} - \tau_{\text{had}}$ *ell*-1p1n in $Z \to \tau\tau$ control region (ZCR). The category "OtherBkgs" such as W, diboson,top, $Z \to ll$ and $H \to WW$.

11.2. Quantifying Sensitivity

The binned likelihood function $\mathcal{L}(\mathbf{x}; \phi_\tau, \theta)$ is a function of the data $\mathbf{x}$, the mixing angle ϕ_τ which is left free floating and the nuisance parameters, θ which are how the systematic uncertainties, discussed in Chapter 10, enter the fit. It uses the weighted signal templates defined in Section 11.1.1 to evaluate the likelihood function at different ϕ_τ intervals leaving the background unchanged. The test statistic used for this parameter is the Negative Log Likelihood (NLL). This metric provides a measure how far the observed data and expected data deviate from one another at different values of ϕ_τ to construct the NLL Curve. This test statistic can be constructed as a function of ϕ_τ using the Equation 11.1 [148].

$$q = -2 \ln \frac{\mathcal{L}(\vec{\kappa}, \hat{\hat{\vec{\theta}}}(\vec{\kappa}))}{\mathcal{L}(\vec{\kappa}, \vec{\theta}(\vec{\kappa}))} = -2 \ln \lambda(\vec{\kappa}) \tag{11.1}$$

where the numerator and the denominator are the conditional and unconditional maximum-likelihood estimators respectively and $\vec{\kappa}$ is a combination of $\mathbf{x}$ and ϕ_τ. For this analysis, the test statistic (NLL) is defined as $\frac{q}{2}$. The confidence range is therefore $[\phi_\tau - \sigma_{\phi_\tau}, \phi_\tau + \sigma_{\phi_\tau}]$ which comes from the NLL using the Neyman construction [148] shown in Equation 11.2

$$-\log\mathcal{L}(\phi_\tau \pm N\sigma_{\phi_\tau}) = -\log\mathcal{L}_{\max} + \frac{N^2}{2} \tag{11.2}$$

The 68% confidence limit(1σ, the N in Equation 11.2 represents the number of standard double-sided gaussian quantiles) can be determined from the best estimator $\hat{\phi_\tau}$ by reading off ΔNLL (defined as NLL-NLL$_{min}$ at 0.5). In this interval the true value of ϕ_τ is contained in 68% of cases.

11.3. Fit Results

This section summarises the two sets of results produced for this analysis. The first uses simulated Asimov data shown in Section 11.3.1, the second uses real data from the ATLAS experiment shown in Section 11.3.2.

11.3.1. Asimov Fits

An Asimov dataset is generated for a set of parameters such that the maximum likelihood best fit values match the values that were chosen at generation. The Asimov dataset is a binned dataset, the count in each bin is set to the expected yield given the parameters that were chosen in the generation of the dataset. Asimov datasets allow for the testing of a hypothesis by creating a sample which represents a given outcome (modelled by assigning the parameters in its generation), in the case of this analysis that the Higgs is CP-even. The dataset then contains particles with properties (momenta, energies, decay products, etc) that one would expect to see given the hypothesis used in the generation of the dataset. This then allows for the measurement of the difference between observed and simulated data to evaluate the significance of a given hypothesis. This chapter examines the results of the Asimov fit using the $\tau_{\text{had}}\tau_{\text{had}}$ and $\tau_{\text{lep}}\tau_{\text{had}}$ combined fit.

The 1D NLL uses 30 data points ranging from -90° to 89.9°. As expected by construction for an Asimov dataset the expected value was $0^{\circ} \pm 28^{\circ}$, when running the analysis with Asimov data, the behaviour of the systematics, shape of the NLL curve and width of the expected confidence limit are the relevant factors. This NLL graph also places a 2.24σ exclusion on CP-odd exclusion for the stat only case (where the fit is run without the inclusion of systematics) and 2.1σ for the full-syst fit (where systematics are included).

The 2D fit is provided in Figure 11.12 where the signal strength $\mu_{\tau\tau}$ is included as the second axis. Signal strength is defined as the ratio of decay rates with the predictions made by the Standard Model, thus a of $\mu_{\tau\tau}$ of 1 would indicate that the measurement is in agreement with the Standard Model prediction. It is formed of 29 points on each axis for a total of 841 and central contour of 1σ shows the limits of Standard Model agreement.

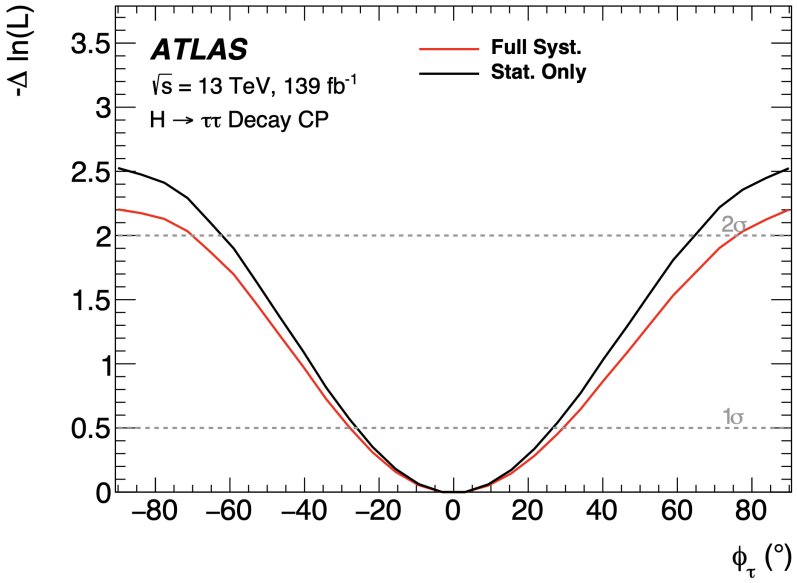

Figure 11.11.: The expected ΔNLL for ϕ_τ generated using the combined $\tau_{\text{lep}} - \tau_{\text{had}}$ and $\tau_{\text{had}} - \tau_{\text{had}}$ channels from Asimov data. Both the stat-only (black-line, generated using only statistical uncertainty) and the full-syst(red line, generated using both statistical uncertainties and systematic uncertainties) fits are included. The expected value of of ϕ_τ is $0 \pm 28^\circ$ for the full fit and $0 \pm 27^\circ$ for the stat only fit.

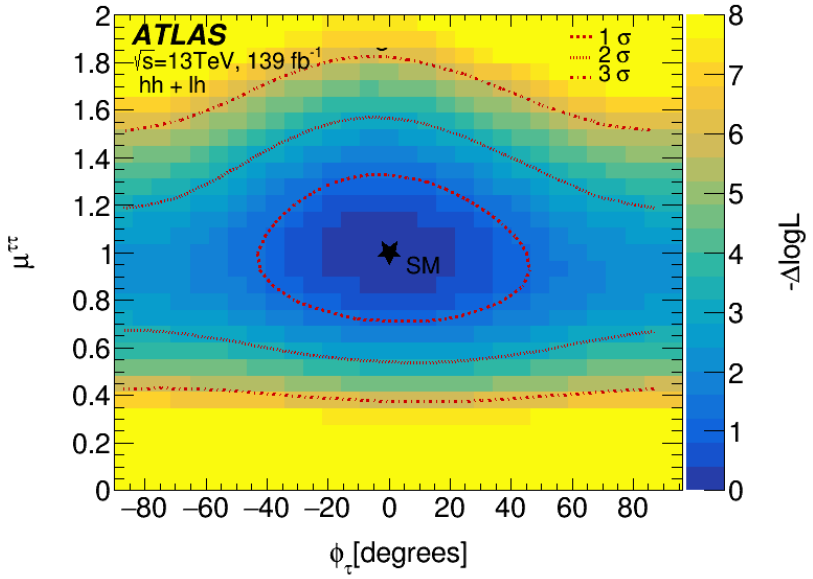

Figure 11.12.: The contours for the expected 2D ΔNLL generated from Asimov data using the $\tau_{\text{lep}} - \tau_{\text{had}}$ and $\tau_{\text{had}} - \tau_{\text{had}}$ channels for the full-syst fit, including both statistical and systematic uncertainties. Plotting the mixing angle ϕ_τ against the signal strength, $\mu^{\tau\tau}$ of the $H \to \tau\tau$ signal.

The total uncertainties for the Asimov fits are dominated by the statistical uncertainty of the Asimov dataset. Examining the systematic uncertainties, these are dominated by the systematic uncertainties coming from jets. The next most dominant systematic uncertainy comes from the limited simulated sample size (MC stat.) of the Asimov dataset. The dominance of the jet uncertainties is due to their strong dependence on the Missing Mass Calculator (MMC) between the Z control region and signal region, aswell the MMC dependence in the jet selection for the categorisation into either VBF or Boost categories. This effect is further demonstrated in the ranking plot (Figure 11.13) where most of the top 40 systematics are related to the jets. Additionally in this plot it can be seen that the normalisation factors have all been pulled to the maximum value, this is because they are not constrained by the fit because they are left free floating, then their final values can be seen in Figure 11.1 which are all 1.00 due to this fit being conducted on Asimov Data.

Tau related uncertainties are dominated by systematics relating the tau energy scale and have a small overall impact. The tau categorisation uncertainties primarily impacts the normalisation factors and accordingly have a lower impact on the mixing angle. Fake estimation, theory, lepton, track and MET uncertainties have a lower impact as shown in Table 11.2 while the lowest impact uncertainties such as from flavour tagging and luminosity are negligible.

Normalisation factors	Post-fit
$\mu_{H\to\tau\tau}$	$1.00^{+0.21}_{-0.21}$
NF Ztt VBF 1	$1.00^{+0.08}_{-0.08}$
NF Ztt VBF 0	$1.00^{+0.08}_{-0.08}$
NF Ztt Boost Tight	$1.00^{+0.04}_{-0.04}$
NF Ztt Boost Loose	$1.00^{+0.05}_{-0.05}$

Table 11.1.: The expected post-fit values and uncertainties of the Normalisation Factors (NF) in the VBF and boost regions which are left free-floating during the fit and the signal strength $\mu_H^{\tau\tau}$. These are obtained from the combined $\tau_{\text{lep}} - \tau_{\text{had}}$ and $\tau_{\text{had}} - \tau_{\text{had}}$ channels using Asimov data.

Parameter of interest	Central Value (°)
ϕ_τ	0.00
Set of nuisance parameters	Impact on uncertainty
Total	+29.12 / -27.65
DataStat	+26.46 / -25.94
FullSyst	+12.18 / -9.59
Signal normalisation	+5.00 / -0.18
Background normalisation	+2.53 / -0.40
Jet	+9.82 / -8.04
MET	+1.46 / -0.99
Electron	+0.94 / -0.84
Muon	+1.74 / -1.32
Tau	+1.80 / -1.84
Fake Estimation	+1.79 / -1.19
Tau Decay Mode Classification	+0.61 / -0.60
Neutral Pion	+0.32 / -0.72
Luminosity	+0.07 / -0.14
Track	+1.36 / -0.69
Flavour Tagging	+0.13 / -0.02
Theory unc. ($H \to \tau\tau$)	+1.83 / -0.78
Theory unc. ($Z \to \tau\tau$)	+3.33 / -2.20
MC stat.	+3.67 / -3.58

Table 11.2.: The Grouped impact from different sources on the fit result produced from the combined $\tau_{\text{lep}} - \tau_{\text{had}}$ and $\tau_{\text{had}} - \tau_{\text{had}}$ channels using Asimov data.

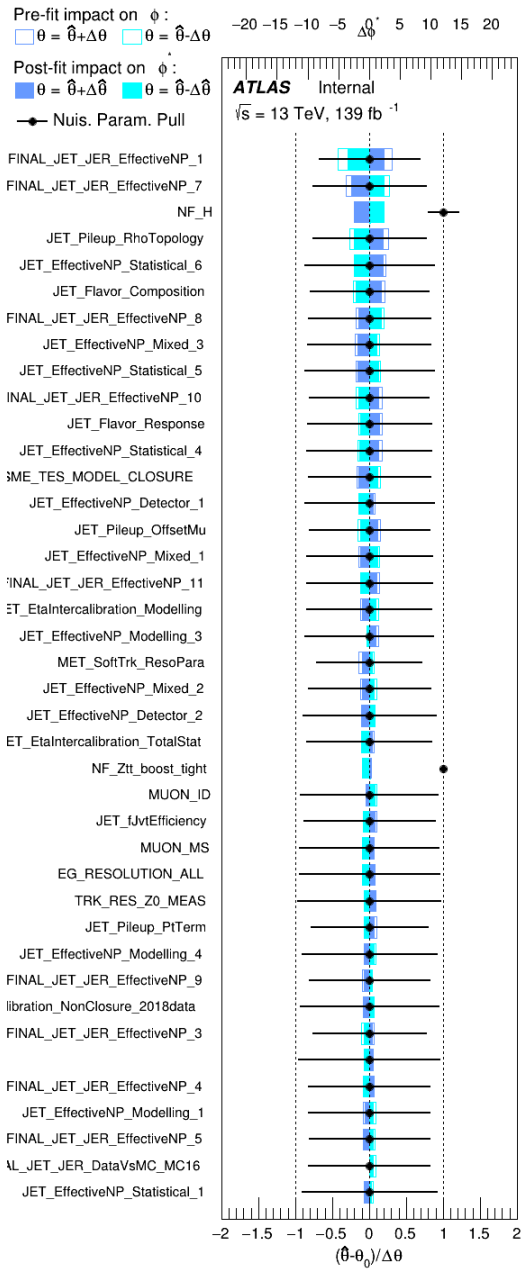

Figure 11.13.: A ranking of the 40 nuisance parameters with the highest post-fit impact on the combined $\tau_{\text{lep}} - \tau_{\text{had}}$ and $\tau_{\text{had}} - \tau_{\text{had}}$ Asimov fit result.

11.3.2. Unblinded Fits

The unblinded 1D and 2D NLL curves are shown in Figures 11.14 and 11.16 respectively. The 1D fit has an NLL minimum at 8.68° which corresponds to the measured value of ϕ_τ with a 1σ width ranging from 17.77° to 16.16°. Both this and the 2D scan (performed using the same method as the Asimov fit) are compatible with the Standard model prediction ($\phi_\tau = 0$). The CP-odd hypothesis is rejected at a confidence level of 3.4σ. Figures 11.17 and 11.18 show the φ^*_{CP} distributions and predictions in both the $\tau_{\text{lep}} - \tau_{\text{had}}$ and $\tau_{\text{had}} - \tau_{\text{had}}$ channels in the High, Medium and Low signal regions. Figure 11.15 shows a binned postfit distribution of all signal regions combined, weighted using $\ln\left(1 + \frac{\text{signal}}{\text{background}}\right)$. This too shows a disfavouring of the pure CP-odd scenario.

The unblinded results show the same uncertainty trends as the Asimov fits. The systematic uncertainties are primarily dominated by the jet uncertainties and the $H \to \tau\tau$ theory uncertainties as shown in Table 11.4. The less impactful uncertainties that follow the jets and $H \to \tau\tau$ theory are the MC stats and tau uncertainties for the same reasons and discussed in Section 11.3.1. In the ranking plot, Figure 11.19, all the normalisation factors have been pulled to near their maximum values, as with the Asimov plots this is due to the fact they are unconstrained in the fit.

The unblinding process was performed in multiple phases of "conditional unblinding" as follows:

1. ϕ_τ fixed at 0, $\mu_{H\to\tau\tau}$ fixed at 1: Used to examine the pulls on nuisance parameters.
2. ϕ_τ fixed at 0, $\mu_{H\to\tau\tau}$ free floating: Used to examine pulls on $\mu_{H\to\tau\tau}$.
3. ϕ_τ free floating, $\mu_{H\to\tau\tau}$ fixed at 1: Used to examine ϕ_τ sensitivity.

During this process multiple toy studies were also conducted in order to assess the compatability of the Asimov data fits with the conditionally unblinded fits. In these studies, each toy dataset is generated by throwing a random distribution from the initial Asimov dataset. Each toy dataset is then fitted to produce a value for ϕ_τ and only statistical uncertainties are considered. Out of the 1000 toy datasets generated, 717 returned usable datasets which could then be fitted. The mean positive and negative uncertainties for the value of ϕ_τ were $+25.64 \pm 0.33°$ and $-24.84 \pm 0.31°$ which indicates that the Asimov fit measurement is compatible with the observed measurement.

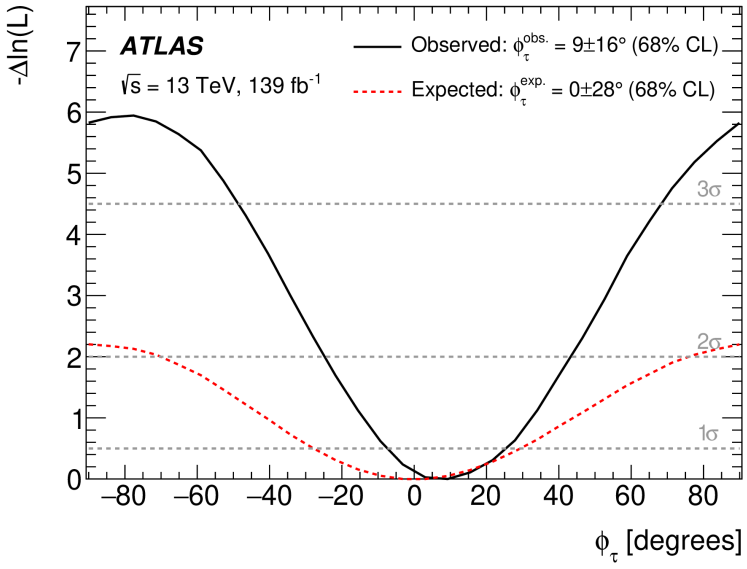

Figure 11.14.: A comparison between the Asimov (red dotted line) and observed, fully unblinded (black solid line) ΔNLL curves for the combined $\tau_{\text{lep}} - \tau_{\text{had}}$ and $\tau_{\text{had}} - \tau_{\text{had}}$. The observed value of ϕ_τ is 8.68° (+16.77°,-16.16°) at one standard deviation.

Normalisation factors	Post-fit
$\mu_{H\to\tau\tau}$	$1.02^{+0.20}_{-0.20}$
NF Ztt VBF 1	$1.04^{+0.08}_{-0.08}$
NF Ztt VBF 0	$0.95^{+0.07}_{-0.07}$
NF Ztt Boost Tight	$1.01^{+0.05}_{-0.05}$
NF Ztt Boost Loose	$1.02^{+0.05}_{-0.05}$

Table 11.3.: The observed post-fit values and uncertainties of the Normalisation Factors (NF) in the VBF and Boost regions which are left free-floating during the fit and the signal strength $\mu_H^{\tau\tau}$. These are obtained from the combined $\tau_{\text{lep}} - \tau_{\text{had}}$ and $\tau_{\text{had}} - \tau_{\text{had}}$ channels using fully unblinded data.

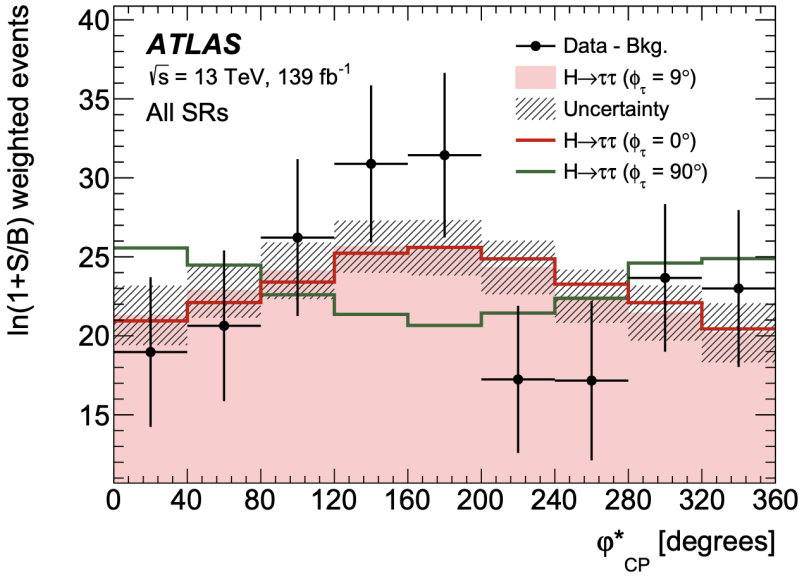

Figure 11.15.: Combined post-fit distribution of φ^*_{CP} across all signal regions for both $\tau_{\text{lep}} - \tau_{\text{had}}$ and $\tau_{\text{had}} - \tau_{\text{had}}$ channels. Events are weighted using $\ln\left(1 + \frac{\text{signal}}{\text{background}}\right)$ from their corresponding signal region. The background is subtracted from the data. The solid pink shows the best fit for $H \to \tau\tau$ signal and red and green lines show the CP-even and CP-odd hypotheses respectively scaled to the $\to \tau\tau$ signal best fit. The hatched uncertainty shows all sources of uncertainty after the fit to data. It represents the same uncertainty as in Figures 11.17 and 11.18

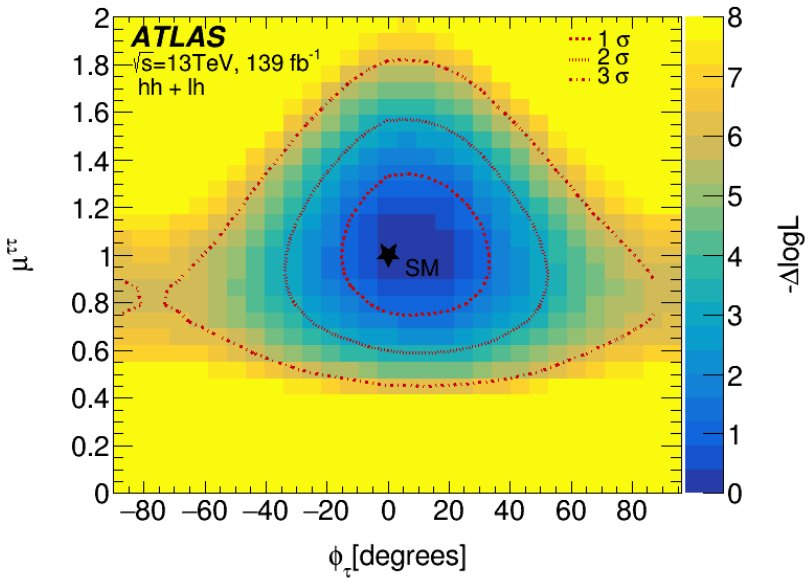

Figure 11.16.: The contours for the observed, fully unblinded 2D ΔNLL using the $\tau_{\text{lep}} - \tau_{\text{had}}$ and $\tau_{\text{had}} - \tau_{\text{had}}$ channels for the full-syst fit, including both statistical and systematic uncertainties. Plotting the mixing angle ϕ_τ against the signal strength, $\mu^{\tau\tau}$ of the $H \to \tau\tau$ signal.

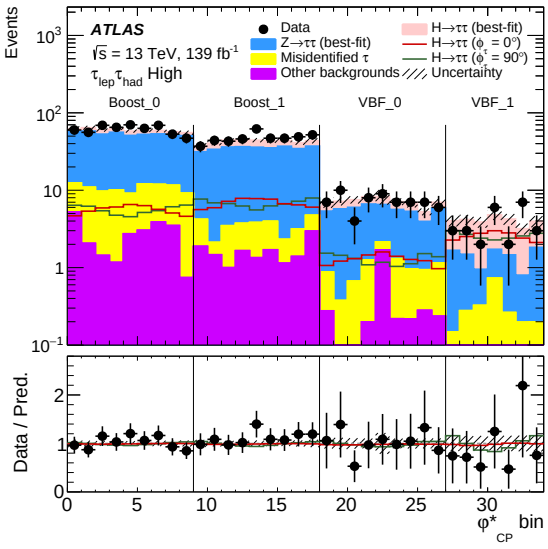

(a) $\tau_{\text{lep}} - \tau_{\text{had}}$ High SR

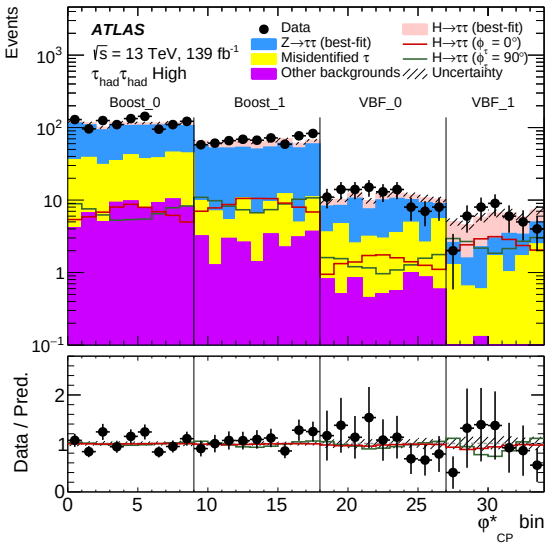

(b) $\tau_{\text{had}} - \tau_{\text{had}}$ High SR

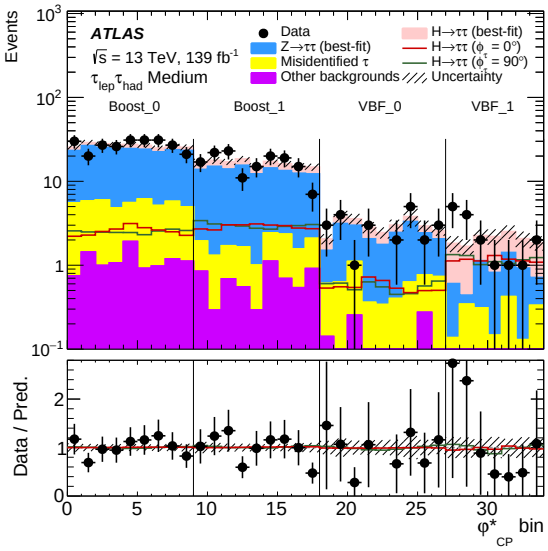

(c) $\tau_{\text{lep}} - \tau_{\text{had}}$ Medium SR

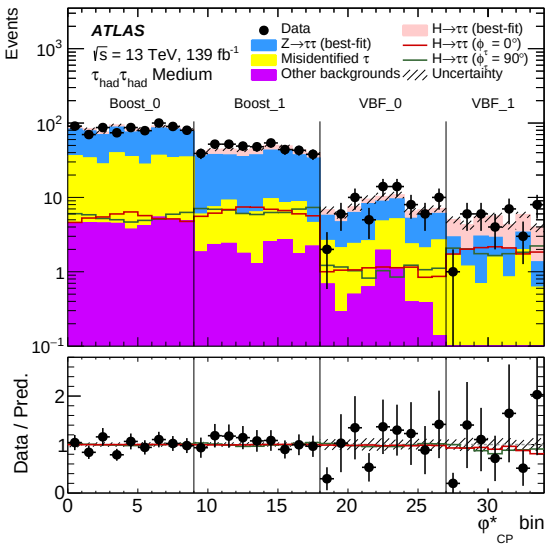

(d) $\tau_{\text{had}} - \tau_{\text{had}}$ Medium SR

Figure 11.17.: The post-fit distributions of φ^*_{CP} in the different signal regions for the most sensitive regions, 11.17a $\tau_{\text{lep}} - \tau_{\text{had}}$ High SR, 11.17b $\tau_{\text{had}} - \tau_{\text{had}}$ High SR, 11.17c $\tau_{\text{lep}} - \tau_{\text{had}}$ Medium SR 11.17d $\tau_{\text{had}} - \tau_{\text{had}}$ Medium SR. For each subcategory Boost_0, Boost_1, VBF_0 and VBF_1 the φ^*_{CP} bins cover the full range between 0° and 360°. The solid pink shows the best fit for $H \to \tau\tau$ signal and red and green lines show the CP-even and CP-odd hypotheses respectively (scaled to the predicted signal yield). The purple "Other backgrounds" includes W, diboson,top, $Z \to \ell\ell$ and $H \to WW^*$. The hatched uncertainty includes any source of uncertainty after the fit to data.

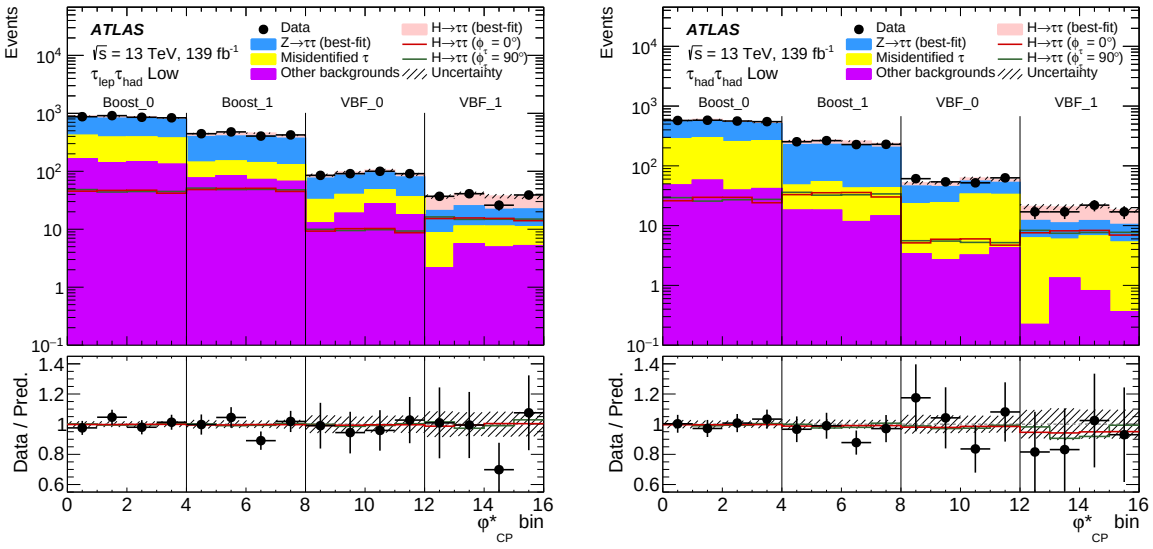

(a) $\tau_{\text{lep}} - \tau_{\text{had}}$ Low SR

(b) $\tau_{\text{had}} - \tau_{\text{had}}$ Low SR

Figure 11.18.: The post-fit distributions of φ^*_{CP} in the different signal regions for the least sensitive regions, 11.18a $\tau_{\text{lep}} - \tau_{\text{had}}$ Low SR 11.18b $\tau_{\text{had}} - \tau_{\text{had}}$ Low SR. For each subcategory Boost_0, Boost_1, VBF_0 and VBF_1 the φ^*_{CP} bins cover the full range between 0° and 360°. The solid pink shows the best fit for $H \to \tau\tau$ signal and red and green lines show the CP-even and CP-odd hypotheses respectively (scaled to the predicted signal yield). The purple "Other backgrounds" includes W, diboson,top, $Z \to \ell\ell$ and $H \to WW^*$. The hatched uncertainty includes any source of uncertainty after the fit to data.

Parameter of interest	Central Value ($^\circ$)
ϕ_τ	8.68
Set of nuisance parameters	Impact on uncertainty
Total	+16.77 / -16.16
DataStat	+15.90 / -15.32
FullSyst	+5.32 / -5.14
Signal normalisation	+2.11 / -0.64
Background normalisation	+1.19 / –nan
Jet	+4.22 / -4.46
MET	+0.87 / -nan
Electron	+0.32 / -0.25
Muon	+0.87 / -0.91
Tau	+1.07 / -1.02
Fake Estimation	+0.89 / -0.33
Tau Decay Mode Classification	+0.38 / -0.31
Neutral Pion	+0.30 / -nan
Luminosity	+0.24 / -nan
Track	+0.99 / -0.41
Flavour Tagging	+0.29 / -nan
Theory unc. ($H \to \tau\tau$)	+2.08 / -0.89
Theory unc. ($Z \to \tau\tau$)	+1.39 / -0.85
MC stat.	+1.44 / -1.34

Table 11.4.: The observed grouped impact from different sources on the fit result produced from the combined $\tau_{\text{lep}} - \tau_{\text{had}}$ and $\tau_{\text{had}} - \tau_{\text{had}}$ channels using fully unblinded data.

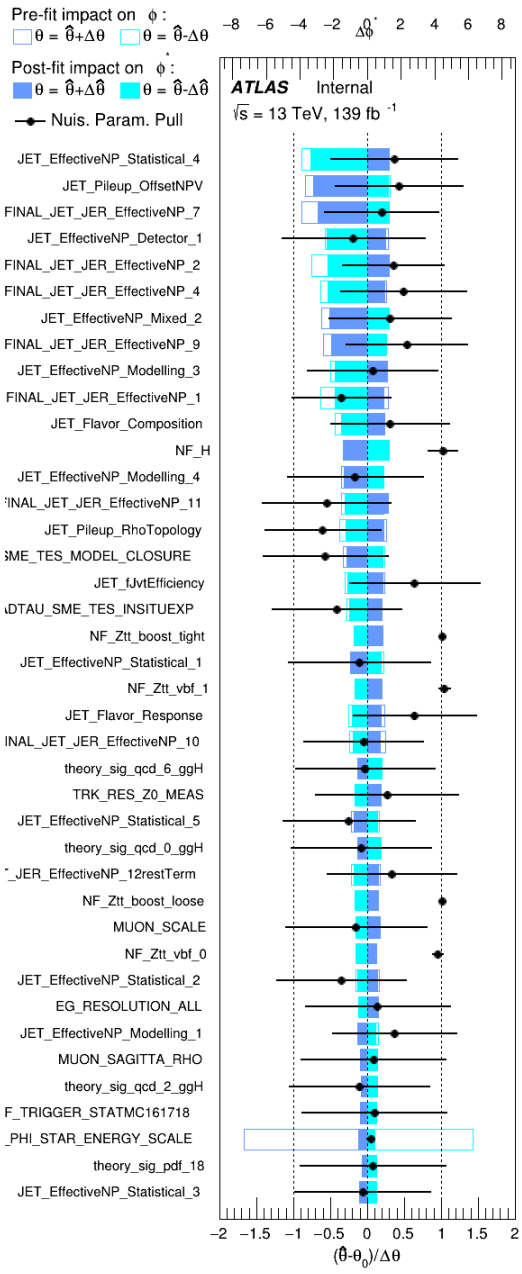

Figure 11.19.: Observed ranking of 40 systematic uncertainties with the highest post-fit impact on ϕ_τ in the $\tau_{\text{had}}\tau_{\text{had}}$+$\tau_{\text{lep}}\tau_{\text{had}}$combined fit on the fully unblinded dataset.

Chapter 12.

Conclusion

This thesis presents a study of the CP-properties of the Higgs to $\tau\tau$ decay, including both the semi-leptonic and fully hadronic decay channels. A single mixing angle, ϕ_τ, describes the CP-properties of this decay in the generalised Yukawa interaction.

The measurement is conducted using 139fb^{-1} of proton-proton collision data with a centre of mass energy, $\sqrt{s}$ of 13TeV. This data was collected at the Large Hadron Collider by the ATLAS detector in the period 2015-2018. The measurement is based on a maximum likelihood fit of the observable φ^*_{CP} constructed from the visible decay products of the Higgs to $\tau\tau$ decay, using different methods depending on the exact decay channel.

The expected value of ϕ_τ produced by the Asimov fit is $0 \pm 28^\circ$ at the 68% confidence level (CL) and -70/+75° at the 95.5% CL. The measured value of ϕ_τ is $9 \pm 16^\circ$ at the 68% confidence level and $\pm 34^\circ$ at 95.5% confidence level. The measured result disfavours the pure CP-Odd Higgs hypothesis to 3.4 standard deviations (σ).

A comparable measurement of the CP-properties of the Higgs using H$\to \tau\tau$ decays was conducted at the other general purpose detector present at the LHC, CMS [72]. The CMS results exclude pure CP-Odd Higgs hypothesis to 3.0σ. The observed (expected) CP Mixing angle produced by the CMS experiment was $-1^\circ \pm 19^\circ$ ($0^\circ \pm 21^\circ$) at the 68% CL, with 95% CL at $\pm 49^\circ$ ($\pm 41^\circ$).

The analysis presented in this thesis was accepted by the "The European Physical Journal C (EPJC)" this is available at [68]. The next generation of H$\to \tau\tau$ CP studies will be using data from Run 3 of the LHC operation. Started in Spring 2022, Run 3 has proposed to deliver 280 fb^{-1} of integrated proton-proton luminosity over the run in comparison to 140 fb^{-1} of usable physics data in Run 2. The sheer increase in data

combined with a small energy upgrade (from 13.0 TeV to 13.6 TeV) and the numerous detector upgrades including a fourth pixel layer, new Liquid Argon Calorimeter digital trigger electronics, upgrades to the muon spectrometer and calorimetry systems should allow the Run 3 H$\rightarrow \tau\tau$ CP studies to further increase the confidence level of the results presented in this thesis [149].

Appendix A.

$H \rightarrow \tau\tau$ Additional Information

Trigger	Data period	HLT Chain name (in the menu)
Single electron	2015	`e24_lhmedium_L1EM20VH`, `e60_lhmedium` or `e120_lhloose`
	2016-2018	`e26_lhtight_nod0_ivarloose`, `e60_lhmedium_nod0` or `e140_lhloose_nod0`
Single muon	2015	`mu20_iloose_L1MU15` or `mu50`
	2016-2018	`mu26_ivarmedium` or `mu50`
Ditau	2015	`tau35_medium1_tracktwo_tau25_medium1_tracktwo_L1TAU20IM_2TAU12IM`
	2016	`tau35_medium1_tracktwo_tau25_medium1_tracktwo`
	2017	`tau35_medium1_tracktwo_tau25_medium1_tracktwo_03dR30_L1DR_TAU20ITAU12I_J25`
	2018	`tau35_medium1_tracktwoEF_tau25_medium1_tracktwoEF_03dR30_L1DR_TAU20ITAU12I_J25`

Table A.1.: A summary of the trigger items used in this analysis. The $\tau_{\text{lep}}\tau_{\text{had}}$ channel uses single lepton triggers while the $\tau_{\text{had}}\tau_{\text{had}}$ channel uses di-hadronic τ triggers.

Bibliography

[1] S. L. Glashow, "Partial-symmetries of weak interactions," *Nuclear Physics*, vol. 22, no. 4, pp. 579–588, 1961.

[2] A. Salam and J. Ward, "Electromagnetic and weak interactions," *Physics Letters*, vol. 13, no. 2, pp. 168–171, 1964.

[3] S. Weinberg, "A model of leptons," *Phys. Rev. Lett.*, vol. 19, pp. 1264–1266, Nov 1967.

[4] G. 't Hooft and M. Veltman, "Regularization and renormalization of gauge fields," *Nuclear Physics B*, vol. 44, no. 1, pp. 189–213, 1972.

[5] ATLAS Collaboration, "Observation of a new particle in the search for the Standard Model Higgs boson with the ATLAS detector at the LHC," *Phys. Lett. B*, vol. 716, pp. 1–29, Sept. 2012.

[6] CMS Collaboration, "Observation of a new boson at a mass of 125 GeV with the CMS experiment at the LHC," *Physics Letters B*, vol. 716, p. 30–61, Sept. 2012.

[7] CMS Collaboration, "Constraints on the spin-parity and anomalous HVV couplings of the Higgs boson in proton collisions at 7 and 8 TeV," *Phys. Rev.*, vol. 92, July 2015.

[8] Planck Collaboration, "Planck 2015 results: Xiii. cosmological parameters," *Astronomy & Astrophysics*, vol. 594, p. A13, Sept. 2016.

[9] I. J. R. Aitchison and A. J. G. Hey, *Gauge theories in particle physics: A practical introduction, volume 1: From relativistic mechanics to QED*. Graduate student series in physics, Boca Raton, FL: CRC Press, 4 ed., Mar. 2013.

[10] I. J. R. Aitchison and A. J. G. Hey, *Gauge theories in particle physics: A practical introduction, volume 2: Non-abelian gauge theories non-abelian gauge theories*. Boca Raton, FL: CRC Press, 4 ed., Dec. 2013.

[11] J. Ellis, M. K. Gaillard, and D. V. Nanopoulos, "A historical profile of the higgs boson," in *Advanced Series on Directions in High Energy Physics*, pp. 255–274, WORLD SCIENTIFIC, Oct. 2016.

[12] E. Noether, "Invariante Variationsprobleme," *Nachr. d. König. Gesellsch. d. Wiss. zu Göttingen, Math-phys. Klasse, Seite 235-157*, 1918.

[13] I. I. Bigi and A. I. Sanda, *CP Violation*. Cambridge monographs on particle physics, nuclear physics and cosmology, Cambridge, England: Cambridge University Press, 2 ed., Apr. 2009.

[14] W. Pauli, *Exclusion Principle, Lorentz Group and Reflection of Space-Time and Charge*, pp. 459–479. Wiesbaden: Vieweg+Teubner Verlag, 1988.

[15] O. W. Greenberg, "cpt violation implies violation of lorentz invariance," *Phys. Rev. Lett.*, vol. 89, p. 231602, Nov 2002.

[16] C. Patrignani, "Review of particle physics," *Chinese Physics C*, vol. 40, p. 100001, oct 2016.

[17] M. Sozzi, *Discrete symmetries and CP violation*. Oxford Graduate Texts, London, England: Oxford University Press, June 2012.

[18] T. D. Lee and C. N. Yang, "Question of parity conservation in weak interactions," *Phys. Rev.*, vol. 104, pp. 254–258, Oct 1956.

[19] R. T. Cox, C. G. McIlwraith, and B. Kurrelmeyer, "Apparent evidence of polarization in a beam of β-rays," *Proc. Natl. Acad. Sci. U. S. A.*, vol. 14, pp. 544–549, July 1928.

[20] C. T. Chase, "The scattering of fast electrons by metals. ii. polarization by double scattering at right angles," *Phys. Rev.*, vol. 36, pp. 1060–1065, Sep 1930.

[21] C. S. Wu, E. Ambler, R. W. Hayward, D. D. Hoppes, and R. P. Hudson, "Experimental test of parity conservation in beta decay," *Phys. Rev.*, vol. 105, pp. 1413–1415, Feb 1957.

[22] J. H. Christenson, J. W. Cronin, V. L. Fitch, and R. Turlay, "Evidence for the 2π decay of the k_2^0 meson," *Phys. Rev. Lett.*, vol. 13, pp. 138–140, Jul 1964.

[23] H. Burkhardt, P. Clarke, D. Coward, and D. e. a. Cundy, "First evidence for direct CP violation," *Phys. Lett. B*, vol. 206, pp. 169–176, May 1988.

[24] KTeV Collaboration, "Observation of direct cp violation in $k_{s,l} \to ßß$ decays," *Phys. Rev. Lett.*, vol. 83, pp. 22–27, Jul 1999.

[25] NA48 Collaboration: V. Fanti, et al, "A new measurement of direct cp violation in two pion decays of the neutral kaon," *Physics Letters B*, vol. 465, no. 1, pp. 335–348, 1999.

[26] LHCb Collaboration, "First observation of cp violation in the decays of B_s^0 mesons," *Phys. Rev. Lett.*, vol. 110, p. 221601, May 2013.

[27] F. Betti, "Observation of cp violation in charm decays at lhcb," 2019.

[28] T2K Collaboration, "Constraint on the matter-antimatter symmetry-violating phase in neutrino oscillations," *Nature*, vol. 580, pp. 339–344, Apr. 2020.

[29] A. D. Sakharov, "Violation of CP Invariance, C asymmetry, and baryon asymmetry of the universe," *Pisma Zh. Eksp. Teor. Fiz.*, vol. 5, pp. 32–35, 1967.

[30] ATLAS Collaboration, "Evidence for the spin-0 nature of the Higgs boson using ATLAS data," *Physics Letters B*, vol. 726, no. 1, pp. 120–144, 2013.

[31] ATLAS Collaboration, "Study of the spin and parity of the Higgs boson in diboson decays with the ATLAS detector," *Eur. Phys. J. C Part. Fields*, vol. 75, p. 476, Oct. 2015.

[32] CMS Collaboration, "Study of the mass and spin-parity of the Higgs boson candidate via its decays to Z boson pairs," *Phys. Rev. Lett.*, vol. 110, p. 081803, Feb. 2013.

[33] ATLAS Collaboration, "Test of CP invariance in vector-boson fusion production of the Higgs boson in the $h \to \tau\tau$ channel in proton–proton collisions at $\sqrt{s}$=13TeV with the ATLAS detector," *Physics Letters B*, vol. 805, p. 135426, 2020.

[34] ATLAS Collaboration, "Probing the CP nature of the top–higgs yukawa coupling in $tt^{-}h$ and th events with $H \to bb^{-}$ decays using the ATLAS detector at the LHC," *Phys. Lett. B*, vol. 849, p. 138469, Feb. 2024.

[35] ATLAS Collaboration, "CP properties of higgs boson interactions with top quarks in the $t\bar{t}$H and tH processes using $H \to \gamma\gamma$ with the ATLAS detector," *Phys. Rev. Lett.*, vol. 125, p. 061802, Aug. 2020.

[36] C. Grojean, "Higgs Physics," pp. 143–158, 2016. 12 pages, contribution to the

CERN in the Proceedings of the 2015 CERN-Latin-American School of High-Energy Physics, Ibarra, Ecuador, 4 - 17 March 2015.

[37] LHC Higgs Cross Section Working Group Collaboration, "Cern yellow reports: Monographs, vol 2 (2017): Handbook of lhc higgs cross sections: 4. deciphering the nature of the higgs sector," 2017.

[38] Particle Data Group, "Review of particle physics," *Prog. Theor. Exp. Phys.*, vol. 2022, Aug. 2022.

[39] O. S. Brüning, J. Poole, P. Collier, P. Lebrun, R. Ostojic, S. Myers, and P. Proudlock, "LHC design report," 2004.

[40] E. Mobs, "The CERN accelerator complex. Complexe des accélérateurs du CERN," 2016. General Photo.

[41] ATLAS Collaboration, "Public ATLAS Online Luminosity Plots for Run-2 of the LHC." https://twiki.cern.ch/twiki/bin/view/AtlasPublic/LuminosityPublicResultsRun2#Online_Luminosity_Summary_Plots. [Accessed 11-09-2024].

[42] ATLAS Collaboration, "Luminosity Public Results." https://twiki.cern.ch/twiki/bin/view/AtlasPublic/LuminosityPublicResults. [Accessed 11-09-2024].

[43] ATLAS Collaboration, "The ATLAS experiment at the CERN large hadron collider," *J. Instrum.*, vol. 3, pp. S08003–S08003, Aug. 2008.

[44] P. F. Akesson, T. Atkinson, M. J. Costa, M. Elsing, *et al.*, "ATLAS Tracking Event Data Model," tech. rep., CERN, Geneva, 2006. All figures including auxiliary figures are available at https://atlas.web.cern.ch/Atlas/GROUPS/PHYSICS/PUBNOTES/ATL-SOFT-PUB-2006-004.

[45] ATLAS Collaboration, *ATLAS magnet system: Technical Design Report, 1*. Technical design report. ATLAS, Geneva: CERN, 1997.

[46] ATLAS Collaboration, "The ATLAS Inner Detector commissioning and calibration," *The European Physical Journal C*, vol. 70, p. 787–821, Aug. 2010.

[47] M. Capeans, G. Darbo, K. Einsweiller, M. Elsing, *et al.*, "ATLAS Insertable B-Layer Technical Design Report," tech. rep., 2010.

[48] K. Potamianos, "The upgraded Pixel detector and the commissioning of the Inner Detector tracking of the ATLAS experiment for Run-2 at the Large Hadron Collider," 2016.

[49] ATLAS Collaboration, "Topological cell clustering in the ATLAS calorimeters and its performance in LHC Run 1," *The European Physical Journal C*, vol. 77, July 2017.

[50] P. Branchini, F. Ceradini, S. Di Luise, M. Iodice, and F. Petrucci, "Global time fit for tracking in an array of drift cells: The drift tubes of the atlas experiment," *IEEE Transactions on Nuclear Science*, vol. 55, no. 1, pp. 620–627, 2008.

[51] ATLAS Collaboration, "Electron reconstruction and identification in the ATLAS experiment using the 2015 and 2016 LHC proton–proton collision data at $\sqrt{s} =$ 13 TeV," *The European Physical Journal C*, vol. 79, Aug. 2019.

[52] ATLAS Collaboration, "Electron and photon performance measurements with the ATLAS detector using the 2015–2017 LHC proton-proton collision data," *Journal of Instrumentation*, vol. 14, p. P12006–P12006, Dec. 2019.

[53] ATLAS Collaboration, "Muon reconstruction performance of the ATLAS detector in proton-proton collision data at $\sqrt{s}$=13 TeV," *Eur. Phys. J. C Part. Fields*, vol. 76, p. 292, May 2016.

[54] ATLAS Collaboration, "Identification of hadronic tau lepton decays using neural networks in the ATLAS experiment," tech. rep., CERN, Geneva, 2019. All figures including auxiliary figures are available at https://atlas.web.cern.ch/Atlas/GROUPS/PHYSICS/PUBNOTES/ATL-PHYS-PUB-2019-033.

[55] ATLAS Collaboration, "Measurement of the tau lepton reconstruction and identification performance in the ATLAS experiment using pp collisions at $\sqrt{s}$=13TeV," tech. rep., CERN, Geneva, 2017. All figures including auxiliary figures are available at https://atlas.web.cern.ch/Atlas/GROUPS/PHYSICS/CONFNOTES/ATLAS-CONF-2017-029.

[56] ATLAS Collaboration, "Jet reconstruction and performance using particle flow with the ATLAS detector," *The European Physical Journal C*, vol. 77, July 2017.

[57] M. Cacciari, G. P. Salam, and G. Soyez, "The anti-ktjet clustering algorithm," *J.*

High Energy Phys., vol. 2008, pp. 063–063, Apr. 2008.

[58] ATLAS Collaboration, "Reconstruction, Energy Calibration, and Identification of Hadronically Decaying Tau Leptons," tech. rep., CERN, Geneva, 2011. All figures including auxiliary figures are available at https://atlas.web.cern.ch/Atlas/GROUPS/PHYSICS/CONFNOTES/ATLAS-CONF-2011-077.

[59] ATLAS Collaboration, "Jet energy scale measurements and their systematic uncertainties in proton-proton collisions at $\sqrt{s} = 13$ TeV with the ATLAS detector," *Phys. Rev. D*, vol. 96, p. 072002, Oct 2017.

[60] ATLAS Collaboration, "Tagging and suppression of pileup jets with the ATLAS detector," tech. rep., CERN, Geneva, 2014. All figures including auxiliary figures are available at https://atlas.web.cern.ch/Atlas/GROUPS/PHYSICS/CONFNOTES/ATLAS-CONF-2014-018.

[61] F.H. Bescherer, P. Bechtle, A.K. Becker, Q. Buat et al., "Measurement of the Higgs boson coupling properties in the H$\rightarrow \tau\tau$ decay channel at $\sqrt{s}$ = 13 TeV with the ATLAS detector," tech. rep., CERN, Geneva, 2020.

[62] ATLAS Collaboration, "$E_{\mathrm{T}}^{\mathrm{miss}}$ performance in the ATLAS detector using 2015-2016 LHC p-p collisions," tech. rep., CERN, Geneva, 2018. All figures including auxiliary figures are available at https://atlas.web.cern.ch/Atlas/GROUPS/PHYSICS/CONFNOTES/ATLAS-CONF-2018-023.

[63] ATLAS Collaboration, "Reconstruction of hadronic decay products of tau leptons with the ATLAS experiment," *The European Physical Journal C*, vol. 76, May 2016.

[64] S. Berge, W. Bernreuther, and S. Kirchner, "Prospects of constraining the Higgs boson's CP nature in the tau decay channel at the LHC," *Phys. Rev. D*, vol. 92, p. 096012, 2015.

[65] ATLAS Collaboration, "A detailed map of higgs boson interactions by the atlas experiment ten years after the discovery," *Nature*, vol. 607, pp. 1–8, 07 2022.

[66] S. Berge, W. Bernreuther, and S. Kirchner, "Determination of the Higgs CP-mixing angle in the tau decay channels," *Nucl. Part. Phys. Proc.*, vol. 273-275, pp. 841–845, 2016.

[67] K. Bai, E.V. Bouhova-Thacker, H.C. Cheng et al., "Test of CP Invariance in Higgs Boson Decays to Tau Leptons with the ATLAS Detector," tech. rep., CERN, Geneva, 2020.

[68] ATLAS Collaboration, "Measurement of the CP properties of Higgs boson interactions with τ-leptons with the ATLAS detector," *Eur. Phys. J. C*, vol. 83, no. 7, p. 563, 2023.

[69] S. Berge and W. Bernreuther, "Determining the CP parity of Higgs bosons at the LHC in the τ to 1-prong decay channels," *Phys. Lett. B*, vol. 671, pp. 470–476, Feb. 2009.

[70] R. Józefowicz, E. Richter-Was, and Z. Was, "Potential for optimizing the Higgs boson CP measurement in $H \to \tau\tau$ decays at the LHC including machine learning techniques," *Phys. Rev. D*, vol. 94, no. 9, p. 093001, 2016.

[71] P. A. Zyla *et al.*, "Review of Particle Physics," *PTEP*, vol. 2020, no. 8, p. 083C01, 2020.

[72] CMS Collaboration, "Analysis of the CP structure of the Yukawa coupling between the Higgs boson and τ leptons in proton-proton collisions at $\sqrt{s} = 13$ TeV," *Journal of High Energy Physics*, vol. 2022, June 2022.

[73] V. Cherepanov, E. Richter-Was, and Z. Was, "Monte carlo, fitting and machine learning for tau leptons," 2019.

[74] S. Jadach, J. H. Kuhn, and Z. Was, "TAUOLA: A Library of Monte Carlo programs to simulate decays of polarized tau leptons," *Comput. Phys. Commun.*, vol. 64, pp. 275–299, 1990.

[75] M. Jezabek, Z. Was, S. Jadach, and J. H. Kuhn, "The tau decay library TAUOLA, update with exact O(alpha) QED corrections in tau —> mu. (e) neutrino anti-neutrino decay modes," *Comput. Phys. Commun.*, vol. 70, pp. 69–76, 1992.

[76] S. Jadach, Z. Was, R. Decker, and J. H. Kuhn, "The tau decay library TAUOLA: Version 2.4," *Comput. Phys. Commun.*, vol. 76, pp. 361–380, 1993.

[77] D. M. Asner *et al.*, "Hadronic structure in the decay $\tau^- \to \nu_\tau \pi^- \pi^0 \pi^0$ and the sign of the tau-neutrino helicity," *Phys. Rev. D*, vol. 61, p. 012002, 2000.

[78] S. Alioli, P. Nason, C. Oleari, and E. Re, "A general framework for implementing nlo calculations in shower monte carlo programs: the powheg box," *Journal of*

High Energy Physics, vol. 2010, June 2010.

[79] P. Nason, "A new method for combining nlo qcd with shower monte carlo algorithms," *Journal of High Energy Physics*, vol. 2004, p. 040–040, Nov. 2004.

[80] S. Frixione, P. Nason, and C. Oleari, "Matching nlo qcd computations with parton shower simulations: the powheg method," *Journal of High Energy Physics*, vol. 2007, p. 070–070, Nov. 2007.

[81] T. Sjöstrand, S. Ask, J. R. Christiansen, R. Corke, N. Desai, P. Ilten, S. Mrenna, S. Prestel, C. O. Rasmussen, and P. Z. Skands, "An introduction to pythia 8.2," *Computer Physics Communications*, vol. 191, p. 159–177, June 2015.

[82] T. Przedzinski, E. Richter-Was, and Z. Was, "Tauspinner: a tool for simulating CP effects in $h \to \tau\tau$ decays at LHC," *The European Physical Journal C*, vol. 74, Nov. 2014.

[83] Z. Czyczula, T. Przedzinski, and Z. Was, "TauSpinner program for studies on spin effect in tau production at the LHC," *Eur. Phys. J. C Part. Fields*, vol. 72, Apr. 2012.

[84] A. Kaczmarska, J. Piatlicki, T. Przedzinski, E. Richter-Was, and Z. Was, "Application of TauSpinner for studies on τ-lepton polarization and spin correlations in Z, W and H decays at the LHC," *Acta Phys. Pol. B*, vol. 45, no. 10, p. 1921, 2014.

[85] K. Hamilton, P. Nason, E. Re, and G. Zanderighi, "Nnlops simulation of higgs boson production," *Journal of High Energy Physics*, vol. 2013, Oct. 2013.

[86] K. Hamilton, P. Nason, and G. Zanderighi, "Finite quark-mass effects in the nnlops powheg+minlo higgs generator," 2015.

[87] K. Hamilton, P. Nason, and G. Zanderighi, "Minlo: multi-scale improved nlo," *Journal of High Energy Physics*, vol. 2012, Oct. 2012.

[88] J. M. Campbell, R. K. Ellis, R. Frederix, P. Nason, C. Oleari, and C. Williams, "Nlo higgs boson production plus one and two jets using the powheg box, madgraph4 and mcfm," *Journal of High Energy Physics*, vol. 2012, July 2012.

[89] K. Hamilton, P. Nason, C. Oleari, and G. Zanderighi, "Merging h/w/z + 0 and 1 jet at nlo with no merging scale: a path to parton shower + nnlo matching," *Journal of High Energy Physics*, vol. 2013, May 2013.

[90] S. Catani and M. Grazzini, "Next-to-next-to-leading-order subtraction formalism in hadron collisions and its application to higgs-boson production at the large hadron collider," *Physical Review Letters*, vol. 98, May 2007.

[91] J. Butterworth, S. Carrazza, A. Cooper-Sarkar, A. D. Roeck, *et al.*, "PDF4LHC recommendations for LHC run 2," *Journal of Physics G: Nuclear and Particle Physics*, vol. 43, p. 023001, Jan. 2016.

[92] ATLAS Collaboration, "Measurement of the Z/γ * boson transverse momentum distribution in pp collisions at $\sqrt{s} = 7$ TeV with the ATLAS detector," *Journal of High Energy Physics*, vol. 2014, Sept. 2014.

[93] A. Djouadi, J. Kalinowski, and M. Spira, "Hdecay: a program for higgs boson decays in the standard model and its supersymmetric extension," *Computer Physics Communications*, vol. 108, p. 56–74, Jan. 1998.

[94] M. Spira *Fortschritte der Physik*, vol. 46, p. 203–284, Apr. 1998.

[95] A. Djouadi, M. M. Muhlleitner, and M. Spira, "Decays of supersymmetric particles: the program susy-hit (suspect-sdecay-hdecay-interface)," 2006.

[96] A. Bredenstein, A. Denner, S. Dittmaier, and M. M. Weber, "Radiative corrections to the semileptonic and hadronic higgs-boson decays h→ww/zz→4 fermions," *Journal of High Energy Physics*, vol. 2007, p. 080–080, Feb. 2007.

[97] A. Bredenstein, A. Denner, S. Dittmaier, and M. M. Weber, "Precise predictions for the higgs-boson decay h $\to ww/zz \to$ 4 leptons," *Physical Review D*, vol. 74, July 2006.

[98] A. Bredenstein, A. Denner, S. Dittmaier, and M. Weber, "Precise calculations for the higgs-boson decay h $\to zz/ww \to$ 4 leptons," *Nuclear Physics B - Proceedings Supplements*, vol. 160, p. 131–135, Oct. 2006.

[99] P. Nason and C. Oleari, "Nlo higgs boson production via vector-boson fusion matched with shower in powheg," *Journal of High Energy Physics*, vol. 2010, Feb. 2010.

[100] M. Ciccolini, A. Denner, and S. Dittmaier, "Strong and electroweak corrections to the production of higgs + 2 jets via weak interactions at the large hadron collider," *Physical Review Letters*, vol. 99, Oct. 2007.

[101] M. Ciccolini, D. A., and D. S., "Electroweak and qcd corrections to higgs pro-

duction via vector-boson fusion at the cern lhc," *Physical Review D*, vol. 77, Jan. 2008.

[102] P. Bolzoni, F. Maltoni, S.-O. Moch, and M. Zaro, "Higgs boson production via vector-boson fusion at next-to-next-to-leading order in qcd," *Physical Review Letters*, vol. 105, July 2010.

[103] M. L. Ciccolini, S. Dittmaier, and M. Krämer, "Electroweak radiative corrections to associatedwhandzhproduction at hadron colliders," *Physical Review D*, vol. 68, Oct. 2003.

[104] O. Brein, A. Djouadi, and R. Harlander, "Nnlo qcd corrections to the higgs-strahlung processes at hadron colliders," *Physics Letters B*, vol. 579, p. 149–156, Jan. 2004.

[105] O. Brein, R. V. Harlander, M. Wiesemann, and T. Zirke, "Top-quark mediated effects in hadronic higgs-strahlung," *The European Physical Journal C*, vol. 72, Feb. 2012.

[106] L. Altenkamp, S. Dittmaier, R. V. Harlander, H. Rzehak, and T. J. E. Zirke, "Gluon-induced higgs-strahlung at next-to-leading order qcd," *Journal of High Energy Physics*, vol. 2013, Feb. 2013.

[107] A. Denner, S. Dittmaier, S. Kallweit, and A. Mück, "Hawk 2.0: A monte carlo program for higgs production in vector-boson fusion and higgs strahlung at hadron colliders," *Computer Physics Communications*, vol. 195, p. 161–171, Oct. 2015.

[108] O. Brein, R. V. Harlander, and T. J. Zirke, "vh@nnlo—higgs strahlung at hadron colliders," *Computer Physics Communications*, vol. 184, p. 998–1003, Mar. 2013.

[109] R. V. Harlander, A. Kulesza, V. Theeuwes, and T. Zirke, "Soft gluon resummation for gluon-induced higgs strahlung," *Journal of High Energy Physics*, vol. 2014, Nov. 2014.

[110] S. Frixione, G. Ridolfi, and P. Nason, "A positive-weight next-to-leading-order monte carlo for heavy flavour hadroproduction," *Journal of High Energy Physics*, vol. 2007, p. 126–126, Sept. 2007.

[111] H. Hartanto, B. Jäger, L. Reina, and D. Wackeroth, "Higgs boson production in association with top quarks in the powheg box," *Physical Review D*, vol. 91, May

2015.

[112] R. D. Ball, V. Bertone, S. Carrazza, C. S. Deans, L. Del Debbio, S. Forte, A. Guffanti, N. P. Hartland, J. I. Latorre, J. Rojo, and M. Ubiali, "Parton distributions for the lhc run ii," *Journal of High Energy Physics*, vol. 2015, Apr. 2015.

[113] ATLAS Collaboration, "ATLAS Pythia 8 tunes to 7 TeV data," tech. rep., CERN, Geneva, 2014. All figures including auxiliary figures are available at https://atlas.web.cern.ch/Atlas/GROUPS/PHYSICS/PUBNOTES/ATL-PHYS-PUB-2014-021.

[114] D. J. Lange, "The EvtGen particle decay simulation package," *Nucl. Instrum. Methods Phys. Res. A*, vol. 462, pp. 152–155, Apr. 2001.

[115] E. Bothmann, G. Singh Chahal, S. Höche, J. Krause, *et al.*, "Event generation with sherpa 2.2," *SciPost Physics*, vol. 7, Sept. 2019.

[116] T. Gleisberg and S. Höche, "Comix, a new matrix element generator," *Journal of High Energy Physics*, vol. 2008, p. 039–039, Dec. 2008.

[117] F. Buccioni, J.-N. Lang, J. M. Lindert, P. Maierhöfer, *et al.*, "Openloops 2," *The European Physical Journal C*, vol. 79, Oct. 2019.

[118] F. Cascioli, P. Maierhöfer, and S. Pozzorini, "Scattering amplitudes with open loops," *Physical Review Letters*, vol. 108, Mar. 2012.

[119] A. Denner, S. Dittmaier, and L. Hofer, "Collier: A fortran-based complex one-loop library in extended regularizations," *Computer Physics Communications*, vol. 212, p. 220–238, Mar. 2017.

[120] S. Schumann and F. Krauss, "A parton shower algorithm based on catani-seymour dipole factorisation," *Journal of High Energy Physics*, vol. 2008, p. 038–038, Mar. 2008.

[121] S. Höche, F. Krauss, M. Schönherr, and F. Siegert, "A critical appraisal of nlo+ps matching methods," *Journal of High Energy Physics*, vol. 2012, Sept. 2012.

[122] S. Höche, F. Krauss, M. Schönherr, and F. Siegert, "Qcd matrix elements + parton showers. the nlo case," *Journal of High Energy Physics*, vol. 2013, Apr. 2013.

[123] S. Catani, F. Krauss, B. R. Webber, and R. Kuhn, "Qcd matrix elements + parton showers," *Journal of High Energy Physics*, vol. 2001, p. 063–063, Nov. 2001.

[124] S. Höche, F. Krauss, S. Schumann, and F. Siegert, "Qcd matrix elements and truncated showers," *Journal of High Energy Physics*, vol. 2009, p. 053–053, May 2009.

[125] C. Anastasiou, L. Dixon, K. Melnikov, and F. Petriello, "High-precision qcd at hadron colliders: Electroweak gauge boson rapidity distributions at next-to-next-to leading order," *Physical Review D*, vol. 69, May 2004.

[126] ATLAS Collaboration, "Studies on top-quark Monte Carlo modelling for Top2016," tech. rep., CERN, Geneva, 2016. All figures including auxiliary figures are available at https://atlas.web.cern.ch/Atlas/GROUPS/PHYSICS/PUBNOTES/ATL-PHYS-PUB-2016-020.

[127] R. D. Ball, V. Bertone, S. Carrazza, C. S. Deans, *et al.*, "Parton distributions with LHC data," *Nuclear Physics B*, vol. 867, p. 244–289, Feb. 2013.

[128] S. Alioli, P. Nason, C. Oleari, and E. Re, "NLO single-top production matched with shower in POWHEG: s- and t-channel contributions," 2009.

[129] R. Frederix, E. Re, and P. Torrielli, "Single-top t-channel hadroproduction in the four-flavour scheme with powheg and amc@nlo," *Journal of High Energy Physics*, vol. 2012, Sept. 2012.

[130] E. Re, "Single-top wt-channel production matched with parton showers using the powheg method," *The European Physical Journal C*, vol. 71, Feb. 2011.

[131] S. Frixione, E. Laenen, P. Motylinski, C. White, and B. R. Webber, "Single-top hadroproduction in association with awboson," *Journal of High Energy Physics*, vol. 2008, p. 029–029, July 2008.

[132] ATLAS Collaboration, "Cross-section measurements of the Higgs boson decaying into a pair of tau-leptons in proton-proton collisions at $\sqrt{s}$=13 TeV with the ATLAS detector," *Physical Review D*, vol. 99, Apr. 2019.

[133] ATLAS Collaboration, "Performance of the ATLAS muon triggers in Run 2," *Journal of Instrumentation*, vol. 15, no. 09.

[134] R. Ellis, I. Hinchliffe, M. Soldate, and J. Van Der Bij, "Higgs decay to $\tau + \tau - a$ possible signature of intermediate mass Higgs bosons at high energy hadron colliders," *Nuclear Physics B*, vol. 297, p. 221–243, Feb. 1988.

[135] A. Elagin, P. Murat, A. Pranko, and A. Safonov, "A new mass reconstruction technique for resonances decaying to di-tau," *Nuclear Instruments and Methods in Physics Research Section A: Accelerators, Spectrometers, Detectors and Associated Equipment*, vol. 654, p. 481–489, Oct. 2011.

[136] ATLAS Collaboration, "Jet energy resolution in proton-proton collisions at $\sqrt{s} =$ 7TeV recorded in 2010 with the ATLAS detector," *Eur. Phys. J. C Part. Fields*, vol. 73, p. 2306, Mar. 2013.

[137] G. Avoni, M. Bruschi, G. Cabras, D. Caforio, *et al.*, "The new LUCID-2 detector for luminosity measurement and monitoring in ATLAS," *JINST*, vol. 13, no. 07, p. P07017, 2018.

[138] ATLAS Collaboration, "Luminosity determination in pp collisions at $\sqrt{s} = 13$ TeV using the ATLAS detector at the LHC," tech. rep., CERN, Geneva, 2019. All figures including auxiliary figures are available at https://atlas.web.cern.ch/Atlas/GROUPS/PHYSICS/CONFNOTES/ATLAS-CONF-2019-021.

[139] J. K. Anders and M. D'Onofrio, "V+Jets theoretical uncertainties estimation via a parameterisation method," tech. rep., CERN, Geneva, 2016.

[140] "Final Tracking CP Recommendations for Run 2." https://twiki.cern.ch/twiki/bin/viewauth/AtlasProtected/TrackingCPRecsRun2Final, 2021. [Online; accessed 13-September-2024].

[141] "Algorithmn description." https://gitlab.cern.ch/atlas/statistics/SystematicSmoothingTool/-/blob/master/doc/algorithm_description.md. [Accessed 11-09-2024].

[142] F. Becherer. private communication, Sep. 2020.

[143] "Trexfitter." https://gitlab.cern.ch/ATauLeptonAnalysiS/TRExFitter. [Accessed 11-09-2024].

[144] K. Cranmer, G. Lewis, L. Moneta, A. Shibata, and W. Verkerke, "HistFactory: A tool for creating statistical models for use with RooFit and RooStats," tech. rep., New York U., New York, 2012.

[145] W. Verkerke and D. Kirkby, "The roofit toolkit for data modeling," 2003.

[146] G. Schott, "Roostats for searches," 2012.

[147] A. L. Read, "Linear interpolation of histograms," *Nucl. Instrum. Methods Phys. Res. A*, vol. 425, pp. 357–360, Apr. 1999.

[148] G. Cowan, K. Cranmer, E. Gross, and O. Vitells, "Asymptotic formulae for likelihood-based tests of new physics," *The European Physical Journal C*, vol. 71, Feb. 2011.

[149] ATLAS Collaboration, "The ATLAS Experiment at the CERN Large Hadron Collider: A Description of the Detector Configuration for Run 3," 2023.

List of figures

List of tables